

A STUDY OF JETS AT THE STAR EXPERIMENT
AT THE RELATIVISTIC HEAVY ION COLLIDER
VIA TWO-PARTICLE CORRELATIONS

by

LÉON GAILLARD

A thesis submitted to
The University of Birmingham
for the degree of
DOCTOR OF PHILOSOPHY

School of Physics and Astronomy
The University of Birmingham

Monday 10th March 2008.

Synopsis

Jets have been studied in high energy heavy ion collisions by measuring the angular correlation between particles at high transverse momentum. Differences in the yield and shape of the angular correlations as a function of system size give information on the medium produced in the collision. Such modifications can be used to infer the presence of a Quark-Gluon Plasma phase, wherein parton degrees of freedom are manifest over nuclear rather than nucleonic scales.

In the present work, two-particle correlations were studied in $d + Au$ and $Au + Au$ collisions at $\sqrt{s_{NN}} = 200$ GeV measured by the STAR experiment at RHIC. The technique was extended to include pseudo-rapidity, permitting jets to be characterised in two-dimensions, and enabling the jet shape to be studied in greater detail. Corrections were developed for the incomplete detector acceptance and finite two-track resolution. Both unidentified and identified particle correlations were studied, using charged tracks and neutral strange particles Λ , $\bar{\Lambda}$, and K_{Short}^0 reconstructed from their characteristic $V0$ decay topology.

The focus of the analysis was the correlation peak centred at zero azimuthal separation, which is significantly enhanced in central $Au + Au$ collisions compared to lighter systems. The modified peak was found to comprise a jet-like peak broadened in the pseudo-rapidity direction, sitting atop a long range pseudo-rapidity correlation. The former is suggestive of jet modification by the medium, and the latter may indicate a medium response to jets. Correlations with identified particles indicated the modified same side peak may in part be formed from particles originating from the underlying event.

Author's Contribution

The initial assignment given to the author was to study neutral strange particles reconstructed in $d+Au$ collisions at $\sqrt{s_{NN}} = 200$ GeV. Geometrical and dE/dx cuts were tuned to give populations of Λ , $\bar{\Lambda}$, and K_{short}^0 particles with low backgrounds. This cut analysis was later extended to $Au+Au$ datasets at $\sqrt{s_{NN}} = 62.4$ GeV and $\sqrt{s_{NN}} = 200$ GeV.

Two-particle correlations were produced using the reduced samples of $V0$ tracks and unidentified charged tracks in $d+Au$ and $Au+Au$ collisions at $\sqrt{s_{NN}} = 200$ GeV. Azimuthal, $\Delta\phi$, correlations were extended to two-dimensions by including pseudo-rapidity difference, $\Delta\eta$. To this end the author studied two-particle acceptance effects and developed algorithms to correct correlations. The author also studied two-track resolution, which affected many similar analyses and had not previously being accounted for. Two-track resolution was found to reduce extracted yields by $\sim 10\%$ in the momentum range considered in the analysis, and increased with the level of combinatorial background in correlations. The effect was therefore largest in central heavy ion collisions. An algorithm was developed to determine the degree of merging for a given pair of tracks, which was integrated with the acceptance correction process. This algorithm was generalised for any particle pair, including single charged tracks and secondary vertices including singly and multiply strange particles, so that it could be incorporated into other analyses. Studies of simulated pairs embedded into real data were also made to support this work.

In addition to the two-particle effects listed above, the present analysis also required reconstruction efficiencies and estimates of elliptic flow in the $Au+Au$ system. This project benefited from parameterisations of these two features that were offered

by colleagues who had studied them directly.

The author's time in the RHI group at Birmingham coincided with the installation of a new local computing farm. The author assisted in this process by testing a number of features of the new system, in particular its parallel processing capabilities. Scripts were developed to submit multiple processes to the farm via the Sun Grid Engine architecture.

As a member of the STAR collaboration, the author contributed to experimental operations. Throughout the term of the project several eight day shifts were undertaken, where the author formed part of the detector operating team at the STAR experiment. All shifts were during physics running periods, and the work entailed monitoring the detectors; bringing up systems to data-taking readiness at the start of a beam fill; adjusting the various configurations for different data and calibration arrangements; shutting down high voltage components prior to a beam dump; and responding to faults.

The author attended regular phone conferences and quarterly collaboration meetings, contributing to discussions of parallel analyses. Contributions were also made to draft papers circulated for collaboration review. The author additionally spent a week at Yale University, working with colleagues on correlation analyses. Finally, the author was fortunate to have the opportunity to present the results of this analysis at three international conferences dedicated to ultra relativistic heavy ion physics and quark-gluon plasma, and also was invited to give a plenary talk at the annual UK Nuclear Physics conference in 2006.

Acknowledgements

Here I would like to show my appreciation to those who have been the most instrumental in supporting my project. No doubt without all of their contributions this thesis could not have approached its final form. Four years is a long time to recall though, and so my apologies to anyone who deserves to be listed here but has been neglected.

First and foremost, to my supervisor Peter Jones. I could not have asked for a better introduction to this fascinating field of study, to which I arrived completely anew at the start of this project. I was fortunate to benefit from his thorough grasp of the subject, and a little of his understanding eventually passed to me after much effort on both sides. In terms of the analysis, his insights offered throughout the project were invaluable, and I'm very grateful for them. Finally, I also greatly appreciate the wealth of opportunities given to me by Peter to attend several international conferences and summer schools, each of which had a profound impact upon my work.

It has been a distinct privilege to undertake this research project in the School of Physics and Astronomy at the University of Birmingham, also the site my undergraduate studies. Many members of the institution have directly assisted me throughout my time here. Firstly, I would like to thank Lee Barnby and Matt Lamont for physics discussions, as well as introducing me to the STAR experiment and nuances of its computing infrastructure. Both offered a continuous stream of advice throughout the course of the work, graciously meeting a barrage of questions from myself, and whenever an answer was not immediately to hand, they often knew where to find it. Also, along with Peter, Matt and Lee introduced me to survival at

Brookhaven, and showed how to make trips to the site a more bearable experience, including a tour of the culinary delights available in the lab surroundings. I am also thankful for the guidance of John Nelson, John Adams, Gordon Squire, and Charles Blyth. Since my arrival to the group, several new members have helped me at all levels: Anthony Timmins, Tom Burton, and Marek Bombara. I will fondly remember winter visits to Long Island, digging out the car from a snow drift with only a waste paper bin to hand. Thanks to my colleagues the long hours spent in the STAR control room passed more swiftly, as did the hours outside of work. On a more serious note, I have come to understand the value of being able to discuss analysis issues with my contemporaries, and none more so than Marek who deserves special mention. Most recently the arrival of Essam Elhalhuli to the group gave me the opportunity to talk about my analysis in detail, and I hope our discussions proved as useful to Essam as they did to me.

At various times during the last four years I have benefited from the expertise and insight of other members of the Physics department at Birmingham, and in particular I would like to thank Tom Bloxham, Dave Price, and Peter Haigh for interesting conversations, and Neil Curtis, Nick Ashwood, Martin Freer, Dave Parker and Dave Forest for instructive lectures. I am also grateful to both Garry Tungate and Martin Freer for help on numerous occasions when physics got the better of me, and to Ray Jones for guidance on some of the mathematical techniques linked to my studies. Lastly I am thankful to the High Energy Physics group at Birmingham for allowing me to attend their programme of postgraduate lectures.

These acknowledgements would be incomplete without mention of several members of the STAR collaboration who have been particularly influential to my studies. Most notably I would like to thank Jana Bielcikova for her endless assistance at every stage of the analysis. I am also very grateful for the advice and direction offered to me by Ying Guo, Rene Bellwied, Joern Putschke, Helen Caines, Fuqiang Wang,

Mark Heinz, Mike Lisa, Marco van Leeuwen, Lanny Ray, Frank Laue, and Gene Van Buren. Thanks also to Betty Abelev, Christine Nattrass, Jason Ulery, Terry Tarnowsky, and Mark Horner. Outside of STAR, I would also like to express my gratitude to Thorsten Renk and Rudi Hwa, who both kindly boosted my understanding of current theory.

Finally I turn my attention to family. I would just like to give a special thanks to Mum and Dad, whom I hold entirely responsible for igniting my interest in the natural world. Lastly, my greatest debt of gratitude falls to my partner Geraldine. Completion of this thesis is thanks in large part to her tireless support through the darker moments of the last four years. Most of all, her choice to come to live in Birmingham allowed me to realise a lifetime dream of working at the frontier of understanding, and to make my own small contribution to the progress of Physics.

to G raldine

*L'absence diminue les mediocres passions et augmente les grandes,
comme le vent  teint les bougies et allume le feu.*

– *La Rochefoucauld c.1665*

Contents

1	Introduction	1
1.1	Quantum chromodynamics	2
1.1.1	Quark parton model	2
1.1.2	Confinement	4
1.1.3	Asymptotic freedom	5
1.1.4	Spontaneous chiral symmetry breaking	8
1.2	Nuclear matter at high temperature and density	9
1.2.1	Debye screening	9
1.2.2	Properties of a quark-gluon plasma	10
1.2.3	The phase diagram of strongly interacting matter	12
1.3	Ultra-relativistic heavy ion collisions	13
1.4	Highlights at RHIC	16
1.4.1	Collective flow	16
1.4.2	Suppression of high- p_T particles	17
1.4.3	Jet suppression	21
1.4.4	Summary	22
1.5	Outline of thesis	24
2	Theory	26
2.1	Jet phenomena	26

2.1.1	High- p_T particle production	26
2.1.2	Quark and gluon jets	30
2.2	Jets in heavy ion collisions	31
2.2.1	Models of parton attenuation	32
2.2.2	Comparisons to data	34
2.3	Particle production at intermediate- p_T	36
2.4	Hydrodynamics	38
2.4.1	Anisotropic transverse flow	39
3	Experimental Facility	42
3.1	The Relativistic Heavy Ion Collider	42
3.2	The Solenoidal Tracker At RHIC	43
3.3	The Time Projection Chamber	44
3.4	Event triggering	47
3.5	Event reconstruction	50
3.6	Off-line centrality selection	51
3.7	Particle identification and neutral strange particle reconstruction . . .	52
3.7.1	Embedding	58
4	Azimuthal two-particle correlations	62
4.1	Introduction	62
4.2	Procedure	63
4.2.1	Single particle reconstruction efficiency	64
4.3	Correlation function for $d + Au$ collisions	65
4.3.1	Physical interpretation of azimuthal correlations	67
4.3.2	Trigger bias	67
4.4	Correlation function for $Au + Au$ collisions	68
4.4.1	Elliptic flow in two-particle correlations	70

4.4.2	Estimation of combinatorial background level	72
5	Two-dimensional correlations	74
5.1	Introduction	74
5.2	Pair-wise acceptance	75
5.2.1	Introduction to event mixing	76
5.2.2	Event selection	80
5.2.3	Acceptance-corrected correlations	81
5.2.4	Summary	85
5.3	Two-track resolution	86
5.3.1	Detailed diagnosis of the dip in unidentified correlations . . .	88
5.3.2	Genuine track merging observed in low momentum correlations	91
5.3.3	Studies of track merging with embedded pairs	92
5.3.4	Mirror image correction	93
5.3.5	Introduction to anti-merging algorithms	93
5.3.6	Hit determination from track helices	95
5.3.7	Fraction of merged hits cut in the anti-merging correction . .	99
5.3.8	Limitations of anti-merging algorithms integrated with mixed events	103
5.3.9	Conclusion	105
5.4	Analysis of the same side peak	105
5.4.1	Projection of the same side peak onto $\Delta\phi$ and $\Delta\eta$ axes . . .	106
5.4.2	Estimations of the jet and ridge components in the same side peak	108
6	Results	112
6.1	Introduction	112
6.2	Unidentified Correlations	113

6.2.1	Minimum bias $d + Au$ collisions	113
6.2.2	Minimum bias $Au + Au$ collisions	119
6.2.3	Central $Au + Au$ collisions	123
6.2.4	Discussion	128
6.3	Correlations involving $V0$ tracks	131
6.3.1	Minimum bias $Au + Au$ collisions	133
6.3.2	Central $Au + Au$ collisions	135
6.3.3	Correlations with associated $V0$ tracks	138
6.3.4	Discussion	138
6.4	Summary of research findings	141
7	Interpretation and Outlook	142
7.1	Theoretical treatments of modifications to the same side peak	142
7.1.1	Coupling to longitudinal flow	142
7.1.2	Coupling to radial flow	144
7.1.3	Parton recombination	144
7.1.4	Non-equilibrium QGP	146
7.2	Recent studies of away side peak	146
7.2.1	Re-emergence of di-jets at high- p_T	146
7.2.2	Medium response to jets at low- p_T	147
7.3	Prospects for correlation analyses	149
7.3.1	Correlations with identified particles	150
7.3.2	Three particle analysis of the same side	151
7.3.3	Momentum-weighted correlations	152
7.3.4	Outlook	153
	Appendices	154
A	Collision Kinematics	155

B	Physical interpretation of correlation peak widths	161
B.1	Same side width	161
B.2	Away side width	162
C	Non-jet contributions in two-particle correlations	164
C.1	Uncorrelated background	164
C.2	Momentum conservation in two-particle correlations	166
C.3	Elliptic flow in two-particle correlations	169
D	Software and Infrastructure	171
D.1	Data Filtering	171
D.2	Correlation pipeline using a dedicated local farm	172
	References	175
E	Published Proceedings to the Conference:	
	Hot Quarks 2006	182

List of Figures

1.1	Quark Confinement	5
1.2	Running of strong coupling	6
1.3	Vacuum polarisation in QED and QCD	8
1.4	Lattice QCD predictions of QGP phase transition	11
1.5	Phase diagram of QCD	12
1.6	Collision centrality, impact parameter, and reaction plane	14
1.7	Simulation of a ultra-relativistic heavy ion collision viewed from the c.m.s. frame	14
1.8	Space-time evolution of an ultra-relativistic nuclear collision	15
1.9	Elliptic flow at RHIC	17
1.10	Schematic representation of di-jets in nuclear collisions	19
1.11	High- p_T suppression observed in $Au + Au$ collisions at STAR	20
1.12	Meson-Baryon difference at intermediate- p_T in $Au + Au$ collisions	21
1.13	Two-particle correlations at RHIC indicating jet suppression	23
2.1	Parton distribution functions of the proton, observed at ZEUS [5].	27
2.2	Calculated relative abundance of quark and gluon jets in $p + p$ collisions at $\sqrt{s_{NN}} = 200$ GeV	28
2.3	Fragmentation functions in e^+e^- annihilations	29
2.4	Λ and K_{Short}^0 production in quark and gluon jets at OPAL	32
2.5	Nuclear modification factor compared to calculations	35

2.6	Nuclear modification factor of direct photons in $Au + Au$ collisions at $\sqrt{s_{NN}} = 200$ GeV at RHIC	36
2.7	Baryon enhancement at intermediate- p_T in $Au + Au$ collisions at $\sqrt{s_{NN}} = 200$ GeV at RHIC	38
2.8	Predicted spatial and momentum anisotropy as a function of time for a $Au + Au$ collision	40
3.1	Schematic plan view of the RHIC accelerator-collider facility	43
3.2	The main detectors of the STAR experiment	44
3.3	The Time Projection Chamber at STAR	45
3.4	The TPC proportional region	46
3.5	Cathode pad rows on one sector of the TPC	47
3.6	Distribution of CTB and ZDC signals for $Au + Au$ events at $\sqrt{s_{NN}} = 200$ GeV	48
3.7	Reconstructed tracks from TPC hits, as viewed parallel to the beam axis	51
3.8	Reference multiplicity distribution for off-line centrality definition	52
3.9	Particle identification by energy loss of tracks, dE/dx	53
3.10	V0 reconstruction, detailing geometric cut parameters	54
3.11	Demonstration of geometrical cut tuning	55
3.12	Invariant mass spectra for V0 candidates in $Au + Au$ collisions at $\sqrt{s_{NN}} = 200$ GeV after geometrical cuts have been applied	57
3.13	Reconstructed trigger particle spectra for a sample of 20 million 0 – 10% central $Au + Au$ events from the online central triggered dataset.	58
3.14	Parameterisation of primary track reconstruction efficiency	60
3.15	Parameterisation of charged π reconstruction efficiencies for nine centrality bins, as a function of momentum and pseudorapidity.	61

4.1	Schematic representation of a di-jet overlaying a real heavy-ion collision observed in the STAR TPC	63
4.2	Schematic representation of a two-particle correlation.	64
4.3	Two-particle correlation function in $d + Au$ collisions at $\sqrt{s_{NN}} = 200$ GeV	66
4.4	Two-particle correlation function in $Au + Au$ collisions at $\sqrt{s_{NN}} = 200$ GeV	69
4.5	$v_2\{2\}$, $v_2\{4\}$ and $v_2\{6\}$ for charged hadrons produced in $Au + Au$ collisions at $\sqrt{s_{NN}} = 200$ GeV measured at STAR [32] as a function of centrality. . .	73
5.1	Reconstructed primary track pseudo-rapidity and azimuthal distributions	76
5.2	Raw two-particle correlation of primary tracks in 0-10% central $Au + Au$ events at $\sqrt{s_{NN}} = 200$ GeV	77
5.3	Schematic representation of the event buffer mixing routine.	78
5.4	Unidentified $\Delta\eta$ - $\Delta\phi$ correlations in $d + Au$ collisions at $\sqrt{s_{NN}} = 200$ GeV	83
5.5	Unidentified $\Delta\eta$ - $\Delta\phi$ correlations in 0–10% central $Au + Au$ collisions at $\sqrt{s_{NN}} = 200$ GeV	84
5.6	Two track resolution in unidentified $\Delta\eta - \Delta\phi$ correlations	86
5.7	Detailed inspection of $\Delta\eta - \Delta\phi$ correlations of unidentified charged tracks with small opening angles revealing four distinct dips	88
5.8	Detailed inspection of $\Delta\eta - \Delta\phi$ correlations of unidentified charged tracks, separated into charge combinations	89
5.9	Relationship between dip location and the minimum and maximum azimuthal separations of two tracks that cross within the STAR TPC active volume	90
5.10	Genuine track merging observed in low momentum correlations	92

5.11	Helix parametrisation.	96
5.12	Hit positions inferred from helix parameters of charged tracks	97
5.13	Results of anti-merging algorithm applied to mixed event pairs. . . .	100
5.14	$\Delta\eta - \Delta\phi$ correlations after applying a maximal anti-merging cut . . .	100
5.15	Side by side comparison of corrected $\Delta\eta$ projections before and after applying the anti-merging algorithm with $f_{mh} < 0.1$	101
5.16	Estimation of enhancement offered by the anti-merging algorithm for correlations with unidentified, K_{Short}^0 , and $\Lambda + \bar{\Lambda}$ triggers	102
5.17	The percentage increase to the $\Delta\phi$ jet yield component of the same side peak following correction for track merging.	104
5.18	Visualisation of function used to analyse same side peak	107
5.19	Projection analysis of $\Delta\eta - \Delta\phi$ correlations.	111
6.1	Pair statistics for correlations in a selection of 20 million 0 – 10% central $Au + Au$ collisions at $\sqrt{s_{NN}} = 200$ GeV	114
6.2	Correlation functions of unidentified charged tracks in minimum bias $d + Au$ collisions with $p_T^{asso.} > 2.0$ GeV/c and three $p_T^{trig.}$ intervals . .	116
6.3	Same side peak characteristics as a function of $p_T^{trig.}$, for unidentified charged track correlations in minimum bias $d + Au$ collisions with $p_T^{asso.} > 2.0$ GeV/c	117
6.4	Same side peak characteristics as a function of $p_T^{asso.}$, for unidentified charged track correlations in minimum bias $d + Au$ collisions with $3.0 \leq p_T^{trig.} \leq 6.0$ GeV/c	118
6.5	Correlation functions of unidentified charged tracks in minimum bias $Au + Au$ collisions for three centrality bins	120
6.6	Same side peak properties for correlations of unidentified charged tracks in minimum bias $Au + Au$ collisions as a function of centrality, with $3.0 \leq p_T^{trig.} \leq 6.0$ GeV/c and $2.0 \leq p_T^{asso.} \leq p_T^{trig.}$	121

6.7	Same side peak properties for correlations of unidentified charged tracks in 0 – 10% central $Au + Au$ collisions as a function of $p_T^{trig.}$. .	125
6.8	Same side peak characteristics as a function of $p_T^{asso.}$ in correlations of unidentified charged tracks in 0 – 10% central $Au + Au$ collisions with $3.0 \leq p_T^{trig.} \leq 6.0$ GeV/c	127
6.9	Correlations in central $Au + Au$ collisions involving Λ , $\bar{\Lambda}$, and K_{Short}^0 trigger tracks	132
6.10	Same side peak properties for correlations with Λ , $\bar{\Lambda}$, and K_{Short}^0 triggers tracks in minimum bias $Au + Au$ collisions as a function of centrality, with $3.0 \leq p_T^{trig.} \leq 6.0$ GeV/c and $2.0 \leq p_T^{asso.} \leq p_T^{trig.}$	134
6.11	Same side peak properties for correlations with Λ , $\bar{\Lambda}$, and K_{Short}^0 triggers tracks in 0 – 10% central $Au + Au$ collisions as a function of $p_T^{trig.}$	136
6.12	Same side peak properties for correlations with Λ , $\bar{\Lambda}$, and K_{Short}^0 triggers tracks in 0 – 10% central $Au + Au$ collisions as a function of $p_T^{asso.}$	137
6.13	Total same side yields as a function of $p_T^{trig.}$ and $p_T^{asso.}$ of correlations with identified associated particles in 0 – 10% central $Au + Au$ collisions.	139
7.1	Schematic representation of longitudinal flow coupled to jet attenuation.	143
7.2	Re-emergence of di-jets at high- p_T	147
7.3	Away side peak enhancement at intermediate- p_T	148
7.4	Intermediate- p_T three-particle correlations	150
A.1	Schematic representation of hard scatter between constituent partons, factorised into non-perturbative and perturbative elements.	156
B.1	Schematic representation of the same side peak in a two particle correlation	162
B.2	Schematic representation of the away side peak in a two particle correlation	163

C.1	Convolution of trigger and associated particle pseudorapidity distributions	165
C.2	Convolution of trigger and associated particle azimuthal distributions	166

Chapter 1

INTRODUCTION

At present, four fundamental forces are believed to account for all interactions in nature: gravitation, electromagnetism, and the weak and strong nuclear forces. Each of these can be described in terms of virtual mediating particles called exchange bosons, whose properties dictate the strength and range of the force. The latter is characterised by the exchange particle's energy, which can be borrowed from the vacuum for a duration limited by the uncertainty principle. Indeed an interaction may take place via several virtual particles, and as this detailed behaviour cannot be observed, all possible arrangements contribute to the cross-section of a particular process.

The theories of both electromagnetism and the weak interaction have been experimentally verified to high precision. This great achievement is thanks largely to the availability of free elementary charged and weakly interacting particles (electrons and neutrinos) in nature. Additionally, the coupling strengths of these interactions are small, and hence the simpler diagrams of virtual particles dominate calculations of cross-sections.

Unfortunately, studies of the strong interaction are more challenging. Theoretical approaches suffer from the need to consider large coupling strengths. Moreover all observed hadrons (particles that interact strongly) in nature are composite par-

ticles, which hampers experimental investigations. In order to understand these observations, and how these limitations might be overcome, it is first necessary to review the theory of the strong interaction, quantum chromodynamics (QCD).

1.1 Quantum chromodynamics

The strong nuclear force binds nucleons (protons and neutrons) into nuclei and is responsible for the periodic table of elements, from which the visible universe is formed. Nucleons are however not elementary hadrons. Thus despite its prevalence, the fundamental interactions by which the strong force acts are to a large extent hidden. The reason for this is inherent to the nature of the strong force, for unlike electromagnetism, the weak interaction and gravity, strong exchange bosons (gluons) carry (colour) charge. This allows gluons to interact independently, which substantially complicates the dynamics of strongly bound systems.

1.1.1 Quark parton model

In the early 1960s particle accelerators surpassed an energy frontier, allowing the interiors of nucleons to be revealed [1]. Bjorken showed that the differential electron-nucleus cross-section could be explained assuming protons and neutrons to be composite bodies of point-like partons [2]. This interpretation transformed the theory of the strong interaction from a set of scattering amplitudes, to elementary particle interactions more akin to electromagnetism and the weak interaction.

Another feature of early accelerator experiments was the huge variety of observed hadronic states. At a similar time to the discovery of partons, the quark model was devised to describe the multiplicity of hadronic states [3]. It appeared that all hadrons could be described as combinations of fractionally charged, spin $\frac{1}{2}$ ‘quarks’ and ‘anti-quarks’: (anti-) baryons contain three (anti-) quarks, and mesons

are quark–anti-quark pairs. At the time, three varieties, or ‘flavours’, of quarks were needed to account for charge, isospin and strangeness. There are now understood to be six quark flavours: the original u (up), d (down), and s (strange), are accompanied by c (charm), b (bottom), and t (top). The model gained credibility through predictions of formerly unknown states that were later confirmed experimentally.

The discovery of the Δ^{++} baryon posed a problem: the model described it as three up-quarks with parallel spins and symmetric spatial wavefunctions. As quarks are fermions, the Pauli exclusion principle demanded the inclusion of an additional quantum number. This quantum number is not exhibited by observed hadrons and so it must sum to zero in these states. It was postulated that quarks possess one of three ‘colours’: red, green, blue, with anti-quarks possessing anti-colour. The three colours sum to ‘white’ or ‘colourless’ as do combinations of colour and anti-colour. The fact that only baryons and mesons appear to exist suggests that other combinations of colour are unbound. Since nucleons are colour-neutral, their binding within nuclei must be a residual interaction, somewhat analogous to the Van der Waal force between electrically neutral atoms, and is understood in terms of the exchange of hadronic bosons (mesons) [4].

Quarks are identified with partons, and together are described in the quark-parton model (QPM). The interiors of hadrons are described in terms of parton distribution functions (PDF), which describe the probability of finding a particular parton i inside the hadron with a given fraction of the hadron momentum, x . Deep inelastic electron-nucleon scattering experiments indicate that hadrons contain large populations of partons, quarks, anti-quarks and gluons, particularly at low x [5]. This observation is consistent with the QPM description of hadrons, providing the

net content of a hadron obeys a sum rule. For example in the case of protons,

$$\begin{aligned}\Sigma u &= \int_0^1 dx(u(x) - \bar{u}(x)) = 2 \\ \Sigma d &= \int_0^1 dx(d(x) - \bar{d}(x)) = 1 \\ \Sigma s &= \int_0^1 dx(s(x) - \bar{s}(x)) = 0,\end{aligned}$$

where Σu , Σd and Σs represent the total number of u , d , and s flavours. As for strangeness, other flavours sum to zero for protons. The net quarks are labelled the valence quarks.

1.1.2 Confinement

Neither free quarks, nor any open colour charges have been observed in nature. This absence can be understood by considering what happens when two quarks are pulled apart. As illustrated schematically in figure 1.1, short range strong interactions can be described by single gluon exchange, and at larger separations more gluons can form between the charge centres. On a fundamental level, the strong interaction is described as a colour exchange reaction, and for this to be possible gluons must themselves carry colour. Consequently gluons can strongly interact with each other independently of quarks. This self interaction confines the gluons between our two conceptual quarks into a *flux tube*, or *string* [6, 7]. As a result the nuclear potential follows a linear dependence; a behaviour similar to that of a stretched spring. Taking into account these two features, the strong interaction potential between two quarks can be written

$$V(r) = -\frac{4\alpha_S}{3r} + kr, \tag{1.1}$$

where r is the separation between the interacting quarks; α_S is the strong coupling

1.1. QUANTUM CHROMODYNAMICS

constant; and k is the equivalent tension of the flux tube. A lattice QCD calculation of the potential between two heavy quarks is shown in figure 1.1 [7]. As the two quarks are drawn further apart, the potential energy stored in the flux tube increases, until eventually the tension exceeds the energy required to create a new $q - \bar{q}$ pair. At this point the tube breaks, a new quark and anti-quark appear at the ends, and colour confinement is preserved independently in two separate hadrons.

Confinement not only governs the size of nucleons, but is also responsible for generating most of their mass¹. The bare masses of the lightest quarks, u, d , are expected to be $\lesssim 10$ MeV, compared to the mass of a nucleon ~ 1 GeV. Quark masses feature as scale-dependent parameters in QCD, and u, d, s quarks are often treated as massless in calculations. No direct experimental estimation of bare quark masses has been devised to date.

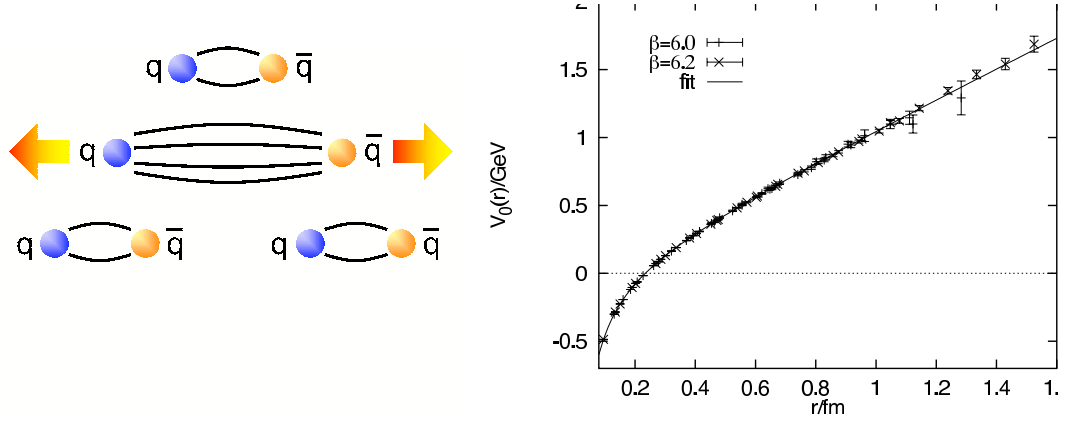


Figure 1.1: Left: Schematic description of confinement for a quark–anti-quark pair drawn apart, forming a new pair. Black lines represent field lines constrained into a fluxtube due to gluon self-interaction. Right: Lattice QCD calculation of the static nuclear potential between two heavy quarks [7].

1.1.3 Asymptotic freedom

According to equation (1.1), the strong interaction becomes inversely proportional to separation as $r \rightarrow 0$. However, the coupling α_S is also dependent upon r , which

¹This is the case for all hadrons containing only u, d, s valence quarks.

1.1. QUANTUM CHROMODYNAMICS

is inversely proportional to Q^2 .

$$\alpha_S(Q^2) = \frac{\alpha_S(\mu^2)}{[1 + (\alpha_S(\mu^2))^{\frac{33-2n_f}{12\pi}} \ln(\frac{Q^2}{\mu^2})]} \quad (1.2)$$

The coupling strength is expressed in terms of $Q^2 = -q^2$, where q is the four-momentum transfer of the interaction in which α_S is being measured. This is related to the range of the interaction by the uncertainty principle and is a more appropriate quantity to consider as it is directly observable. Unlike the electromagnetic interaction, the coupling cannot be scaled with respect to the coupling at infinite separation. Instead, a particular range, μ^2 , is chosen. The critical figure is the number of flavours, $n_f = 6$, which means that α_S decreases to zero as $Q^2 \rightarrow \infty$ or $r \rightarrow 0$. This dominates over the dependence in equation (1.1), and therefore the strong interaction asymptotically decreases as $r \rightarrow 0$. Figure 1.2 presents results from e^+e^- collisions studied at LEP demonstrating the variation of α_S with the collision energy [8].

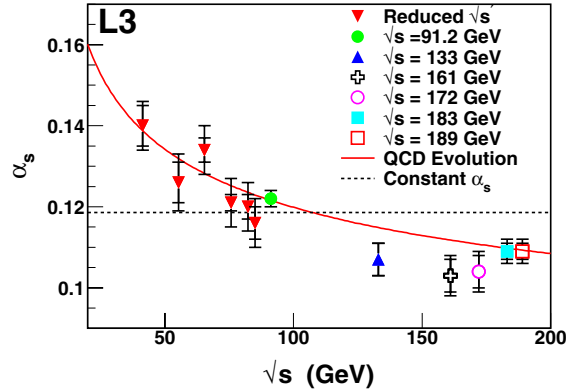


Figure 1.2: Running of α_S from hadronic event shapes at LEP, measured by L3 [8]. The mean Q^2 increases with increasing collision energy, \sqrt{s} .

The variation of α_S with separation can be explained by considering the action of the QCD vacuum. For QED, the vacuum is populated by virtual photons and virtual electron—positron pairs. These act like mini-dipoles and will become polarised by the electric field of a real charge, just like a dielectric medium, as shown in figure 1.3a.

The observable outcome is that the measured charge of, say, an electron, increases asymptotically with the momentum of the probe, up to the bare charge. This is due to charge screening by virtual positron—electron pairs. In QCD the same process occurs for colour charges and polarised virtual quark—anti-quark pairs screen the bare colour. However, the QCD vacuum is complicated by the charge carried by gluons, as shown in figure 1.3b. In fact, the gluon contribution causes anti-screening of the bare charge, and the gluon degrees of freedom dominate over the screening effect of virtual $q - \bar{q}$ pairs. Consequently the strong interaction weakens at small separations, and moreover the theory is asymptotically free at zero separation. One can begin to understand the behaviour of the gluons by analogy to a paramagnetic medium [9]. The virtual gluons can be thought of as colour magnetic dipoles which align in the presence of the colour field of a test quark. At suitably high energies, the resolving power of the projectile is much smaller than the size of a nucleon, which therefore appears as a collection of independent partons (for the purpose of the initial interaction). Thus the parton-parton scattering cross-section can be calculated via a perturbative treatment of QCD, using the same analytical tools as employed in QED calculations.

Taking the premise of a running strong coupling parameter one step further, one leads to the remarkable prediction that under extremely high density, nuclear matter reduces to a system of non interacting partons. This novel state of nuclear matter is commonly called the Quark-Gluon Plasma (QGP). In transition from confined nuclear matter to a QGP, hadrons would lose ownership of their constituent partons, which would be free to propagate across the whole extent of the medium. Indeed the concept of a hadron would no longer apply. Governed by parton degrees of freedom with vanishing α_S , a QGP would offer a useful testing ground for pQCD in bulk nuclear matter.

An asymptotically free QGP is not expected to exist naturally in the observable

1.1. QUANTUM CHROMODYNAMICS

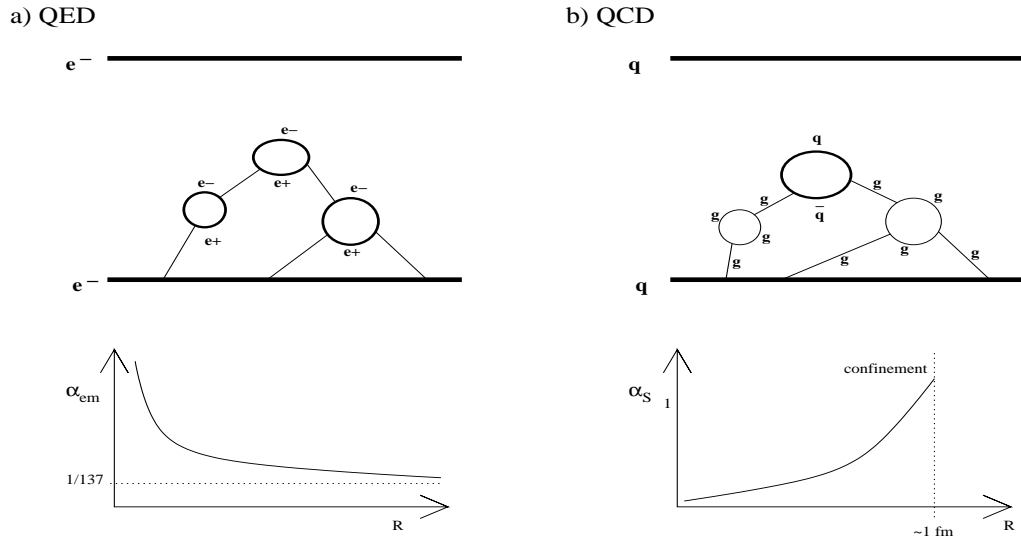


Figure 1.3: Vacuum polarisation in QED leads to shielding of the electric charges. The QCD vacuum differs from the QED vacuum because of the self interaction of gluons, which causes an overall anti-shielding of colour charges.

universe, as the necessary energy density is not believed to be reached in compact stellar bodies before the Chandrasekhar limit is exceeded and a black hole is formed. However, the early universe may have undergone a phase transition from a asymptotically free QGP shortly after the Big Bang.

1.1.4 Spontaneous chiral symmetry breaking

A large part of hadronic mass is attributed to the dynamical behaviour of the quarks and gluons, but this is not the whole story. For massless quarks, one would expect mass degenerate hadrons with equal spin and opposite parity. This is due to chiral symmetry: travelling at the speed of light, massless particles possess helicity, or chirality, defined as the vector product of spin and momentum. Helicity would be unaffected by gluon exchange, thus left-handed and right-handed quarks would not interact by this means.

Although the lighter quarks have small bare masses, in hadrons they exhibit large constituent masses $\sim 300 \text{ MeV}/c^2$, and thus chiral symmetry is spontaneously

broken. In nature chiral partner hadrons do have mass differences; moreover, these typically represent large fractions of the hadron mass, indicating that not only chiral symmetry is broken but also that it is a significant feature to the hadron spectrum.

In an asymptotically free QGP quarks are described by their bare masses. Thus as the asymptotic limit is approached, chiral symmetry may be restored for at least the lighter quark flavours.

1.2 Nuclear matter at high temperature and density

For high energy, short range interactions where $\alpha_S \ll 1$, pQCD accurately describes the cross-sections of observed phenomena, such as the scattering cross-sections of constituent partons. Detracting from this great success is the divide between the perturbative regime and that of the interactions responsible for hadronic spectra. The interiors of baryons and mesons are necessarily governed by many body, low Q^2 dynamics. However, if it were possible to promote matter to the asymptotic QGP state, then QCD could be tested in a system where colour degrees of freedom are manifest and the coupling α_S is small. The high energy density required poses a challenge to reaching the asymptotic limit experimentally. Fortunately, deconfined QCD matter may exist away from the asymptotic limit.

1.2.1 Debye screening

Long before approaching the asymptotic limit, nuclear matter would reach a density where the classical boundaries of nucleons would overlap. In bulk QCD matter the phenomenon that gives rise to parton deconfinement is Debye screening, which is analogous to the Mott transition of insulator to conductor for media subjected to external pressure [10]. In condensed matter when atoms are forced together

their outer electron shells eventually begin to overlap, developing a delocalised electron shell (conduction band) from part of the valence band. A similar transition is expected to occur for densely packed nuclear matter, with constituent quarks becoming free to propagate over nuclear distance scales. The screening of colour centres by the medium relaxes colour confinement. Individual colour charges only interact with neighbours within the Debye radius, which also defines the criterion for deconfinement. The classical electromagnetic definition can be written

$$V_{screened}(r) = \frac{Q_1 Q_2}{4\pi\epsilon r} \exp\left(\frac{-r}{R_{Debye}}\right) \quad (1.3)$$

$$R_{Debye} \sim \frac{1}{\sqrt[3]{n}}$$

where n is the number density of charges in the system. Debye screening may be accompanied by (partial) restoration of chiral symmetry for light quark flavours, or deconfinement and chiral symmetry restoration may be separate transitions.

1.2.2 Properties of a quark-gluon plasma

Lattice QCD offers predictions of the critical parameters associated to the transition to a QGP, and the order of the transition to hadronic nuclear matter [11, 12]. Predictions of dynamic quantities such as pressure and energy density are usually presented in the literature divided by the fourth power of the temperature, which isolates the behaviour of the degrees of freedom. This is an appropriate factor because in the limit of asymptotic freedom and massless quarks, a QGP would behave as an ultra-relativistic ideal gas and be described in terms of the Stefan-Boltzmann law. With consideration to the number of degrees of freedom for gluons and quarks respectively, one arrives at the relation for the pressure [13],

$$\frac{p_{SB}}{T^4} = \left[2(N_c^2 - 1) + 2N_c N_f \frac{7}{4} \right] \frac{\pi^2}{90} \quad (1.4)$$

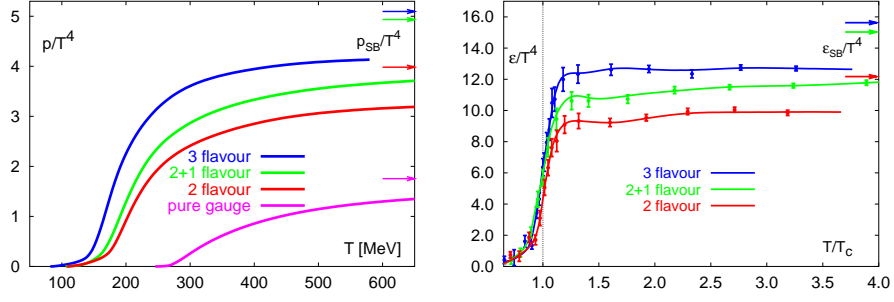


Figure 1.4: The pressure (left) and energy density (right) of strongly interacting matter predicted by lattice QCD. Several combinations of light and heavy quarks have been considered, including a pure gluonic system. Arrows indicate ideal relativistic gas values [11].

where N_c is the number of colours, N_f the number of flavours, and the factor $\frac{7}{4}$ arises from the different degrees of freedom for the quark fermions and gluon bosons.

The critical temperature of the anticipated phase transition depends upon the specific mix considered in the calculation, for instance [11] predicts $T_c = 173 \pm 8$ MeV (2 flavours) $T_c = 154 \pm 8$ MeV (3 flavours). The expected order of the transition also depends on the number of quark flavours considered [12]. As the temperature of the lattice passes this temperature, the energy density rises sharply, reflecting an increase in the number of degrees of freedom. The results suggest a critical energy density of ~ 0.7 GeV/fm³; the energy density of a ‘cold’ nucleus is ~ 0.1 GeV/fm³. The predicted pressure and energy density evolution through the phase transition are shown in figure 1.4. The quantity appears to saturate just above the critical temperature, but at a notably lower level than $\frac{p_{SB}}{T^4}$, suggesting considerable strong interactions persist in the QGP phase (i.e. the transition is far from asymptotic limit). Chiral symmetry restoration is often predicted by lattice calculations to accompany the hadron-QGP phase transition. A substantial modification to hadron masses would be expected in the medium, which could lead to different relative particle abundance observed experimentally [14].

1.2.3 The phase diagram of strongly interacting matter

The notion of nuclear matter existing in different states leads to the phase diagram of strongly interacting matter [13], as shown in figure 1.5. Three distinct phases of matter are shown in the diagram, which are defined in terms of temperature, T , and quark chemical potential, μ (net baryon density). Solid lines indicate first order transitions. For low temperature and chemical potential, strongly interacting matter exists in the hadronic phase. The nuclear ground state is shown at $(T, \mu) = (0, 308)$ MeV. A solid line extending from this point indicates the liquid-gas phase transition for hadrons, which only exists for temperatures below 10 MeV.

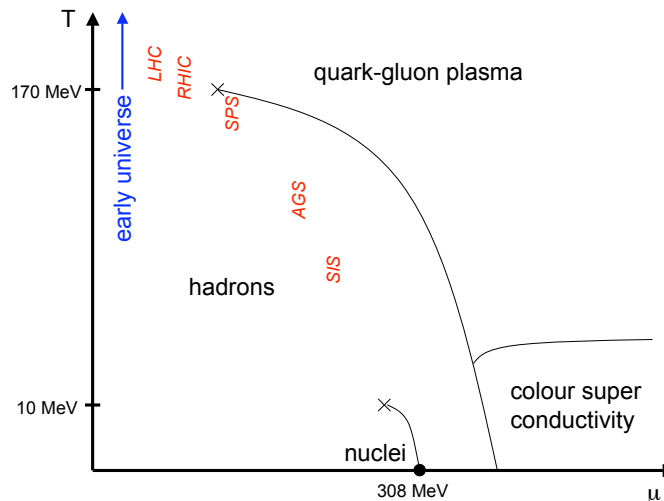


Figure 1.5: The (schematic) phase diagram of strongly interacting matter as a function of temperature and chemical potential. Solid lines indicate first order transitions. The ground state is shown at zero temperature and $\mu = 308$ MeV. The short line leading from this point indicates the liquid-gas phase transition for hadrons. The conditions observed or expected at several experimental facilities are indicated in red. Adapted from [13].

Heating the hadronic phase constitutes increasing the density of on-shell pions, which emerge from the vacuum. Hence the hadronic regime is often characterised in terms of the vacuum condensate $\langle q\bar{q} \rangle \neq 0$. As shown in the figure, the transition to QGP should be second order for low chemical potentials, and a critical point should exist. Predictions from Lattice QCD suggest the location of the critical point is

sensitive to the specific mix of quark flavours and masses [13]. The QGP present in the early universe would be found at the top left of the phase diagram, as the amounts of matter and anti-matter were approximately equal.

Although it is not the focus of this project, in order to present a complete picture of the phase diagram, it should be noted that at least one phase of superconducting quark-matter is expected at low temperature and high chemical potential. In this region another non-zero condensate would be found, $\langle qq \rangle \neq 0$, relating to Cooper pairing of quarks. Superconducting quark-matter may exist naturally in compact stellar cores, such as the interior of neutron stars.

1.3 Ultra-relativistic heavy ion collisions

In order to promote ordinary nuclear material into a deconfined state, the energy density must be increased via the application of heat and pressure. Ultra-relativistic heavy ion collisions are a candidate for producing high temperature – low baryon density QGP, qualitatively similar to the early universe. The order of the phase transition and the properties of the deconfined medium are characterised by the (quark) chemical potential and energy density, as illustrated in section 1.2.3 above. These can be varied by changing the collision energy per nucleon-nucleon collision, $\sqrt{s_{NN}}$, and, to some extent, the choice of projectiles. The impact parameter defines the amount of participating matter, as illustrated in figure 1.6. This cannot be measured experimentally; instead, the observed multiplicity is used. This is expressed in terms of the collision centrality, which ranges from 0 – 100% from head-on to peripheral collisions.

Figure 1.7 displays ‘snap shots’ of a simulated nuclear collision at $\sqrt{s_{NN}} = 200$ GeV observed from the centre-of-momentum frame. The nuclear projectiles appear almost transparent to each other, resulting in a baryon to anti-baryon ratio close to unity in the system of produced particles [16, 17]. Expansion in the transverse plane

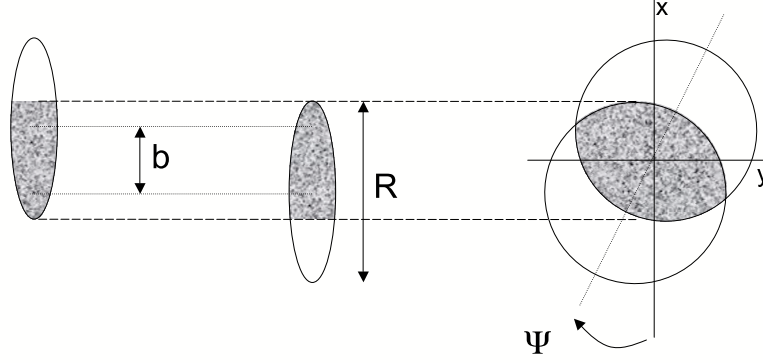


Figure 1.6: The geometrical overlap of a non-central nuclear collision, illustrated in a plane parallel to the beam axis (left), and in the transverse plane (right). Impact parameter, b , is the separation of the nuclear centres. The angle between the reaction plane and laboratory co-ordinates is labelled Ψ .

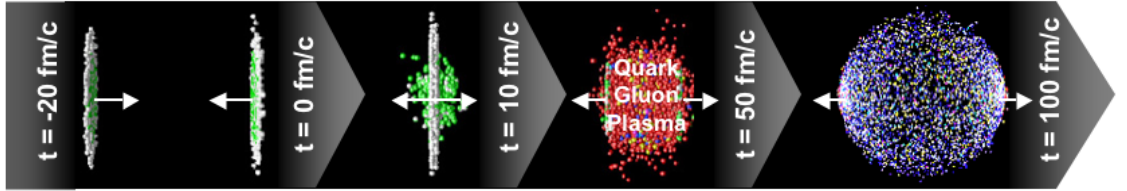


Figure 1.7: Simulation of a ultra-relativistic heavy ion collision viewed from the c.m.s. frame [15].

is driven by pressure gradients, which are anisotropic except for head-on collisions involving spherical projectiles. The initial energy density, estimated from the total transverse energy E_T of observed particles [18], significantly exceeds that predicted by Lattice QCD calculations for the phase transition [19, 11]. Thus the system produced is situated towards the upper left of the phase diagram shown in figure 1.5. The slope of the transverse momentum, p_T , distribution gives an indication of the system temperature. In the longitudinal direction rapidity, y , is the preferred quantity used to describe the system. See appendix A for an introduction to collision kinematics.

A space-time diagram describing the possible evolution of the system is shown in figure 1.8. A QGP phase may exist if the parton phase reaches equilibrium before

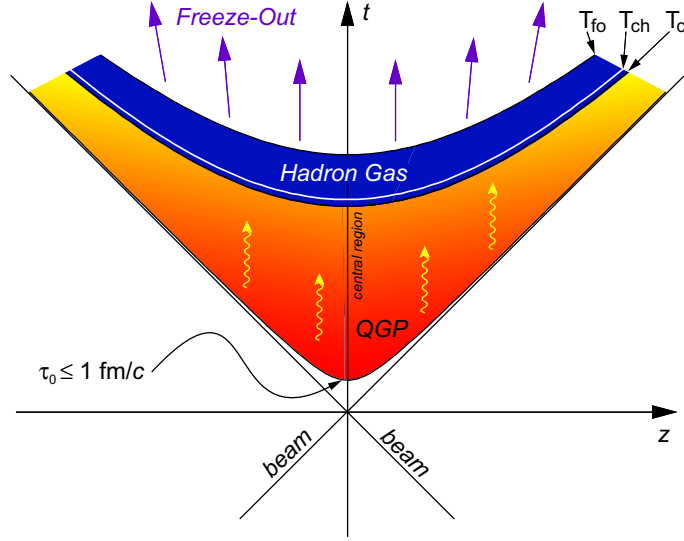


Figure 1.8: Schematic representation of the space-time evolution of a nuclear collision including a QGP phase. The critical transition, chemical freeze-out and kinetic freeze-out points are designated by T_c , T_{ch} and T_{fo} respectively [20].

the system becomes too dilute and hadronises [18]. The system cools as it expands; when the ‘chemical freeze-out’ temperature is reached no further inelastic collisions can occur, and the chemical composition of the system becomes fixed. Beyond the ‘thermal freeze-out’ temperature no more elastic collisions take place, and the final state hadrons stream freely. Allowing for the possibility of subsequent (weak) decays, these particles form the observable remnant of the nuclear collision.

Experimental studies were first pursued in fixed target experiments at the Bevelac at Berkley and the Alternating Gradient Synchrotron (AGS) at BNL, NY in the late 1980s, and later at the Super Proton Synchrotron (SPS) at CERN. The world’s first heavy ion collider, the Relativistic Heavy Ion Collider (RHIC) at BNL began taking data in 1999. Five years since the first measurements, each of the four experiments at RHIC produced a review article on their results [21, 22, 23, 24]. This thesis concerns the analysis of data at the STAR experiment at RHIC.

1.4 Highlights at RHIC

Several signature measures have been proposed to discriminate between QGP and hot hadron gas descriptions of the medium. Among these the enhancement of strangeness in QGP due to additional production channels and (partial) chiral symmetry restoration [25], and charmonium suppression due to Debye screening [26], have been studied the most extensively, and measurements support the hypothesis of QGP formation, both at RHIC [27, 28] and previous experiments [29, 30]. However these signatures all rely on model assumptions, and results from RHIC have revealed these measures to be less clear indicators than at first predicted.

1.4.1 Collective flow

Some of the strongest evidence for QGP at RHIC has been provided by studies of collective behaviour, and in particular anisotropic transverse flow. The initial spatial anisotropy illustrated in figure 1.6 results in a larger energy density gradient in the reaction plane than perpendicular to it. From a hydrodynamical perspective this implies a higher pressure gradient, and thus the initial spatial anisotropy drives momentum anisotropies [31]. Consequently, the final state hadron distribution may exhibit a modulation relative to the reaction plane, which can be characterised in terms of a Fourier series as described in section 2.4.1. The second harmonic, v_2 , called elliptic flow, measures the in-plane to out-of-plane momentum anisotropy, and is the largest contribution in the plane of the initial collision.

Strong elliptic flow was observed at RHIC, as shown in figure 1.9 for minimum bias $Au + Au$ collisions with $\sqrt{s_{NN}} = 200$ GeV [32]. Lines represent predictions from an ideal hydrodynamic model. Good agreement is seen at $p_T \lesssim 1.5$ GeV/c, where the bulk of the produced particles are found, including a mass ordering indicative of collective flow. For higher p_T , hydrodynamic models should not describe the data, as the system should be too dilute for substantial flow and v_2 should fall to

zero. However, strong elliptic flow does persist to high- p_T , and appears larger for baryons than mesons. This unexpected observation shall be discussed in the context of high- p_T suppression in the following section.

Critically, the system becomes more spherical as the system expands until kinetic freeze-out is reached. Thus the result provides a compelling case for a very early onset of thermal equilibrium, which requires substantial interactions ($\alpha_S \neq 0$) and a vanishing mean free path, and a short time to kinetic freeze-out. The medium therefore appears to act as a “perfect fluid”.

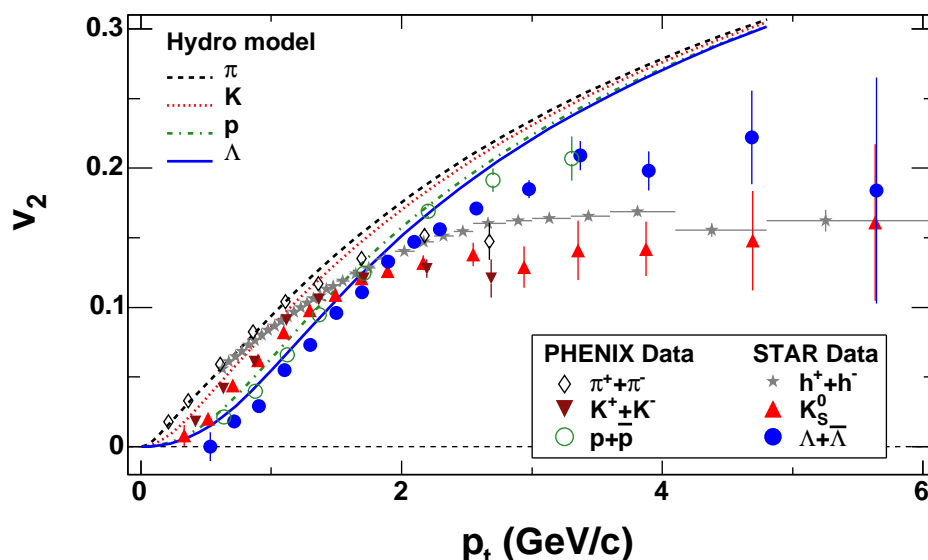


Figure 1.9: Elliptic flow, v_2 as a function of p_T for pions, kaons, protons and lambda particles from minimum bias $Au + Au$ collisions measured at STAR and PHENIX [32]. Hydrodynamical model predictions are overlaid.

1.4.2 Suppression of high- p_T particles

The most direct means to study the QGP would be to transmit a strongly interacting probe through the medium. In practice this is unfeasible, as the system extends only a few nuclear radii in the transverse plane for a duration of ~ 10 fm/c, and in current experiments collisions take place within an interaction ‘diamond’ a few

centimetres in length. Fortunately di-jets, which originate from the scatter of two partons through large angles, represent a natural probe that is produced in the initial nuclear collision.

An illustration of a di-jet in a $p + p$ collision is shown in figure 1.10. Confinement causes the scattered partons to fragment, producing two jets of hadrons that are back-to-back in the transverse plane. Using empirical descriptions of initial parton distributions, and hadronisation, di-jet cross-sections are calculable from pQCD.

In nuclear collisions the partons must traverse the medium in which they are formed. A large degree of attenuation is expected in the case of a QGP due to radiative interactions [33, 34], which should be visible as a suppression in the yield of hadrons at high- p_T compared to a system with no medium. See section 2.2 for a review of parton attenuation. Once observed, the degree of attenuation can then be used to estimate properties of the medium such as gluon density. In the absence of additional phenomena, the ratio of spectra in heavy ion collisions to $p + p$ should reach unity at high- p_T , after scaling by the number of nucleon-nucleon collisions, or ‘binary collisions’, n_{bin} . This scaled ratio, called the nuclear modification factor, is defined

$$R_{AA}(p_T, y) = \frac{d^2 N^{AA}/dp_T dy}{\langle T_{AA} \rangle_c d^2 \sigma^{NN}/dp_T dy} , \quad (1.5)$$

where the nuclear overlap function $\langle T_{AA} \rangle_c = \langle N_{bin} \rangle / \sigma_{nsd}^{NN}$ includes n_{bin} , and σ_{nsd}^{NN} is the $p + p$ inelastic (non-singly diffractive) cross-section. The ratio should fall below unity at low p_T where spectra should instead depend upon the volume of the system, or the number of participating nucleons, n_{part} . Figure 1.11 presents R_{AA} observed at STAR for several centralities. In $Au + Au$ collisions at $\sqrt{s_{NN}} = 200$ GeV, the factor decreases with increasing centrality to ~ 5 at $p_T \gtrsim 6$ GeV/c for most central data [35].

The observed suppression could be the result of final state effects, such as the

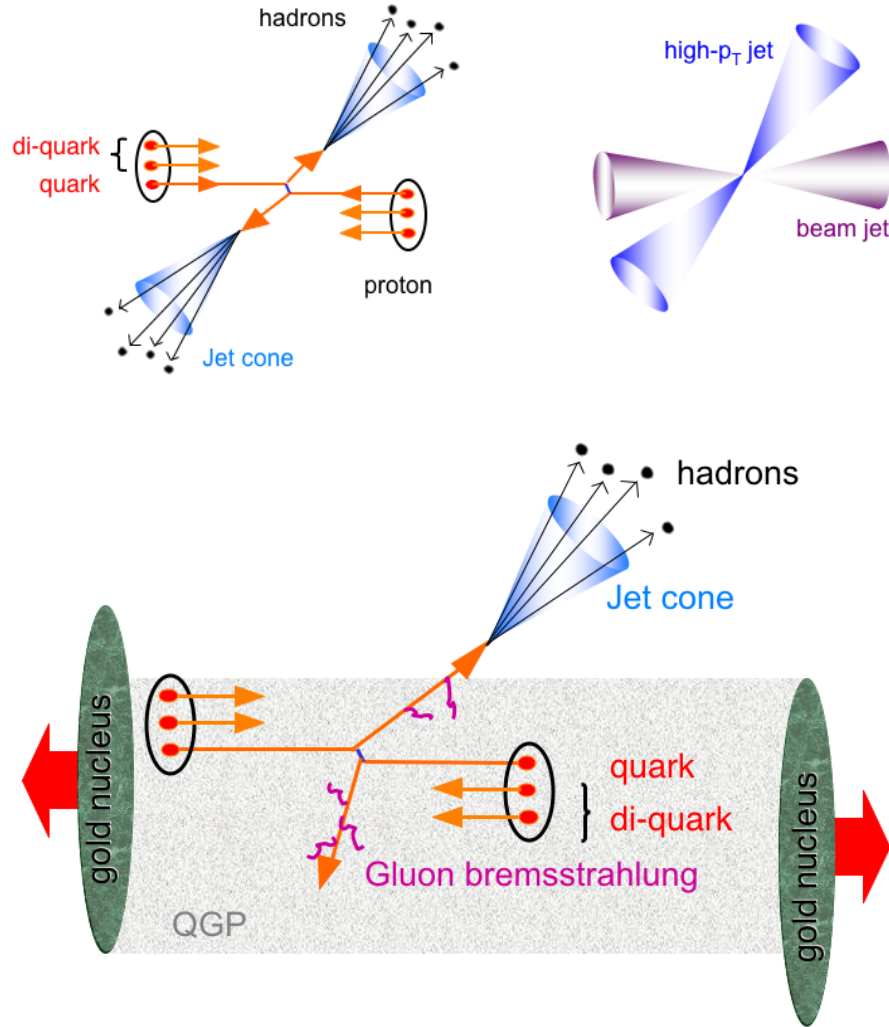


Figure 1.10: Schematic representation of di-jets. The left and centre images illustrate di-jets in $p + p$ collisions, from the 'parton' view (left) and 'hadronic' perspective (centre), which shows that jets may be accompanied by beam jets resulting from the fragmentation of projectile remnants. The right image illustrates the same process in $A + A$ collisions where the presence of a colour-deconfined medium may delay fragmentation and strongly attenuate the partons via radiative mechanisms. See text for details.

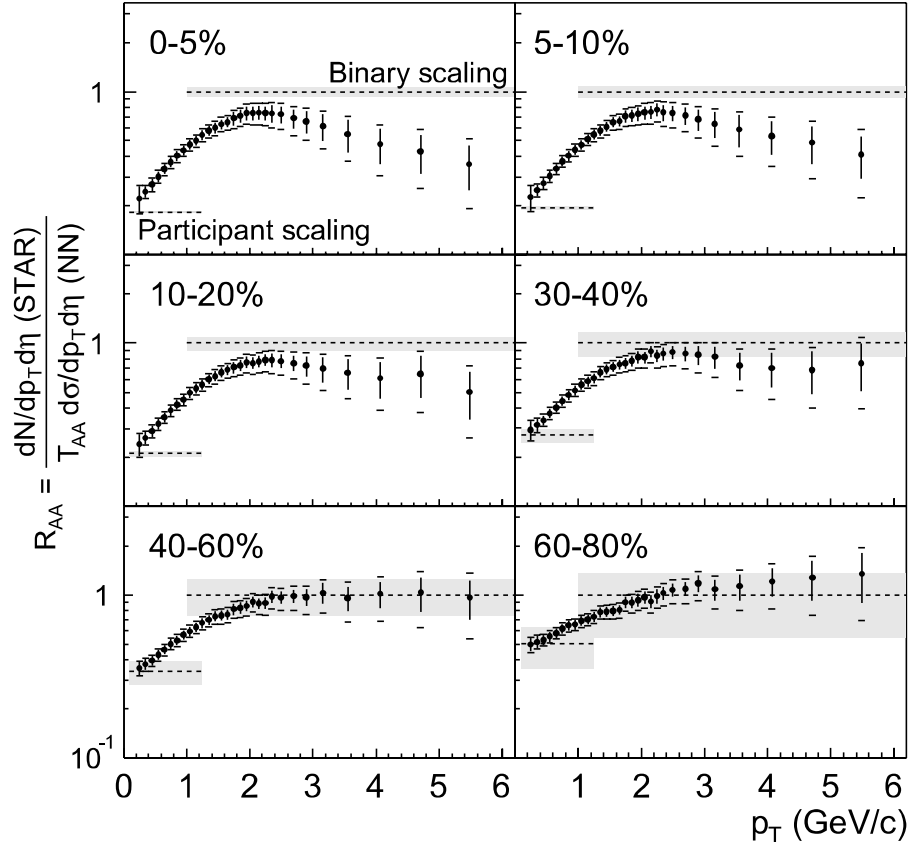


Figure 1.11: High- p_T suppression observed in $Au + Au$ collisions at STAR. Spectra are plot in terms of R_{AA} : the ratio of yield in $Au + Au$ to $p + p$ collisions, and events have been divided into centrality bins.

presence of a QGP, or initial state effects such as nuclear shadowing, and the onset of gluon saturation [36]. The latter could lead to the formation of a Colour-Glass Condensate, from which high energy partons could scatter to form mono-jets instead of di-jets, thus reducing the yield of high- p_T hadrons relative to $p + p$ collisions [37]. Initial state suppression scenarios were excluded by studies of $d + Au$ collisions [38], where instead of a suppression, initial state scattering resulted in an enhancement attributed to the Cronin effect [39]. Since this process should also be present in $Au + Au$, the actual suppression factor is even greater than first estimated.

Identified particle spectra have provided further evidence of QGP formation at RHIC. In figure 1.12 the ratio of central to peripheral $Au + Au$ collisions, R_{CP} , is

shown for several species of hadron [40]. Transverse flow shifts the baryon p_T distribution more than mesons, resulting in a relative enhancement of baryons in the interval $2 \lesssim p_T \lesssim 6$ GeV/c, as was shown in figure 1.9. The shape of R_{CP} is well described by models of hadron production via the coalescence of co-moving thermal (dressed) partons [41]. In fact, all species appear to follow the same trend in both R_{CP} and v_2 if they are first scaled by the number of valence quarks. Beyond $p_T \gtrsim 6$ GeV/c, baryon and meson R_{CP} are consistent, suggesting that at high- p_T (suppressed) jet fragmentation dominates hadron production.

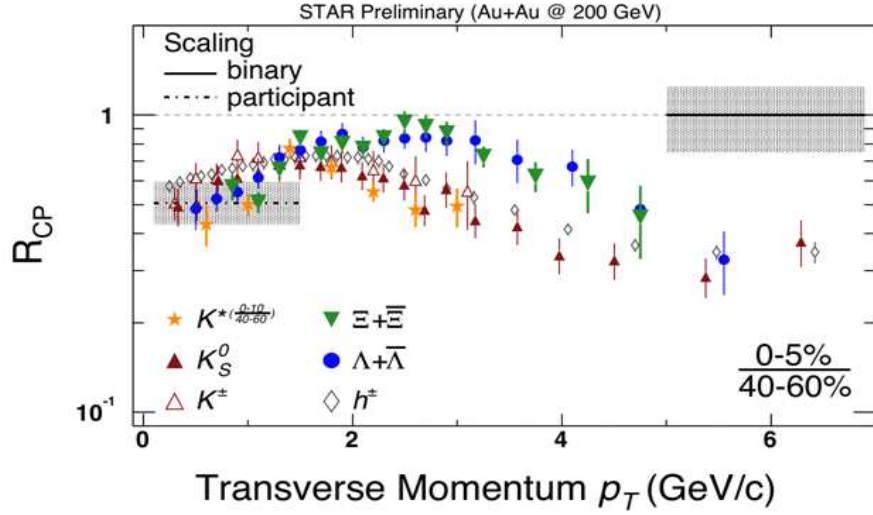


Figure 1.12: Identified particle p_T spectra in $Au + Au$ events, showing a meson—baryon difference in the range $2 \text{ GeV/c} \lesssim p_T \lesssim 6 \text{ GeV/c}$ [40].

1.4.3 Jet suppression

In order to complete the understanding of high- p_T suppression, it was necessary to link the observation to the attenuation of jets. It is not possible to fully reconstruct jets in $Au + Au$ collisions as jet fragments are indistinguishable from the underlying event. Instead, jets have been studied in heavy ion collisions via two-particle correlations, which represent the angular distribution of high- p_T particles relative to a very high- p_T ‘trigger’ particle, approximating to a jet axis. Since di-jets are

back-to-back in the transverse plane, correlations between high- p_T particles should contain peaks at azimuthal separations of $\Delta\phi = 0$ and $\Delta\phi = \pi$ radians, hereafter labelled the same side and away side peaks.

Azimuthal two-particle correlations of unidentified charged tracks in $p + p$, $d + Au$ and $Au + Au$ collisions are shown in figure 1.13. Unique to the $Au + Au$ system, the away side peak is substantially suppressed [42, 38]. Similar same side peaks are expected for all systems due to a surface bias. The correlation measurement requires a high- p_T trigger track. Hence, for a medium that has a high opacity to hard partons, trigger tracks will preferentially originate from hard parton scattering that occurs close to the surface of the collision system [42]. Indeed this arrangement is beneficial to jet studies in high energy nuclear collisions, as the recovery of a same side peak gives a good indication that the measurement does relate to hard parton scatter.

The $d + Au$ result also included in figure 1.13 again rejects initial state hypotheses such as a colour-glass condensate produced by gluon saturation. Thus final state effects are responsible for the attenuation in $Au + Au$ collisions, with a QGP phase favoured by consideration of known hadronic cross-sections.

The ratio of peak yields in $Au + Au$ to $p + p$ collisions, I_{AA} , is shown in the lower frame of figure 1.13. Circles display the away side yield, and squares show the same side yield. The away side yield exhibits a smooth decrease with increasing centrality (N_{part}), in agreement with the trend seen in R_{AA} . Additionally, the same side I_{AA} is unexpectedly observed to increase with centrality. The study of this enhancement formed the focus of the present analysis.

1.4.4 Summary

The evidence presented above provides a compelling case for QGP formation at RHIC, especially because the system produced exhibits a high degree of collective

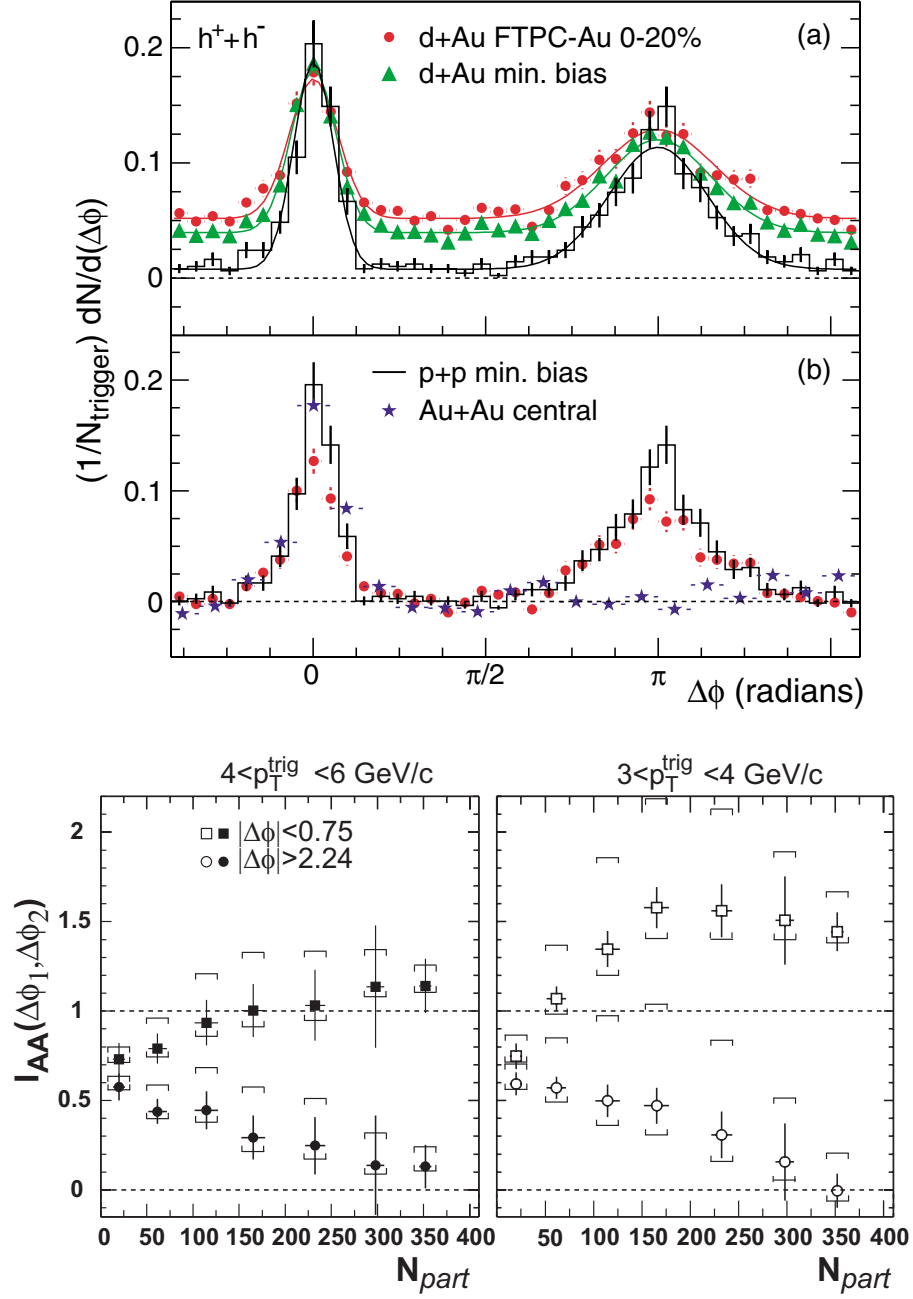


Figure 1.13: Top: Two-particle azimuthal correlations revealing di-jet features at high- p_T for $p + p$, $d + Au$, and central $Au + Au$ collisions. Bottom: Ratio of correlation peak yields in $Au + Au$ to $p + p$ collisions, for the same side peak (squares, $|\Delta\phi| < 0.75$) and away side peak (circles, $|\Delta\phi| > 2.24$) as a function of centrality for two trigger momentum intervals. The horizontal bars indicate the systematic uncertainties due to subtraction of the background [42, 38].

flow and is opaque to jets. However, the medium is a strongly interacting fluid of Debye screened partons, not an asymptotically free parton gas. Combined, the observed high- p_T suppression and jet attenuation indicate the attenuation of hard partons, and disfavour hadronic mechanisms [43]. Identified particle spectra have revealed evidence of parton coalescence, which appears to dominate particle production at intermediate p_T .

The observations have generated new questions. For instance, the mechanism for the apparent rapid thermalisation is unknown. The high opacity to hadronic probes presents a challenge to further enquiries as in order to make quantitative measures of the system's properties, something of the probe must survive. Since the same side peak survives it may retain some evidence of interaction with the medium, which could explain the increase in yield observed in central collisions. The mechanism responsible for the observed baryon enhancement could influence the distribution of particles in jet-like correlations, and so it would be interesting to study identified particle correlations in this regime.

1.5 Outline of thesis

In the present analysis the correlation studies introduced in section 1.4.3 were developed with the aim to find further evidence to discriminate between hadronic and partonic descriptions of the medium. These studies were extended to two-dimensions to gain a more complete description of the same side peak. Additionally, identified particle correlations were considered by utilising neutral strange particles characterised by their characteristic $V0$ decay. In previous studies at STAR, correlations were made in $Au + Au$ collisions at $\sqrt{s_{NN}} = 200$ GeV with $V0$ triggers and unidentified associated tracks [44]. Despite large uncertainties, similar features were observed in azimuthal correlations for all species. The present analysis benefits from new $Au + Au$ datasets with superior statistics, plus a $d + Au$ dataset at the same

energy.

The remainder of this thesis is set out as follows. In chapter 2, the theoretical topics most relevant to the present analysis shall be reviewed. Jet phenomena shall be described in greater detail, followed by the theoretical review of high- p_T suppression, and a discussion of collective flow in heavy ion collisions. In chapter 3, the experimental facilities involved in this investigation will be described, together with the process by which recorded events are reconstructed. The method used in the present analysis to obtain identified particle samples will also be described. The main correlation analysis is described in chapters 4 and 5, including an introduction to the two-particle correlation technique; the method of generating two-dimensional two-particle correlations, and the approach taken to characterise modified same side peak. In chapter 6 the results of this analysis are summarised for minimum bias $d + Au$, minimum bias $Au + Au$, and central $Au + Au$ collisions, all at $\sqrt{s_{NN}} = 200$ GeV. In the last chapter, recent theoretical and experimental advances are discussed, in order to provide some interpretation and context of the results of this analysis. Finally, an outlook is presented, considering the future prospects of correlation techniques in further studies of heavy ion collisions.

Chapter 2

THEORY

2.1 Jet phenomena

Di-jets were introduced in section 1.4.2 in relation to studies of high- p_T particle production in high energy nuclear collisions. In the following sections, jets and their possible modification in the presence of a QGP shall be reviewed. Additionally, particle production at intermediate- p_T shall be revisited, as well as hydrodynamics in high energy nuclear collisions, as these features have particular relevance to the present analysis.

2.1.1 High- p_T particle production

Hadron jets characterise particle production in both high energy electron–positron annihilations and hadron collisions. In the former case, a quark–anti-quark pair is produced by an intermediate photon or Z boson, $e^+e^- \rightarrow \gamma, Z \rightarrow q\bar{q}$. In hadronic collisions, the initial interaction involves the elastic scatter of constituent partons, which may be valence quarks, sea quarks, or gluons. Thus di-jets observed in these collisions may originate from hard quarks or gluons, with the sub-processes, $qq \rightarrow qq$, $qg \rightarrow qg$, and $gg \rightarrow gg$, all contributing to the total cross-section. Although the Q^2 of

the scattering is suitably large to allow a pQCD treatment of the cross-sections, the initial parton distribution is incalculable by pQCD because the interiors of hadrons are governed by many low energy processes, as introduced in section 1.1.1.

Fortunately, the two components of the di-jet cross-section in hadronic collisions are independent and can be separated. Thus, given a description of the initial parton distribution, the cross-section can be determined. In figure 2.1 the parton distribution function (PDF) of a proton is shown, measured via studies of deep inelastic electron scattering at ZEUS [5]. The relative distribution of each type of parton is shown as a function of the fraction of momentum carried by that parton, x . The valence quarks dominate the PDF at high- x , and the distribution of gluons and sea quarks become more significant towards low- x .

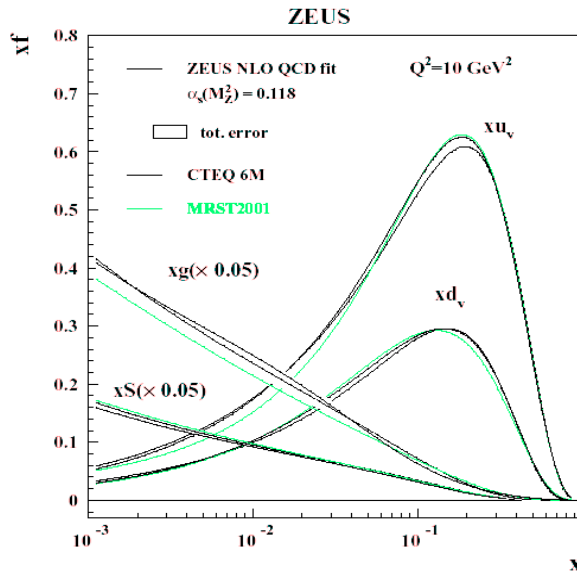


Figure 2.1: Parton distribution functions of the proton, observed at ZEUS [5].

Combining the PDFs and pQCD cross-section, the relative abundance of jets originating from scattered quarks and gluons varies as a function of the transverse momentum of the scattered parton (total jet p_T). Figure 2.2 shows the predicted relative cross-sections of quark and gluon jets for $p + p$ collisions at $\sqrt{s_{NN}} = 200$

GeV. Most jets with $p_T \gtrsim 40$ GeV/c originate from quark-quark scatter, but for lower p_T quark-gluon, and gluon-gluon scatter dominates the cross-section.

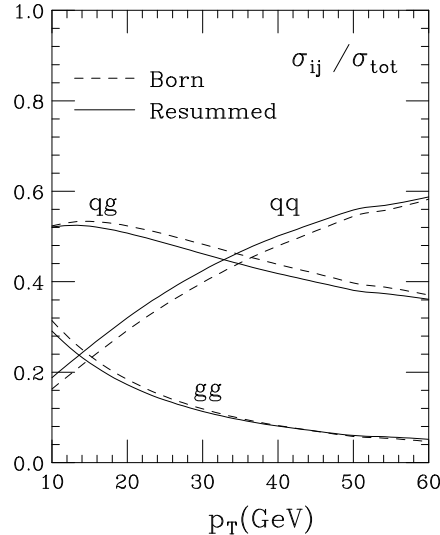


Figure 2.2: Calculated relative abundance of jets originating from qq , qg , and gg hard scatter in $p + p$ collisions at $\sqrt{s_{NN}} = 200$ GeV, as a function of parton p_T . The dashed and solid lines represent two different pQCD summations, with the calculation represented by the solid line including higher order interactions [45].

Hadronisation occurs via the fragmentation of strings drawn between the escaping partons (and other colour-charge centres if present). The resulting jets of hadrons share the momentum of the initial partons, and thus are located within cones around the axis of the scattered parton trajectory (jet axis). The projectile remnants may also undergo fragmentation, resulting in jets near the beam axis.

Particle production via jet fragmentation has been studied extensively and is described empirically by fragmentation functions, $D(h, z)$. These parameterisations are analogous to PDFs, in the respect that they provide the probability distribution of hadrons, h , with a given fraction of momentum of the initial parton, z . In figure 2.3 fragmentation functions are shown for inclusive charged hadron production in e^+e^- annihilations at LEP [46]. Jet fragmentation is independent of the production mechanism responsible for the hard partons, and therefore e^+e^- data can be used to determine jet cross-sections in hadronic collisions [47].

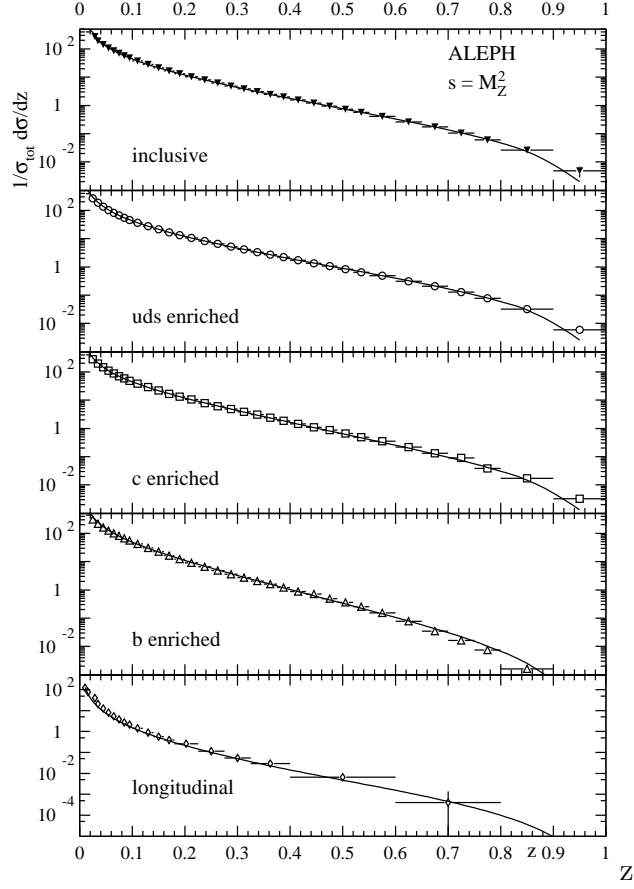


Figure 2.3: Inclusive fragmentation functions for charged particle produced in e^+e^- annihilations at LEP [46]. Subsets of jets relating to different parton flavours were recovered via final state hadrons.

Combining the three necessary components, in high energy nuclear collisions the hadron cross-section due to hard parton scatter can be calculated as the convolution of three groups of terms, which can be schematically written

$$\sigma_{di-jet} = \sum_{abcd} \int dx_a dx_b dz PDF(i, x_a) PDF(i, x_b) \otimes \sigma_{ab \rightarrow cd} \otimes D(h, z_c) D(h, z_d) \quad (2.1)$$

where $PDF(i, x)$ provides the probability density of incident partons of type i with fraction of total momentum x ; $\sigma_{ab \rightarrow cd}$ is the pQCD elastic parton scattering cross-section for the scattering of partons ab to cd , and $D(h, z)$ provides the distribution

of observed hadrons h carrying a fraction of the total jet momentum z . See appendix for a more detailed treatment of the di-jet cross-section.

The p_T distribution of jet fragments follow a steeply falling trend, and hence a jet typically includes one particle that carries the majority of the available energy. The mean transverse momentum, p_T , carried by this leading particle increases with x [48], and was observed to account for 75 – 90% of the total jet momentum in $p + A$ collisions with $\sqrt{s_{NN}} = 38.8$ GeV/c at Fermi Lab [49]. Furthermore, the fraction was observed to increase with leading particle p_T . For jets in higher energy collisions, the fraction of momentum carried by the leading particle is typically lower. However in the two-particle correlation analysis presented in this thesis, the selection criteria biases the sample of jets to include those where the trigger particle does tend to carry the majority of the available energy.

2.1.2 Quark and gluon jets

As described in the preceding section, jet fragmentation is the result of both quark and gluon scatter. Since the colour charge of a gluon is essentially twice that of a quark, the fragmentation of the two types of partons should not be the same. From a naive consideration of colour charge factors, one would expect the multiplicity of gluon jets to be 9/4 larger than quark jets.

Quark and gluon jets were studied at OPAL [50]. Three-jet events were used in the analysis, which are understood to be di-jets where one of the scattered partons radiates a high momentum gluon that subsequently propagates as a third jet. The multiplicity of gluon jets do indeed appear to be $\approx 50\%$ larger, in broad agreement with theoretical predictions. Similarly, gluon jet cones appear wider than quark jets [50].

The species composition of jets also differs between parton types. Leading baryons are preferentially found in quark jets compared to anti-baryons. This is

a reflection of the tendency for the leading particle to carry the baryon number of the parent parton. Consequently no such bias is present in gluon jets. Studies at OPAL of particle production rates showed clear differences in the species composition of quark and gluon jets [51]. In figure 2.4 the production rates of Λ and K_{Short}^0 particles are shown as a function of jet energy. The abundance of K_{Short}^0 in jets was found to be considerably larger than Λ . In the right frames of the figure, quark and gluon jets have been isolated. Gluon jets were found to contain more Λ than quark jets, and conversely the production rate of K_{Short}^0 was greatest in quark jets.

These known differences between anti-quark, quark and gluon jets can in principle offer some discrimination. For instance, jets can be tagged according to the species of their leading particle. A sample of jets containing leading anti-baryons will be deficient in quark-jets relative to a sample with leading baryons. Similarly, the multiplicity and shape of jets can be used to obtain samples containing mostly quark and anti-quark jets or gluon jets.

2.2 Jets in heavy ion collisions

Hard parton scatter should occur in much the same way in heavy ion collisions as in $p + p$ collisions. Adopting appropriate PDFs, the di-jet cross-section is calculable. However the description of the system following the initial collision may be quite different, and depending upon the nature of the medium produced, a substantial degree of attenuation may be expected. Hence jet studies in heavy ion collisions may indicate the presence of a QGP, and furthermore can infer the properties of the medium.

High- p_T (jet) suppression represents a resilient test of QGP production in heavy ion collisions because hadronic interpretations are disfavoured by a simple consideration of timescale and the formation time of a hadron [52]. The finite time required

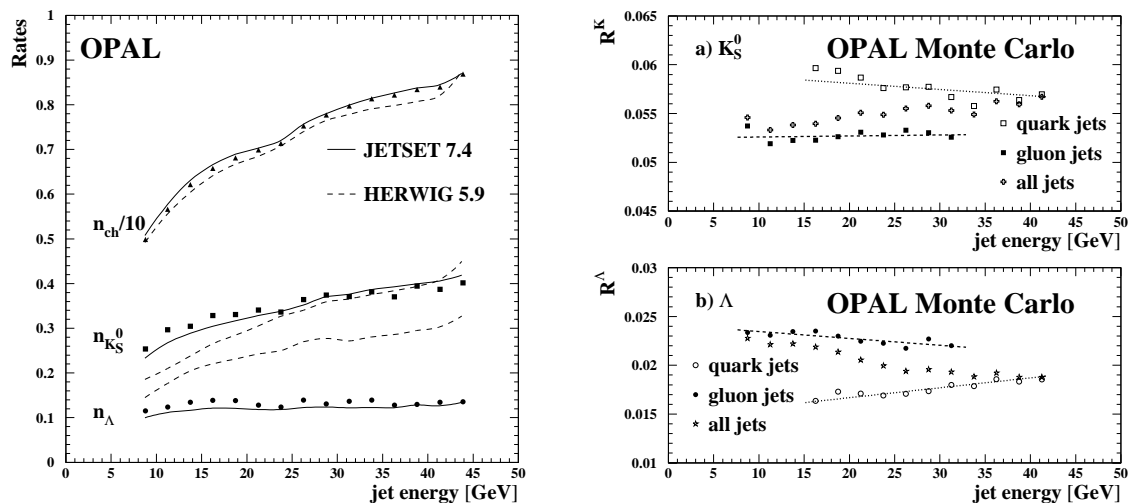


Figure 2.4: Unidentified charged particle, Λ particle and K_{Short}^0 particle production rates in jets as a function of jet energy measured in e^+e^- collisions at OPAL [51]. The left frame shows total rates for all jets, and the right frames show K_{Short}^0 production (upper frame) and Λ production (lower frame) in isolated quark and gluon jets. Solid and dotted lines represent predictions from models of jet phenomena.

for the non-perturbative ‘dressing’ of a bare quark with partons from the vacuum is generally estimated to be $0.5 \text{ fm/c} \lesssim R \lesssim 1.0 \text{ fm/c}$. In the lab frame a high- p_T hadron gains a relativistic boost $\gamma = \frac{E_h}{m_h}$. So for example, a pion with $p_T = 10 \text{ GeV/c}$ has a lab formation time $\sim 50 \text{ fm/c}$. Given that the fireball is thought to expand at $\sim 0.6 c$ [27], the particle is likely remain as a pre-formed hadron while it traverses the medium, and therefore hadronic cross-sections may not be applicable.

2.2.1 Models of parton attenuation

A colour-deconfined medium will interact with fast moving colour charge centres passing through it. Although collisional attenuation is expected to be small [53], several different calculations of radiative processes have predicted a substantial degree of energy loss. Previous studies of bremsstrahlung in dense electromagnetic plasmas aided the early development of such calculations in this field, highlighting

the importance of features such as interference effects in the emitted spectrum [54].

Two main approaches have been pursued to date, with attenuation either modelled by multiple soft gluon radiations (BDMPS) [33], or the emission of a few hard gluons (GLV) [34]. A typical feature of gluon bremsstrahlung calculations is that for finite plasmas, the amount of energy loss, ΔE , either depends weakly upon or is independent of the initial parton energy (apart from setting an upper bound) [55].

Each approach relates the amount of energy loss, ΔE , to physical properties of the QGP. In BDMPS calculations, the quantity of interest is the transport coefficient \hat{q} , defined as the average transverse momentum squared transferred to the projectile parton per unit pathlength, $\hat{q} = \langle q_T^2 \rangle / L$. This is related to the energy density of the medium, $\hat{q} \propto \epsilon^{3/4}$ [56], which in turn gives the gluon density dN_g/dy . In GLV calculations dN_g/dy is included directly.

The path length dependence of ΔE varies amongst calculations from $\Delta E \sim L^2$ for thick, static QGP, to $\Delta E \sim L$ for thin, expanding plasmas. Relatively thick plasmas were considered by BDMPS, limited by considering partons of sufficiently high energy, E , that the path length is smaller than a critical length set by the extent of the screening, $L < L_{crit} = \sqrt{\lambda_g E / \mu^2}$, where λ_g is the mean free path of a radiated gluon, and μ the Debye screening mass ($\mu = 1/R_{Debye}$) [33]. In contrast, GLV calculations were applicable to thinner plasmas, where few or single gluon emission was favoured [57]. In some predictions the L^2 dependence survives for high energy partons, but reduces to a linear relationship at lower energies [58]. These differences may offer important insights into the nature of parton attenuation when compared to data, if measurements can be made as a function of path length (e.g. with respect to the reaction plane) in heavy ion collisions.

Finally, more recent studies have also considered the ability of hard partons to gain momentum from the medium. Thermal absorption and stimulated emission of gluons by hard partons undergoing multiple scattering in a hot QGP were considered

by Wang and Wang [59]. In their calculation, thermal absorption was found to dominate stimulated emission, and that for intermediate $p_T \sim 10$ GeV/c it should significantly reduce the total amount of parton energy loss.

2.2.2 Comparisons to data

The nuclear modification factor for unidentified charged hadrons, measured by the four experiments at RHIC, is shown in figure 2.5, together with predictions for a range of transport coefficient [56]. The expected trend for no medium is also included. Even for the lowest considered value of \hat{q} , the model predicts the suppression of R_{AA} to extend to $p_T \gtrsim 50$ GeV/c, far beyond the reach of current datasets ($p_T \gtrsim 20$ GeV/c at the time of writing).

Unfortunately the measure appears somewhat insensitive, with a wide range of densities predicted to give similar results. Additionally some theoretical uncertainties remain relating to the maximum parton energy loss, which is shown in the diagram by the two lines for each set of parameters. The apparent independence of R_{AA} on p_T suggests the medium is strongly opaque, limiting particle production to surface emission.

The approximately flat trend exhibited by R_{AA} at high- p_T disfavors hadronic attenuation: as shown in figure 2.6, for $p_T \gtrsim 6$ GeV/c the observed R_{AA} for hadrons suggest the suppression is fairly independent of p_T . In contrast, hadronic attenuation mechanisms would intuitively decrease towards higher p_T if the attenuation only begins after hadronisation, due to the effect of time dilation on formation time. More recent studies of possible pre-hadronic interactions have shown that approximately half of the observed attenuation could be accounted for without a QGP phase [60].

Having excluded initial state effects via $d + Au$ studies, high- p_T suppression must be interpreted as evidence of final state interactions. Much effort has been

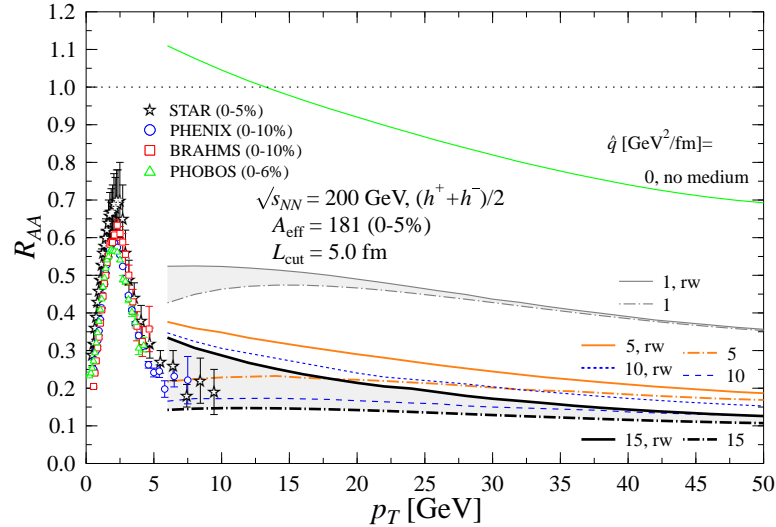


Figure 2.5: The nuclear modification factor R_{AA} for charged hadrons $h \equiv (h^+ + h^-)/2$ in the 0 – 5% most central Au+Au collisions at $\sqrt{s_{NN}} = 200$ GeV. Different lines are for a lifetime of the medium $\tau \sim L_{\text{cut}} = 5$ fm and different values of the transport coefficient \hat{q} . The shaded region between the curves calculated with reweighted (solid curves) and non-reweighted (dotted-dashed curves) quenching weights is indicative of uncertainties related to finite energy corrections.

devoted to ascertain whether such an attenuation can be explained without including partonic interactions in a deconfined medium. In fact, the observed attenuation is not much larger than that of static cold nuclear matter, but the rapid system expansion demands a gluon density some ~ 30 times that of normal nuclear matter [61].

Finally, the production of direct photons in heavy ion collisions provides a further test of parton attenuation models, as no suppression should be observed compared to $p + p$. In figure 2.6, the direct photon spectrum measured at PHENIX for Au + Au collisions at $\sqrt{s_{NN}} = 200$ GeV is shown divided by a binary-scaled NLO pQCD calculation for $p + p$ collisions at the same energy [62]. As predicted, the ratio is consistent with unity throughout the observed range, to at least $p_T \gtrsim 13$ GeV/c, in clear contrast to the included hadron spectra.

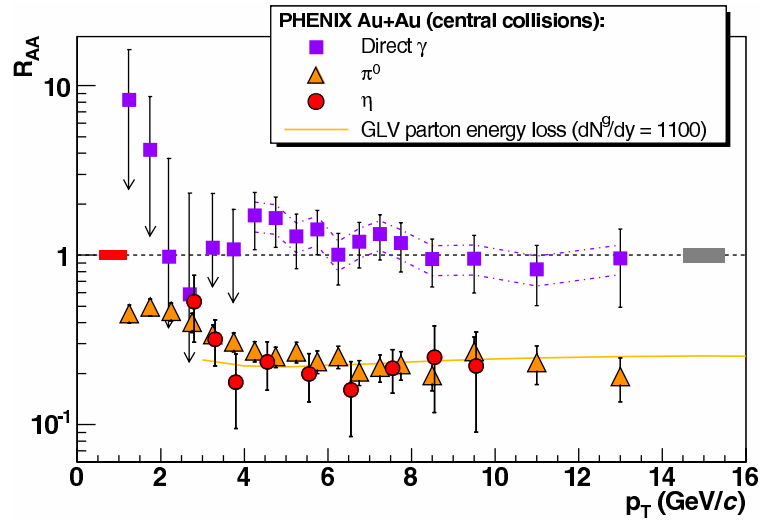


Figure 2.6: Nuclear modification factor of direct photons (squares), π^0 (triangles), and η (circles) mesons in $Au + Au$ collisions at $\sqrt{s_{NN}} = 200$ GeV measured at PHENIX, using a NLO pQCD calculation as the $p + p$ reference for photons [62]. The solid line represents a GLV parton attenuation calculation. Solid bars represent systematic uncertainties.

2.3 Particle production at intermediate- p_T

In the intermediate transverse momentum interval $2 \lesssim p_T \lesssim 6$ GeV/c, high- p_T jet fragmentation in $Au + Au$ collisions at $\sqrt{s_{NN}} = 200$ GeV competes with hadronisation from the bulk. The nuclear modification factor for identified particles in this range shown in figure 1.12 revealed an intriguing enhancement of baryons relative to mesons. As illustrated in figure 2.7, the ratio of baryons to mesons is found to exceed unity at intermediate- p_T , which contradicts expectations from both fragmentation functions and statistical arguments for relative abundance in consideration of the particle masses. A similar baryon-meson difference is also observed in elliptic flow measurements, and it was found that all species could be made to follow a single trend in both measurements if the axes are scaled by the number of constituent quarks.

Parton recombination has been proposed to explain the baryon-meson difference [41, 64, 65]. In this framework the momentum distribution of final state hadrons

is driven by the distribution of their constituents: partons with $p_T = 2$ GeV/c will combine to give a 6 GeV/c baryon or 4 GeV/c meson. In contrast, to produce the same via fragmentation requires a parton of momentum greater than the hadrons it creates. Assuming a steeply falling distribution with p_T , parton recombination is therefore a far more efficient mechanism than fragmentation and should dominate the spectra of hadrons providing the phasespace density of the partons is high.

Predictions from a selection of parton recombination models are included in figure 2.7. Overall a good qualitative description of the data is achieved, with all models predicting the ratio to increase above unity at intermediate- p_T before decreasing towards high- p_T . Similar treatments of thermal parton recombination were employed in the models, but they notably differed in their treatment of recombination between soft partons and high- p_T shower partons related to jets. The DUKE model [41] ignored shower partons, whereas predictions of the TEXAS model [64] are shown both with and without hard processes, which shows that inclusion pushes the turnover to higher- p_T . The OREGON model [65] also considered hard processes, but through a framework of mini-jet shower partons rather than fragmentation functions. Combined, the predictions suggest that at intermediate- p_T , recombination of thermal partons dominates particle production, with a negligible contribution from shower partons.

Providing an intuitive explanation for both spectra and elliptic flow at intermediate- p_T , recombination remains the most compelling description of particle production in this region. Alternative models to parton recombination have been able to achieve better agreements with data, although they must typically evoke exotic mechanisms such as gluonic baryon junctions [66], and so are disfavoured. If recombination is indeed the dominant particle production mechanism at intermediate- p_T , few baryons should originate from jets relative to mesons in this region despite their enhanced abundance.

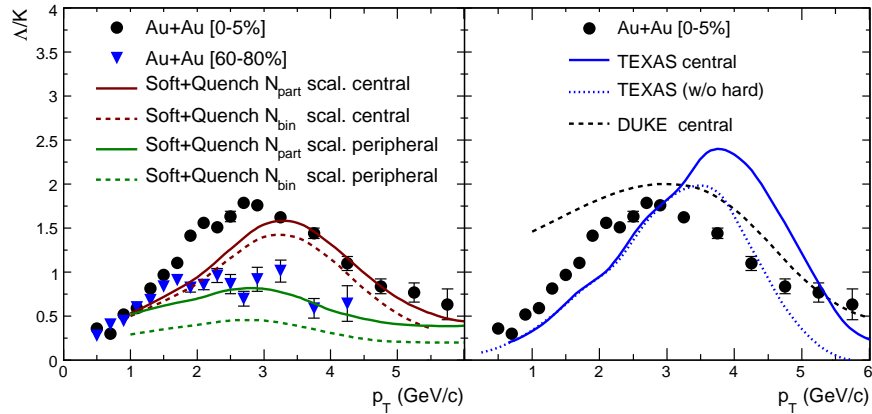


Figure 2.7: The ratio of Λ / K_{Short}^0 particles produced in $Au+Au$ collisions at $\sqrt{s_{NN}} = 200$ GeV at RHIC [63]. An enhancement of baryons relative to mesons is observed at intermediate- p_T . Predictions from the DUKE, TEXAS and OREGON parton recombination models overlayed in the right frame. In the left frame predictions are shown for a model including gluonic baryon junctions, employing either N_{part} or N_{bin} scaling.

2.4 Hydrodynamics

As introduced in section 1.4.1, one of the key results at RHIC was the observation of substantial anisotropic transverse flow, indicating early thermalisation, and providing evidence for QGP formation in heavy ion collisions. Although this is not the topic of the present analysis, back-to-back correlations due to flow contribute to the background seen in two-particle correlations. It is therefore important to understand the origin of this feature and to correct for it.

Hydrodynamical treatments were first proposed to describe high energy heavy ion collisions by Landau in the early 1950s [67]. Although more commonly applied to statistically large systems, such frameworks may be suitable here providing certain conditions are met. In particular, the local relaxation timescale must be much smaller than the dynamical timescale of the system. Rapid thermalisation is essential, hence in systems involving relatively few particles, interactions are necessarily strong, and the mean free path of particles must be small to ensure high scattering rates.

The dynamical timescale of the system can be approximated as the ratio of spatial extent to the speed of sound in the medium, i.e. $\sim 10 \text{ fm}$ to $c_s \lesssim c/\sqrt{3}$ (massless ideal gas limit) [68]. However a further constraint is introduced by the expansion of the fireball, which acts to reduce the timescale of interest to just a few fm/c [69]. Therefore thermalisation must be achieved within $\sim 1 \text{ fm}$ in order to describe the medium with hydrodynamics. This is a difficult requirement to meet, and is compounded by the possibility of large fluctuations in a quasi-statistical system, but providing equilibrium is reached, hydrodynamical models may be used to describe the subsequent evolution.

Anisotropic transverse flow is not unique to heavy ion collisions, but has also been observed in studies of sub-statistical systems of cold Lithium atoms in anisotropic magnetic traps [70].

2.4.1 Anisotropic transverse flow

In non-central collisions, as the fireball expands the momentum anisotropy, ϵ_p , counteracts the initial spatial anisotropy, ϵ_x . In figure 2.8 theoretical expectations for this evolution are shown as a function of time for a $Au + Au$ collision with impact parameter $b = 7 \text{ fm}$ [71]. Two sets of initial conditions were considered in the study. In the figure the system described by the solid line was defined by the initial conditions and freezeout temperature determined from measurements of $\sqrt{s_{NN}} = 130 \text{ GeV}$ $Au + Au$ collisions. The dotted line represents the consequence of more extreme initial conditions plus a lower freezeout temperature. In the latter case a QGP phase exists throughout the displayed evolution, whereas in the more realistic scenario hadronisation causes a stalling of the momentum anisotropy before $t \sim 5 \text{ fm}/c$. An additional component that must be added by hand to models of the fireball evolution is the point at which the system becomes too dilute for hydrodynamics to apply. The distributions of observed final state particles will reflect the momentum

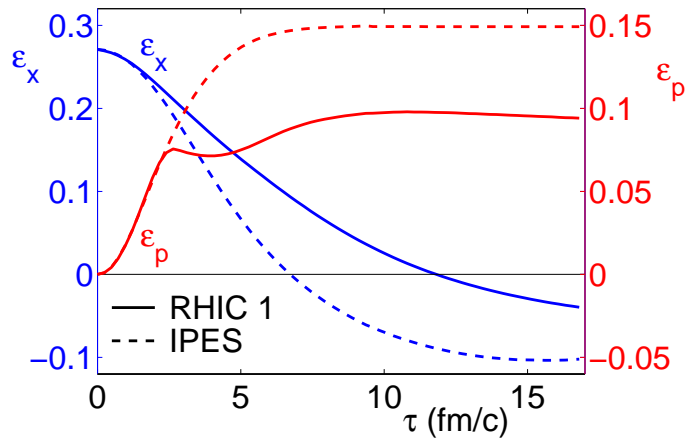


Figure 2.8: Spatial and momentum anisotropy as a function of time for a $Au+Au$ collision with impact parameter $b = 7\text{fm}$, for two sets of initial conditions. The system described by the solid line was defined by the initial conditions and freezeout temperature determined from $\sqrt{s_{NN}} = 130\text{ GeV}$ $Au+Au$ collisions. The dotted line represents the consequence of more extreme initial conditions plus a lower freezeout temperature. In the latter case a QGP phase exists throughout the displayed evolution, whereas in the more realistic scenario hadronisation causes a stalling of the momentum anisotropy before $t \sim 5\text{fm/c}$. [71].

anisotropy integrated to this moment.

In order to quantify anisotropic flow, Voloshin and Zhang [72] suggested decomposing the distribution of particles in the transverse plane relative to the reaction plane using a Fourier expansion. In the central rapidity region of a symmetric collision system, the second order term, called elliptic flow, v_2 , is expected to dominate. Thus the distribution of particles in the transverse plane as a function of p_T and rapidity y , should be described by

$$\frac{dN_i}{p_T dp_T dy d\phi} = \frac{1}{2\pi} \frac{d^2 N_i}{p_T dp_T dy} (1 + 2 v_2^i(p_T) \cos(2\phi) + \dots). \quad (2.2)$$

where ϕ describes the azimuthal angle relative to the reaction plane, v_2 is the amplitude of the modulation, and i denotes particle species. Hydrodynamics predicts a mass ordering in identified particle studies of flow as a function of transverse momentum, since collective motion implies that particles of different masses with a common velocity will have different momenta [73].

For head on collisions, no initial spatial anisotropy exists, and in peripheral collisions insufficient matter is involved for flow to develop. Thus elliptic flow should reach a maximum in mid-central collisions. Correspondingly, in two-particle correlations the background contribution due to elliptic flow will vary as a function of centrality, and reach a maximum in mid-central events. The form of the contribution shall be described in section 4.4.1 of this thesis.

Chapter 3

EXPERIMENTAL FACILITY

3.1 The Relativistic Heavy Ion Collider

The accelerator-collider complex called the Relativistic Heavy Ion Collider (RHIC) [74] consists of two 2.4 mile circumference rings maintained at high vacuum, surrounded by a series of superconducting magnet arrays for the shaping and redirection of relativistic beams of nuclei. Ions are accelerated by RF cavities. It became operational in 2000, and since then has provided collision events for four experiments, which are located around the ring [75]. Figure 3.1 gives a schematic representation of the site. Each experiment operates independently of its counterparts, and each one has been designed according to different experimental aims.

BRAHMS [76] is one of the two smaller experiments, consisting of a two arm spectrometer and capable of studying particles from mid rapidity out to high rapidity beam debris. PHOBOS [77] (which was decommissioned in 2005) is the second small detector and takes advantage of silicon detectors to achieve high event sampling rates. PHENIX [78] and STAR [79] comprise the two larger experiments. The former was designed to observe rare particles, and in particular electromagnetic probes. In contrast STAR is a high acceptance experiment directed towards the study of hadrons.

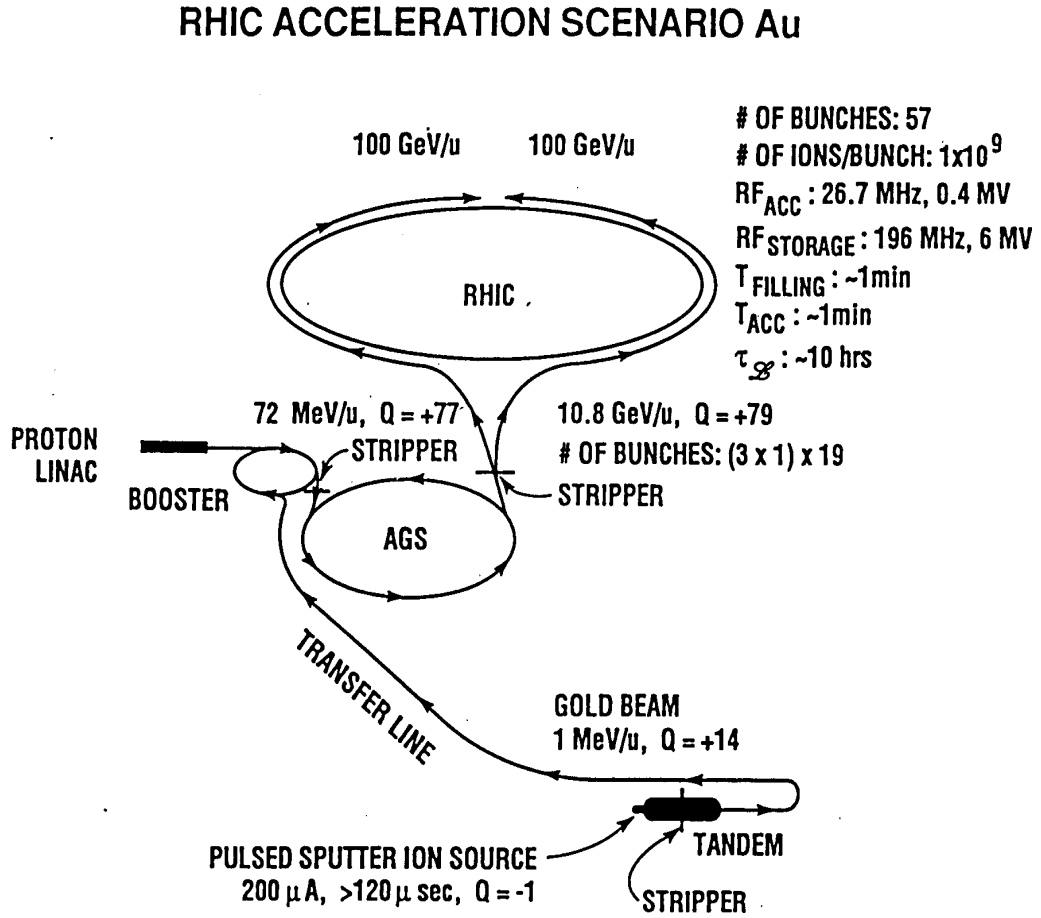


Figure 3.1: Schematic plan view of the RHIC accelerator-collider facility.

RHIC itself is served by the pre-existing Alternating Gradient Synchrotron (AGS) complex which injects beams of fully stripped nuclei into RHIC at its maximum energy of 10.8 GeV/A for gold ions. The RHIC then accelerates these in its two concentric ring cavities up to an energy of 100 GeV/A and is able to store the beams in this state for a period of several hours. The two opposing beams are made to intersect at six interaction regions located around the ring.

3.2 The Solenoidal Tracker At RHIC

The Solenoidal Tracker At RHIC (STAR) consists primarily of a 4.2 m long cylindrical ion drift chamber, called a Time Projection Chamber (TPC), with a beryllium

3.3. THE TIME PROJECTION CHAMBER

beam pipe running along the axis. The detector has an outer radius of 2 m, and extends to within 50 cm of the beam pipe. The inner cavity is occupied by another detector: the Silicon Vertex Tracker (SVT). These systems are accompanied by an assortment of other detectors used to either identify events of interest or add to the particle information delivered by the TPC, as shown in figure 3.2. With the exception of detectors placed at high rapidity (i.e. several metres along the beam pipe from the intersection region), the array of detectors is surrounded by a solenoidal magnet that provides an axial 0.5 T field [79].

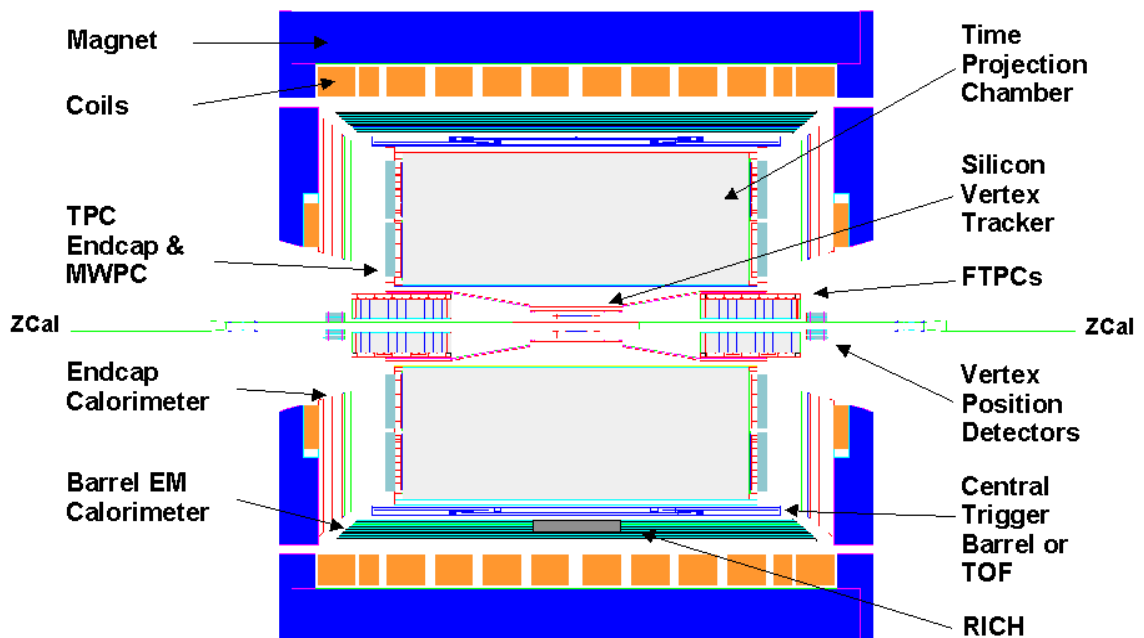


Figure 3.2: The main detectors of the STAR experiment.

3.3 The Time Projection Chamber

The main tracking detector is the Time Projection Chamber (TPC) [79]. The TPC is a cylindrical ion drift chamber filling the dimensions described above, as shown in figure 3.3. It consists of an outer and inner field cage to maintain electric field

3.3. THE TIME PROJECTION CHAMBER

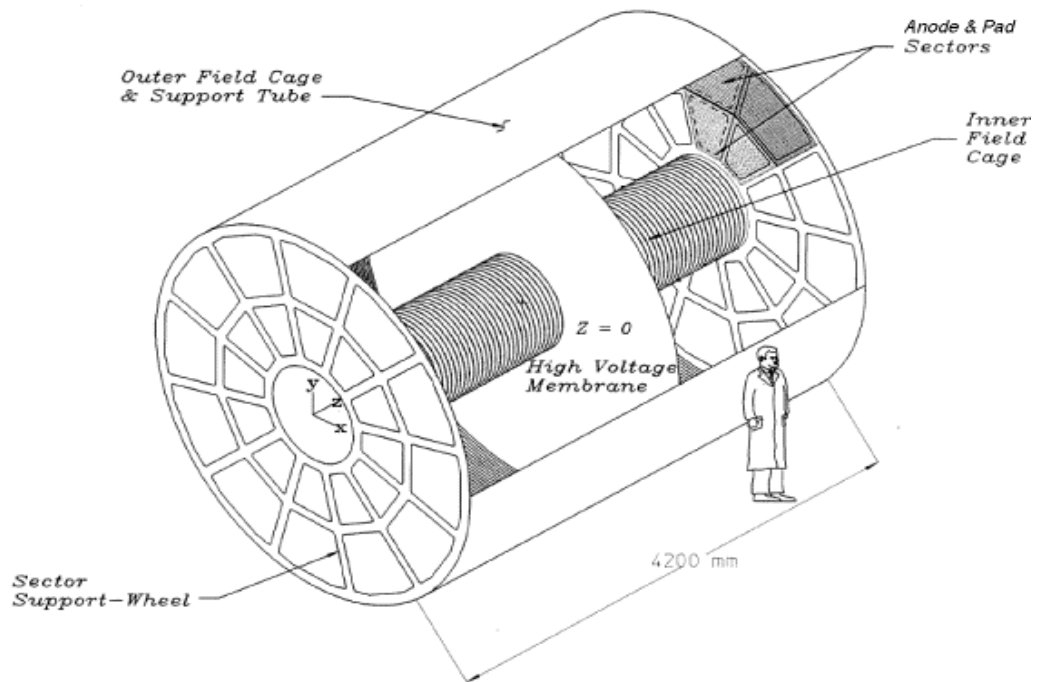


Figure 3.3: The Time Projection Chamber at STAR.

uniformity, and the drift potential is maintained between each end (grounded) and a thin circular membrane at its midpoint (at -31 kV). The detector is operated at (just above) atmospheric pressure.

A charged particle traversing the chamber follows a helical path due to the magnetic field. It ionizes nearby atoms, liberating electrons which then drift towards the nearest end of the chamber at ~ 5 cm/ μ s. At the end of the drift region the electrons meet a gating grid. Beyond lies a proportional region, as shown in figure 3.4. If the event has passed the criteria (trigger) for it to be recorded, the gating grid is ‘opened’, by setting it to the ambient potential. Electrons entering the proportional region pass a shield grid where the field lines of the drift gradient terminate and then avalanche towards anode wires at a potential of 1265 V. The gas gain is $\sim 10^4$. An array of cathode pads is situated behind the anode wires. An image charge is induced by the positive ions as they drift in the potential (away from the pads), and this constitutes the TPC signal. Charge accumulation is slow

3.3. THE TIME PROJECTION CHAMBER

because the positive ion drift is considerably slower than the electrons. Instead of collecting the full charge, front end electronics are used to generate a pulse based upon the fractional charge developed over a shorter time scale.

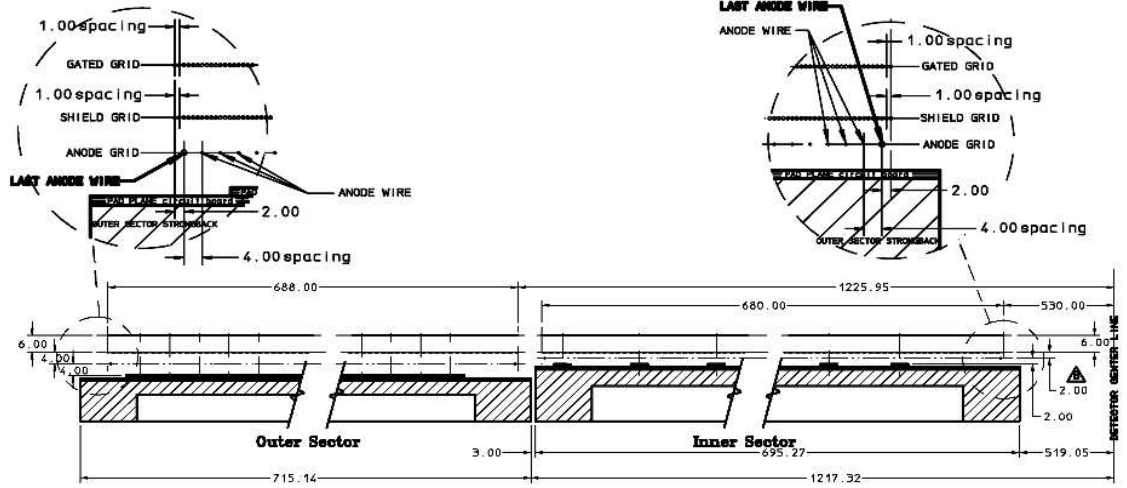


Figure 3.4: The TPC proportional region.

The cathode pads are arranged into rows on sectors as shown in figure 3.5: 5690 pads divided over 45 pad rows, on each of 12 sectors, at each end of the TPC. These 137000 spatial elements are sampled in 512 time bins, giving an array of ~ 70 million pixels per event.

In principle the drift time of the STAR TPC limits the data sampling rate somewhat lower than the beam luminosity, which reached approximately ten thousand collisions per second for heavy ions for the dataset used in the present analysis, and up to a factor of one hundred greater for p+p beams. Consequently, tracks originating from several events can be recorded simultaneously. This unwanted feature, known as ‘pile-up’, has increased in severity with improvements to RHIC luminosity. Pile-up is dealt with at the reconstruction phase, as described in section 3.5 below.

The readout and discrimination of events reduce the data sampling rate further.

3.4. EVENT TRIGGERING

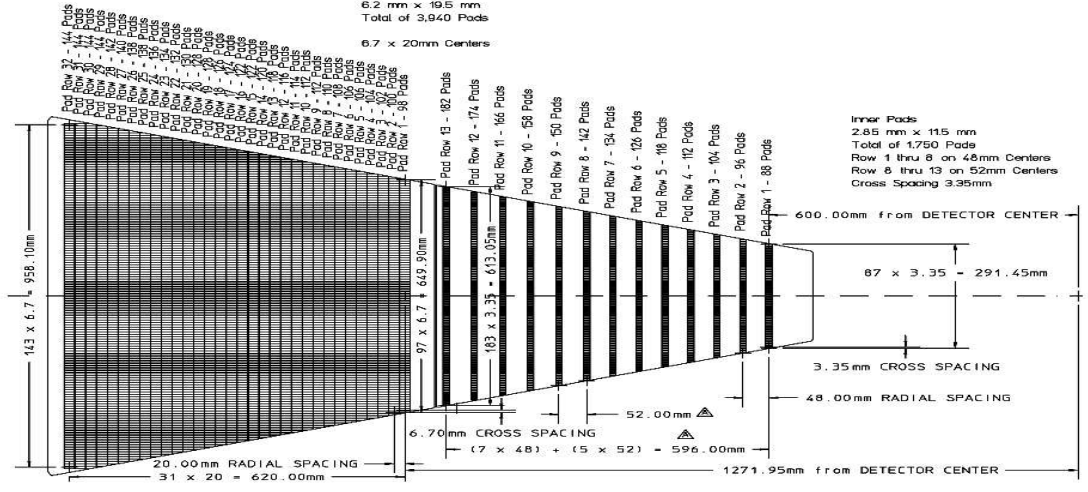


Figure 3.5: Cathode pad rows on one sector of the TPC.

At the start of the experimental programme STAR took data at a rate of ~ 5 Hz (~ 50 MB/s). Subsequent improvements to data acquisition (DAQ) increased this to ~ 100 Hz for the $Au + Au$ data set used in the present analysis. Future runs will benefit from further upgrades to front-end electronics that will increase the data sampling rate to ~ 1 kHz.

3.4 Event triggering

Heavy ion collisions occur over the complete range of impact parameter. Central events (those with small impact parameters) include more participating matter and thus these events offer the best conditions for a QGP to be produced. It would therefore be advantageous to be selective over events. However, neither impact parameter nor number of participants are directly observable quantities. Instead, multiplicity is used as an indicator. There are several detectors in place at STAR with the purpose of identifying events rapidly with particular multiplicities in different regions of rapidity.

The STAR experiment implements a pipelined trigger system comprising four

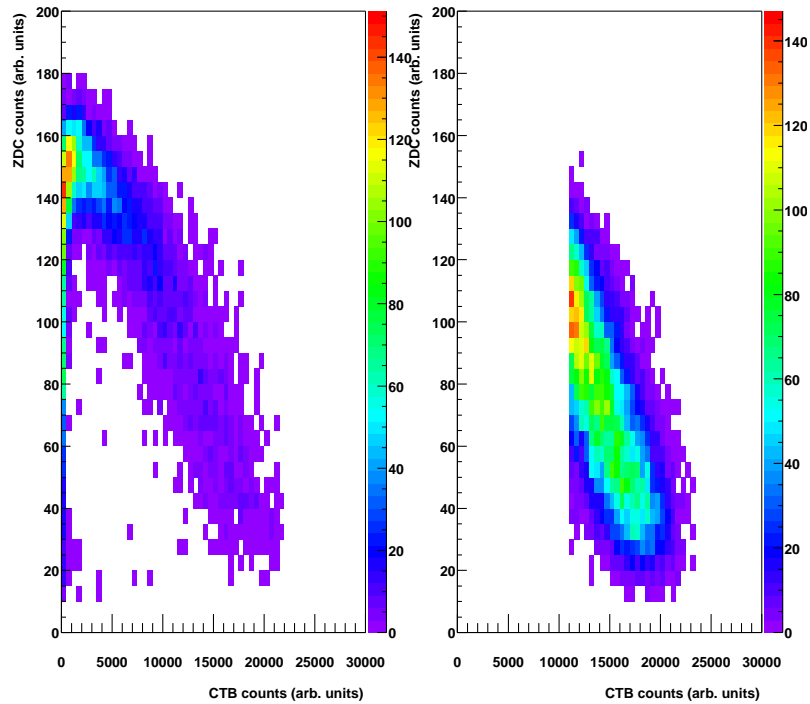


Figure 3.6: Distribution of CTB and ZDC signals for $Au + Au$ events at $\sqrt{s_{NN}} = 200$ GeV. The left frame includes minimum bias collisions. Low ZDC counts coincident with high CTB signals correspond to central collisions. This correlation is used to apply a fast online central trigger to the events included in the right frame [82].

levels, designed to simultaneously handle several triggers with different criteria, and also to operate at the RHIC bunch crossing frequency of ~ 10 MHz [80]. Successive levels utilise increasingly detailed descriptions of the event and are correspondingly afforded larger time budgets to complete their operations. Levels 0, 1 and 2 of the STAR trigger make use of data recovered from fast detectors, and the last level also makes use of the slow tracking detectors. The full digitisation of the event signal takes longer than the bunch crossing time of ~ 100 ns, but by operating the system as a pipeline the trigger dead time is low enough to operate within the available time scale.

For each bunch crossing, the trigger detector channels are digitised and fed to Data Storage and Manipulation boards (DSM), where the data is processed in a fast decision tree. This constitutes the level 0 trigger, and delivers an output signal

3.4. EVENT TRIGGERING

within $1.5 \mu\text{s}$ of the bunch crossing (interaction). The output signal is passed to a Trigger Control Unit (TCU), which sends activation commands to the detectors specified for that trigger. This may include the signal to open the amplifier grid of the Time Projection Chamber (TPC).

During the following period whilst the detectors are digitising the event, the trigger data is reprocessed in greater detail by the level 1 and 2 stages, which can send abort signals within $100 \mu\text{s}$ and 5 ms respectively. The level 1 trigger makes use of a coarse pixel array of trigger data, whilst the level 2 stage uses the complete trigger dataset. Providing the event is not aborted, the level 2 trigger then hands over to the Data Acquisition (DAQ) system, which stores all trigger data and handles the remainder of the event readout and storage.

The most commonly used trigger for a central event, and the one used for the present analysis, is the coincidence of a high multiplicity observed in the Central Trigger Barrel (CTB), which is a cylindrical array of scintillation detectors, 4m in length 2m in radius, surrounding the TPC, and small energy deposited in the two identical Zero Degree Calorimeters (ZDC) located $\pm 18 \text{ m}$ down the beam pipe in each direction, which measure spectator neutron energy [81]. A typical distribution of minimum bias $Au + Au$ events is presented in figure 3.6, from which the online central trigger criterion is based. Minimum bias $Au + Au$ data was taken using a coincidence in both ZDCs combined with a minimal CTB threshold. A $0 - 12\%$ central $Au + Au$ online-triggered dataset was taken by requiring ZDC coincidences with low signals, and a high CTB signal. This corresponded to high multiplicity events with few spectator neutrons. In addition to minimum bias and central $Au + Au$ datasets, the present analysis also utilised a third dataset of $d + Au$ collisions at $\sqrt{s_{NN}} = 200 \text{ GeV}$. For these data the trigger criterion was a coincidence between the Au side ZDC and CTB.

The above described suite of trigger detectors have now been accompanied by

several fast detectors that offer triggering and in some cases tracking. In particular, STAR now benefits from a full barrel electro-magnetic calorimeter (EMC), and one endcap EMC, both of which are used for high- p_T (jet) triggers.

3.5 Event reconstruction

Charge clusters collected in the spatial and temporal bins in the front end electronics are fit to 2-dimensional gaussians in order to identify their centroids. This results in a spatial resolution in the TPC of $\sim 300 \mu\text{m}$. These are passed to the next stage in event processing as spatial co-ordinates after corrections are made to account for the non uniformity of the electric and magnetic fields. These TPC space-points are then used to reconstruct tracks, producing an image of the event as shown in figure 3.7. Starting with the outer pad row where track density is a minimum, hits are linked together as tracks, called global tracks. The two track resolution is $\sim 1\text{cm}$, equivalent to the width of about three pads on an inner sector. These tracks are then extrapolated to the beam axis and a minimization is performed to find the collision ‘primary’ vertex. With the primary vertex defined, an attempt is made to fit each track again with the primary vertex included as another hit. Tracks that point back to the primary vertex are collected together as primary tracks. The initial track collection, labelled global tracks, is also retained.

As introduced in section 3.3 above, tracks from collisions before or after the triggered event may be falsely collected in the track list of a single event. Typically pile-up events are separated in time by several bunch crossing times, $\sim 120 \text{ ns}$, and the different starting times for electron drifts result in the hits of untriggered events being artificially separated in the z -direction to either side of the central membrane. Consequently two apparent primary vertices may be found, with asymmetric pseudo-rapidity distributions of tracks, lower multiplicities, and in general less well defined vertices. Consequently, the reconstruction algorithm offers some protection from

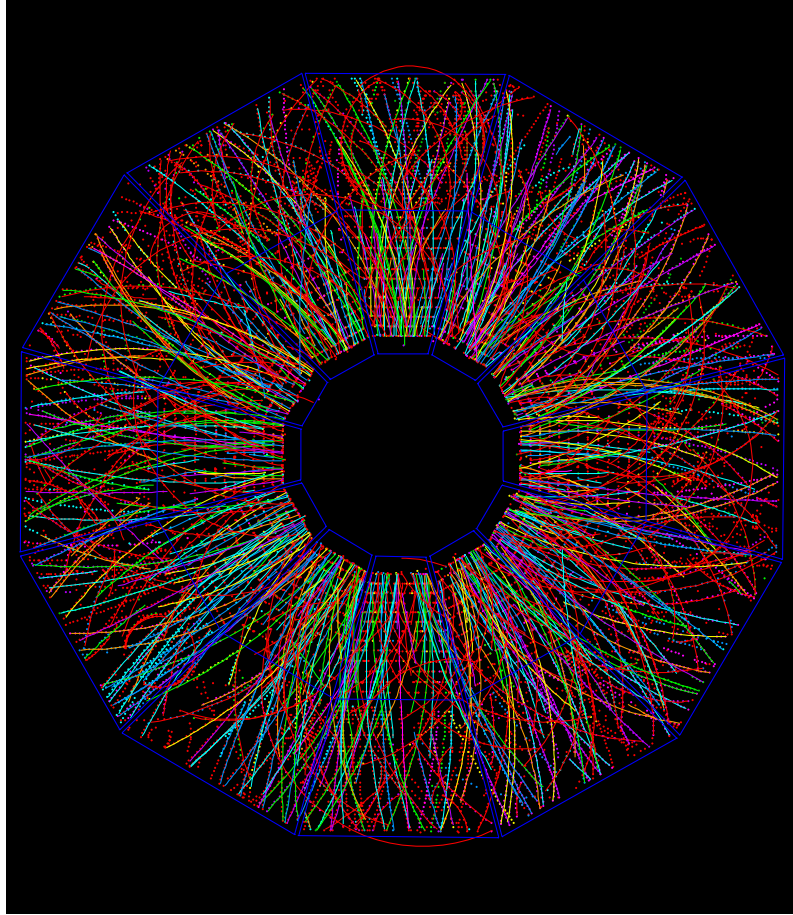


Figure 3.7: Reconstructed tracks from TPC hits, as viewed parallel to the beam axis, for a central $Au + Au$ collision at $\sqrt{s_{NN}} = 200$ GeV.

pile-up events, especially for more central triggered events where the primary vertex is more accurately defined. For the datasets used in this analysis, pile-up was not a significant issue in the centrality ranges under study. In principle pile-up can also result from multiple collisions in a single bunch crossing. However, at RHIC this is a small contribution and pile-up from different bunches dominates.

3.6 Off-line centrality selection

Both minimum bias and online central-triggered data can be sub divided into centrality classes after event reconstruction. Off-line centrality selection is achieved by

selecting events within ranges of reconstructed track multiplicity. In order to avoid variations in tracking efficiency as a function of primary vertex position, a reference multiplicity is used, which only includes tracks with pseudo-rapidity $|\eta| < 0.5$. A typical reference multiplicity distribution for minimum bias $Au + Au$ collisions at $\sqrt{s_{NN}} = 200$ GeV is shown in figure 3.8, with centrality classes indicated by fill colour. Glauber model Monte Carlo calculations [83], are used to relate centrality to the number of participants, impact parameter, number of binary collisions and so on. One must be somewhat cautious of such derived quantities, since there is a dependence upon the detailed treatment of the model [84].

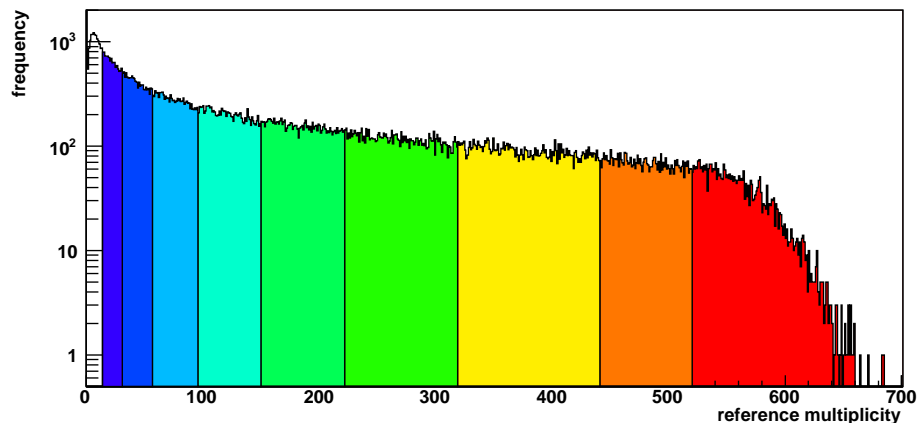


Figure 3.8: Reference multiplicity distribution for off-line centrality definition, in $Au + Au$ collisions at $\sqrt{s_{NN}} = 200$ GeV. Fill colour represents centrality class. From red to blue: 0–5%, 5–10%, 10–20%, 20–30%, 30–40%, 40–50%, 50–60%, 60–70%, 70–80%.

3.7 Particle identification and neutral strange particle reconstruction

In addition to the momenta, the rate of energy loss of charged particles traversing the TPC gas can be determined. This affords some particle identification capabilities for the TPC via the relativistic Bethe Bloch formula [85],

$$-\frac{dE}{dx} = \frac{e^2 (Ze)^2 n_e}{4\pi\epsilon_0^2 m_e c^2 \beta^2} \left[\ln \left(\frac{2m_e c^2 \beta^2 \gamma^2}{I} \right) - \ln(1 - \beta^2) - \beta^2 \right] \quad (3.1)$$

where e , m_e and n_e are the charge, mass and number density of electrons in the material with ionisation potential I , and Ze is the charge of the hadron. The mass dependence is included implicitly via $\beta\gamma = p/m$, where p and m are the momentum and mass of the charged particle. Thus by displaying energy loss as a function of momentum, particles of different masses can be discriminated.

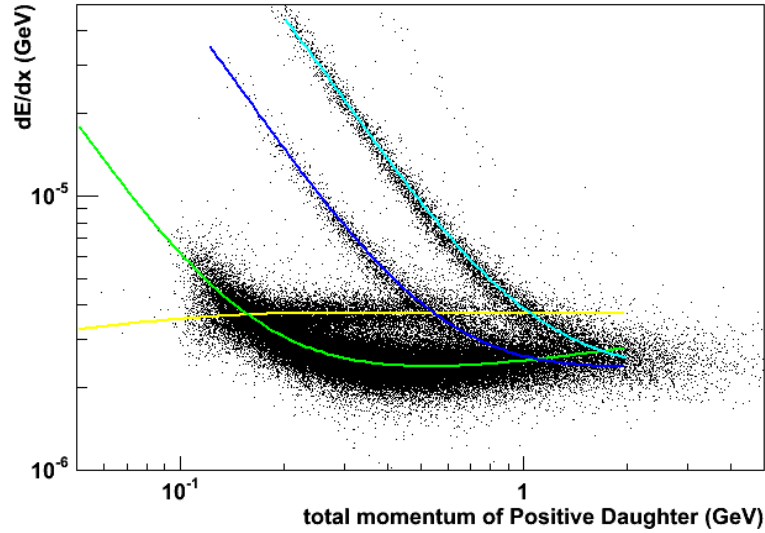


Figure 3.9: Particle identification by energy loss of tracks, dE/dx . Overlying the data for reconstructed positive tracks in $Au + Au$ collisions at $\sqrt{s_{NN}} = 62.4$ GeV are theoretical predictions from the Bethe-Bloch function: (from right to left) light blue for protons, darker blue for kaons, green for pions, and in yellow is the trend for positrons. Selection cuts are typically made via $n\sigma$ criteria, taking into account the uncertainty in track properties on an individual basis.

Figure 3.9 shows the momentum distribution of positive charged tracks against dE/dx energy loss in the STAR TPC, observed in $Au + Au$ collisions at $\sqrt{s_{NN}} = 200$ GeV. Overlaid are lines representing the expected trends for various species, including considerations for material thickness effects [86]. As can be seen, these intersect between 1 – 2 GeV, and converge at high momentum. Hence, this measure provides limited particle identification in two momentum regions.

3.7. PARTICLE IDENTIFICATION AND NEUTRAL STRANGE PARTICLE RECONSTRUCTION

Particles that undergo weak decays can be identified via the reconstruction of secondary vertices. Singly strange, neutral hadrons that decay by two charged daughters are called $V0$ s due to the characteristic tracks left in the bubble chambers where they were first discovered. The STAR TPC similarly observes $V0$ s as pairs of tracks leading from secondary vertices, as opposed to the primary vertex of the nuclear collision. A schematic representation of a $V0$ is presented in figure 3.10. A set of geometrical quantities that can be used to assess the quality of the vertex are defined in the figure. In the present analysis three species were reconstructed: Λ (uds), $\bar{\Lambda}$ ($\bar{u}\bar{d}\bar{s}$), and K_{Short}^0 (mixed state of $\bar{d}s + \bar{s}d$), providing a source of baryons, anti-baryons and mesons respectively. The $V0$ decay channels for each of these particles are given below, together with the branching ratios.

$$\Lambda \rightarrow p^+ \pi^- \quad (BR = 63.9 \pm 0.5)\% \quad (3.2)$$

$$\bar{\Lambda} \rightarrow p^- \pi^+ \quad (BR = 63.9 \pm 0.5)\% \quad (3.3)$$

$$K_{Short}^0 \rightarrow \pi^+ \pi^- \quad (BR = 68.95 \pm 0.14)\% \quad (3.4)$$

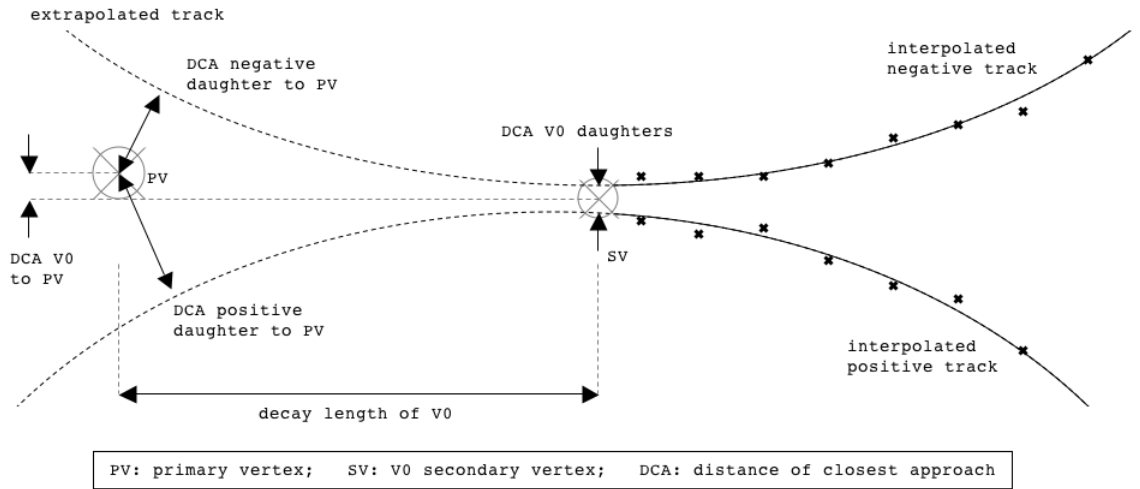


Figure 3.10: $V0$ reconstruction, detailing geometric cut parameters.

The principal means to differentiate between the species is to reconstruct the

3.7. PARTICLE IDENTIFICATION AND NEUTRAL STRANGE PARTICLE RECONSTRUCTION

invariant mass of the $V0$ by assuming the identities of the daughters, which may be assisted by the dE/dx method described above. However, the main issue to overcome when extracting a $V0$ signal from the fragments of a nuclear collision is the combinatoric background from random pairs of tracks.

For this analysis, $V0$ tracks were analysed in $d + Au$ collisions at $\sqrt{s_{NN}} = 200$ GeV, and in $Au + Au$ events at $\sqrt{s_{NN}} = 200$ GeV. The cut analysis procedure was identical in both datasets. The multiplicity of a typical $d + Au$ event is significantly lower than that for a typical $Au + Au$ event; the lower track density allows a more relaxed set of geometrical cuts. Cuts were optimised by plotting candidates on axes of hypothesised invariant mass versus each geometrical parameter. A cut-off was then chosen for each one in order to remove as much uncorrelated background as possible whilst preserving the signal. An example of such a distribution is shown in figure 3.11. The rejected candidates have been coloured red. A summary of the geometrical cuts tuned to $d + Au$ and $Au + Au$ collisions is given in table 3.1. Additionally dE/dx particle identification cuts were applied to $V0$ daughters.

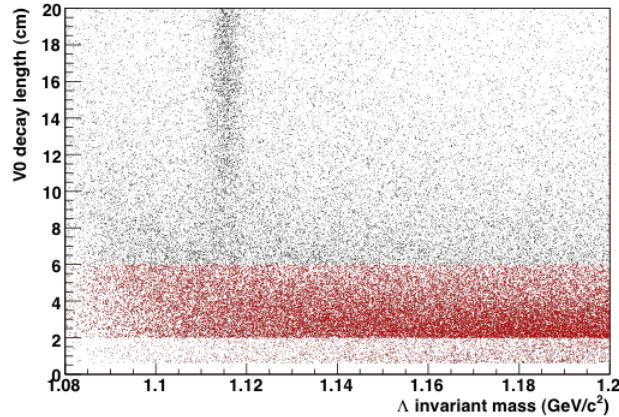


Figure 3.11: Demonstration of geometrical cut tuning. The hypothesised Λ mass of $V0$ candidates is displayed against decay length of the $V0$ track. Candidates coloured red are rejected from the selection.

Following these cuts, the majority of the remaining background was found to be caused by $V0$ candidates with ambiguous invariant masses. The distributions of

3.7. PARTICLE IDENTIFICATION AND NEUTRAL STRANGE PARTICLE RECONSTRUCTION

Table 3.1: The results of cut tuning $V0$ candidates, Λ , $\bar{\Lambda}$, K_{Short}^0 , in $d+Au$ and $Au+Au$ collisions at $\sqrt{s_{NN}} = 200$ GeV. The distance of closest approach is abbreviated DCA, and PV is the primary vertex. See figure 3.10 for a definition of geometrical parameters.

Geometrical Parameter	$d + Au$			$Au + Au$		
	Λ	$\bar{\Lambda}$	K_{Short}^0	Λ	$\bar{\Lambda}$	K_{Short}^0
DCA $V0$ to PV		< 1.0 cm			< 0.6 cm	
DCA $V0$ Daughters		< 0.8 cm			< 0.6 cm	
decay length of $V0$		> 2.5 cm			> 6.0 cm	
DCA Pos. daughter to PV		> 0.0 cm		> 0.7	> 1.2	> 1.2 cm
DCA Neg. daughter to PV		> 0.0 cm		> 1.2	> 0.7	> 1.2 cm
Pos. track No. TPC hits		> 15			> 15	
Neg. track No. TPC hits		> 15			> 15	

Λ and $\bar{\Lambda}$ candidates were contaminated by $V0$ tracks that also passed the K_{Short}^0 criteria (et vice versa). This contamination was found to be most significant for the K_{Short}^0 sample. Hence a final cut was applied to the $V0$ tracks, whereupon Λ and $\bar{\Lambda}$ candidates with hypothesised K_{Short}^0 masses close to the true K_{Short}^0 mass were rejected, and similarly K_{Short}^0 candidates where $V0$ tracks that could be Λ or $\bar{\Lambda}$ particles were also removed. The net result of all the above cuts is shown figure 3.12 for $V0$ tracks found in $0 - 5\%$ central $Au + Au$ collisions at $\sqrt{s_{NN}} = 200$ GeV, for the momentum interval $3.0 \leq p_T^{trig.} \leq 6.0$ GeV/c. As can be seen in the figure, high purity populations of the three species were obtained.

Together with reconstructed unidentified charged tracks, these identified particles formed the input to the correlation analyses to be described in the following chapters. The reconstructed spectra of each population are overlaid in figure 3.13, for a sample of 20 million $0 - 10\%$ central $Au + Au$ events from the online central triggered dataset. Note that the unidentified charged tracks have been scaled by a factor $1/50$ to aid their display. The spectra offer some initial expectations for correlations. In particular, since the tails of the charged track and K_{Short}^0 distributions appear

3.7. PARTICLE IDENTIFICATION AND NEUTRAL STRANGE PARTICLE RECONSTRUCTION

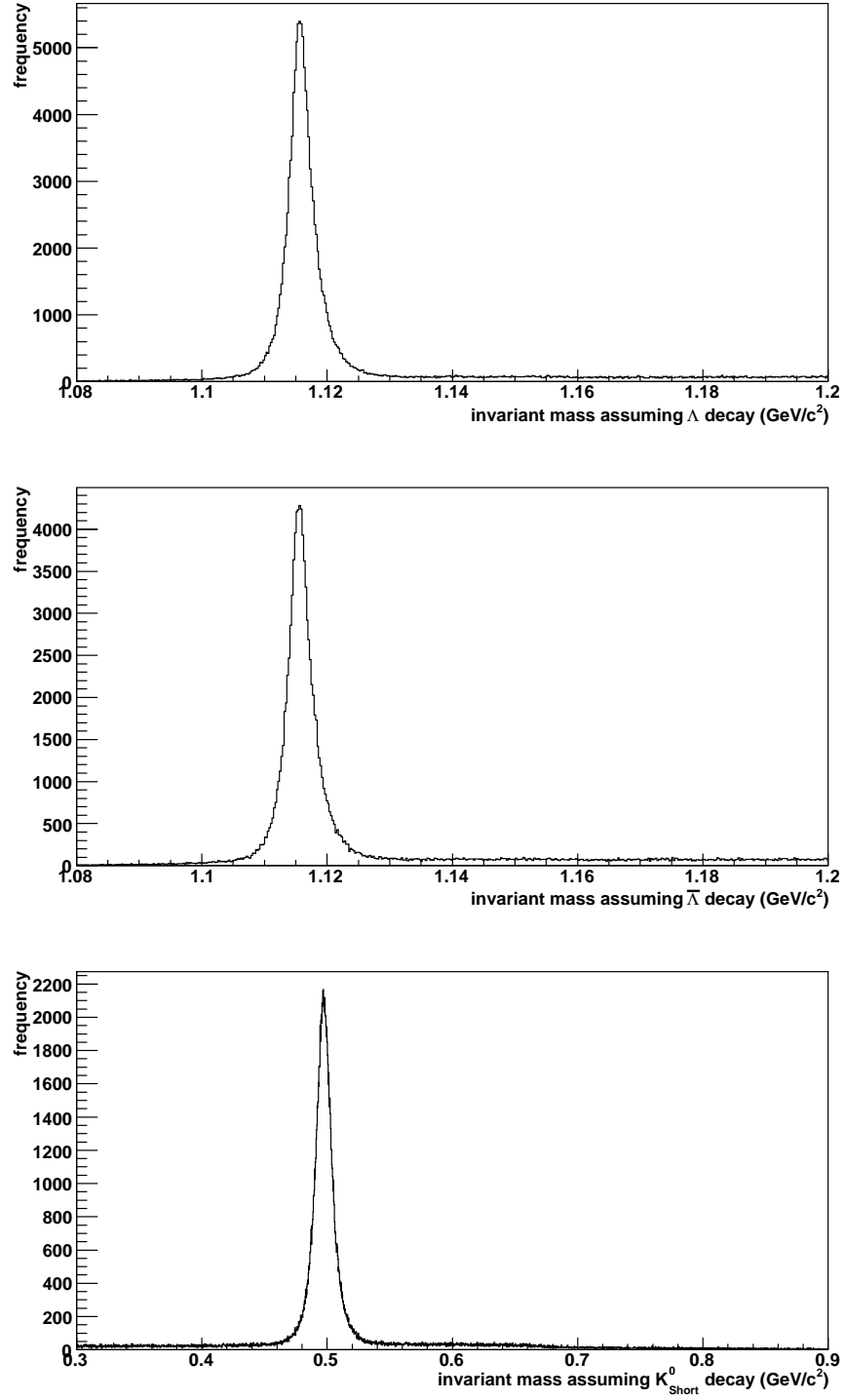


Figure 3.12: Invariant mass spectra for V0 candidates with $2.0 \leq p_T^{\text{trig.}} \leq 6.0$ GeV/c in $Au + Au$ collisions at $\sqrt{s_{NN}} = 200$ GeV after geometrical cuts have been applied and V0 candidates with ambiguous hypothesised invariant masses have been rejected. Species are from top to bottom: Λ , $\bar{\Lambda}$, K_{Short}^0 particles. The vertical axis has been scaled by the number of events.

3.7. PARTICLE IDENTIFICATION AND NEUTRAL STRANGE PARTICLE RECONSTRUCTION

more shallow than the baryons, one could expect jet-like correlations to be more pronounced for these species.

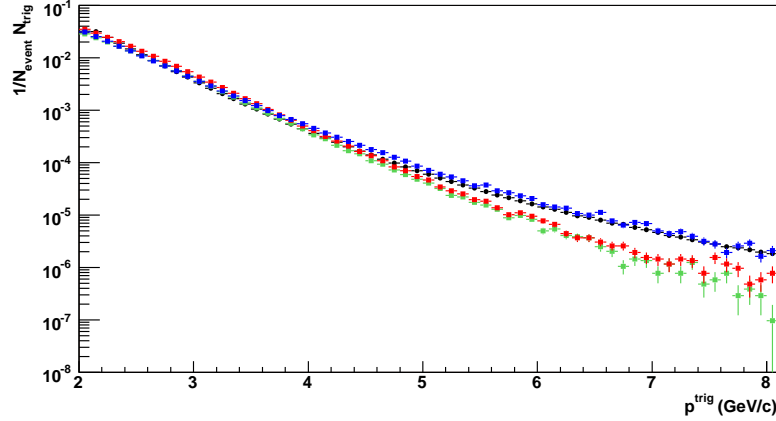


Figure 3.13: Reconstructed trigger particle spectra for a sample of 20 million 0 – 10% central $Au + Au$ events from the online central triggered dataset. Black markers represent unidentified charge tracks, and have been scaled by a factor 1/50 to aid their display. Red, Green and Blue markers represent Λ , $\bar{\Lambda}$, and K_{Short}^0 particles respectively, reconstructed from V0 tracks. Note these spectra have not been corrected for reconstruction efficiency as this is eliminated from correlations normalised by the number of found trigger particles.

3.7.1 Embedding

In the present analysis, particle yields (in correlations) were corrected for reconstruction efficiency using parameterisations derived from particle embedding studies. Embedding comprises inserting MC generated particles into real events and calculating reconstruction efficiencies based upon the success rate of finding the artificial tracks. In this process the real events provide a true representation of the background from which particles are reconstructed.

The embedding chain begins by using a MC generator to produce a distribution of particles of interest. At this stage the primary vertex information of the real event is used as the vertex for simulated particles. The p_T distribution of MC tracks is either made to mimic the real data, or is set to flat, in which case additional corrections are required at the analysis phase to account for the distribution of

3.7. PARTICLE IDENTIFICATION AND NEUTRAL STRANGE PARTICLE RECONSTRUCTION

particles within a p_T bin. The number of MC particles to be embedded per event must be small compared to the real multiplicity to avoid significantly altering the reconstruction efficiency. Typically 5% of a given event multiplicity is generated.

The generated particles are next made to propagate through an accurate GEANT simulation of the STAR apparatus [87]. In the case of particles that are studied by their decays (such as $V0$ s), branching ratios are typically ignored and all particles are forced to decay via the channel of interest. The derived efficiency is then weighted by the branching ratio.

The resulting tracks of electron-ion pairs in the simulated TPC are then passed to an algorithm that models the TPC response function [87]. The same algorithm also simulates the avalanche and image charge generation at the pad plane, before finally converting the readout to a digital signal.

The digital signal, which constitutes the simulated response of the TPC to the MC particles, is then added to the real event signal. The resulting modified event is then passed through the standard reconstruction chain (although distortion corrections are not applied as the simulated particles are undistorted). The reconstructed event includes the initial MC distribution, as well as a list of reconstructed tracks that are associated to MC particles. From these two populations the reconstruction efficiency of the particles can be determined.

A parameterisation of the reciprocal of the estimated reconstruction efficiency correction factor of charged primary tracks in $Au + Au$ collisions is shown in figure 3.14 as a function of transverse momentum. Embedding was performed using minimum bias events that were divided into nine centrality subsets according to reference multiplicity. The reconstruction efficiency is observed to decrease with increasing centrality due to the increase in track density.

An alternative reconstruction efficiency parameterisation was available that, in addition to p_T and centrality, returned efficiencies for charged tracks dependent upon

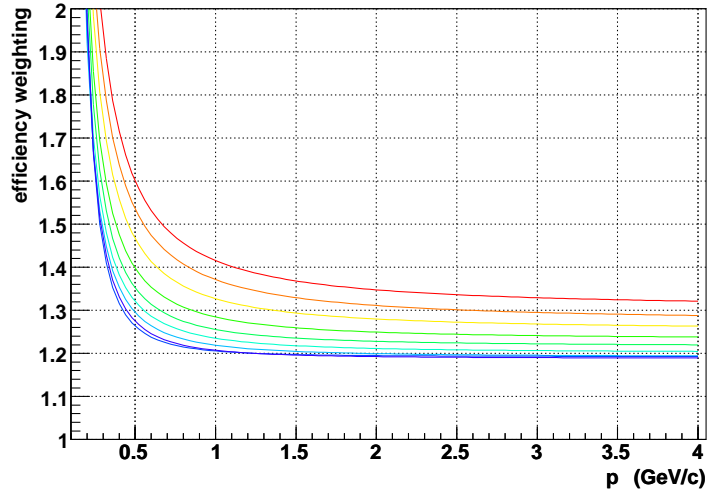


Figure 3.14: Parameterisation of primary track reconstruction efficiency, as a function of p_T and centrality in $Au + Au$ events with $\sqrt{s_{NN}} = 200$ GeV. The vertical axis is the reciprocal of the efficiency. Colour represents centrality selection. From red to violet (upper to lower): 0 – 5%, 5 – 10%, 10 – 20%, 20 – 30%, 30 – 40%, 40 – 50%, 50 – 60%, 60 – 70%, 70 – 80%.

the pseudo-rapidity of a track [88]. The functional form of this parameterisation is displayed graphically in figure 3.15. This parameterisation was constructed using events from an integrated range in primary vertex $|z| < 25$ cm, and embedded charged pions over a momentum range encompassing that used for the present correlation analysis. In an ideal case, the z-position of primary vertex would also be retained as a variable in studies of reconstruction efficiency. To date however, this has been unfeasible due to the limited size of the MC dataset that can be generated using current computing resources.

3.7. PARTICLE IDENTIFICATION AND NEUTRAL STRANGE PARTICLE RECONSTRUCTION

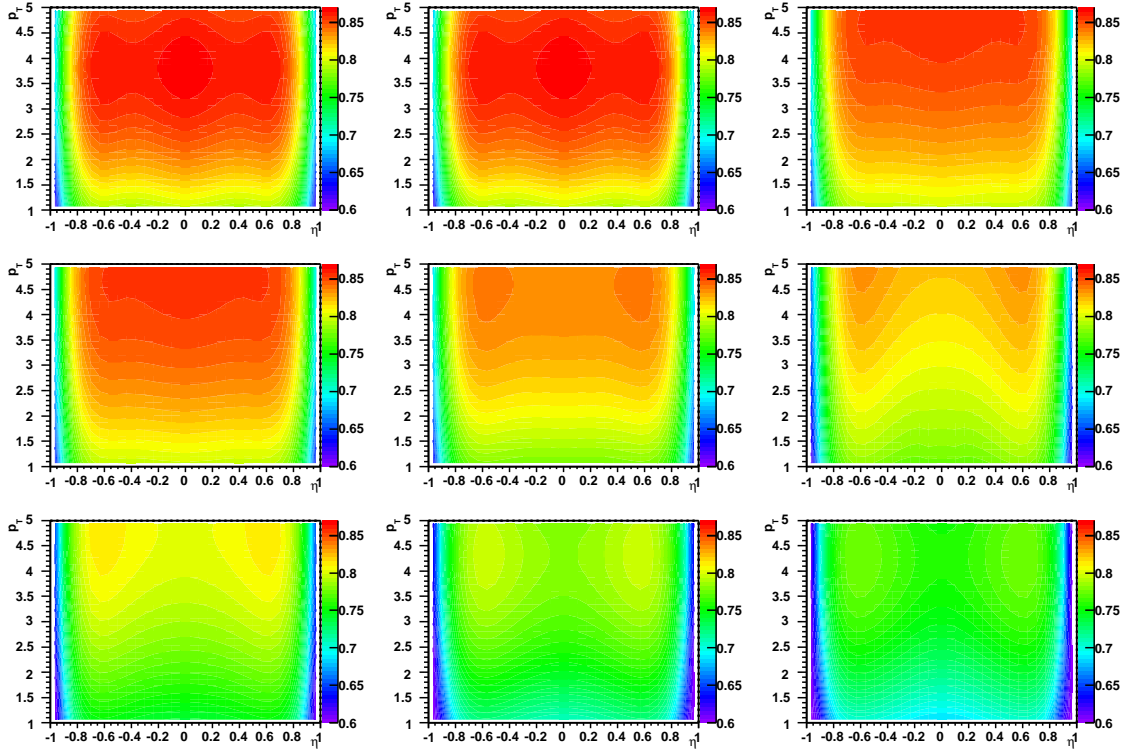


Figure 3.15: Parameterisation of charged π reconstruction efficiencies for nine centrality bins, as a function of momentum and pseudorapidity. From upper left to lower right centrality selections are 0 – 5%, 5 – 10%, 10 – 20%, 20 – 30%, 30 – 40%, 40 – 50%, 50 – 60%, 60 – 70%, 70 – 80%.

Chapter 4

AZIMUTHAL TWO-PARTICLE CORRELATIONS

4.1 Introduction

In general, two-particle correlations reveal the angular relationship between particles in a system. They comprise the distribution of pairs displayed as a function of the angular separation of the pair. This technique is well suited to the study of jet-like phenomena in high energy nuclear collisions, where jet fragments only account for a small fraction of the total multiplicity, and are indistinguishable from other collision products. This is illustrated in figure 4.1, which shows the distribution of tracks recorded at STAR for a $Au + Au$ collision at $\sqrt{s_{NN}} = 200$ GeV. The large background in the heavy ion system compromises the effectiveness of the techniques historically implemented to study jets such as jet finding algorithms and hemisphere analyses. Two-particle correlations avoid the need to identify jets on an event-by-event basis, and instead they offer a means to study jets on a statistical basis, summing over many events.

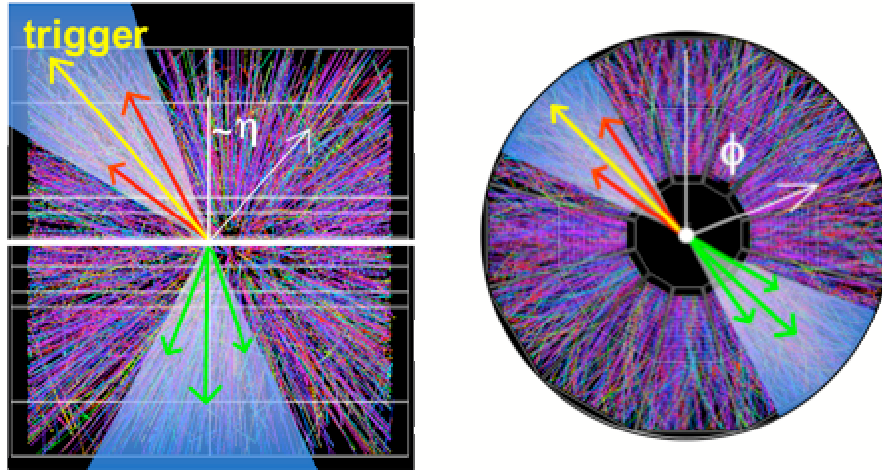


Figure 4.1: Schematic representation of a di-jet overlaying a real heavy-ion collision observed in the STAR Time Projection Chamber (TPC). The left image shows the projection transverse to the beam axis. The right image illustrates the azimuthal projection. Arrows represent jet daughter tracks, with lengths indicating momenta.

4.2 Procedure

Correlations were produced in the present analysis according to the following recipe. The routine begins by searching for high- p_T tracks in an event, hereafter labelled trigger tracks. For each trigger track, pairs are formed with all other high- p_T tracks in the event with momenta less than the trigger. This second set are called associated tracks. The angular separation of each pair is added to the correlation distribution, and then the routine proceeds to the next event to repeat the process. After the correlation has been made with all the triggers in the dataset, it is normalised by the number of triggers. This results in a correlation yield per trigger, that is independent of the size of the dataset and the jet production cross-section. This step is inspired by measurements of fragmentation functions where the yield of hadrons was normalised by the number of jets.

The p_T ranges of accepted trigger and associated tracks are critical to the nature of the resulting correlation, and the physical processes it gives access to. In order to observe correlations due to jets, a significant fraction of trigger tracks need to

correspond to the leading particles in jets. This can be ensured by imposing a high- p_T threshold for trigger tracks. Similarly, the associated track population can be biased towards jet fragments by rejecting low- p_T tracks.

In figure 4.2 a schematic representation of an azimuthal, $\Delta\phi$, two-particle correlation is shown as would be expected for a light hadronic collision system with no QGP. Note that the axis is periodic over the range shown. The peaks near $\Delta\phi = 0$ and $\Delta\phi = \pi$ radians are caused by back-to-back di-jets. These shall hereafter be referred to as the same side and away side peaks respectively, reflecting the relationship of the pairs. The same side peak is caused by both members of the pair belonging to the same jet, whereas the away side peak results from picking associated tracks in the opposing jet. The third feature in the correlation is a flat pedestal, containing pairs where one or both of the tracks in the pair are not jet fragments.

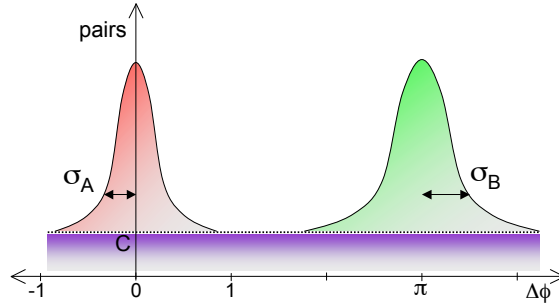


Figure 4.2: Schematic representation of a two-particle azimuthal correlation. The horizontal axis represent the angular separation of trigger and associated tracks. The widths of the same side and away side peaks are labelled σ_A and σ_B respectively. The level of the pedestal is given by C . See text for details.

4.2.1 Single particle reconstruction efficiency

The yield of pairs measured in a given region of phasespace depends upon the distributions of reconstructed tracks, which is the real particle distribution modified by the detector acceptance efficiency. Since the probability of reconstructing a track varies with both multiplicity and momentum, this efficiency must be eliminated prior

to studying the dependence of correlation features as a function of either centrality or kinematic variables. As previously stated, in the present analysis correlations were scaled by the number of found triggers. Therefore only the associated particle efficiencies persisted in the observed distribution of pairs.

This analysis utilised parameterisations of reconstruction efficiencies derived from embedding studies (see section 3.7.1). A graphical representation of these functions can be found in figure 3.14. Parameters included centrality, momentum, species, and later pseudorapidity position (see section 5.2.2). This was then inverted to return a weighting by which correlations could be scaled.

Correlations can be corrected for the reconstruction efficiency of associated tracks either after they have been produced or during the correlation routine. In the former approach a single set of parameters is required to describe all the pairs, thus some average momentum must be assigned to the associated particles found in the permitted range. The preferred approach, and the one adopted in this analysis, was to calculate efficiencies on a pair-wise basis, and weight each pair accordingly as the correlation histograms were filled.

4.3 Correlation function for $d + Au$ collisions

The azimuthal correlation distribution, $D(\Delta\phi)$, is defined in equation 4.1 below where $1/\epsilon$ represents the detector acceptance, and $\Delta\eta$ the pseudorapidity interval. In the case of $d + Au$ collisions, the di-jet correlation can be approximated by two Gaussians as described in equation 4.2, where A and B represent same side and away side terms respectively, and the constant C accounts for the pedestal of uncorrelated pairs.

$$D(\Delta\phi) \equiv \frac{1}{N_{trigger}} \frac{1}{\epsilon} \int d\Delta\eta \frac{dN}{d\Delta\phi d\Delta\eta} \quad (4.1)$$

$$D^{dAu} = \mathcal{I}_A e^{-\frac{1}{2}(\frac{\Delta\phi}{\sigma_A})^2} + \mathcal{I}_B e^{-\frac{1}{2}(\frac{\Delta\phi - \pi}{\sigma_B})^2} + C \quad (4.2)$$

4.3. CORRELATION FUNCTION FOR $D + AU$ COLLISIONS

Equation 4.2 can be rewritten such that the amplitude, \mathcal{I} , is substituted for yield, Y , using the indefinite integral identity, $Y = \mathcal{I}/(\sigma\sqrt{2\pi})$. This is advantageous in analyses where the yield is to be determined, as it allows the covariance of the errors in width and amplitude to be handled by the fitting algorithm.

In figure 4.3 the correlation function is shown for trigger charged tracks with $3.0 \leq p_T^{trig.} \leq 6.0$ GeV/c and associated charged tracks with $2.0 \leq p_T^{asso.} \leq p_T^{trig.}$ in $d+Au$ collisions at $\sqrt{s_{NN}} = 200$ GeV, with a fit to equation 4.2 overlaid. The means of each Gaussian term were fixed by definition, but the yields and widths were free parameters.

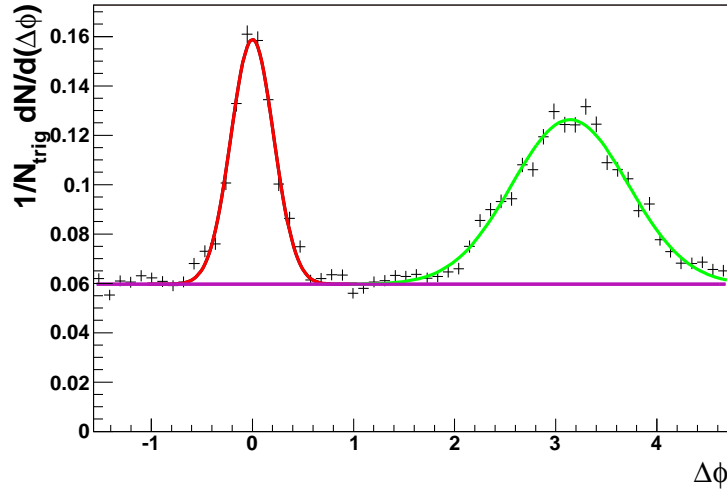


Figure 4.3: Correlation function for unidentified charged tracks with $3.0 \leq p_T^{trig.} \leq 6.0$ GeV/c and associated charged tracks with $2.0 \leq p_T^{asso.} \leq p_T^{trig.}$ in $d + Au$ collisions at $\sqrt{s_{NN}} = 200$ GeV. Equation 4.2 has been fit to the data.

As can be seen in figure 4.3, the same side and away side peaks are qualitatively different. In general the same side peak is narrower. There is no requirement for the yields to equate as these do not represent the inclusive yields of the jets. Peak characteristics are a combination of the physical properties of the di-jet system, and trigger bias introduced by the pair selection criteria.

4.3.1 Physical interpretation of azimuthal correlations

The peak yields relate to fragmentation functions, and a correlation analysis of $d + Au$ collisions can be used as a benchmark with which to compare larger systems where different hadronisation mechanisms and additional interactions may occur. The same side and away side peak widths include the jet cone width, which is set by the fragmentation process. The away side peak width also contains a measure of the acoplanarity of the di-jets due to the intrinsic transverse momentum of the incident partons. The associated particle spectra are also of interest, as the slope of their distributions can be compared to that of inclusive particle spectra, and changes as a function of system size can indicate a modification of the particle production mechanism.

Both the width and yield of correlation peaks carry information relating to the physics of jet phenomena, although the incomplete reconstruction of jets makes it difficult to derive the quantities historically used to describe jets such as the transverse momentum of particles with respect to the jet axis, j_T , and the fragmentation yield as a function of z . Instead, the correlation parameters can be used directly in comparisons of different systems, and investigations into the variation of trigger and associated track kinematics. This was the adopted approach in the present analysis. For more information regarding the estimation of jet properties from correlation peak widths, refer to appendix B.

4.3.2 Trigger bias

In addition to the physical features outlined above, the pair selection criteria result in differences between the same side and away side peaks. The requirement that the same side jet peak contains both trigger and associated tracks, whilst the away side peak only needs to contain associated tracks results in different subsets of jets being included in same side and away side peaks. For a given total momentum,

fragmentation via the production of a trigger leaves less momentum to be shared amongst other jet daughters. Therefore the same side peak is biased towards jets that fragment into a few, high momentum daughters. Consequently, the away side peak would be expected to have a larger yield than the same side, and increasingly so for higher trigger and associated p_T thresholds.

The trigger bias may also result in a different mixture of quark and gluon jets in the two peaks. Quark fragmentation is generally harder than gluon fragmentation as stated in section 2.1.2 above. Therefore for a population of di-jets originating from quarks and gluons may not equally contribute to the same side and away side peaks. The trigger requirement may bias same side peak to preferentially contain quark jets. This affects the nature of the away side peak as well, since many di-jets at RHIC energies originate from quark-gluon scattering [45].

A further bias originates from intrinsic parton p_T , which serves to boost the p_T of observed hadrons, and hence trigger particles will tend to align with this vector. Consequently the total transverse momentum of the away side jet in the lab frame will on average be less than the same side peak.

Overall trigger bias leads to correlations that reflect a particular subset of jets, with different contributions to the same side and away side peaks. Therefore one can expect the yield and widths of the peaks in two particle correlations to vary with trigger and associated p_T ranges purely due to the bias. In the present analysis correlations were first studied in $d + Au$ collisions in order to form a reference with which to compare correlations in heavy ion collisions, and hence reveal physical effects that were not caused by trigger bias.

4.4 Correlation function for $Au + Au$ collisions

In figure 4.4 a correlation is shown for unidentified charged tracks passing the same criteria as for figure 4.3, but for 0 – 10% central $Au + Au$ collisions at the same

energy. In the higher multiplicity system, the pedestal dominates the di-jet signal. Moreover this background is no longer flat, but instead contains a $\cos 2\Delta\phi$ modulation resulting from elliptic flow. Consequently the correlation function is modified from 4.2 to

$$D^{AuAu} = \mathcal{I}_A e^{-\frac{1}{2}(\frac{\Delta\phi}{\sigma_A})^2} + \mathcal{I}_B e^{-\frac{1}{2}(\frac{\Delta\phi - \pi}{\sigma_B})^2} + C \left(1 + 2v_2^{trig} v_2^{asso} \cos(2\Delta\phi) \right), \quad (4.3)$$

where C is a constant and v_2^{trig} and v_2^{asso} are the mean v_2 amplitudes of the trigger and associated particle distributions respectively. The form of the modulation is explained in appendix C.3. Although the background is irreducible, once characterised it can be subtracted from the correlation function. Note that the fit to the away side peak is not shown in the figure as the medium modification results in a structure that is poorly described by a Gaussian. Also note that the correlation function shown in figure 4.4 has been corrected for detector acceptance effects, which are more apparent in higher multiplicity events. See section 5.2 for details.

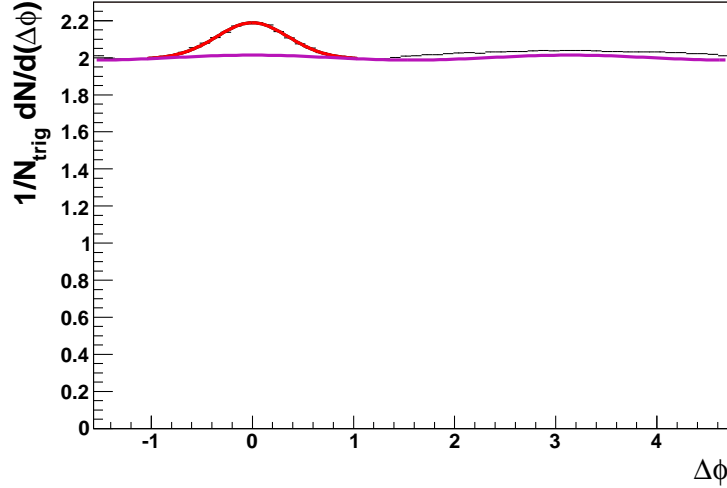


Figure 4.4: Correlation function for unidentified charged tracks with $3.0 \leq p_T^{trig.} \leq 6.0$ GeV/c and associated charged tracks with $2.0 \leq p_T^{asso.} \leq p_T^{trig.}$ in $Au + Au$ collisions at $\sqrt{s_{NN}} = 200$ GeV. Equation 4.3 has been fit to the data. The fit to the away side peak is not shown as the data is poorly described by a Gaussian.

4.4.1 Elliptic flow in two-particle correlations

The amplitude of the elliptic flow modulation could be estimated by including it as a free parameter in a fit to the correlation function. However such an approach compromises the accuracy of fits in statistics limited analyses. Additionally this would rely upon an accurate description of the shapes of other structures in the correlation, which were not known. Instead, in the present analysis the elliptic flow modulation was fixed using a parameterisation of flow studies at STAR [32]. For a given correlation the v_2 amplitude was determined by taking the product of v_2^{trig} and v_2^{asso} for the mean p_T of each population. The parameterisation also varied as a function of centrality, and a baryon-meson difference was included.

In principle a more accurate account of the v_2 amplitude would have been achieved by applying the parameterisation on a pair-wise basis (as was performed for the reconstruction efficiency correction). However this was not possible due to a large systematic uncertainty in the v_2 estimated from different flow analyses. The upper and lower limits of these were found to be the dominant systematic errors to feature in the present analysis.

Due to the significance of these measurements on the present analysis, the two flow analyses used will be described in the following discussion. First, the reaction plane method will be reviewed, which is understood to overestimate the flow [89]. Second, the multi-particle cumulant approach will be introduced, from which the four particle cumulant results were used to set the lower limit of the flow modulation [89]. The last part of this section contains a discussion of the background level estimation.

Two-particle correlations: reaction plane method

Relative to the reaction plane angle Ψ (defined in figure 1.6), azimuthal two-particle correlations of the bulk ($p_T \lesssim 2$ GeV/c) exhibit the sinusoidal harmonics described

in section 2.4.1. Therefore, in order to sum the correlation over many events, Ψ must be measured on an event-by-event basis. Moreover, estimates of v_2 must be corrected for the resolution of the reaction plane. The resolution varies with centrality (multiplicity dependence combined with the strength of the anisotropy). Unfortunately in the absence of an external definition (such as another detector), the reaction plane itself is best defined by the correlation, or to be more precise, by the flow vector, which is the vector sum of the azimuthal distribution of particles. This interdependence is overcome by considering sub-events [89].

Typically events are sub-divided either randomly, by charge sign or by pseudorapidity sign. Each of these have different sensitivities to non-flow effects, which then can be evaluated by comparison. The difference in reaction planes measured two sub events a and b gives a measure of the resolution, which then can be used to correct the results of the full-event correlation. The measured reaction plane resolution ranged from $\langle \cos(2(\Psi_a - \Psi_b)) \rangle = 0.8$ in mid-central collisions to ≈ 0.5 in both the most central and most peripheral samples. It was found that by weighting particles by their p_T ¹, the resolution of v_2 could be greatly improved [89].

Each harmonic yields a different estimate of the same reaction plane, with the v_2 providing the lowest resolution. The v_2 plane has been used in some studies of other harmonics in a approach referred to as mixed harmonic methods [32].

Defining the reaction plane via particle correlations relies upon the assumption that non-flow effects are small, but this cannot be guaranteed. Measurements derived by the above recipe tend to overestimate the magnitude of v_2 as a result of Coulomb, quantum, jet, resonance decays and momentum conservation effects.

¹ v_2 increases with p_T thus weighting by p_T suppresses the weak flow of the numerous low p_T particles

Four-particle correlations: cumulant method

A cumulant is a global property of a system that can only be defined in terms of several particles. Cumulants are particularly useful to the analysis of anisotropic flow in URHIC because non-flow effects are subtracted out. For example, the four particle cumulant is defined as the difference between the four-particle correlation and the square of the two-particle correlation [89]. The cumulant is typically equal to the v_n harmonic raised to some power, in this case v_n^4 . Statistical uncertainties increase with the order of the cumulant.

Four particle cumulants, have been applied to STAR data. With multiplicities $\sim 10^3$ it is impractical to consider all four-particle combinations. At the expense of statistics, the computation can be simplified by deriving the four-particle correlation using at least four sub events.

Due to the reduced sensitivity to non-flow, the cumulant method is believed to provide a lower limit for v_2 . Studies of six-particle correlations are consistent with four-particle results, suggesting that the non-flow is already adequately removed from the four-particle cumulant measurement [32]. Note that the cumulant measurement is believed to underestimate the flow due to v_2 fluctuations. In figure 4.5 the measured level of v_2 is shown for two, four and six particle cumulants. Two-particle cumulant results are equivalent to the reaction plane method.

4.4.2 Estimation of combinatorial background level

Similar to the elliptic flow modulation, allowing the level of combinatorial background to be a free parameter reduced the stability of fits to statistics limited correlation functions. A more reliable approach comprised making the assumption that a certain region of the correlation function contained no yield above the background. Previous analyses at PHENIX have referred to this as the zero yield at minimum (ZYAM) approximation [90]. This assumption essentially represents the maximum

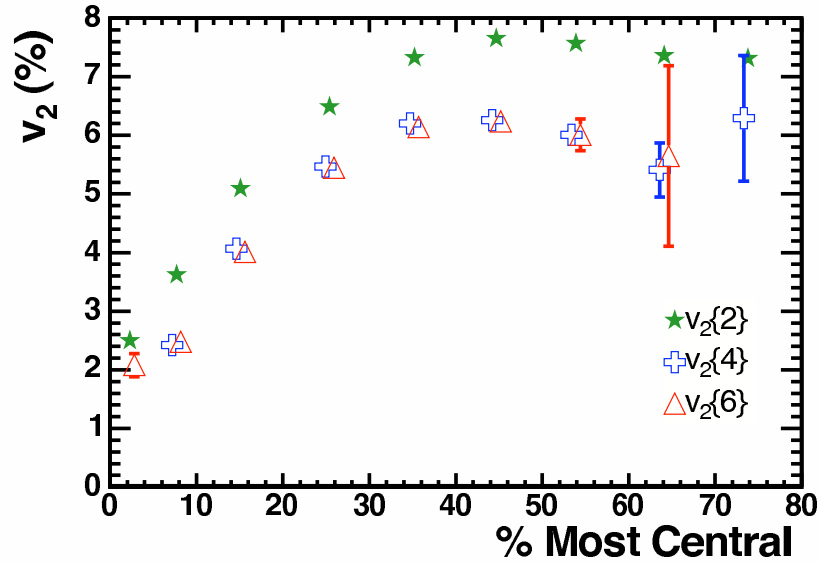


Figure 4.5: $v_2\{2\}$, $v_2\{4\}$ and $v_2\{6\}$ for charged hadrons produced in $Au + Au$ collisions at $\sqrt{s_{NN}} = 200$ GeV measured at STAR [32] as a function of centrality.

estimate of the background level, and therefore the extracted peak yields are in fact the lower limits. However, it is in principle possible for interactions between the jet and medium to deplete the medium and hence reduce the background level in the vicinity of the jet, which would lead to the ZYAM approach overestimating the background level. Two variants of ZYAM estimations were attempted, either by taking the average of the minima to each side of the same side peak, or by assuming zero yield at $|\Delta\phi| = 1.0$ radians. Both offered estimates with similar attached uncertainties. Assuming the former procedure, the level of the background would be determined from the measured minimum Z by the relation

$$C = \frac{Z}{(1 + 2 \cos(2\Delta\phi_{min}))}, \quad (4.4)$$

where ϕ_{min} is the location of the minimum. The ZYAM approach is applicable to correlations providing the same side and away side peaks are sufficiently narrow that a region in $\Delta\phi$ space exists with negligible contributions from each.

Chapter 5

TWO-DIMENSIONAL CORRELATIONS

5.1 Introduction

Through the course of the present analysis, correlations were extended to include pseudo-rapidity difference, $\Delta\eta$, providing a two-dimensional analysis of jets. A schematic representation of a di-jet in the longitudinal plane overlaying a real event measured at STAR is shown in figure 4.1. Including pseudo-rapidity difference allowed a more complete description of peak shapes to be developed. In particular studying correlations in $(\Delta\eta, \Delta\phi)$ space significantly improved the description of the same side peak in high multiplicity events. As a result earlier observation of a large same side I_{AA} was identified with a substantial broadening in $\Delta\eta$. The method developed to characterise this modification is given at the end of this chapter.

As a new analysis, two-dimensional jet correlations introduced several analytical challenges. In addition to physical correlations, raw two-particle correlations are heavily influenced by the acceptance of the detector from which the trigger and associated particles are sourced. This acceptance translates into a probability of finding

a pair of tracks in a given region of the $(\Delta\eta, \Delta\phi)$ space. Corrections were required for single particle reconstruction efficiency, pair-wise acceptance and two-track resolution. The former correction remained unchanged from azimuthal correlations. Procedures were developed to account for detector acceptance and two-track resolution, which had not previously been implemented. This formed the greater part of the present work.

5.2 Pair-wise acceptance

The acceptance of the STAR TPC is only approximately uniform in azimuth and finite in pseudo-rapidity. Consequently the probability of finding a pair of tracks varies as a function of angular separation. In figure 5.1 typical distributions of tracks reconstructed from TPC data are presented, for the momentum range used in this analysis. Although the detector occupies a full 2π radians in the azimuthal plane, regions of reduced acceptance lie between the twelve sectors. The boundaries are responsible for reduced track densities at regular intervals in ϕ . For a primary vertex located at the central membrane, the reconstruction efficiency of charged tracks is approximately linear within $|\eta| < 0.931$, and rapidly decreases beyond this as tracks leave through the ends of the TPC and thus cross fewer pad rows whilst traversing the active volume. For primary vertices away from the central membrane, the distribution is skewed and the limits in η are shifted. Consequently, for the present analysis events were constrained to the range $|z| < 30$ cm.

A raw two-particle correlation involving charged tracks reconstructed from central $Au + Au$ events is shown in figure 5.2. Note that the origin of the azimuthal axis has been displaced to give a range of $-\pi/4 < \Delta\phi < 3\pi/4$. The correlation is dominated by an approximately triangular structure along the pseudo-rapidity difference ($\Delta\eta$) axis, and in the azimuthal ($\Delta\phi$) projection the physical features are modulated by a set of peaks at regular intervals. In appendix C.1 these structures

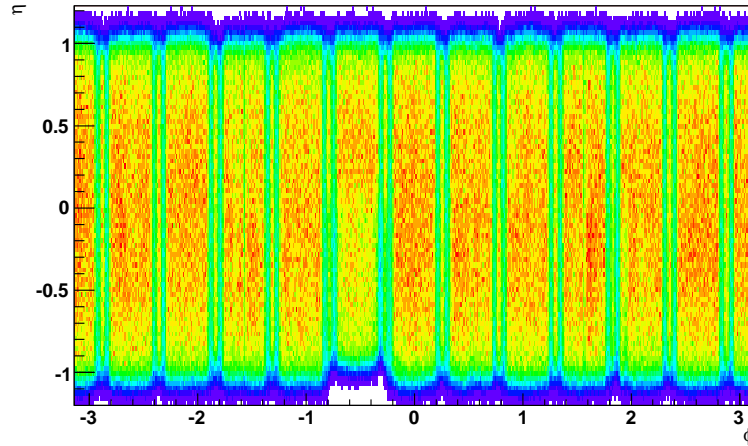


Figure 5.1: Reconstructed primary track distributions in a sample of $\sim 10^6$ minimum bias $Au + Au$ events at $\sqrt{s_{NN}} = 200$ GeV. The vertical and horizontal axes represent pseudorapidity η and azimuthal angle ϕ . Colour indicates track density, increasing from blue to red. Sector boundaries are responsible for reduced track densities at regular separations in ϕ . Similarly the acceptance in η rapidly declines beyond $\eta \approx 1$.

are demonstrated to correspond to the convolution of single particle distributions.

In the present analysis, two particle correlations were corrected for the detector acceptance by dividing through by the distribution that only contained acceptance effects. The method developed to reproduce the pair-wise acceptance distribution is discussed in the following sections. Only the shape of the distribution was required for the present analysis; the efficiency of finding pairs as a function of $(\Delta\eta, \Delta\phi)$ space was applied as a correction relative to the maximum acceptance at $\Delta\eta = 0$. The estimation of this maximum and the actual correction procedure will be discussed in section 5.4.

5.2.1 Introduction to event mixing

Although in principle the detector acceptance can be reproduced by taking a convolution of trigger and associated particle distributions, in practise the necessary discretisation limits the ability to faithfully reproduce the feature present in a correlation. Attempts to correct correlations using (discrete) convolutions failed towards

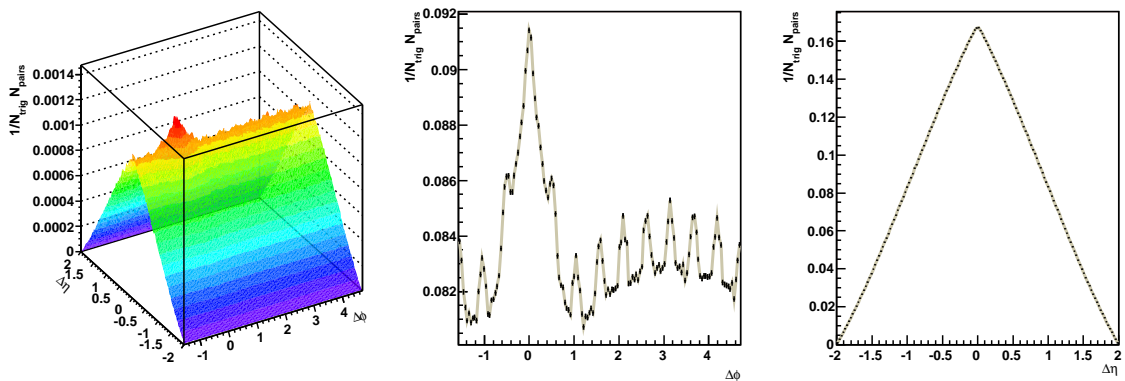


Figure 5.2: Raw two-particle correlation of primary tracks in 0-10% central $Au+Au$ events at $\sqrt{s_{NN}} = 200$ GeV. Triggers satisfied $2.5 \leq p_T^{trig.} \leq 3.0$ GeV/c and associated particles were accepted in the range $2.0 \leq p_T^{asso.} \leq p_T^{trig.}$. The left panel displays the $\Delta\eta - \Delta\phi$ correlation, from which the $\Delta\phi$ and $\Delta\eta$ distributions have been projected to obtain the graphs in the centre and right frames.

the limits of the $\Delta\eta$ range due to an inconsistency in the resolution of the convolution. Consider a convolution to be formed by scanning one single particle distribution across another in incremental shifts, and for each step the product of the overlap gives the convolution amplitude in the corresponding $\Delta\eta$ space. The width of a $\Delta\eta$ bin in a convolution is set by the resolution of the single particle distributions, and specifically the upper and lower bounds of individual η bins. However, pairs of bins in the single particle distributions describing the same η location contribute to a smaller range in $\Delta\eta$ than for pairs at different η . This discrepancy, which is more evident at the limits of the convolution range where the fewer η bins contribute, results in a distortion of the acceptance shape simulated by the convolution. Increasing the resolution of the single particle distributions was found to provide some improvement, but a distortion at the limits of the $\Delta\eta$ range was unavoidable.

An alternative means to reproduce detector acceptance is provided by a process called event mixing. This approach involves the construction of a correlation and thus avoids the resolution issues inherent to convolutions. A second advantage is that

5.2. PAIR-WISE ACCEPTANCE

it allows other corrections, such as the single particle reconstruction efficiency, to be applied in the same manner as for real correlations. Indeed in the final version of the correlation routine developed through this analysis, event mixing was performed simultaneously with the collection of real pairs.

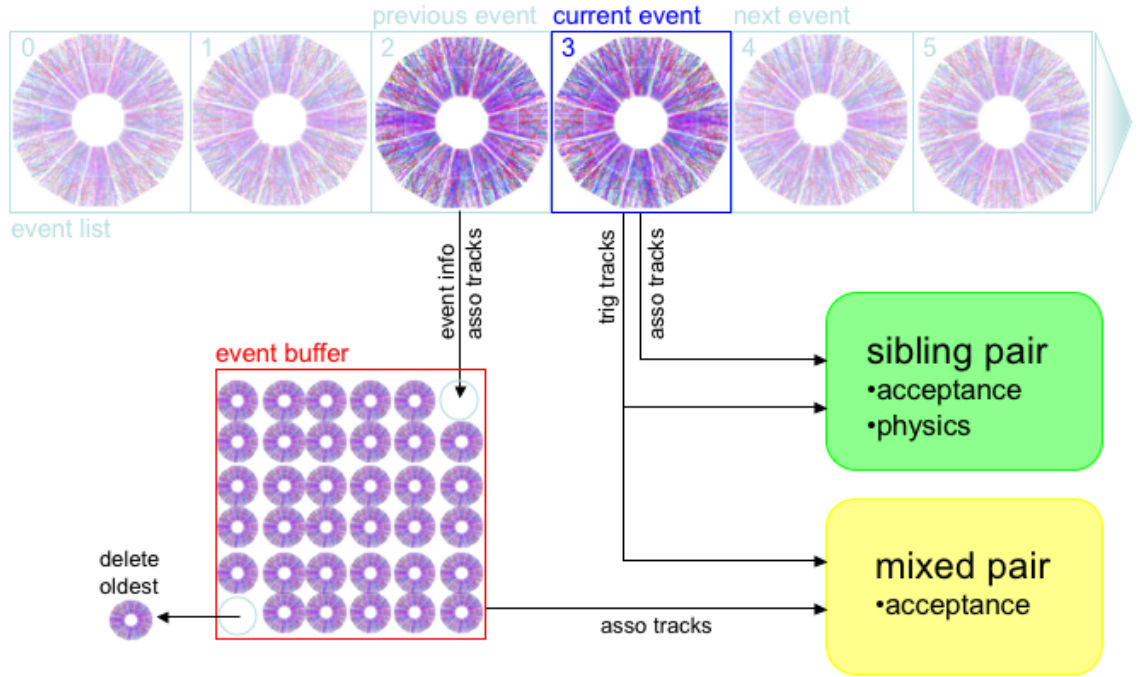


Figure 5.3: Schematic representation of the event buffer mixing routine.

The correlation routine including event mixing is illustrated schematically in figure 5.3. A mixed event correlation is made using trigger and associated tracks sourced from different events. This approach relies on the premise that any two tracks reconstructed in independent events would both still experience the detector acceptance. Hence the distribution of *mixed* pairs should reflect the variable probability of finding pairs in the same manner that real pairs do. Hereafter, the term *sibling* shall be used to refer to real pairs, as this emphasises the relationship of pairs sourced from the same event.

Any one trigger track can be paired with associated tracks from several associated events. Maximal statistics are achieved by mixing every trigger with every other

5.2. PAIR-WISE ACCEPTANCE

event, which would produce a correlation with an occupancy a factor of N_{events} greater than the sibling correlation. However in practise, it is only necessary to generate a mixed event whose statistical uncertainties are small compared to the sibling correlation.

Event mixing can either be performed by retaining triggers from a set of events and forming pairs with the associated tracks of each event, or conversely sourcing associated tracks from a selection of events per trigger. Superficially the two options should be equivalent, however there are practical considerations in terms of both available memory and number of computer operations. Clearly storing trigger tracks is less costly in terms of memory, however the greater abundance of associated tracks can improve the time performance of the routine if it is necessary to find mixing partners. Moreover for rare triggers, such as $V0$ tracks, the desired number of mixing triggers may not exist in the dataset. Therefore it was decided that the second approach would be implemented for this analysis.

Associated events were retained in a buffer as illustrated in figure 5.3, which contained a fixed number of previously accessed events. After the sibling and mixed correlations were made for an event, the associated tracks and event information were passed to the buffer, replacing the oldest event. This procedure was developed in order to minimise the data access from disk, which constituted the most time consuming component of the correlation routine.

To summarise, event mixing provides a bin-by-bin correction for detector acceptance. It avoids the need to parameterise the background shape, and the resolution of any sibling pair distribution is trivially matched since the mixed event correlation is filled in the same manner. Moreover in principle considerably smaller statistical uncertainties can be achieved than sibling pairs.

5.2.2 Event selection

In general mixed events must have similar primary vertex positions and multiplicities in order to give good reproductions of detector acceptance. The background level of mixed events were compared to real correlations by modulating $\Delta\phi$ projections of mixed event correlations with v_2 and then determining the scale factor required to reach an agreement with the ZYAM estimation. It was found that when restricting mixed events to a multiplicity range of < 10 and primary vertex z -position, the mixed event background level could be made to agree within 1% of the expected combinatorial background level after scaling by the trivial factor of the number of associated events per trigger particle. This level of precision was found to be inadequate for central $Au + Au$ events where the correlation peak signal represents an enhancement above background to the same order of magnitude. Additionally, the present analysis also considered rare $V0$ trigger particles, and the available datasets were insufficiently large to allow very narrow multiplicity and vertex position selections to be used for these. As a result, for this analysis only the shape and not the absolute occupancy of mixed events were used. Hence the mixed events were fairly insensitive to multiplicity selection, although mixing was still performed within centrality classes to ensure consistent statistics.

The position of the primary vertex was a far more influential characteristic to the shape of mixed events, for the reason alluded to in section 5.2 above. In order to study the $\Delta\eta$ broadening of the same side peak in central $Au + Au$ events, a wide $\Delta\eta$ range was required. Thus tracks were accepted within $|\eta| < 1.0$. Unfortunately, such a range was also sufficiently wide to show significant variations in reconstruction efficiency in the η direction as a function of primary vertex z -position, which could result in distortions to the mixed event shape. In order to guarantee that mixed trigger and associated tracks experienced similar detector acceptance functions, and hence that the acceptance shape was faithfully reproduced, a 2 cm constraint was

imposed on the difference between the z-positions of the primary vertices for mixed events.

5.2.3 Acceptance-corrected correlations

The performance of the event mixing algorithm is illustrated in figures 5.4 and 5.5, which show unidentified charged track correlations in $d + Au$ and $0 - 10\%$ $Au + Au$ collisions respectively at $\sqrt{s_{NN}} = 200$ GeV. In both figures from top to bottom the sibling correlation, mixed event, and corrected distributions are shown in $(\Delta\eta, \Delta\phi)$ space. These correlations included trigger tracks with $3.0 \leq p_T^{trig.} \leq 6.0$ GeV/c and $2.0 \leq p_T^{asso.} \leq p_T^{trig.}$. Division by the mixed event distribution successfully removed sector gap features in the $\Delta\phi$ direction, and the triangular acceptance shape in $\Delta\eta$, resulting in corrected distributions with flat backgrounds in $\Delta\eta$ and $\Delta\phi$.

In the corrected $d + Au$ correlation, it can be seen that although the same side and away side peaks are qualitatively similar in the $\Delta\phi$ direction, their $\Delta\eta$ distributions are distinctly different. The same side peak is localised around $\Delta\eta = 0$, and is approximately Gaussian. In contrast the away side peak is extended in $\Delta\eta$. This is in part a consequence of the rest frame of the measurement not coincident with the rest frame of the hard parton scatter, since partons' longitudinal momenta are in general unequal in the rest frame of the nuclei. Secondly, even for truly back-to-back jets, the away side peak would appear extended in $\Delta\eta$ unless the difference were redefined $\Delta\eta = |\eta_{asso}| - |\eta_{trig}|$. Correlations using tracks in peripheral $Au + Au$ collisions were comparable to the $d + Au$ result.

The corrected correlation for central $Au + Au$ collisions shown in figure 5.5 exhibits clear differences to that observed in the lighter system. As described in section 1.4.3, the away-side peak in $Au + Au$ collisions is considerably suppressed compared to $d + Au$ (elliptic flow has not been subtracted from this figure). A remarkable

and quite unanticipated observation is the clear modification of the same side peak. Despite the expected surface bias discussed previously, the same side peak shows evidence of interaction with the medium. When viewed in the $\Delta\phi$ plane, no immediate shape difference is apparent. However when pseudo-rapidity separation is also included, two structures are resolved. A peak is found localised around $\Delta\eta = 0$ and somewhat broader in this direction than its counterpart in $d + Au$ collisions. The second structure is a ridge, extending beyond $|\Delta\eta| = 1.5$. The shape of the ridge is similar to the contribution from elliptic flow, however its localisation on the same-side suggests some relationship with the jet process.

The characterisation of the modified same side peak in the $Au + Au$ system formed the focus of the present analysis. The method developed to quantify the peak properties is described in section 5.4 at the end of this chapter. One further correction was required for this analysis, to account for the limited resolution of two tracks. This shall be addressed in section 5.3.

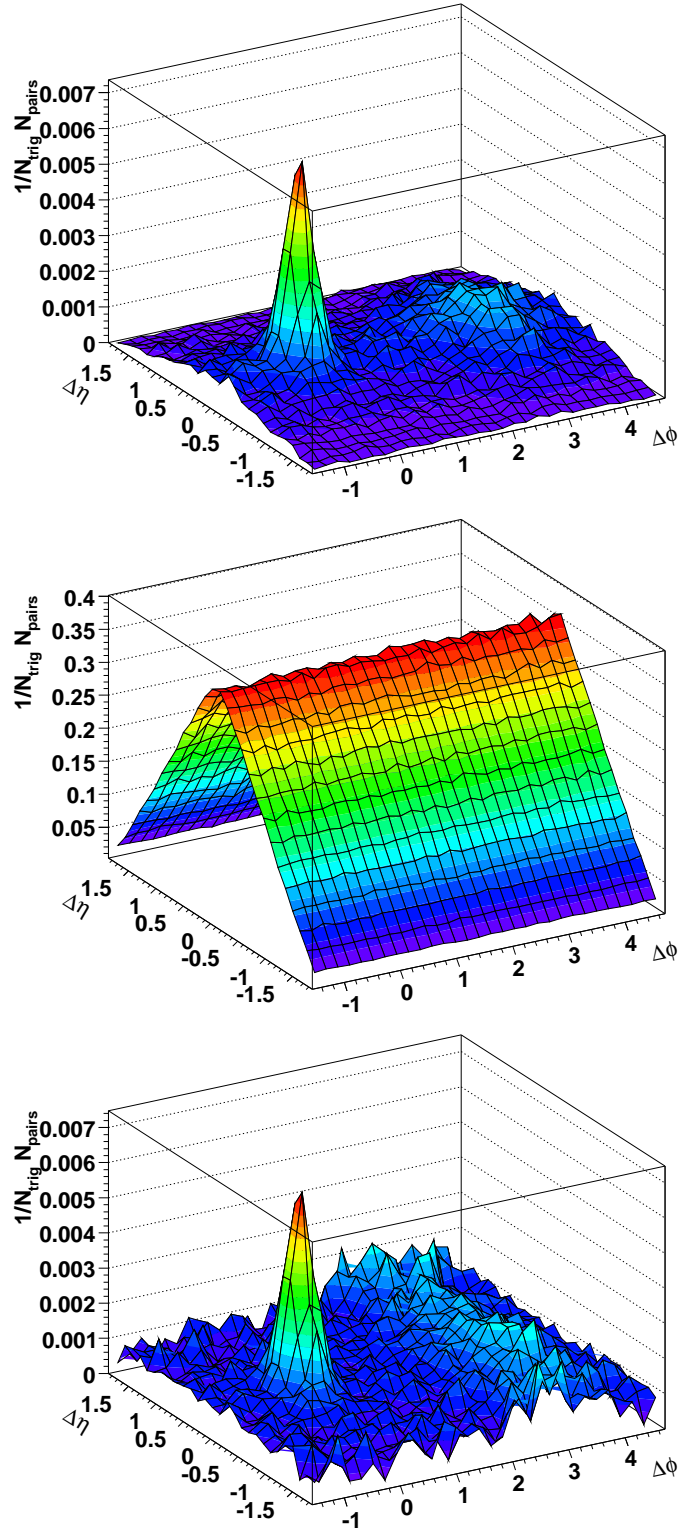


Figure 5.4: Unidentified $\Delta\eta$ - $\Delta\phi$ correlations in $d + Au$ collisions at $\sqrt{s_{NN}} = 200$ GeV. From top to bottom, the distributions are the sibling correlation, mixed event correlation, and their ratio giving the acceptance corrected correlation. Tracks were accepted within $3.0 \leq p_T^{\text{trig.}} \leq 6.0$ GeV/c and $2.0 \leq p_T^{\text{asso.}} \leq p_T^{\text{trig.}}$.

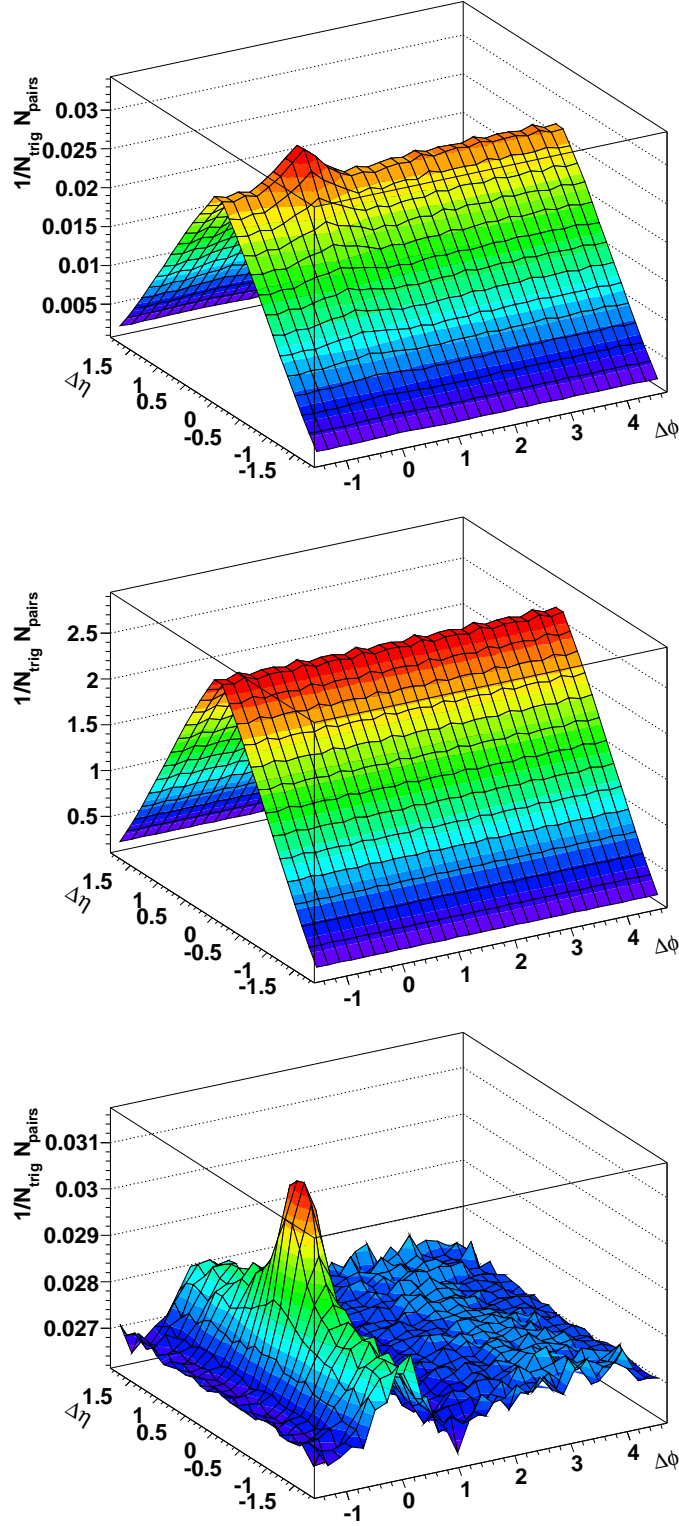


Figure 5.5: Unidentified $\Delta\eta$ - $\Delta\phi$ correlations in 0 – 10% central $Au + Au$ collisions at $\sqrt{s_{NN}} = 200$ GeV. From top to bottom, the distributions are the sibling correlation, mixed event correlation, and their ratio giving the acceptance corrected correlation. Tracks were accepted within $3.0 \leq p_T^{\text{trig.}} \leq 6.0$ GeV/c and $2.0 \leq p_T^{\text{asso.}} \leq p_T^{\text{trig.}}$. Note that the origin of vertical axis has been suppressed.

5.2.4 Summary

Although event mixing can provide correlations with a considerably larger amount of pairs than the equivalent sibling correlation, the process remains limited by size of the dataset, and the need to mix similar events. In principle it would be preferential to divide the dataset into subsets of narrow primary vertex ranges, and correct each one individually. This approach was investigated and it was found that in order to fully correct for acceptance, it would also have been necessary to apply an η - and z - dependent reconstruction efficiency correction. However, this increased accuracy comes at the expense of statistics. Since the acceptance correction involves the division of two distributions, the method is sensitive to statistical fluctuations. Furthermore unoccupied bins in $(\Delta\eta, \Delta\phi)$ space cannot be corrected, and distort the final distribution.

Also due to statistical limitations, event mixing also imposes a constraint upon the p_T ranges of trigger and associated tracks. If too few triggers or associated tracks are available, the single particle distributions will not be sufficiently occupied to display their form, resulting in mixed events that are dominated by the position of the few existing tracks. In the extreme case of a single trigger track, the mixed event distribution describes the single particle distribution of associated tracks.

In the present analysis it was decided that the division of histograms should be relegated to the final step in producing a correlation. Mixed events were produced within narrow data subsets, and then summed to give one acceptance distribution for the complete dataset. This method was found to provide a good acceptance correction to the required precision of the measurements of interest. Should the analysis to be extended to much lower momentum tracks in a future investigation, the signal to background level would reduce and this approximation would no longer be adequate. However, the increased density of pairs could permit the acceptance corrections within subsets of events.

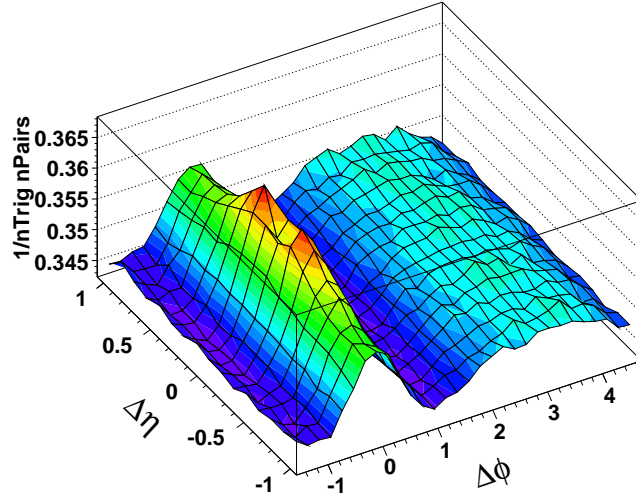


Figure 5.6: $\Delta\eta - \Delta\phi$ correlation of unidentified charged tracks with $3.0 \leq p_T^{trig.} \leq 6.0$ GeV/c and $1.0 \leq p_T^{asso.} \leq 2.5$ GeV/c. The distribution has been corrected for detector acceptance using a mixed event correlation. A deficit is observed in the number of pairs found near $(\Delta\eta, \Delta\phi) = 0$.

5.3 Two-track resolution

By extending the analysis from one-dimensional azimuthal distributions over integrated pseudorapidity ranges to two-dimensional correlations in $(\Delta\eta, \Delta\phi)$ space, the study became sensitive to pairs with small opening angles. In figure 5.6 the $\Delta\eta - \Delta\phi$ distribution of unidentified charged pairs is displayed after correction for pair-wise acceptance using a mixed event correlation as described in section 5.2.1 above. The combinatorial background has been suppressed to emphasise the physical features. In addition to these, a pronounced dip is visible near $(\Delta\eta, \Delta\phi) = 0$. Correlations involving $V0$ tracks exhibited similar dips.

In the following discussion it shall be shown that this dip is caused by a reduced reconstruction efficiency of pairs with small opening angles. In this analysis it was found that both the limiting resolution of nearby tracks and also losses due to crossing tracks contributed to the suppression of pairs. The latter contribution was in

5.3. TWO-TRACK RESOLUTION

part a consequence of the approach taken by the tracking algorithm, which removed associated hits from the data pool after each reconstructed track was found. For crossing tracks, the hits of one track could be erroneously assigned to its neighbour, or alternatively charge clusters could fail to exceed the two hit resolution; in either case the second track would stand a poorer chance of being reconstructed. Hence one can anticipate that the probability of finding pairs in this region of phasespace is low relative to more distant pairs.

The basic mixed event correlations described in section 5.2.1 do not automatically contain any notion of two track resolution. The reconstruction efficiencies of the two tracks that constitute a mixed pair are completely independent since the tracks originate from different events, and thus it is entirely possible to have pairs of tracks with considerable overlap. Hence dividing a sibling correlation by this mixed event only serves to highlight the suppression of yield near the origin.

Before proceeding to the detailed diagnosis of the dip, it is important to emphasise one point regarding its discovery and significance in the present analysis: no dip is observed in $d + Au$ correlations with the same selection as for figure 5.6. Although the reconstruction efficiency of tracks improves in lower multiplicity environments, this absence is not an indication of improved two-track resolution. The critical distinction between the $d + Au$ and $Au + Au$ correlations here is the level of combinatorial background compared to the same side peak since the magnitude of the dip reflects the reconstruction efficiency of all pairs in a given $\Delta\eta - \Delta\phi$ interval. Therefore, even for an identical efficiency in both datasets, the dip would be significantly more pronounced in the $Au + Au$ correlation after background subtraction. For example, if the dip constitutes a 1% loss in both correlations, and the same side peak is a 50% enhancement above background in the $d + Au$ correlation but just a 4% enhancement in the $Au + Au$ correlation, then after background subtraction the dip would appear as a 2% loss for $d + Au$ but a loss of 25% for $Au + Au$.

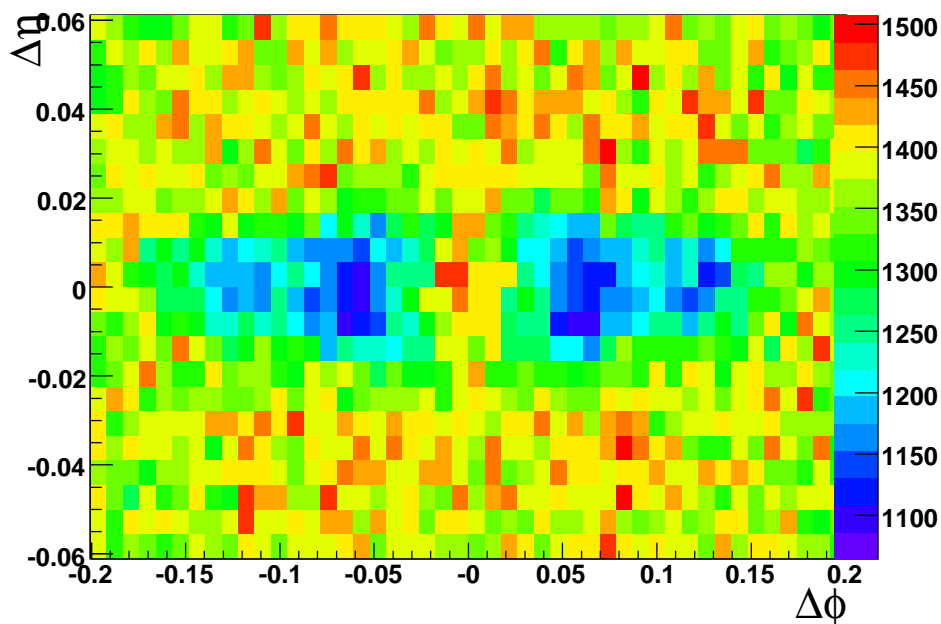


Figure 5.7: Detailed inspection of $\Delta\eta - \Delta\phi$ correlations of unidentified charged tracks with small opening angles revealing four distinct dips. Trigger tracks were selected with $3.0 \leq p_T^{trig.} \leq 6.0$ GeV/c and associated tracks satisfied $1.0 \leq p_T^{asso.} \leq 3.0$ GeV/c .

5.3.1 Detailed diagnosis of the dip in unidentified correlations

In order to gain an understanding of the origin of the dip at $(\Delta\eta, \Delta\phi) \approx 0$, sibling correlations were generated at a far higher resolution than was required for analysis purposes. Upon detailed inspection, the region was resolved into four dips at different $\Delta\phi$ positions, and all centred on $\Delta\eta = 0$. These features are shown in figure 5.7, which displays the $\Delta\eta - \Delta\phi$ correlation of unidentified tracks within $|\Delta\eta| < 0.06$ and $|\Delta\phi| < 0.2$ radians. This correlation was produced using events with both forward and reversed field orientations. When events were separated according to the field setting, and the charge combination of pairs, the origin of these four dips became clear. In figure 5.8 pairs produced in events with a single field setting have been segregated into the four charge combinations. A single dip appears for each case. Since reversals of magnetic field and charge combination give geometrically identical

5.3. TWO-TRACK RESOLUTION

tracks, the dips found in the correlations using events with the reversed field setting superpose those shown in the figure.

Finding dips at finite azimuthal separations suggested the losses were due to crossing tracks, and not genuinely merged tracks. This hypothesis was taken further by considering the radial crossing point of tracks with particular momenta and azimuthal separation. The schematic representation in figure 5.9 illustrates the range of azimuthal separations of a pair that results in a crossing point within the active region of a TPC sector. The trigger and associated track momenta are 3.0 and 1.0 GeV/c respectively. Below these diagrams the limits are shown superposed over a correlation formed using tracks with similar transverse momenta. A qualitative correspondence is seen between the dip width and the affected range.

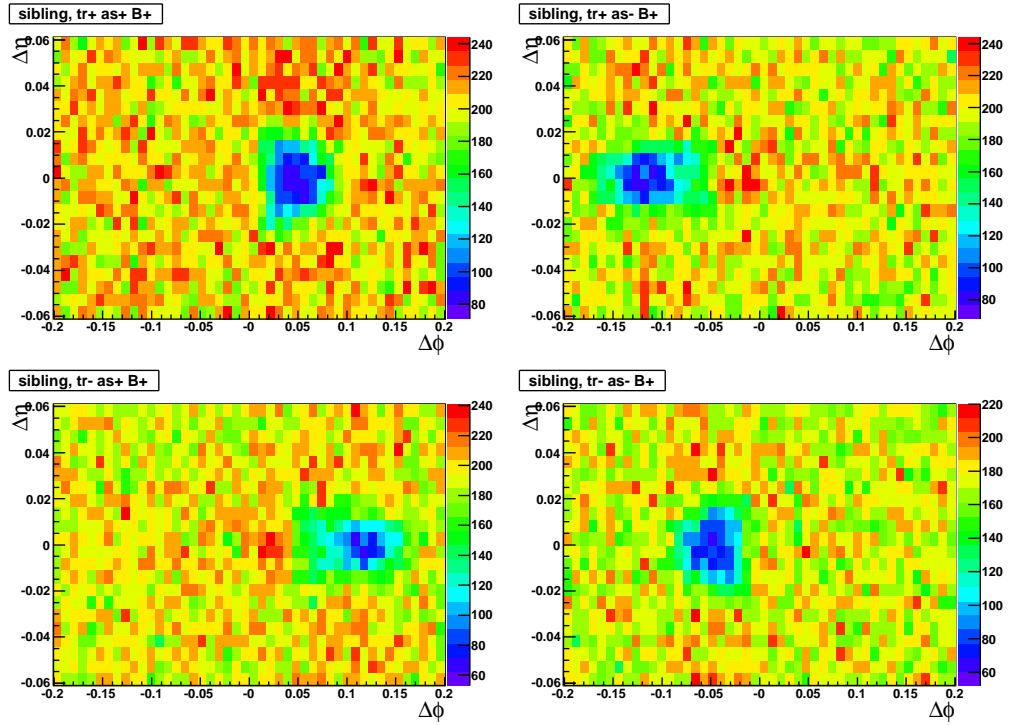


Figure 5.8: Correlations of unidentified charged tracks with small opening angles for a single magnetic field setting. Trigger tracks were selected with $3.0 \leq p_T^{trig.} \leq 6.0$ GeV/c and associated tracks satisfied $1.0 \leq p_T^{asso.} \leq 3.0$ GeV/c. Each frame represents a different charge combination: positive and negative trigger tracks are included in the upper and lower row respectively, and positive and negative associated tracks are included in the left and right columns respectively.

5.3. TWO-TRACK RESOLUTION

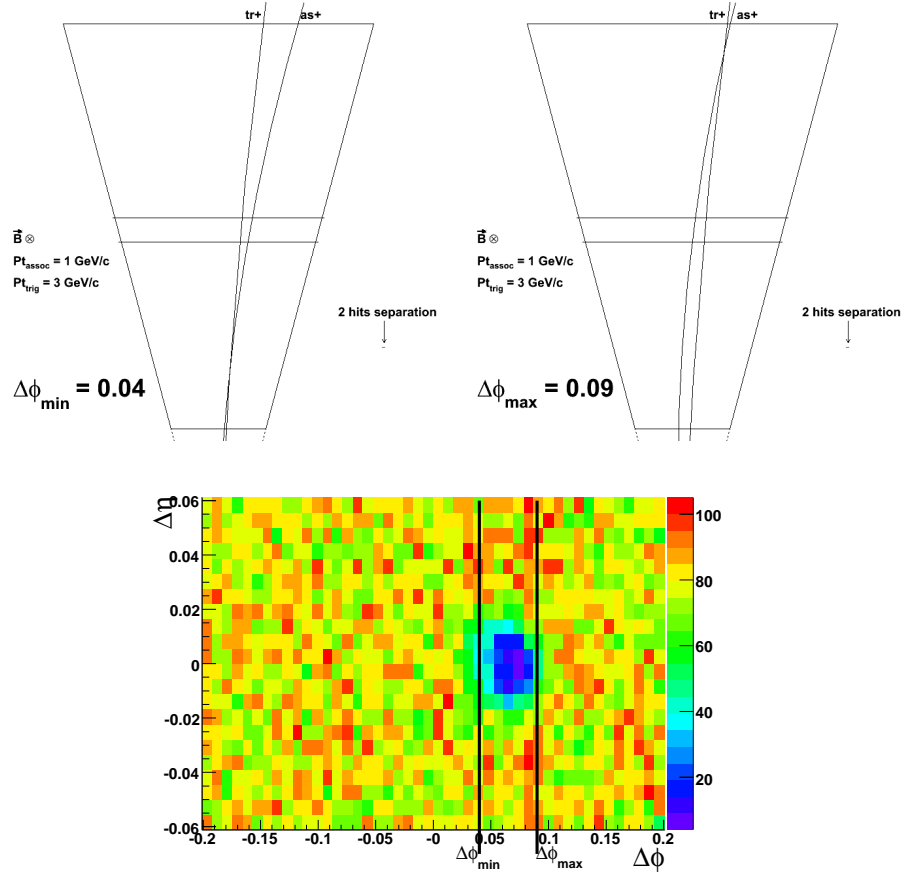


Figure 5.9: Schematic representation of a TPC sector drawn to scale, showing the minimum and maximum azimuthal separations of two tracks that cross within the STAR TPC active volume. The transverse momenta of the two tracks are 1.0 GeV/c and 3.0 GeV/c. The lower image shows a sibling correlation involving a similar selection of tracks, with angular limits illustrated by black lines. A qualitative correspondence is observed with the location of the dip.

The location and width of the dips were found to vary as a function of trigger and associated track momenta, also in agreement with expectations from track crossing points. The dips migrate towards smaller $\Delta\phi$ with increasing track p_T , whilst becoming visibly narrower in the $\Delta\phi$ direction. As anticipated from considerations of track geometry, the dips were more sensitive to changes in the momentum of the associated track than the trigger track.

The probability of track merging should increase with decreasing crossing angle as this defines the path length over which tracks are sufficiently close that their hits

may become confused. In terms of track momentum this implies that the absolute depth of dips should increase as the track momentum is raised. Note however, that the magnitude of the dips relative to the same side peak actually decreases with increasing associated p_T . This is due to the reduction in the level of combinatorial background, which dominates the yield of pairs in $(\Delta\eta, \Delta\phi)$ space.

Two track resolution was also featured in correlations involving the three $V0$ species. Too few statistics were available to study the detailed kinematic behaviour of the dips in these correlations. It was however, possible to look for a species dependence in correlations spanning the whole trigger and associated momentum ranges. No such trigger species dependence was found for the dip location. Instead, within the available resolution, only one dip was apparent for each associated track helicity. This suggested that the kinematic relationship of the daughter tracks is secondary to the properties of the associated track, which may reflect equal degrees of merging between associated tracks and either daughter track.

5.3.2 Genuine track merging observed in low momentum correlations

Through the course of the analysis, correlations were also produced for low momentum triggers with $2.0 \leq p_T^{trig.} \leq 3.0$ GeV/c. These also suffered from the effects of two-track resolution, as illustrated in figure 5.10, which shows an unidentified sibling correlation with trigger tracks in the interval $2.0 \leq p_T^{trig.} \leq 2.25$ GeV/c, and associated tracks with $1.5 \leq p_T^{asso.} \leq p_T^{trig.}$. In addition to the dips identified with track crossings, a fifth depression is observed to develop at $(\Delta\eta, \Delta\phi) = (0, 0)$ when the trigger threshold is reduced below 3.0 GeV/c. The location of this dip indicates genuine track merging to be responsible for the losses, which is also supported by its emergence where the number of triggers and associations with similar momenta is greatest.

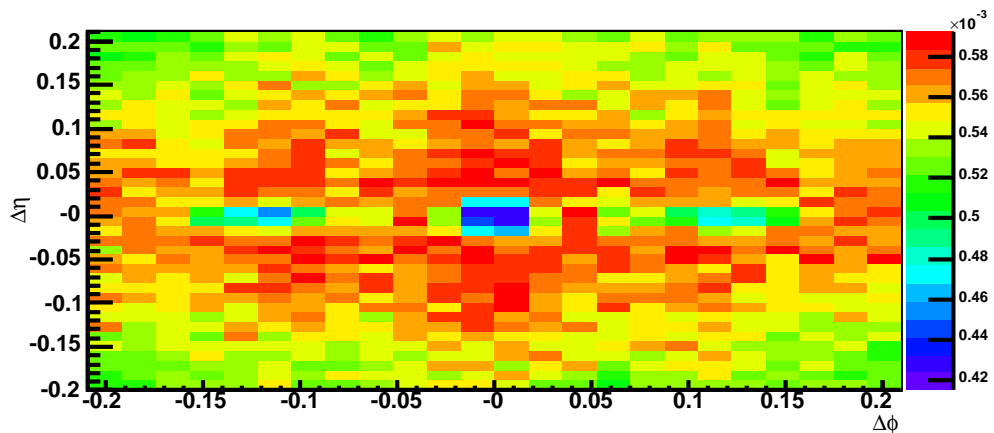


Figure 5.10: Track merging in unidentified charged track sibling correlation with $1.5 \leq p_T^{asso.} \leq p_T^{trig.}$ and $2.0 \leq p_T^{trig.} \leq 2.25$ GeV/c. For triggers with $p_T^{trig.} \lesssim 3.0$ GeV/c the dips related to crossing tracks are accompanied by a fifth dip due to genuine merging at $(\Delta\eta, \Delta\phi) = (0,0)$.

5.3.3 Studies of track merging with embedded pairs

As a final confirmation that the observed dips were indeed caused by two-track resolution, a study was made of embedded pairs. The same embedding chain was used as for single particle reconstruction efficiency studies, except for a modified particle generator. Pairs of particles were randomly produced throughout the (simulated) TPC volume, with the additional criterion that their angular separation should be small.

Correlations were produced using two populations generated by the simulation. The first utilised the embedded particle information, and the second made use of the reconstructed tracks associated to embedded particles. The ratio of these two distributions then provided a relative reconstruction efficiency of pairs in $(\Delta\eta, \Delta\phi)$ space. Embedded pion pairs exhibited a clear depression at small angular separations that was in qualitative agreement to the dip observed in real data.

5.3.4 Mirror image correction

Given that the distribution of pairs is symmetrical about $\Delta\phi = 0$, the missing pairs of a given dip at $\Delta\phi_{dip}$ should be identical to the those found in the unaffected region $-\Delta\phi_{dip}$. Each of the four dipoles related to crossing tracks corresponds to a specific combination of track helicities, and therefore correlations could be corrected for dipoles due to crossing tracks by rejecting pairs in the dip regions and instead filling these with pairs in the donor region at $(\Delta\eta_{donor}, \Delta\phi_{donor}) = (\Delta\eta_{dip}, -\Delta\phi_{dip})$. For unidentified correlations it was necessary to separately consider the different four combinations of track orientations separately. For correlations with V0 triggers, only two dipoles were resolved. Hence for these the dataset was only subdivided into the two helicity states of the associated tracks.

This mirror image correction was effective for dipoles that were distant from $\Delta\phi = 0$, corresponding to tracks with larger crossing angles. For the trigger and associated momenta considered in the present analysis however, the affected region appeared to include pairs at $\Delta\phi = 0$ within the available resolution. Consequently this approach offered a partial correction to two-track resolution. A further drawback of this method was the increased statistical uncertainty due to reduced statistics.

5.3.5 Introduction to anti-merging algorithms

Since two-track resolution is a form of pair-wise acceptance, it was natural to seek a solution integrated with the correction for effects at larger angular separations (event mixing). An algorithm was devised to estimate the degree of merging for a given pair of tracks, so that pairs could be rejected depending on this quantity. A correction was then developed for track merging by modifying mixed events to account for the reduced efficiency of pairs with small angular separations. The correction was implemented by dividing sibling distributions by mixed events.

The philosophy behind the correction is that pairs that would have merged are

5.3. TWO-TRACK RESOLUTION

removed from the mixed event giving a more accurate description of pair-wise acceptance. The algorithm was applied to all pairs with separations less than $(\Delta\eta, \Delta\phi) \leq 0.2$. This approach was motivated by previous analyses at STAR of quantum interference effects in low momentum particle correlations, where track merging was accounted for in this way [91].

Although in the preceding discussion missing pairs have been described as track merging, the underlying process occurs at the hit level. Therefore the measure with which to define the quality of a pair is the fraction of merged hits. The two-hit resolution was defined by the parameters ΔU and ΔZ , which described the minimum separation along a pad row and the minimum separation in the direction parallel to the beam axis (time axis) respectively. Charge clusters are not considered to extend to multiple TPC rows, thus two-hit resolution in the radial direction does not feature in track reconstruction. These proximities were taken from previous simulation and data studies at STAR [87]. For inner sector rows, $\Delta U = 0.8$ cm and $\Delta Z = 3.0$ cm, and for outer sector rows, $\Delta U = 1.4$ cm and $\Delta Z = 3.2$ cm. A final parameter required to label a track pair as being merged was the maximum permissible fraction of merged hits. This was retained as a variable in the correlation routine.

The algorithm was applied to both sibling (real) correlations and mixed event correlations. It is essential that any alteration to track selection in mixed events must be matched in the sibling correlation in order to ensure a faithful reproduction of detector acceptance. Therefore through applying an anti-merging correction, some amount of real pairs are lost but, providing the description of merging describes the data well, few sibling pairs should fail to satisfy the cut. Indeed an overestimation of the maximum fraction of merged hits should still result in an effective correction, but at the expense of reduced statistics in the affected region.

5.3.6 Hit determination from track helices

In order to minimise disk space, hit positions were not retained for STAR TPC tracks in the reconstructed data used for this analysis. Thus the only available course of action was to infer hits from the remaining information available: the helix parameters. These are the radius of curvature, dip angle, phase, origin, and helicity, as defined in equation 5.1 below.

$$\begin{aligned}
x(s) &= x_0 + \frac{1}{\kappa} [\cos(\Phi_0 + h s \kappa \cos \lambda) - \cos \Phi_0] \\
y(s) &= y_0 + \frac{1}{\kappa} [\sin(\Phi_0 + h s \kappa \cos \lambda) - \sin \Phi_0] \\
z(s) &= z_0 + s \sin \lambda
\end{aligned} \tag{5.1}$$

where s is the path length along the helix; x_0, y_0, z_0 is the origin ($s = 0$); λ is the dip angle; κ is the curvature, h is the helicity ($h = -\text{sign}(qB) = \pm 1$, where q and B are particle charge and external magnetic field respectively); and Φ_0 is the azimuth angle of the origin relative to the helix axis ($\Phi_0 = \Psi - h\pi/2$ where Ψ is the azimuthal angle of the track direction at the origin $\arctan(dy/dx)_{s=0}$). These are illustrated in figure 5.11.

Hit positions were calculated by considering the point at which tracks cross each pad row. The first step was to calculate the path length of the helix from its origin to the radial position of a pad row. For this purpose the TPC was simplified to a set of concentric cylinders. Equation 5.2 expresses the relationship between radial position and path length, which gives the point of intersection between a helix and a cylinder of radius $\rho^2 = x(s)^2 + y(s)^2$. Note that the relationship offers two solutions, s_1 and s_2 , with the smaller of the two retained by the algorithm. Also note that solutions are complex for radii within the helix origin, thus for tracks originating outside the radius of the first pad row, it is necessary to first extrapolate the track

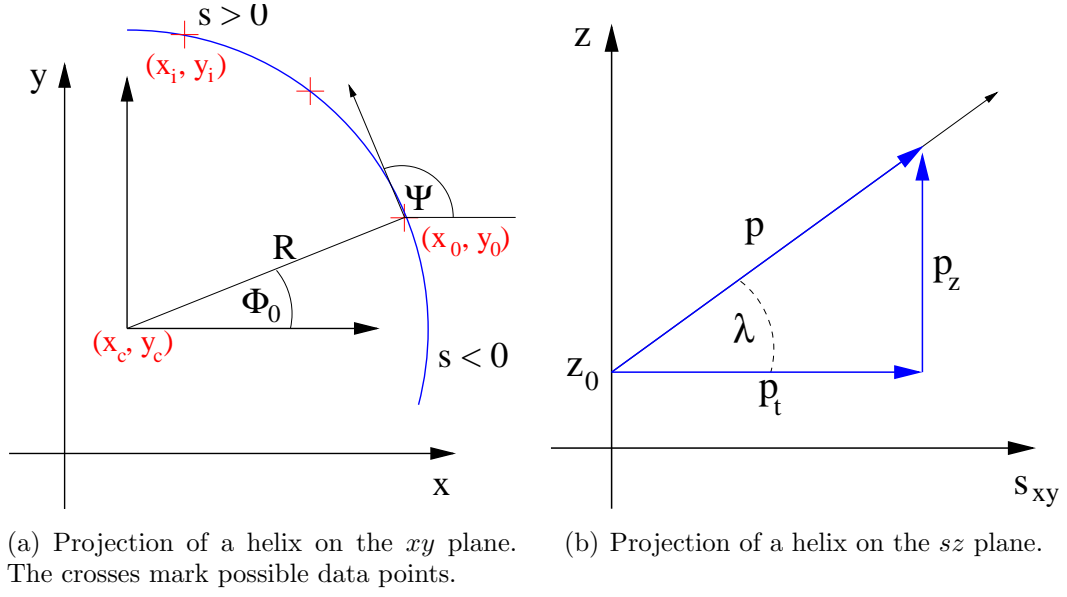


Figure 5.11: Helix parametrisation.

origin closer to the co-ordinate origin.

$$\begin{aligned}
 s_{1/2} = & -(\Phi_0 + 2 \arctan [(2 y_0 \kappa - 2 \sin \Phi_0 \\
 & \pm [-\kappa^2 (-4 \rho^2 + 4 y_0^2 - 2 \rho^2 \kappa^2 x_0^2 - \\
 & 2 \rho^2 \kappa^2 y_0^2 + 2 x_0^2 \kappa^2 y_0^2 + \rho^4 \kappa^2 + x_0^4 \kappa^2 + y_0^4 \kappa^2 - 4 x_0^3 \kappa \cos \Phi_0 + \\
 & 4 x_0^2 \cos^2 \Phi_0 - 4 y_0^2 \cos^2 \Phi_0 - \\
 & 4 y_0^3 \kappa \sin \Phi_0 + 4 \rho^2 \kappa x_0 \cos \Phi_0 + 4 \rho^2 \kappa y_0 \sin \Phi_0 - 4 x_0^2 \kappa y_0 \sin \Phi_0 - \\
 & 4 y_0^2 \kappa x_0 \cos \Phi_0 + 8 x_0 \cos \Phi_0 y_0 \sin \Phi_0)]^{1/2}) / \\
 & (-\rho^2 \kappa^2 + 2 + x_0^2 \kappa^2 + 2 \cos \Phi_0 + y_0^2 \kappa^2 - \\
 & 2 x_0 \kappa - 2 x_0 \kappa \cos \Phi_0 - 2 y_0 \kappa \sin \Phi_0)] h^{-1} \kappa^{-1} (\cos \lambda)^{-1}
 \end{aligned} \tag{5.2}$$

With the path length recovered, the point of intersection was determined in the lab co-ordinates (x, y, z) . A sample set of hit positions is displayed in the left and centre frames of figure 5.12 for primary tracks, in both the (x, y) and (z, y) planes. The z -position of hits can be directly compared to the ΔZ proximities. However, the (x, y) location must be transformed into the local co-ordinate frame of a sector

5.3. TWO-TRACK RESOLUTION

(u, r) , where u is the pad position along a row and r is the pad row index. After transformation, the hit distributions become as shown in the right frame of figure 5.12.

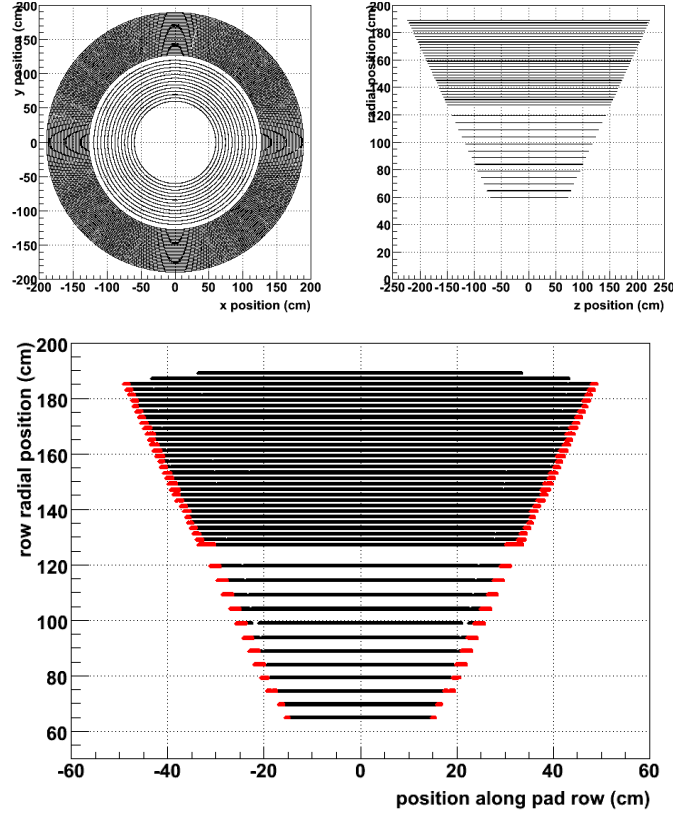


Figure 5.12: Hit positions inferred from helix parameters of charged tracks. The upper frames display hits in the xy (azimuthal) plane and the rz plane. The lower frame shows the azimuthal distribution of hits after transformation to the local frame of a TPC sector. Red hits have been rejected as they exceed the limits of the pad rows.

The operation was performed first by applying the transformation

$$R = x \cos(\alpha) + y \sin(\alpha) \quad (5.3)$$

$$U = -x \sin(\alpha) + y \cos(\alpha) \quad (5.4)$$

where α is the angle between the co-ordinate x -axis and the axis of the sector containing the hit. This is derived from the angle between the line subtended between the origin and hit point, and the z -position of the hit (indicating in which half of

5.3. TWO-TRACK RESOLUTION

the TPC the hit resides), and comparing these to the geometrical orientation of the TPC sectors in the lab frame. Each hit was also assigned an index from 1 – 24 representing the twelve sectors at each end of the TPC. This was to ensure that only hits in the same sectors were compared by the algorithm.

Once the (u, r, z) location of a hit had been recovered, it was necessary to check whether the coordinate lay out of bounds of the pads. Hits were rejected if their radial positions did not correspond to an existing row, next the position along the row was compared to the length of the row, which was determined as the product of pad spacing and number of pads in a given row.

In mixed events the difference in primary vertex positions results in primary tracks that appear to cross in the longitudinal plane. Consequently the region where pairs are rejected by the algorithm is artificially broadened in $\Delta\eta$. In order to avoid this smearing, the tolerance in primary vertex z -position difference was constrained to 2 cm, and tracks were synthetically shifted the remaining separation for the purpose of hit determination.

For correlations involving $V0$ tracks, it was necessary to consider the hit distributions of daughter tracks. The anti-merging algorithm was called to return the fraction of merged hits (FMH) for each possible pair of trigger and associated charged tracks (i.e. twice for $V0$ -triggered with unidentified associated tracks). The total FMH from each call was then summed, taking into account the possibility of multiple crossing points, and this quantity used to ascertain the degree of merging. The FMH was calculated assuming the origins of $V0$ daughter tracks to be the decay vertex. This was obtained by extrapolating the helices to the points of closest approach.

5.3.7 Fraction of merged hits cut in the anti-merging correction

The fraction of merged hits (FMH) of pairs in sibling and mixed event correlations was studied as a function the hit distance of closest approach (DCA) of the pair, the weighted mean separation of tracks, and the row with the DCA. In figure 5.13, these distributions are shown for mixed event pairs with $2.0 \leq p_T^{trig.} \leq 6.0$ GeV/c and $1.5 \leq p_T^{asso.} \leq 3.0$ GeV/c. The distributions of pairs in sibling correlations exhibited qualitatively the same features. Within $|\Delta\eta| \leq 0.2$ and $|\Delta\phi| \leq 0.2$ radians, large concentrations of pairs were found with $0.1 \lesssim \text{FMH} \lesssim 0.2$ in both sets of correlations. Although the majority of pairs are closest at the inner most row, a strong correspondence was found between the radial location of crossing points and the FMH, in reflection of the relationship between radial position and crossing angle for a given set of track p_T (curvature). Similarly in the distribution of FMH versus weighted average separation, a clear correlation was also apparent for larger separations.

No clear distinction was found between the FMH distributions for sibling and mixed event pairs. The effect of applying a maximal anti-merging correction is shown in figure 5.14, which displays sibling and mixed correlations of unidentified charged tracks produced only using pairs with FMH= 0. The dips produced by the algorithm matched well to those observed in real data, again confirming the hypothesis that they are the result of track merging. Pairs with the largest fractions of merged hits are found near the origin in $(\Delta\eta, \Delta\phi)$ space. The acceptance-corrected correlation, formed by dividing the sibling correlation by the mixed event, is shown in the right frame of figure 5.14. As can be seen in the figure, the algorithm correction accounted for much of the losses, although some residual depression was visible even for the strictest cut.

For the more coarse resolution required for analysis purposes, the remaining dips

5.3. TWO-TRACK RESOLUTION

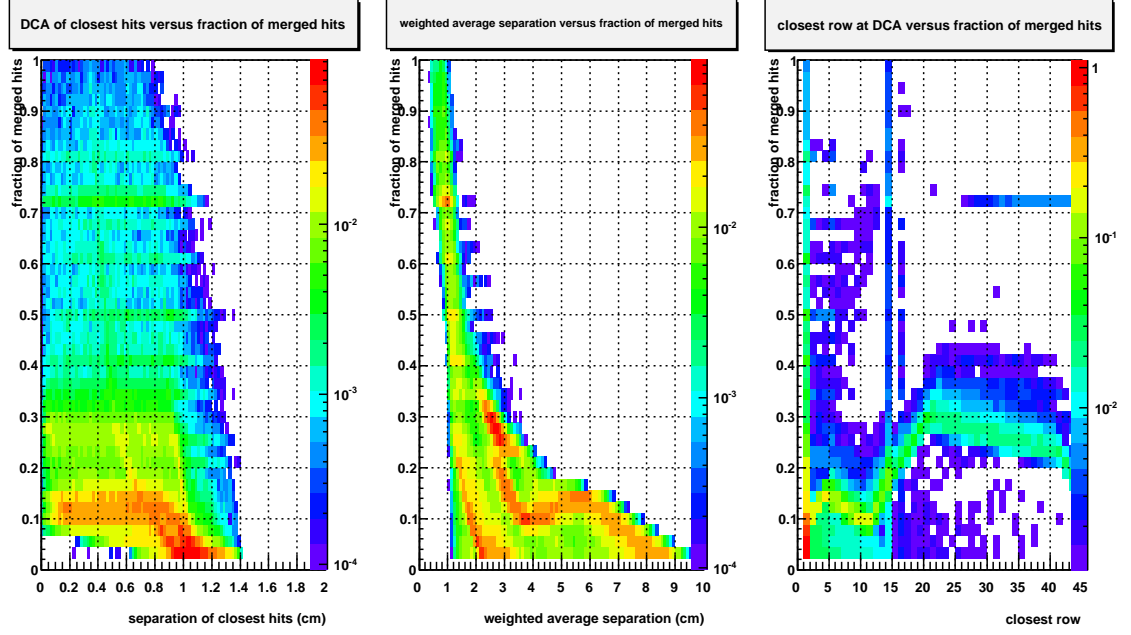


Figure 5.13: Results of anti-merging algorithm applied to mixed event pairs. From left to right, the fraction of merged hits (FMH) is shown (for pairs with $\text{FMH} > 0$) versus hit distance of closest approach (DCA), weighted mean separation of hits, and row at dca. Pairs were selected with $2.0 \leq p_T^{\text{trig.}} \leq 6.0$ GeV/c and $1.5 \leq p_T^{\text{asso.}} \leq 3.0$ GeV/c.

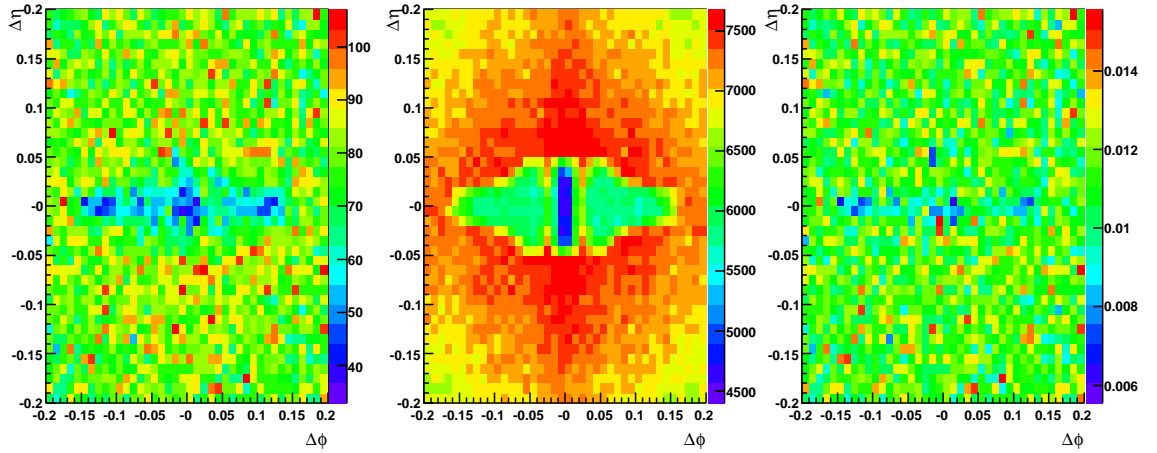


Figure 5.14: $\Delta\eta - \Delta\phi$ correlations after applying a maximal anti-merging cut. Sibling (left), mixed event (centre), and corrected correlations (right) are shown for unidentified charged tracks with $2.0 \leq p_T^{\text{trig.}} \leq 6.0$ GeV/c and $1.5 \leq p_T^{\text{asso.}} \leq 3.0$ GeV/c, and $\text{FMH} = 0$. Colour represents pair density, increasing from violet to red.

5.3. TWO-TRACK RESOLUTION

are small. Adopting a fraction of merged hits cut of $\text{FMH} \leq 10\%$, the antimerging cut works adequately for unidentified charged tracks involving trigger particles with $p_T^{\text{trig.}} > 3.0$ GeV/c. In figure 5.15, acceptance-corrected $\Delta\eta - \Delta\phi$ correlations in $0 - 10\%$ central $Au + Au$ collisions at $\sqrt{s_{NN}} = 200$ GeV are shown for a relatively track momentum interval of $3.0 \leq p_T^{\text{trig.}} \leq 4.0$ GeV/c and $1.0 \leq p_T^{\text{asso.}} \leq p_T^{\text{trig.}}$ where track merging is most severe. The upper row column displays correlations with no anti-merging correction applied. To the right of each $\Delta\eta - \Delta\phi$ correlation is the $\Delta\eta$ projection over $|\Delta\phi| < 0.7$. The correction was effective for this momentum interval, and for higher track momenta where the dips were less pronounced.

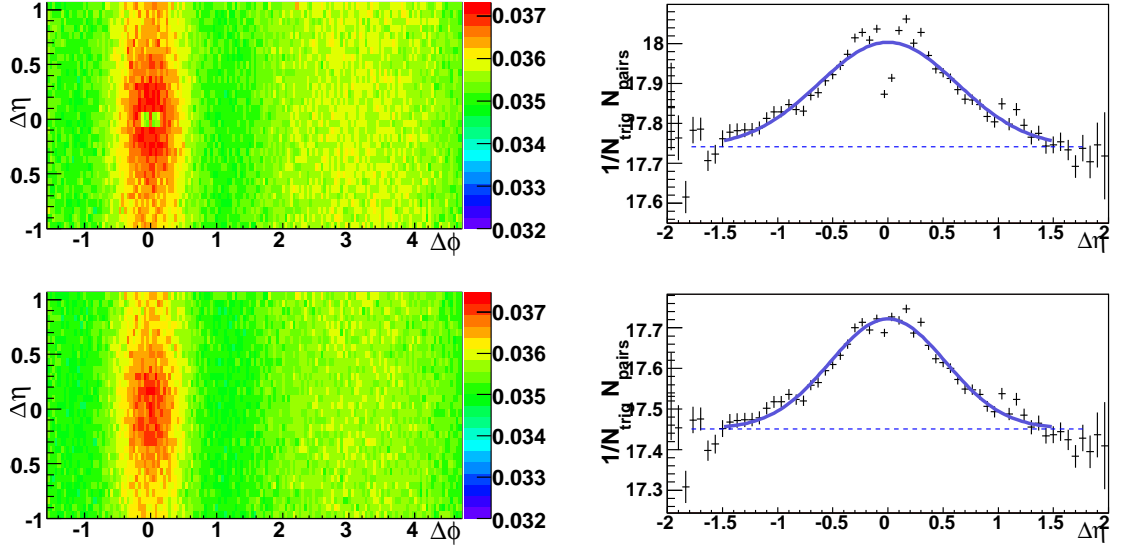


Figure 5.15: Side-by-side comparison of corrected $\Delta\eta - \Delta\phi$ correlations and $\Delta\eta$ projections within $|\Delta\phi| < 0.7$ before (upper row) and after (lower row) applying the anti-merging algorithm with $\text{FMH} < 0.1$. Correlations involved unidentified charged tracks in $0 - 10\%$ central $Au + Au$ collisions with $3.0 \leq p_T^{\text{trig.}} \leq 4.0$ GeV/c and $1.0 \leq p_T^{\text{asso.}} \leq p_T^{\text{trig.}}$.

To offer a quantitative measurement of the improvement offered by the algorithm, the ratio of correlations with and without the correction was formed. In figure 5.16 the ratios of $\Delta\phi$ projections over $|\Delta\eta| < 0.5$ are shown for unidentified correlations, K_{Short}^0 -triggered and $\Lambda + \bar{\Lambda}$ -triggered correlations. Vertical error bars represent the variation in the ratio given a 1σ statistical fluctuation in each correlation. For

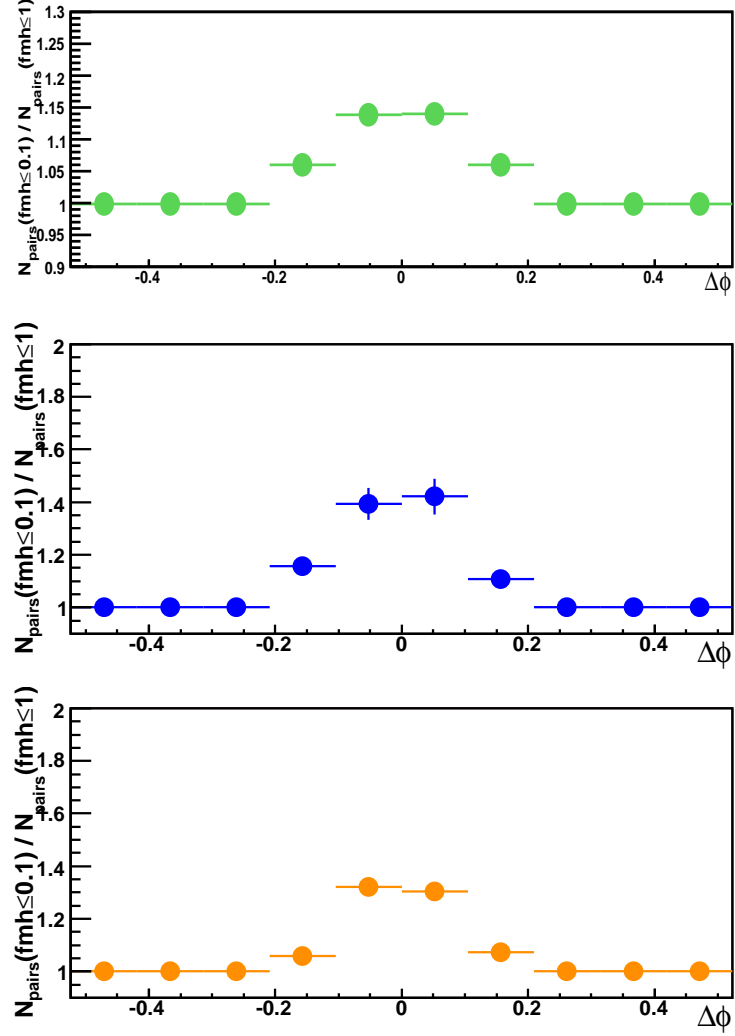


Figure 5.16: Estimation of enhancement offered by the anti-merging algorithm for correlations with unidentified triggers (upper frame), K_{Short}^0 triggers (middle frame), and $\Lambda + \bar{\Lambda}$ triggers (lower frame). Each frame displays the ratio of $\Delta\phi$ projections over $|\Delta\eta| < 0.5$ with and without a $\text{FMH} \leq 0.1$ anti-merging correction applied. Correlations were produced in 0 – 10% central $Au + Au$ collisions at $\sqrt{s_{NN}} = 200$ GeV, using tracks with $3.0 \leq p_T^{\text{trig.}} \leq 4.0$ GeV/c and $1.5 \leq p_T^{\text{asso.}} \leq p_T^{\text{trig.}}$.

5.3. TWO-TRACK RESOLUTION

unidentified correlations, track merging at worst results in a $\sim 15\%$ suppression in the yield of pairs per bin in these projections. The relative enhancement offered by the algorithm was larger for $V0$ -triggered correlations than for unidentified charged tracks, reaching as high as 50% in some bins.

Following correction for track merging, the percentage increase to the $\Delta\phi$ jet yield of the same side peak, defined in section 5.4, is shown in figure 5.17 for unidentified charged and $V0$ triggers with associated charged tracks with $1.5 \leq p_T^{asso.} \leq p_T^{trig.}$ in 0 – 10% central $Au + Au$ collisions at $\sqrt{s_{NN}} = 200$ GeV. For $V0$ triggers, a single $p_T^{trig.}$ range is shown, and for unidentified correlations the correction is shown for several $p_T^{trig.}$ intervals. The effect is similar in magnitude for unidentified and K_{Short}^0 triggers, but is twice as large for $\Lambda + \bar{\Lambda}$ triggers. The correction is greater for low- p_T tracks due to the larger combinatorial background; for unidentified correlations it was found to increase to $\approx 16\%$ for $3.0 \leq p_T^{trig.} \leq 4.0$ GeV/c when the associated track threshold was lowered to $1.0 \leq p_T^{asso.} \leq p_T^{trig.}$, and for $2.0 \leq p_T^{asso.} \leq p_T^{trig.}$ the correction reduced to $\approx 3\%$ for the same $p_T^{trig.}$ interval.

5.3.8 Limitations of anti-merging algorithms integrated with mixed events

Even with a maximal anti-merging correction, some residual dip survived the anti-merging correction. This remnant is believed to be the result of two limitations in the method. Firstly, at some level the hit determination process is inaccurate. In addition to the simplification of considering all 45 hits, the helices used to infer hit locations do not exactly correspond track trajectories. The energy loss of charged particles travelling through the detector is not included in the parameterisation, which could lead to the misidentification of some merged hits.

The second limitation of the correction procedure is introduced by the mixed event. Although care was taken to select similar events, the distribution of tracks in

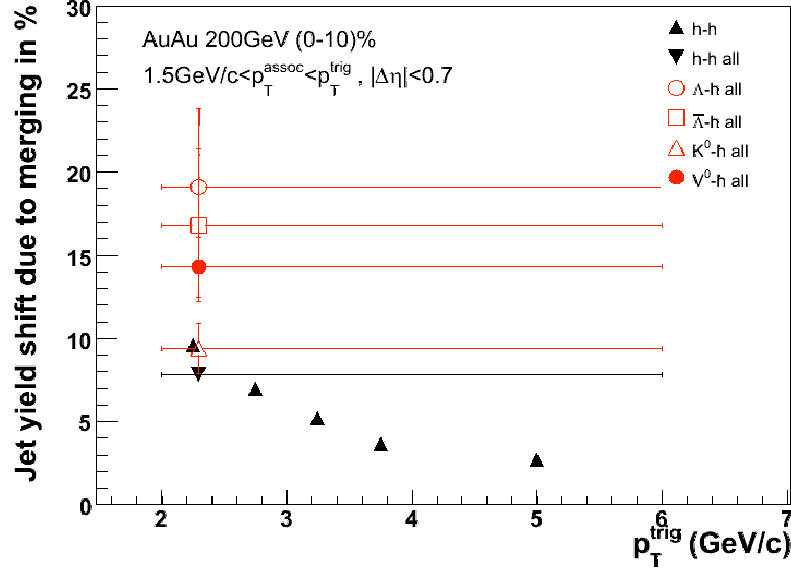


Figure 5.17: The percentage increase to the $\Delta\phi$ jet yield component of the same side peak following correction for track merging. The correction is shown for correlations of unidentified charged tracks (black markers) and V0 triggers (red markers) with $2.0 \leq p_T^{\text{trig.}} \leq 6.0$ GeV/c and $1.5 \leq p_T^{\text{asso.}} \leq p_T^{\text{trig.}}$ in 0 – 10% central Au + Au collisions at $\sqrt{s_{NN}} = 200$ GeV. The correction for unidentified correlations has also been decomposed into $p_T^{\text{trig.}}$ bins.

the immediate vicinity of a jet cone differs from the underlying event. In particular, the physical correlation results in a harder distribution of tracks near a trigger vertex. For a given $\Delta\eta - \Delta\phi$ bin, the amount of rejected pairs (relative to accepted) will differ between sibling and mixed event correlations because the crossing angle of pairs, and hence the fraction of merged hits, depends upon track momenta (curvature). Unless mixed events can be tailored in such a way as to reproduce the momentum distribution of jets, this will remain a limitation of the anti-merging correction. A more elaborate pair embedding parameterisation than the short study described above may be a possible means to correct entirely for the dips, since an efficiency weighting could be applied directly to sibling pairs.

5.3.9 Conclusion

In both unidentified two-particle correlations and correlations involving $V0$ tracks, detailed studies of the same side peak in $(\Delta\eta, \Delta\phi)$ space are compromised by two-track resolution. The feature is more problematic for lower momentum pairs, as the predominant consideration is the magnitude of combinatorial background compared to the correlation peak.

In the present analysis it was found that the dips resulting from two-track resolution could be largely corrected for via either a mirror image approach (substituting affected regions for unaffected regions), or by rejecting pairs with merged hits, inferred from their helices. The former approach was best suited to correcting for crossing tracks with larger $\Delta\phi$ separation. The latter method corrected for all pairs, but was found to be less effective for pairs towards larger $\Delta\phi$ (larger residual dips after correction), which could have as few as one pair of merged hits due to the larger crossing angles.

The two corrections are independent and complementary, and can be applied simultaneously in a correlation routine. Hence the optimal correction for two-track resolution is provided by including both in the analysis.

5.4 Analysis of the same side peak

In figure 5.5 the same side peak was shown to be modified in the $Au + Au$ system compared to $d + Au$. The emergence of these new features implies that two-particle correlation analyses may be sensitive to partially attenuated jets. Although the complete absence of an away side peak in some kinematic ranges was a clear indication of strong high- p_T suppression, the magnitude and nature of the interaction is lost. In contrast, by studying surviving jets one can look for information relating to their passage through the medium. To facilitate future discussions, and since at

the time of writing this was the current convention adopted by the community, the peak localised at $(\Delta\eta, \Delta\phi) = 0$ shall hereafter be labelled the *jet*. The second feature located at $\Delta\phi = 0$ but extended in $\Delta\eta$ shall be referred to as the *ridge*. Collectively both comprise the *same side* peak.

5.4.1 Projection of the same side peak onto $\Delta\phi$ and $\Delta\eta$ axes

Average associated particle yields were initially defined by bin counting over the ranges of interest in corrected correlations. Although it would make better sense in terms of statistical uncertainties to integrate raw and background correlations (see section 5.2) before performing the acceptance correction, additional systematic errors would be introduced by the need to describe the functional form of the background. In order to quantify the width of the same side peak, comparisons were made to the function

$$\begin{aligned} \frac{d^2N}{d(\Delta\phi)d(\Delta\eta)} = & \frac{1}{2\pi} \frac{Y^{jet}}{\sigma_\phi^{jet} \sigma_\eta^{jet}} e^{-\frac{1}{2}(\frac{\Delta\phi}{\sigma_\phi^{jet}})^2} e^{-\frac{1}{2}(\frac{\Delta\eta}{\sigma_\eta^{jet}})^2} + \frac{Y_\phi^{ridge}}{\sigma_\phi^{ridge} \sqrt{2\pi}} e^{-\frac{1}{2}(\frac{\Delta\phi}{\sigma_\phi^{ridge}})^2} \\ & + C(1 + 2v_2^{trig} v_2^{asso} \cos(2\Delta\phi)), \end{aligned} \quad (5.5)$$

where Y is the yield, and σ represents the Gaussian width, with subscripts ϕ and η denoting the $\Delta\phi$ and $\Delta\eta$ directions. The function is displayed graphically in two dimensions in figure 5.18. The expression consists of two terms to describe the same side peak: a two-dimensional Gaussian peak with a fixed mean at $(\Delta\eta, \Delta\phi) = 0$ and two independent widths, resting atop a one-dimensional Gaussian distribution in $\Delta\phi$, also with a fixed mean at $\Delta\phi = 0$. Thus the ridge was assumed flat in $\Delta\eta$ within the range of this measurement, although it must presumably decline at some greater $\Delta\eta$. These features add to a pedestal that has been modulated by a $\cos(2\Delta\phi)$ function to account for elliptic flow (see section 4.4.1). It was decided that no function should be introduced to describe the away side peak, as assumptions

of its form could influence the extracted properties of the same side. Thus when performing the fit, the $\Delta\phi$ range was limited to $|\Delta\phi| < 1.0$ in order to only consider the same side peak. In terms of applying the mixed event acceptance correction, two

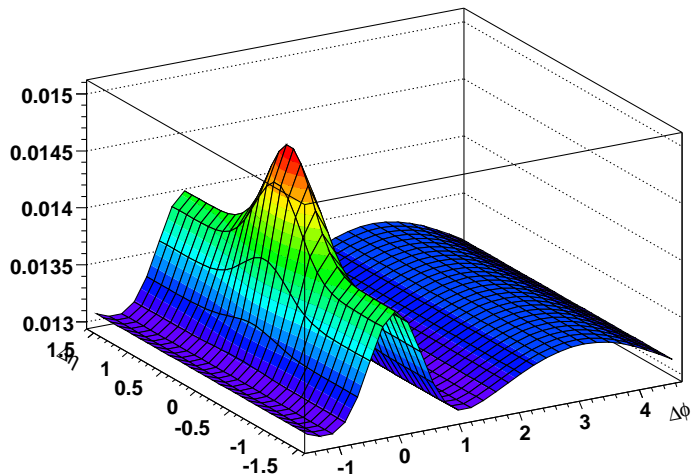


Figure 5.18: Visualisation of equation 5.5, with an additional arbitrary away side Gaussian component. The parameters of the displayed function were obtained by fitting to the distribution shown in figure 5.5.

methods were envisaged. The first possibility was for projections to be made from sibling and mixed events separately, and then the corrected distributions would be recovered by dividing the one-dimensional correlation functions. The second option was to first generate the two-dimensional corrected distribution by taking the ratio of sibling to mixed event $\Delta\eta - \Delta\phi$ correlations, and then make projections. Depending upon the chosen route, the estimation of maximal acceptance would differ due to considerations of bin size.

For the project-then-divide approach (PD), the maximum acceptance level could simply be taken as the peak of the $(\Delta\eta, \Delta\phi)$ mixed event with a fine resolution (statistical uncertainties were negligible). This would be propagated through to projections by normalising the one-dimensional mixed event distributions by multiplying the determined maximum by the degree of rebinning in $\Delta\eta$ and $\Delta\phi$ directions.

In the divide-then-project approach (DP), it is necessary to decrease the resolution of sibling and mixed event before dividing the two in order to reduce the statistical uncertainties to manageable levels. Thus taking the peak of the rebinned mixed event would underestimate the level of the maximum acceptance. Instead polynomials were fit to each side of $\Delta\eta$ projections over several the peaks in $\Delta\phi$, and the peak was estimated by taking an average of the points of intersection. Mixed events were then normalised by this level.

The PD method made best use of available statistics, placing the division operation at the end of the process. The PD and DP were not algebraically equivalent however, and when the yields of $\Delta\phi$ projections at large $\Delta\eta$ were compared between the two approaches, systematic differences were apparent. The PD method gave higher yields, with the largest discrepancy present in yields involving the subtraction of two $\Delta\phi$ correlations over different $\Delta\eta$ windows. The PD ridge yield obtained by subtracting the $\Delta\phi$ jet estimate from the $\Delta\phi$ total same side yield was found to be approximately 25% greater than the DP yield for unidentified charged pairs with $2.0 \leq p_T^{trig.} \leq 3.0$ GeV/c and $1.5 \leq p_T^{asso.} \leq p_T^{trig.}$.

The DP approach was recognised as the more transparent method for the analysis of the same side peak via $\Delta\phi$ projections over different $\Delta\eta$ regions. For $\Delta\eta$ projections either method were suitable as the mixed event normalisation level was approximately independent of $\Delta\phi$. The PD method was preferred, as it provided smaller statistical errors.

5.4.2 Estimations of the jet and ridge components in the same side peak

In order to make best use of available statistics, the novel structures of same side correlations were studied via projections in $\Delta\eta$ and $\Delta\phi$, as illustrated in figure 5.19. For $\Delta\phi$ projections over $\Delta\eta$ ranges including both features, their sum was

5.4. ANALYSIS OF THE SAME SIDE PEAK

assumed to be described by a Gaussian within the observable resolution. Hence the projections were fit by the function

$$\frac{dN}{d(\Delta\phi)} = \frac{Y_{\phi}^{jet+ridge}}{\sigma_{\phi}^{jet+ridge}\sqrt{2\pi}} e^{-\frac{1}{2}\left(\frac{\Delta\phi}{\sigma_{\phi}^{jet+ridge}}\right)^2} + C(1 + 2v_2^{trig}v_2^{asso}\cos(2\Delta\phi)) \quad (5.6)$$

The same side peak was projected onto the $\Delta\eta$ axis by integrating over the range $|\Delta\phi| < 1.0$. This region was assumed to include all of the peak yield, in accordance with the estimation for the combinatorial background level described in section 4.4.2. To this end jet yields derived from $\Delta\eta$ and $\Delta\phi$ projections should be directly comparable. In the $\Delta\eta$ projection, the distribution reduces to a Gaussian peak with mean $\mu = 0$ above a flat pedestal (assuming the ridge has no $\Delta\eta$ dependence), and was fit using the function

$$\frac{dN}{d(\Delta\eta)} = \frac{Y_{\eta}^{jet}}{\sigma_{\eta}^{jet}\sqrt{2\pi}} e^{-\frac{1}{2}\left(\frac{\Delta\eta}{\sigma_{\eta}^{jet}}\right)^2} + C_{v_2+ridge} \quad (5.7)$$

The pedestal contains the ridge, but also elliptic flow-modulated combinatorial background. In principle these could be separated to offer an estimation of ridge yield, but only with the aid of background levels estimated from $\Delta\phi$ correlations. This was not pursued in this analysis. Instead, $\Delta\eta$ projections were only used to determine the properties of the jet component. These measurements proved more statistically demanding than $\Delta\phi$ projections due to the low significance of the peak compared to pedestal in the kinematic range considered in this analysis, and also for low p_T^{asso} the width of the jet peak approached the available axis range of $|\Delta\eta| < 2.0$. Despite this, the $\Delta\eta$ projection offered the most direct measurement of the jet contribution involving the fewest assumptions.

Both jet and ridge components were estimated from $\Delta\phi$ projections. A projection including all $\Delta\eta$ provided a total same side yield, from which the ridge contribution could be extracted using the jet yield from the $\Delta\eta$ projection. Alternatively, the

ridge could be directly measured via projections over large $\Delta\eta$ beyond the tails of the jet peak. A ridge yield over all $\Delta\eta$ was then derived by assuming a constant $dN/d(\Delta\eta)$. Note that in all $\Delta\phi$ projections, an estimation of the combinatorial background level was also required, and obtained as described in section 4.4.2. The jet component could also be extracted from azimuthal projections, by subtracting the ridge projection from a projection over small $\Delta\eta$. The subtraction served to eliminate the background as well, hence the fit to the data neglected the last term in equation 5.6. The drawback of this definition was the assumed jet width in the $\Delta\eta$ direction.

The projection approach assuming distinct jet and ridge components was found to apply well to correlations with associated tracks with $p_T^{asso.} \gtrsim 2.0$ GeV/c, but was hampered in the analysis of lower momentum pairs due to broad peaks in the $\Delta\eta$ direction.

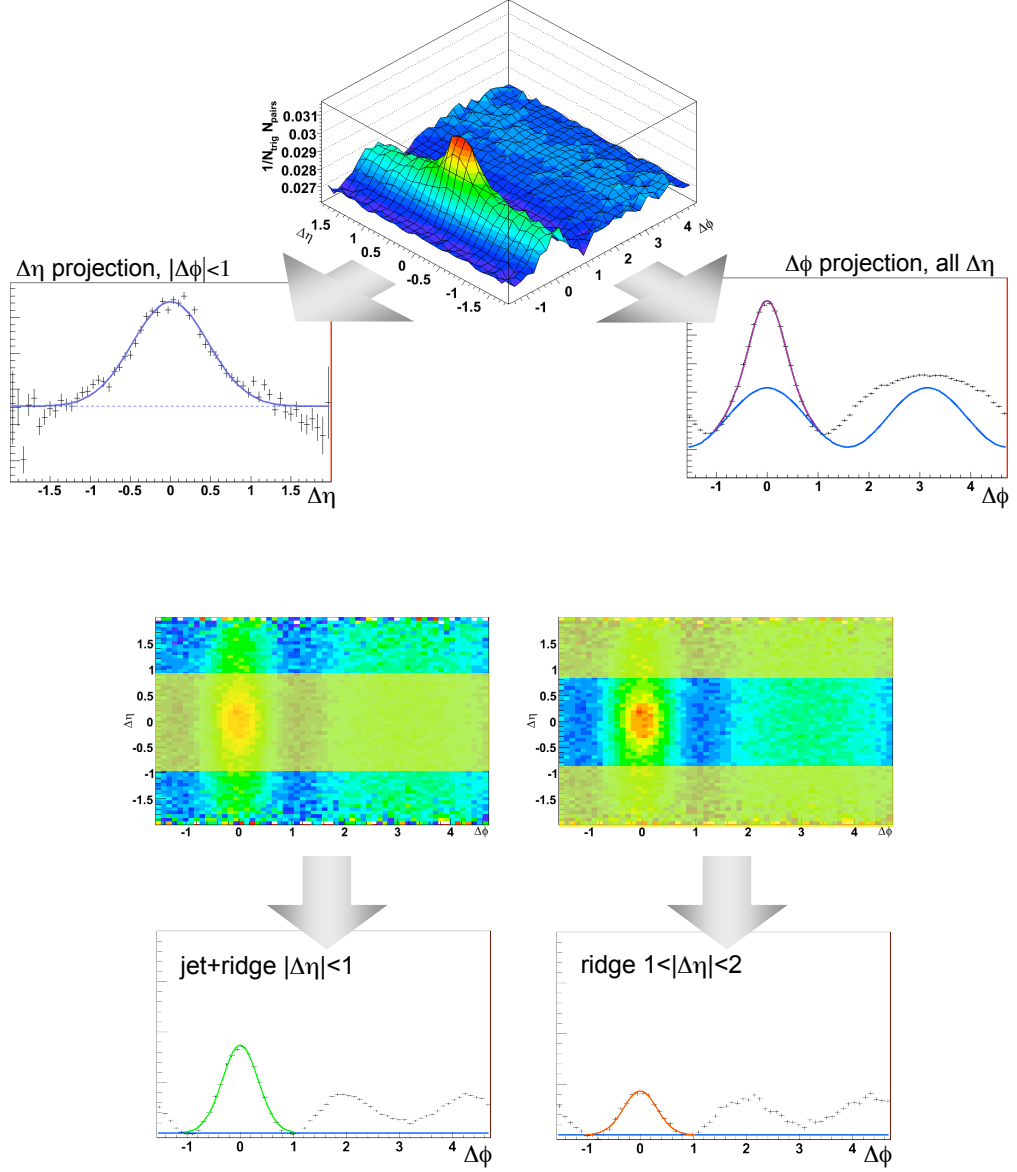


Figure 5.19: Projection analysis of $\Delta\eta - \Delta\phi$ correlations. In the upper half of the figure, the top right frame displays a $\Delta\eta - \Delta\phi$ correlation, accompanied by a $\Delta\eta$ projection of the same side peak to its left, and a $\Delta\phi$ projection over all $\Delta\eta$ in the frame immediately below. In the latter the blue line describes the background. In the lower half of the figure, $\Delta\phi$ projections are illustrated over limited ranges in $\Delta\eta$, which provide jet plus ridge (left) and ridge (right) components. Note that the background has been subtracted from these projections. Also note that the vertical scales are common for all $\Delta\phi$ projections, and hence the away side structure shows no $\Delta\eta$ dependence.

Chapter 6

RESULTS

6.1 Introduction

The projection analysis described in section 5.4 was implemented with three separated datasets: $d + Au$, minimum bias $Au + Au$, and online central triggered $Au + Au$ collisions, all with the same collision energy per nucleon of $\sqrt{s_{NN}} = 200$ GeV. The latter two were in fact taken simultaneously within the same RHIC run, and represent two of the event triggers in the $Au + Au$ run of 2004. In this chapter the results of unidentified correlations will first be reviewed for all datasets as their superior statistics provide a clearer description of the same side peak. Once these features have been established, the characteristics of correlations involving $V0$ tracks shall be summarised.

The lower abundance of $V0$ tracks led to a reduced reach in p_T of these correlations compared to unidentified correlations. This is illustrated in figure 6.1 where distributions of pairs are displayed as a function of trigger and associated momentum ranges. These correlations were produced using a sample of 20 million 0 – 10% central $Au + Au$ events from the online central triggered dataset. Note that these are the total number of pairs, including combinatorial background. Such distributions serve to indicate the limiting resolution available to $\Delta\eta - \Delta\phi$ correlations. For

instance, considering the interval $4.0 \leq p_T^{trig.} \leq 4.5$ GeV/c and $2.5 \leq p_T^{asso.} \leq 3.0$ GeV/c, the unidentified $\Delta\eta - \Delta\phi$ correlation could be subdivided into a 20x20 grid, with statistical uncertainties $\sim 2\%$ for this dataset. However the same selection from K_{Short}^0 -triggered correlations would exhibit errors $\sim 11\%$ per bin.

The same order of magnitude of pairs were found for each V0 trigger species. For the lowest $p_T^{trig.}$ ranges more pairs were returned with Λ triggers, but the K_{Short}^0 -triggered correlations exhibited a higher p_T reach, as one would expect from their spectra (see figure 3.13).

These distributions do not, however, indicate the relative amplitude of correlation structures above the background. Although the number of pairs greatly increases for lower $p_T^{asso.}$ ranges, this is in large part due to an increase in uncorrelated pairs. Thus it is necessary to also use the angular correlations to determine the optimum resolution and the kinematic range that can be considered.

6.2 Unidentified Correlations

6.2.1 Minimum bias $d + Au$ collisions

The $d + Au$ dataset was a low multiplicity system with low backgrounds. In correlations these translated into relatively low and flat pedestals, and thus di-jet correlations were quite prominent within the momentum range of interest. Both $\Delta\eta$ and $\Delta\phi$ projections of the same side correlation peak gave well defined peaks centred upon the origin for unidentified correlations, which were described well by Gaussian functions except for the highest considered p_T intervals where the peaks appeared too narrow.

Unidentified charge track correlations were studied in $d + Au$ collisions as a function of pair kinematics in order to understand trigger bias, and to establish a benchmark for correlations in $Au + Au$ collisions. Sample correlation functions are

6.2. UNIDENTIFIED CORRELATIONS

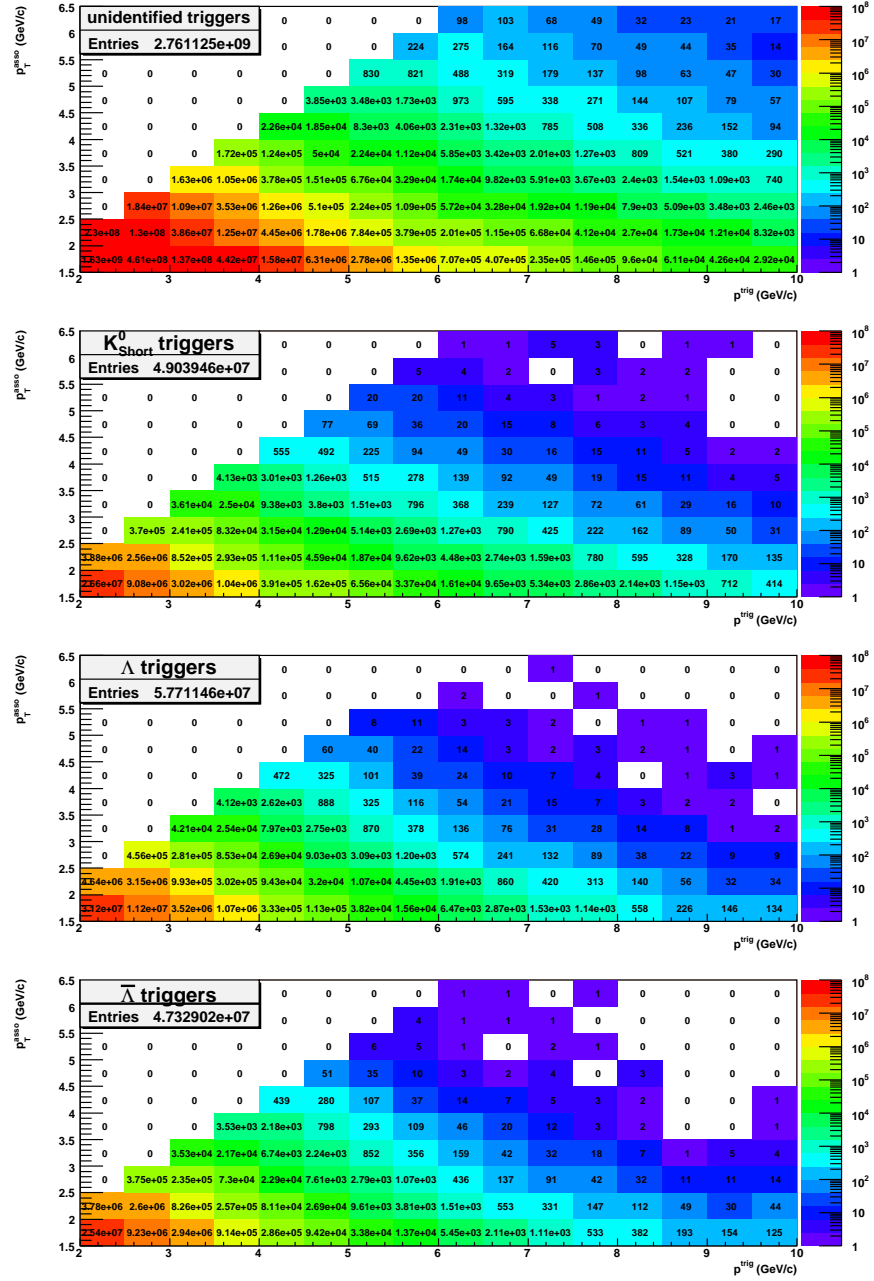


Figure 6.1: Pair statistics for correlations in a selection of 20 million 0–10% central Au+Au collisions at $\sqrt{s_{NN}} = 200$ GeV. Trigger species are from top to bottom: unidentified, K_{Short}^0 , Λ and $\bar{\Lambda}$, with unidentified associated tracks throughout. The numbers of returned pairs are displayed as a function of trigger and associated track p_T .

displayed in figure 6.2 for several p_T^{trig} intervals and $2.0 \leq p_T^{asso} \leq p_T^{trig}$. The upper row shows $\Delta\eta - \Delta\phi$ correlations, from which the projections included in subsequent rows were made. These were used to quantify the same side peak characteristics as

described in section 5.4. The second row in figure 6.2 shows $\Delta\phi$ projections over $|\Delta\eta| < 1.7$. Note that although in these projections the amplitude of the away side peak is larger than the same side peak, the away side peak is extended in $\Delta\eta$ and thus the relative magnitude of the peaks depends upon the $\Delta\eta$ range.

The third row of frames displays the difference between $\Delta\phi$ projections over $|\Delta\eta| < 0.7$ and $0.7 < |\Delta\eta| < 1.4$. The away side peak is eliminated by this means, and allows the same side peak to be studied in isolation. This is particularly important for lower momentum correlations where the away side peak was broader. The $\Delta\eta$ projection of the same side peak is shown for each $p_T^{trig.}$ interval in the lower row of frames. Even for the lowest momentum triggers shown here, the peaks in this projection were completely contained within the observable range of $|\Delta\eta| < 2.0$. Hence fits of Gaussian functions to these projections provided a successful means to quantify both width and yield of the peak.

The widths and yields of the same side peak components are presented as a function of $p_T^{trig.}$ in figure 6.3. As expected, the same side peak width decreased with increasing $p_T^{trig.}$. The yields exhibited a monotonic rise with $p_T^{trig.}$. The widths of both sets of $\Delta\phi$ projections agreed well for most of the $p_T^{trig.}$ intervals considered, indicating that for this kinematic selection, the away side peak did not strongly influence fits to the same side. The yields of $\Delta\eta$ projections also agreed quantitatively with the other estimates, and the width in $\Delta\eta$ translated to a comparable angular range to the observed $\Delta\phi$ widths.

The yield of associated particles as a function of $p_T^{asso.}$ gives a description of the composition of the same side peak, and provides the ‘triggered’ fragmentation function. This is displayed in figure 6.4 along with the estimated widths, which decreased with increasing $p_T^{asso.}$ in line with expectations.

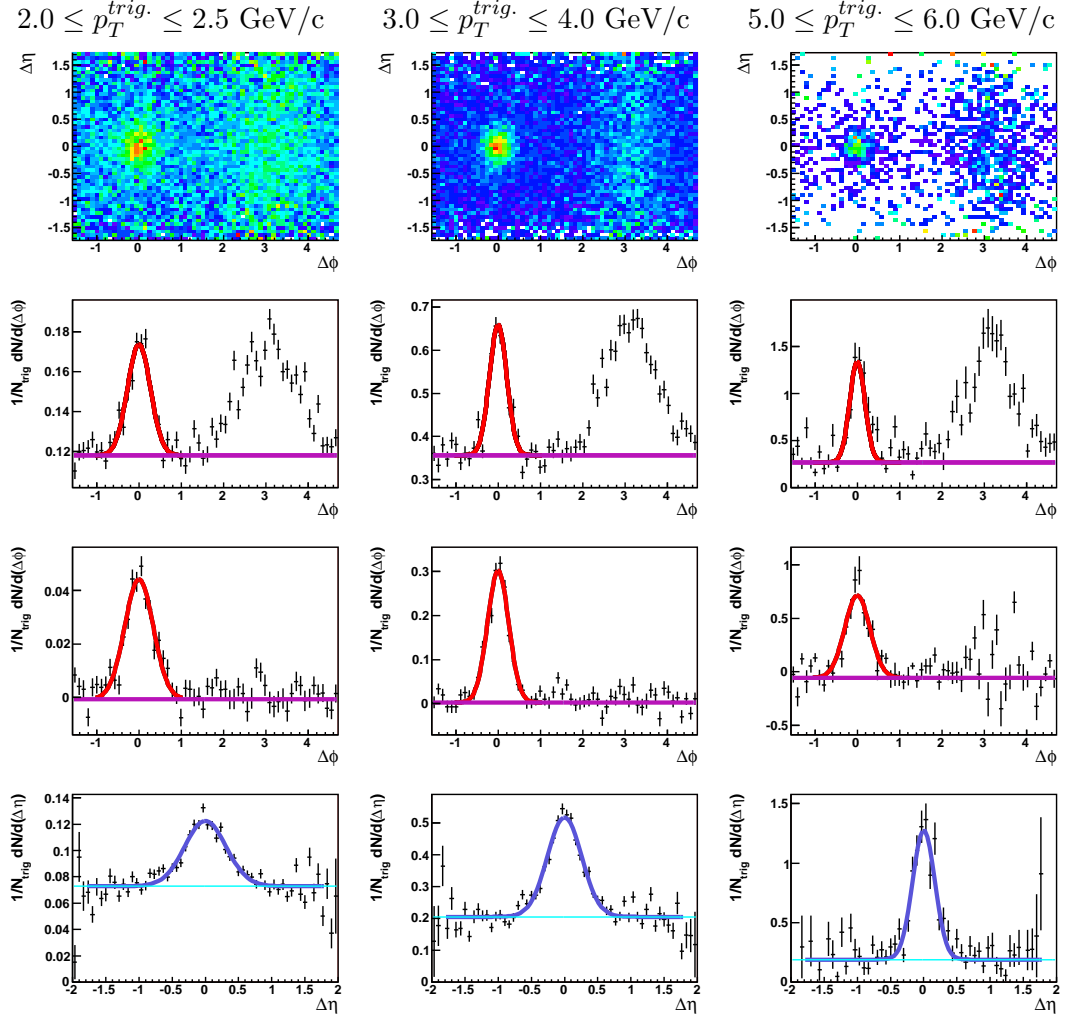


Figure 6.2: Correlation functions of unidentified charged tracks in minimum bias $d + Au$ collisions with $p_T^{asso.} > 2.0$ GeV/c and three $p_T^{trig.}$ intervals. From left to right: $2.0 \leq p_T^{trig.} \leq 2.5$ GeV/c, $3.0 \leq p_T^{trig.} \leq 4.0$ GeV/c, and $5.0 \leq p_T^{trig.} \leq 6.0$ GeV/c. The first row shows $\Delta\eta - \Delta\phi$ correlations. The second row shows $\Delta\phi$ projections within $|\Delta\eta| < 1.7$. The third row shows the $\Delta\phi$ distribution obtained by subtracting the projections over $0.7 < |\Delta\eta| < 1.4$ from $|\Delta\eta| < 0.7$. The fourth row shows the $\Delta\eta$ projection within $|\Delta\phi| < 1.0$.

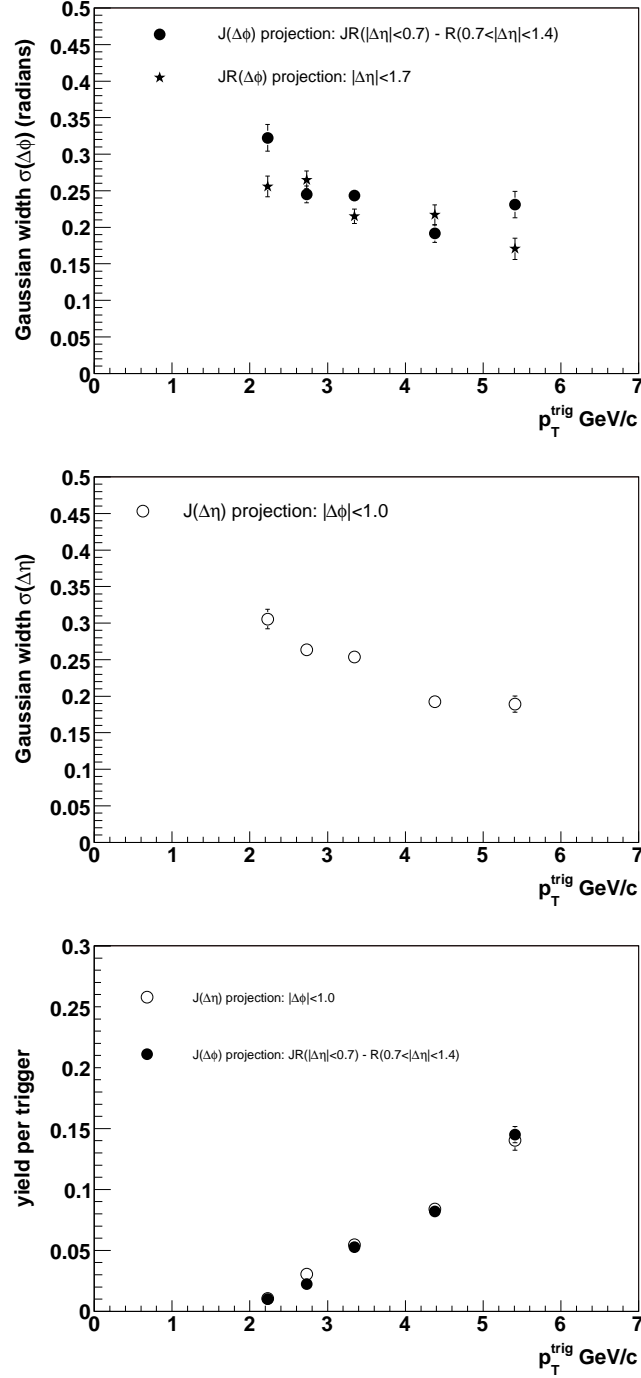


Figure 6.3: Same side peak characteristics as a function of $p_T^{\text{trig.}}$, for unidentified charged track correlations in minimum bias $d + Au$ collisions with $p_T^{\text{asso.}} > 2.0$ GeV/c. Gaussian widths of peaks in $\Delta\phi$ projections are shown in the top frame; stars represent the $\Delta\phi$ widths after projecting over the complete pseudorapidity range and filled circles give the widths of the $\Delta\phi$ projection obtained by subtracting the $\Delta\phi$ projection over $0.7 < |\Delta\eta| < 1.4$ from the $\Delta\phi$ projection over $|\Delta\eta| < 0.7$. In the centre frame the widths of peaks in $\Delta\eta$ projections over $|\Delta\phi| < 1.0$ are shown. The lower panel summarises the yields of the same fits. Error bars represent statistical uncertainties.

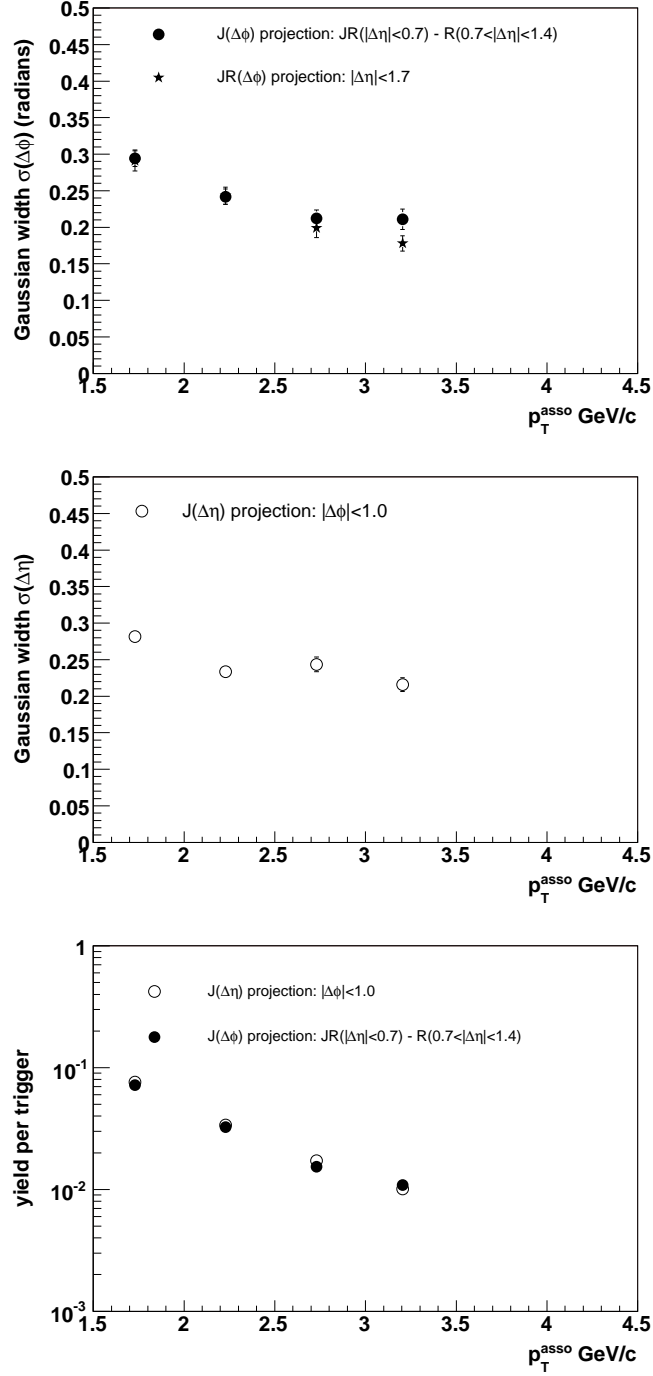


Figure 6.4: Same side peak characteristics as a function of p_T^{asso} , for unidentified charged track correlations in minimum bias $d + Au$ collisions with $3.0 \leq p_T^{trig.} \leq 6.0$ GeV/c. Gaussian widths of peaks in $\Delta\phi$ projections are shown in the top frame; stars represent the $\Delta\phi$ widths after projecting over the complete pseudorapidity range and filled circles give the widths of the $\Delta\phi$ projection obtained by subtracting the $\Delta\phi$ projection over $0.7 < |\Delta\eta| < 1.4$ from the $\Delta\phi$ projection over $|\Delta\eta| < 0.7$. In the centre frame the widths of peaks in $\Delta\eta$ projections over $|\Delta\phi| < 1.0$ are shown. The lower panel summarises the yields of the same fits. Error bars represent statistical uncertainties.

6.2.2 Minimum bias $Au + Au$ collisions

The minimum bias $Au + Au$ dataset allowed for a study of the onset of the ridge and same side modification as a function of system size. This was performed by subdividing the dataset according to centrality ranges, as described in section 3.4.

A sample set of correlation functions of unidentified charged tracks are presented in figure 6.5, in the same arrangement as for figure 6.2, except that in this instance each column represents a different centrality selection, increasing to the left. The $\Delta\eta - \Delta\phi$ correlation produced from the most peripheral subset is qualitatively similar to the $d + Au$ result, with no ridge structure apparent on the same side. Note the vertical axes in the projections have their origins suppressed. In the $\Delta\phi$ projections over $|\Delta\eta| < 1.7$ (second row), the away side is seen to reduce with increasing centrality, in agreement with earlier analyses. Indeed when estimates of the irreducible background, represented by violet lines, are taken into account, a clear modification to the shape of the away side is also apparent in central $Au + Au$ collisions.

In the third row of figure 6.5, the $\Delta\phi$ projection obtained by subtracting the projection over $0.7 < |\Delta\eta| < 1.4$ from the projection within $|\Delta\eta| < 0.7$ now provides the jet component of the same side peak. Assuming the ridge component is flat in $\Delta\eta$, the resultant only contains the jet part of the same side peak. The subtraction similarly eliminates the elliptic flow modulation and background.

Although the associated (correlated) yield greatly increases with centrality, it does not follow that correlation features should be better resolved. Indeed the increase in the number of pairs primarily reflects the rising amount of combinatorial background, and consequently the relative size of the peaks compared to the background actually decrease with increasing centrality. Thus there is an interplay between the degree to which the background is constrained and the prominence of the features of interest.

The dataset was sufficiently large to consider nine centrality ranges within the

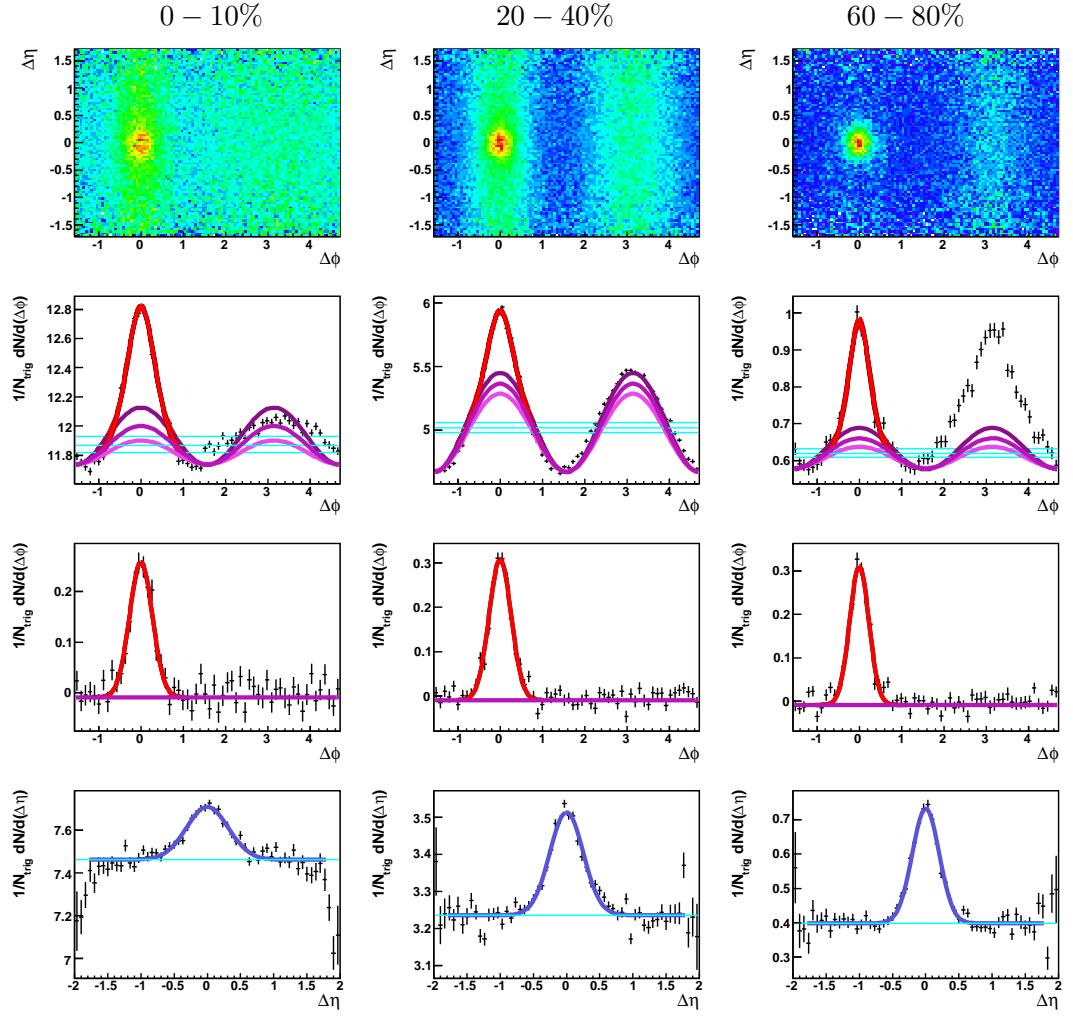


Figure 6.5: Correlation functions of unidentified charged tracks in minimum bias $Au + Au$ collisions for three centrality bins, increasing to the left. Pairs were selected within $3.0 \leq p_T^{trig.} \leq 6.0$ GeV/c and with $2.0 \leq p_T^{asso.} \leq p_T^{trig.}$. From left to right, the centrality ranges are 0 – 10%, 20 – 40%, and 60 – 80%. The first row displays acceptance corrected $\Delta\eta - \Delta\phi$ correlations. The second row shows $\Delta\phi$ projections within $|\Delta\eta| < 1.7$. The third row shows the $\Delta\phi$ jet component obtained by subtracting the projections over $0.7 < |\Delta\eta| < 1.4$ from $|\Delta\eta| < 0.7$. The fourth row shows the $\Delta\eta$ projection within $|\Delta\phi| < 1.0$.

interval 0 – 80%. Fits to the same side peak were well constrained and their characteristics are summarised in figure 6.6. The centrality ranges are displayed in terms of the number of participating nucleons, N_{part} . Statistical uncertainties are represented by error bars. The principle source of systematic error was found to be the uncertainty introduced by the v_2 parameterisation. These errors are represented by

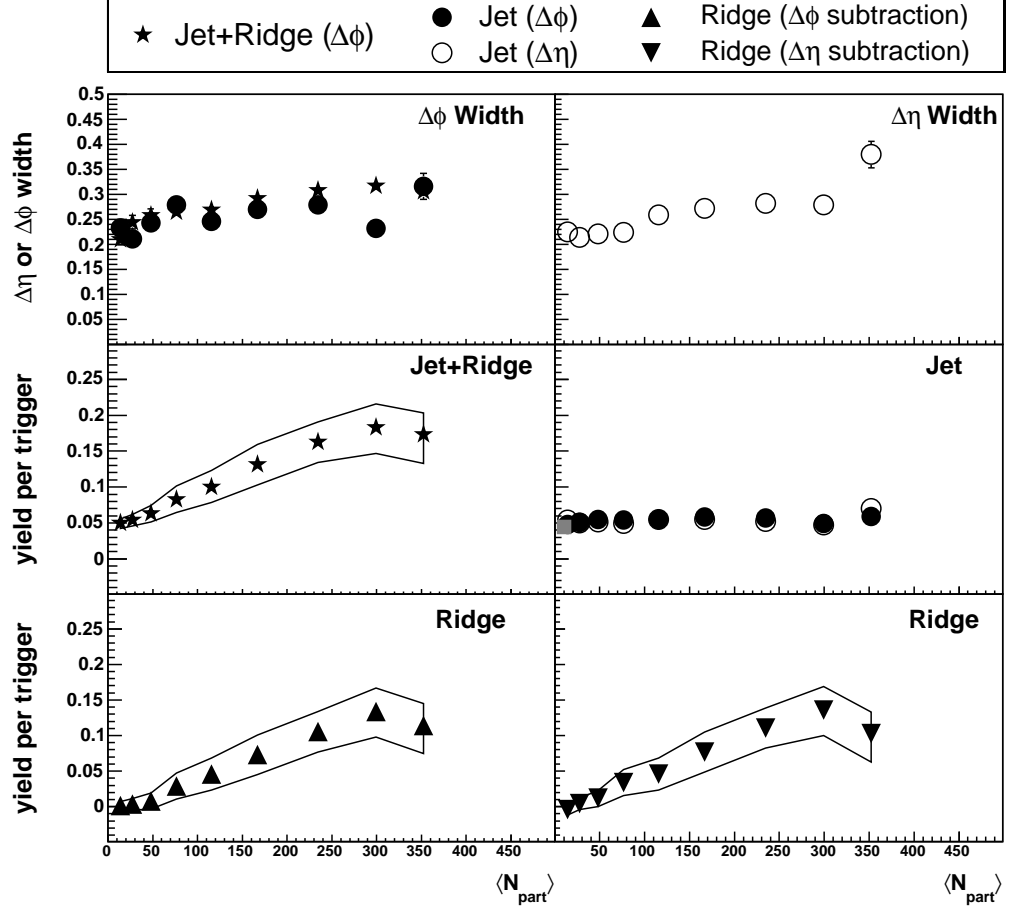


Figure 6.6: Same side peak properties for correlations of unidentified charged tracks in minimum bias $Au + Au$ collisions as a function of centrality, with $3.0 \leq p_T^{trig.} \leq 6.0$ GeV/c and $2.0 \leq p_T^{asso.} \leq p_T^{trig.}$. The upper left panel shows the widths from jet plus ridge $\Delta\phi$ projections (stars), and jet $\Delta\phi$ components (filled circles). The upper right panel displays widths from $\Delta\eta$ projections (open circles). The centre left panel shows the same side yield, extracted from $\Delta\phi$ projections over $|\Delta\eta| < 1.7$. The centre right panel shows the jet component yields, with a square marker representing the $\Delta\phi$ jet yield in $d + Au$ collisions. The lower left and right frames display ridge component yields obtained by subtracting the $\Delta\phi$ and $\Delta\eta$ jet estimates respectively from the same side yields over $|\Delta\eta| < 1.7$. Error bars represent statistical uncertainties. Solid lines represent systematic uncertainties.

solid boundary lines in figure 6.6. Note that although these systematic errors are unique to each data point, the uncertainty is common to all points in the sense that the correct level of v_2 should be some constant fraction of the two estimates of v_2 . If for instance the correct v_2 was provided by the cumulant result, then all data points would be shifted down to the lower line.

The centre left panel in figure 6.6 shows the total same side yield (above v_2 modulated background), extracted from $\Delta\phi$ projections over $|\Delta\eta| < (1.7)$. This measurement corresponds to the yield included in the I_{AA} analysis in [42], albeit unscaled to pp . In agreement with the earlier analysis, the yield is observed to increase steadily with centrality. The yield rises by a factor of ≈ 3.5 over the observed range. The width of the peak in this projection, included as stars in the upper left frame of figure 6.6, increases from 0.25 ± 0.01 radians for peripheral events to 0.32 ± 0.01 radians in central events. The widths of the $\Delta\eta$ and $\Delta\phi$ jet components behave similarly to the same side projection.

The yields of the jet components, shown in the centre right frame of figure 6.6 do not follow the trend of the total yield. Instead both $\Delta\eta$ and $\Delta\phi$ measurements are consistent with no centrality dependence, with a level consistent with the total yield in the peripheral bin, and also $d + Au$ same side yields assuming the same kinematic selection.

The lower row of panels in figure 6.6 includes two estimates of the ridge component yield within $|\Delta\eta| < 1.7$, defined as the difference between the total same side yield and either estimate of the jet component. The results of a third method involving a direct $\Delta\phi$ ridge projection are not shown as this approach was found to be less reliable for peripheral datasets. Common to all three estimates is a steady rise in the ridge yield with centrality. In the most central events the ridge accounts for approximately 70% of the same side yield.

The ridge yields for the most central bin were somewhat lower than the trend

would predict. This may reflect an overestimation of the background level or the magnitude of the v_2 modulation. Instability in the Gaussian fits was ruled out by obtaining a similar trend in yields calculated by integrating over bin ranges instead of fitting.

6.2.3 Central $Au + Au$ collisions

The dataset with the greatest statistical significance was the online-triggered central $Au + Au$ dataset. Approximately half of these data corresponded to $0 - 5\%$ central events, which were equivalent to the subset of events with the same centrality selection included within the minimum bias sample. For the present analysis, a $0 - 10\%$ centrality cut was applied to the central dataset to make fuller use of the available statistics, however this sample was not exactly equivalent to the $0 - 10\%$ subset in minimum bias data due to different trigger efficiencies for the less central events.

The central dataset was used to study the dependence of the same side peak upon the particle kinematics. Correlations were subdivided into ranges of $p_T^{trig.}$ and $p_T^{asso.}$, and the peak was described in terms of jet and ridge components. Fits to $\Delta\phi$ projections matched well to data except for the highest considered $p_T^{trig.}$ interval, where they slightly underestimated the amplitude of the peaks. This could indicate that the width was overestimated due to statistical uncertainties, or that the peak shape was not Gaussian at high p_T .

The $p_T^{trig.}$ dependence of the same side peak widths and yields is displayed in figure 6.7, following the same arrangement as figure 6.6. The same side peak dramatically broadens in the pseudo-rapidity direction as the trigger momentum range is lowered, as shown in the upper right frame. For the smallest trigger momenta the elongation is observed to reach $\Delta\eta = 0.75 \pm 0.05$, which corresponds to angular separations in the range $0.5 \lesssim \Delta\theta \lesssim 0.7$ radians. Thus the jet cone would appear elliptical with the minor axis parallel in the azimuthal plane. Comparing

to $d + Au$ correlations of the same kinematic selection, the $\Delta\eta$ width has doubled. The uncertainties decrease with increasing $p_T^{trig.}$ as the peak is more fully contained within the $\Delta\eta$ range.

A weaker $p_T^{trig.}$ dependence is exhibited by the width of the same side peak projected onto the azimuthal plane. In the upper left frame of figure 6.7, the width of the jet component appears similar to the width of the combined jet plus ridge peak except in an intermediate range where the jet appears to be narrower. The widths of projections over $0.7 < |\Delta\eta| < 1.4$, shown in the same frame, suggest that the ridge component is typically broader than the jet, in agreement with this observation. All $\Delta\phi$ widths converge at low $p_T^{trig.}$ as a result of the elongation of the jet peak in $\Delta\eta$. Throughout the covered $p_T^{trig.}$ range, the behaviour of the $\Delta\phi$ jet projection is similar to the $d + Au$ result.

The yield of the same side peak, as extracted from fits to $\Delta\phi$ projections over $|\Delta\eta| < 1.7$, are displayed in the centre left frame of figure 6.7. Systematic errors due to the uncertainty in the elliptic flow parameterisation are represented by solid lines. The peak is observed to initial increase rapidly with $p_T^{trig.}$ until $p_T^{trig.} \sim 3.5$ GeV/c, after which the yield continues to increase at a much reduced rate. This behaviour is unlike that observed in the $d + Au$ analysis, which exhibited an approximately monotonic rise with $p_T^{trig.}$, with lower yields throughout the range.

The jet component of the same side yield was estimated via $\Delta\eta$ and $\Delta\phi$ projections are shown overlaid in the centre right frame of figure 6.7, together with a dotted line to represent the $\Delta\phi$ jet yields measured in $d + Au$ collisions. The results quantitatively agree to $d + Au$ correlations shown in figure 6.3. The jet component yields exhibit a monotonic rise with $p_T^{trig.}$, and therefore the relative contribution of the jet to the same side peak increases with $p_T^{trig.}$ from initially representing $\sim 20\%$ up to approximately $\sim 75\%$ of the total yield for the highest $p_T^{trig.}$ interval.

Estimates of the ridge contribution shown in the lower row of frames in figure 6.7.

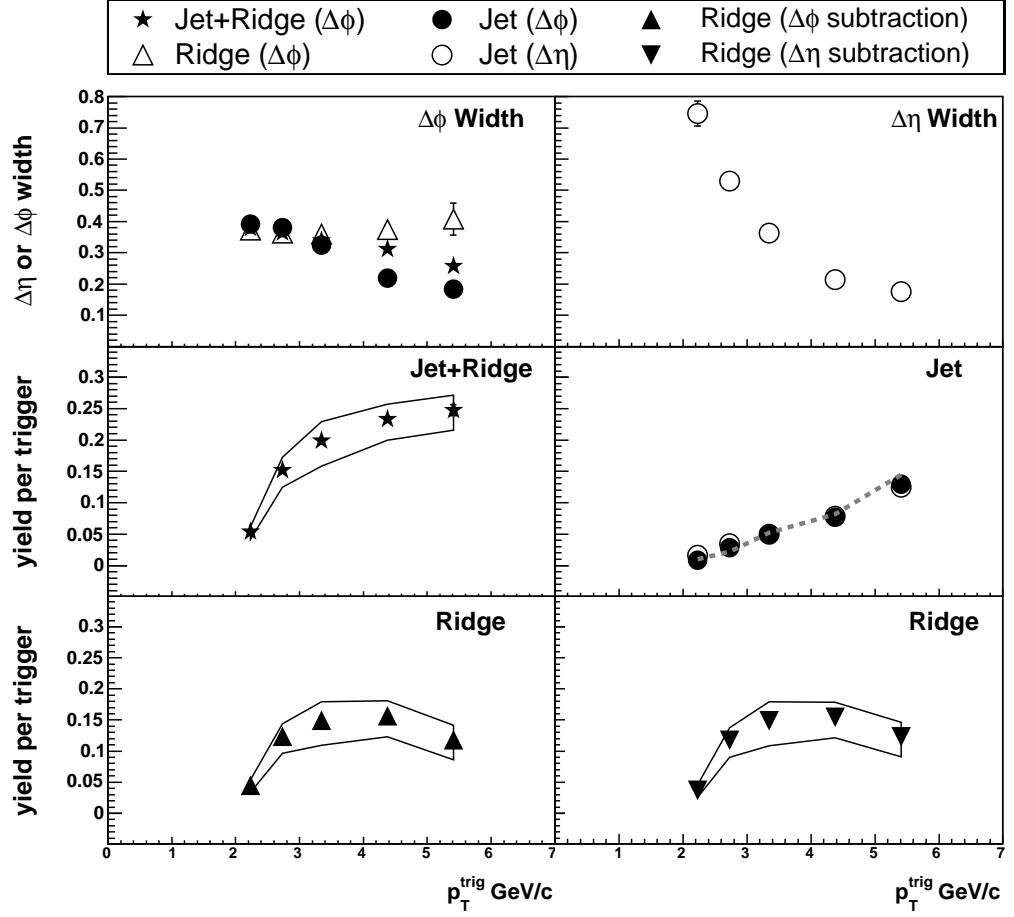


Figure 6.7: Same side peak properties for correlations of unidentified charged tracks in 0 – 10% central $Au + Au$ collisions as a function of $p_T^{trig.}$. Pairs were selected with $2.0 \leq p_T^{asso.} \leq p_T^{trig.}$. The upper left panel shows the widths from jet plus ridge $\Delta\phi$ projections (stars), and jet $\Delta\phi$ components (filled circles). The upper right panel displays widths from $\Delta\eta$ projections (open circles). The centre left panel shows the same side yield, extracted from $\Delta\phi$ projections over $|\Delta\eta| < 1.7$. The centre right panel shows the jet component yields, with the $\Delta\phi$ jet yield in $d + Au$ collisions represented by a dotted line. The lower left and right frames display ridge component yields obtained by subtracting the $\Delta\phi$ and $\Delta\eta$ jet estimates respectively from the same side yields over $|\Delta\eta| < 1.7$. Error bars represent statistical uncertainties. Solid lines represent systematic uncertainties.

The dependence upon $p_T^{trig.}$ is in agreement with the behaviour of the $\Delta\phi$ jet and $\Delta\phi$ jet plus ridge peak widths. These two widths differ the most where the ridge yield is largest. Again the direct ridge component estimate is not shown. After initially rising with $p_T^{trig.}$, all ridge yield estimates appeared to saturate, and may decline for $p_T^{trig.} \gtrsim 5.0$ GeV/c. However, if the lowest $p_T^{trig.}$ bin were to be neglected, the ridge yield could in fact be independent of $p_T^{trig.}$. Considering that the kinematic selection for the first bin is somewhat different to the others, this may be appropriate. The low magnitude of the first data point may be caused by the reduced phase space afforded by permitting trigger and associated particle p_T ranges to coincide. As the jet component elongates in $\Delta\eta$ with decreasing $p_T^{trig.}$, this $\Delta\phi$ ridge projection is contaminated by the tail of the jet peak, which results in the overestimation of a ridge that is assumed to be flat. Moreover this approach suffered most from limited statistics due to its reliance upon pairs in the lower acceptance region in $\Delta\eta$. See section 6.2.4 for a discussion of this observation.

The correlations were next integrated over the $p_T^{trig.}$ range and their dependence upon the $p_T^{asso.}$ was considered. The results of this study are summarised in figure 6.8. The jet component width appears to decrease with increasing $p_T^{asso.}$. The $\Delta\eta$ and $\Delta\phi$ jet peak widths follow more similar trends than in the $p_T^{trig.}$ study, although again the $\Delta\eta$ width appears to decline more steeply. The ridge projection width exhibits little dependence upon this parameter.

The total same side peak yields are displayed as function of $p_T^{asso.}$ in the centre left frame of figure 6.8, providing a decomposition of the structures into transverse momentum bins. These yields were separated into jet and ridge components as before, and these are displayed in the centre right frame and lower row of frames in figure 6.8 respectively. The ridge component was found to be the dominant contribution to the total yield for the majority of this kinematic range, except for the highest $p_T^{asso.}$ interval wherein the two component are of similar magnitude. For

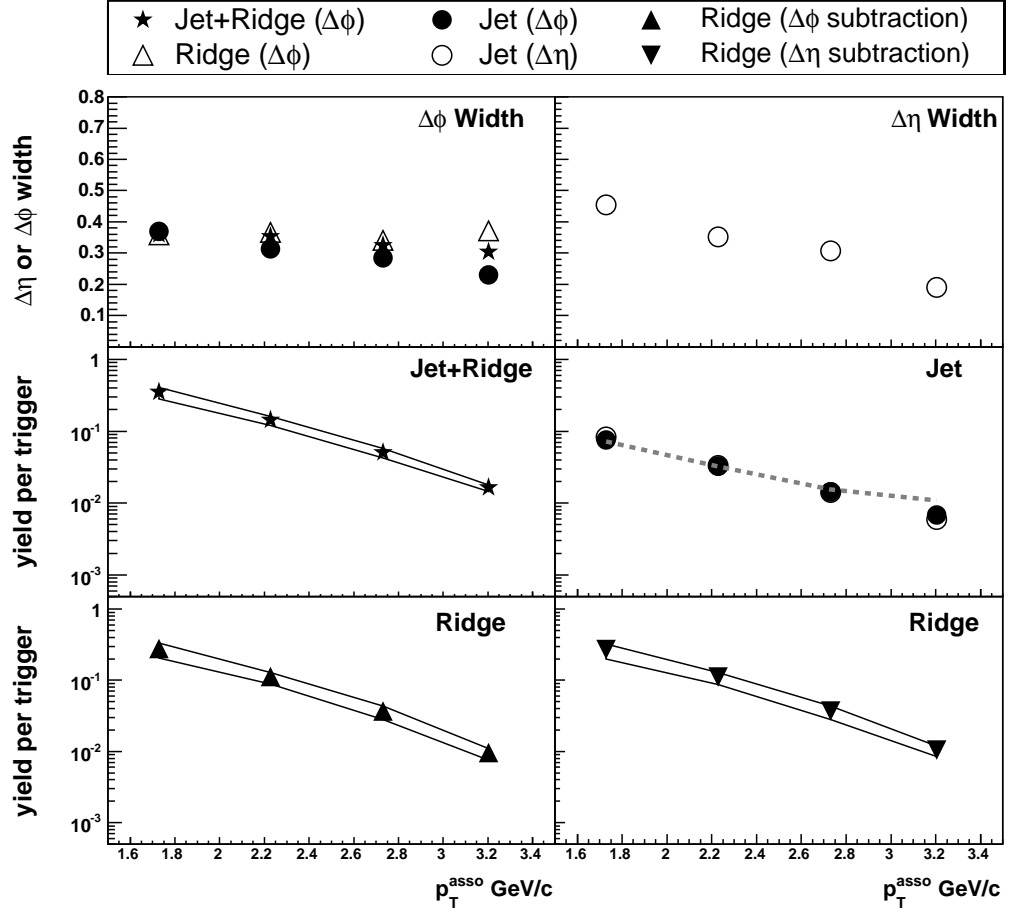


Figure 6.8: Same side peak characteristics as a function of p_T^{asso} in correlations of unidentified charged tracks in 0–10% central $Au + Au$ collisions with $3.0 \leq p_T^{trig.} \leq 6.0$ GeV/c. The upper left panel shows the widths from jet plus ridge $\Delta\phi$ projections (stars), and jet $\Delta\phi$ components (filled circles). The upper right panel displays widths from $\Delta\eta$ projections (open circles). The centre left panel shows the same side yield, extracted from $\Delta\phi$ projections over $|\Delta\eta| < 1.7$. The centre right panel shows the jet component yields, with the $\Delta\phi$ jet yield in $d + Au$ collisions represented by a dotted line. The lower left and right frames display ridge component yields obtained by subtracting the $\Delta\phi$ and $\Delta\eta$ jet estimates respectively from the same side yields over $|\Delta\eta| < 1.7$. Error bars represent statistical uncertainties. Solid lines represent systematic uncertainties.

the lowest $p_T^{asso.}$ bin, the $\Delta\phi$ jet yield was found to be $\approx 27\%$ the magnitude of the ridge estimate from $\Delta\phi$ projections, whereas for the highest $p_T^{asso.}$ bin the jet yield relative to the ridge had risen to $\approx 72\%$. Furthermore, the slope of the jet component appears to be shallower than the ridge. Over the $p_T^{asso.}$ range considered, the $\Delta\phi$ jet yield decreases by $\approx 91\%$, an absolute decrease in yield of 0.0685 ± 0.0019 associations per trigger. In contrast, a fall of $\approx 97\%$, or 0.2690 ± 0.0028 associations per trigger was observed in the ridge component estimated using the $\Delta\phi$ jet estimate. This is indicative of a harder momentum profile for the jet, and hence the jet yield should dominate at higher $p_T^{asso.}$.

6.2.4 Discussion

One of the main aims of this analysis was to gain a better understanding in the increased same side yield in $Au+Au$ collisions relative to $p+p$ as expressed I_{AA} (figure 1.13), presented by STAR [42]. By assuming the same side peak is a composite of a Gaussian jet peak localised at $\Delta\eta = \Delta\phi = 0$ resting atop a ridge in $\Delta\eta$, it is now possible to relate the increase same side yield with centrality with the onset of the second feature.

The invariance of the jet component yield with centrality offers an important insight into its formation. Scaling correlations by the number of triggers eliminated any trivial system size dependence. Jet yields corresponded well to $d + Au$ same side peak yields. Ignoring the elongation in $\Delta\eta$, the simplest interpretation of this observation alone is that vacuum fragmentation is dominant in $Au + Au$ correlations for the kinematic selection used in this study. This supports the expected surface bias for di-jets. Additionally, within the framework of parton attenuation, fragmentation appears to take place according to the reduced parton momentum. The fact that fewer trigger particles are found in a given $p_T^{trig.}$ range is irrelevant to this method due to the N_{trig} scaling. Despite the constant yield, the width in both

$\Delta\eta$ and $\Delta\phi$ projections did increase with centrality, perhaps indicating some degree of interaction with the rest of the system.

Lowering the $p_T^{trig.}$ criterion resulted in a substantial elongation of the jet peak in the $\Delta\eta$ direction compared to $d + Au$, whilst the $\Delta\phi$ width increased in line with the $d + Au$ results. Moreover the yield and p_T distribution of the peak ($p_T^{asso.}$ dependence) extracted from the $\Delta\eta$ projections were similar to $d + Au$ correlations. These observations can be reconciled by noting that the kinematic selections imposed on the pairs only considered the p_T of the tracks. Consequently any momentum transfer perpendicular to p_T , i.e. in the longitudinal direction, would not modify the p_T distribution of the jet. The elongation of the jet peak in the $\Delta\eta$ direction gives a strong indication for the interaction of the particles comprising the jet component with the underlying $Au + Au$ system. For $p_T^{asso.}$ ranges lower than that shown here, the jet component is elongated to such a degree that it became difficult to isolate it from the ridge component. Thus the two component description of the same side peak is only suitable for correlations where the jet peak is prominent. At low- p_T , the tails of the peak in the $\Delta\eta$ direction approach the limits of the observable range of $|\Delta\eta| < 2.0$, and therefore the assumption that the ridge is independent of $\Delta\eta$ is no longer clearly supported by the data. Indeed, a sufficiently elongated $\Delta\eta$ peak is indistinguishable from a ridge. Since the mechanisms responsible for the emergence of the ridge and broadening of the peak in the $\Delta\eta$ direction are unknown (and thus any relationship between the two features), there is no physical motivation to assume a flat ridge persists at low- p_T . It would therefore be unwise to extrapolate the model to low- p_T where the two components cannot be resolved.

The smooth increase in the yield of the ridge component with centrality is qualitatively similar to the onset of high- p_T suppression expressed by R_{AA} . No threshold multiplicity is apparent. The absence of a ridge in $d + Au$ implies that the feature is indeed caused by processes following the initial collision. Although the shape of

the ridge in $\Delta\eta - \Delta\phi$ correlations is somewhat similar to elliptic flow, the ridge does not share the same dependence on centrality. The magnitude of elliptic flow reaches a maximum in mid-central collisions due to the competing influences of system size and spatial eccentricity. In contrast, the ridge yield appears to scale with N_{part} , which may indicate a dependence upon mean path length traversed by the initial parton.

The dependence of the ridge yield upon $p_T^{trig.}$ cannot be explained to date, but may reflect the degree of jet attenuation. The relationship between the momentum of a trigger and the trajectory of a progenitor hard parton cannot be sought experimentally, but some future insights may be made by comparing to simulations.

Finally the $p_T^{asso.}$ dependence of jet and ridge components revealed the two to have different compositions. In particular, the slope of the jet yields was more shallow than that of the ridge component. Both trends were consistent with exponential distributions, and hence a more gradual slope is indicative of a higher temperature.

6.3 Correlations involving V0 tracks

Two particle correlations were produced using samples of Λ , $\bar{\Lambda}$, and K_{Short}^0 particles sourced from V0 tracks that passed the set of cuts described in section 3.7, by making selections on hypothesised invariant mass. The unavoidable contamination of a sample by the residual combinatorial background was studied by producing correlations using V0 candidates outside of the mass cuts. These exhibited peaks of comparable intensity (per trigger) to correlations using the Λ , $\bar{\Lambda}$, and K_{Short}^0 samples, but could be ignored because a good signal-to-noise ratio was achieved in each sample.

Correlations with V0 triggers made using the $d + Au$ dataset exhibited qualitatively similar di-jet peak structures to those seen in unidentified correlations, demonstrating that it was indeed possible to study correlations with baryon, anti-baryon or meson leading particles. Unfortunately, the $d + Au$ dataset contained insufficient V0 triggers to consider correlations differential in pseudorapidity difference. Studies of the same side peak in $\Delta\phi$ correlations indicated that the widths and yields for all three species were consistent, but within large statistical uncertainties.

Correlation functions produced using the $Au + Au$ datasets benefitted from much greater statistics. Example correlations for each trigger species are shown in figure 6.9, wherein the left, centre and right columns of frames display Λ , $\bar{\Lambda}$ and K_{Short}^0 triggered correlations respectively. Two dimensional and $\Delta\eta$ and $\Delta\phi$ projections are arranged in the figure as in figures 6.2 and 6.5 above. For all three trigger species, the elongation of the same side peak in the $\Delta\eta$ direction was clearly visible, and Gaussian peaks were found in the $\Delta\eta$ and $\Delta\phi$ jet component projections. Correlations involving K_{Short}^0 triggers were more clearly defined than for the other two species. In fact it was not possible to use the $\Delta\eta$ projections for the baryon triggers in all data subsets, as the fits failed to converge.

In addition to fits, yields extracted by integrating background-subtracted corre-

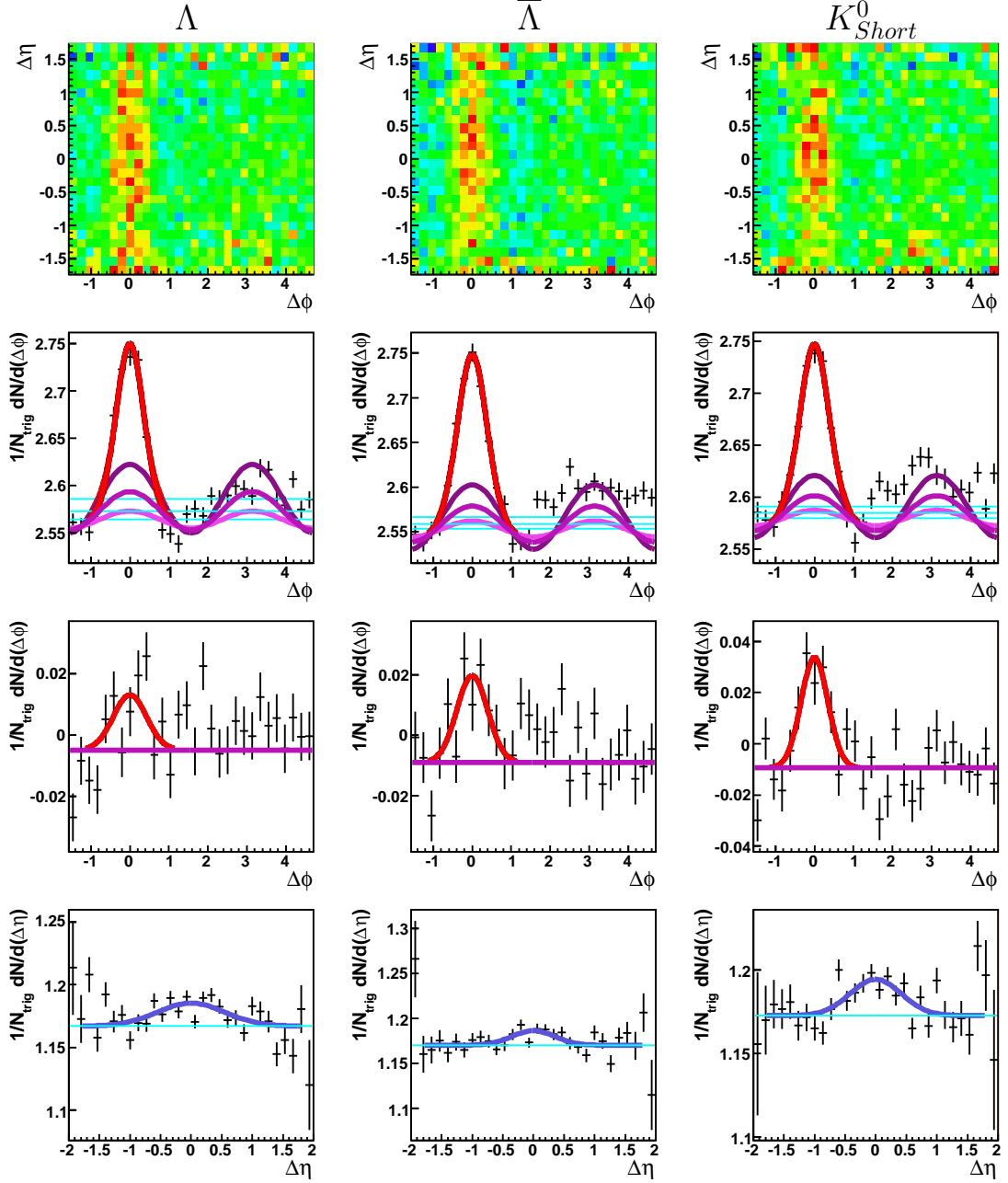


Figure 6.9: Correlation functions involving identified trigger tracks and unidentified charged associated tracks in 0-10% central $Au + Au$ collisions at $\sqrt{s_{NN}} = 200$ GeV within $3.0 \leq p_T^{trig.} \leq 6.0$ GeV/c and $2.0 \leq p_T^{asso.} \leq p_T^{trig.}$. From left to right, columns display correlations with Λ , $\bar{\Lambda}$, and K_{Short}^0 triggers. The first row displays acceptance-corrected $\Delta\eta - \Delta\phi$ correlations. The second row shows $\Delta\phi$ projections within $|\Delta\eta| < 1.7$. The third row shows the $\Delta\phi$ jet projection obtained by subtracting the projections over $0.7 < |\Delta\eta| < 1.4$ from $|\Delta\eta| < 0.7$. The fourth row shows the $\Delta\eta$ projection within $|\Delta\phi| < 1.0$. Lines represent fits to the data. Light blue and violet lines indicate the level of combinatorial background and v_2 modulation respectively.

lations were also considered, but were disfavoured as the related errors were dominated by the estimation of the background level. Despite being a statistics limited analysis, it was possible to obtain estimates of the jet and ridge components using $\Delta\phi$ projections, wherein the same side peak was adequately large relative to the combinatorial background level to obtain statistically significant fits in most centrality and kinematic selections.

6.3.1 Minimum bias $Au + Au$ collisions

The same side peak characteristics of V0 -triggered correlations are summarised in figure 6.10 as a function of centrality. Trigger species are labelled by marker colour: red for Λ triggers, green for $\bar{\Lambda}$ triggers, blue for K_{Short}^0 triggers, and black for unidentified charged tracks. The upper left and right frames of figure 6.10 show the widths of $\Delta\phi$ and $\Delta\eta$ projections respectively. Fits to $\Delta\eta$ projections of correlations with Λ and $\bar{\Lambda}$ triggers were poorly constrained and have been excluded from the figure. Within the statistical uncertainties the widths of the same side peaks are consistent between trigger species.

The centre left row of frames displays the same side yield extracted from $\Delta\phi$ projections over $|\Delta\eta| < 1.7$. Solid lines represent systematic errors due to the uncertainty in estimates of v_2 with the lower limit set by cumulant estimates and the upper limit set by reaction measurements as described in section 4.4.1. Note that the correct level of v_2 is a common fraction of the interval between the boundary lines for a given point. Hence the relative position of data points for different species is invariant. The increase in yield with increasing centrality and thus the emergence of the ridge, is observed for all species. Correlations with K_{Short}^0 triggers exhibit lower total same side peak yields for most of the range.

The jet component yields are shown in the centre right frame of figure 6.10. In agreement with the observation from unidentified correlations, the jet component

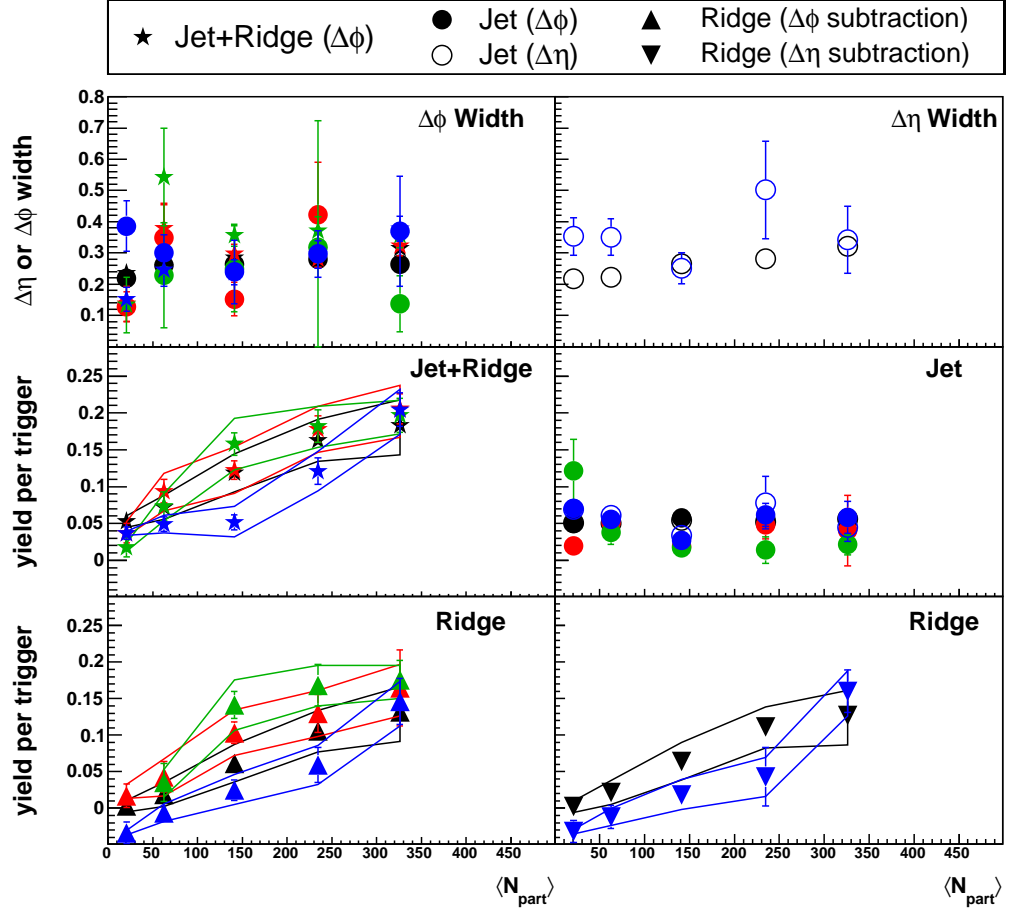


Figure 6.10: Same side peak properties for correlations with Λ (red), $\bar{\Lambda}$ (green), K_{Short}^0 (blue) and unidentified triggers in minimum bias $Au + Au$ collisions as a function of centrality, with $3.0 \leq p_T^{trig.} \leq 6.0$ GeV/c and $2.0 \leq p_T^{asso.} \leq p_T^{trig.}$. The upper left panel shows the widths from jet plus ridge $\Delta\phi$ projections (stars), and jet $\Delta\phi$ components (filled circles). The upper right panel displays widths from $\Delta\eta$ projections (open circles). The centre left panel shows the same side yield, extracted from $\Delta\phi$ projections over $|\Delta\eta| < 1.7$. The centre right panel shows the jet component yields. The lower left and right frames display ridge component yields obtained by subtracting the $\Delta\phi$ and $\Delta\eta$ jet estimates respectively from the same side yields over $|\Delta\eta| < 1.7$. Error bars represent statistical uncertainties. Solid lines represent systematic uncertainties.

does not appear to vary with centrality. Both $\Delta\eta$ and $\Delta\phi$ jet components are shown for K_{Short}^0 triggers, but as described above, the jet component was not clearly resolved in $\Delta\eta$ projections of baryon triggered correlations.

The lower row of graphs includes estimates of the ridge yields calculated by subtracting the jet yields from $\Delta\phi$ projections over $|\Delta\eta| < 1.7$. There is some evidence of a species dependence of the ridge yield; the K_{Short}^0 triggered yields are less than the unidentified correlations, and the Λ and $\bar{\Lambda}$ triggered correlations lie above the unidentified correlations results.

6.3.2 Central $Au + Au$ collisions

As was observed in the analysis of the minimum bias dataset, K_{Short}^0 triggered correlations were more clearly defined than either Λ or $\bar{\Lambda}$ triggered correlations using the online-triggered central dataset. Gaussian peaks were successfully resolved in $\Delta\eta$ projections for all three species for the higher $p_T^{trig.}$ and $p_T^{asso.}$ intervals considered, but failed at low p_T .

The $p_T^{trig.}$ dependence of the jet and ridge components is summarised in figure 6.11 in the same format as figure 6.10, with species indicated by marker colour. The widths are consistent between species within statistical uncertainties. The results suggest that no strong species dependence exists for total same side yields, although as was observed in the minimum bias data, the results give some indication that ridge yields may be larger for baryon triggered correlations. Jet component yields were similar to unidentified correlations, but several datapoints were lower for V0-triggered correlations. This may indicate some remaining systematic difference between the correlations, such as a species (or mass) dependence upon trigger bias (note that unidentified triggers are predominantly pions), or alternatively could reflect the limiting statistics resulting in less well defined mixed events as discussed in section 5.2.4. This should be investigated further in future analyses that benefit

from a larger dataset.

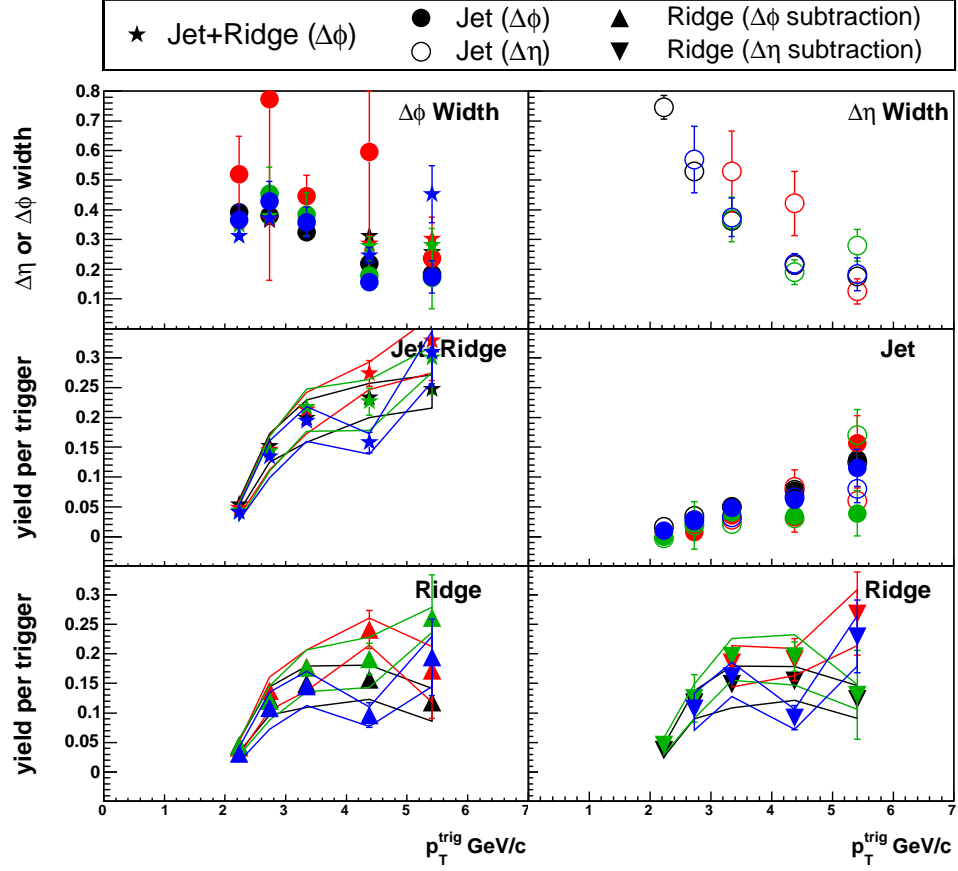


Figure 6.11: Same side peak properties for correlations with Λ (red), $\bar{\Lambda}$ (green), K_{Short}^0 (blue) and unidentified triggers in 0 – 10% central $Au + Au$ collisions as a function of $p_T^{\text{trig.}}$, with $2.0 \leq p_T^{\text{asso.}} \leq p_T^{\text{trig.}}$. The upper left panel shows the widths from jet plus ridge $\Delta\phi$ projections (stars), and jet $\Delta\phi$ components (filled circles). The upper right panel displays widths from $\Delta\eta$ projections (open circles). The centre left panel shows the same side yield, extracted from $\Delta\phi$ projections over $|\Delta\eta| < 1.7$. The centre right panel shows the jet component yields. The lower left and right frames display ridge component yields obtained by subtracting the $\Delta\phi$ and $\Delta\eta$ jet estimates respectively from the same side yields over $|\Delta\eta| < 1.7$. Error bars represent statistical uncertainties. Solid lines represent systematic uncertainties.

The $p_T^{\text{asso.}}$ dependence of same side yields for each trigger species are overlaid in figure 6.12 for triggers in the range $3.0 \leq p_T^{\text{trig.}} \leq 6.0$ GeV/c. Fairly good agreement is seen between species for both widths and yields, with similar trends to the unidentified correlations. The total same side yields for all species appear

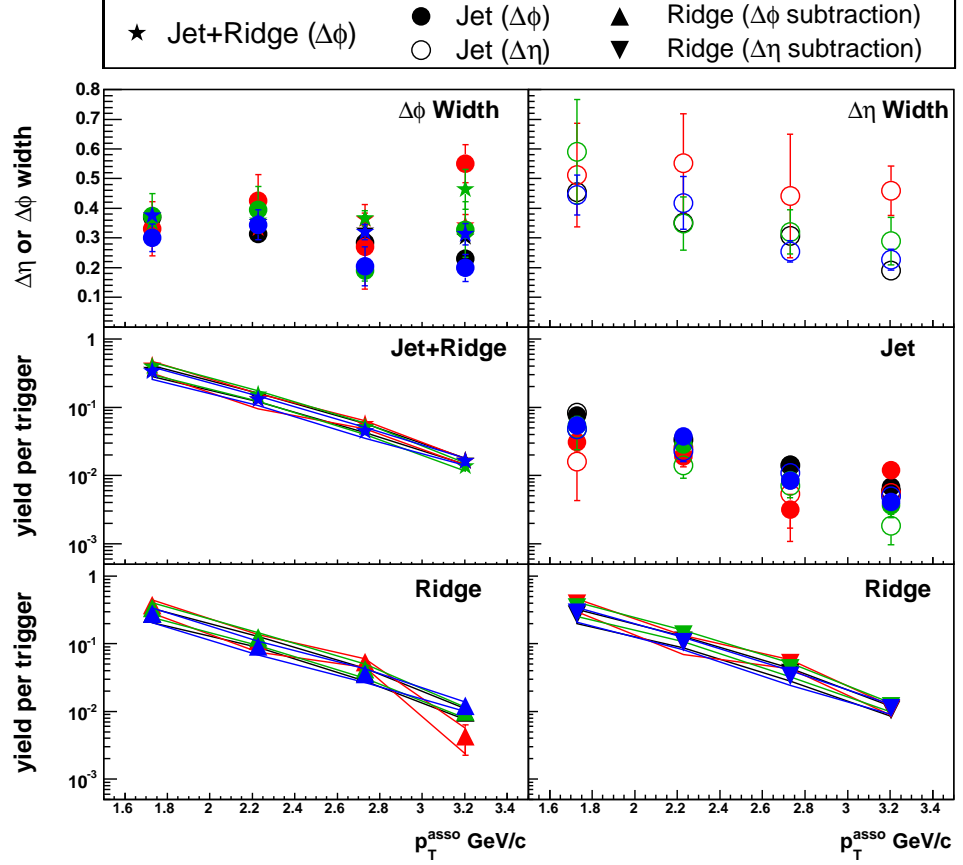


Figure 6.12: Same side peak properties for correlations with Λ (red), $\bar{\Lambda}$ (green), K_{Short}^0 (blue) and unidentified triggers in 0–10% central $Au + Au$ collisions as a function of p_T^{asso} , with $3.0 \leq p_T^{trig} \leq 6.0$ GeV/c. The upper left panel shows the widths from jet plus ridge $\Delta\phi$ projections (stars), and jet $\Delta\phi$ components (filled circles). The upper right panel displays widths from $\Delta\eta$ projections (open circles). The centre left panel shows the same side yield, extracted from $\Delta\phi$ projections over $|\Delta\eta| < 1.7$. The centre right panel shows the jet component yields. The lower left and right frames display ridge component yields obtained by subtracting the $\Delta\phi$ and $\Delta\eta$ jet estimates respectively from the same side yields over $|\Delta\eta| < 1.7$. Error bars represent statistical uncertainties. Solid lines represent systematic uncertainties.

to decline with increasing $p_T^{asso.}$ according to a common slope. As was observed in unidentified correlations, the ridge component dominates the yield of low $p_T^{asso.}$ tracks in the same side peak. The ridge component shows no clear species dependence for this kinematic range, with V0 triggered correlations exhibit a similar slope to the unidentified correlations, which is steeper than the trend observed in the jet component.

6.3.3 Correlations with associated V0 tracks

Correlations were produced taking unidentified charged track triggers and associated V0 tracks. For these correlations each species combination was corrected for reconstruction efficiency by a unique parameterisation, derived from embedding studies (see section 3.7.1). The resulting distributions in $(\Delta\eta, \Delta\phi)$ space were qualitatively similar to other arrangements, with a same side peak that appeared extended in $\Delta\eta$.

The identified associated correlations produced in this analysis were less populated than those with identified triggers. Given available statistics, only total same side yields are reported here. In figure 6.13 the $p_T^{trig.}$ and $p_T^{asso.}$ dependence of the total sameside yields, extracted via $\Delta\phi$ projections over $|\Delta\eta| < 2.0$, are shown for associated Λ , $\bar{\Lambda}$, and K_{Short}^0 particles. In both sets of results, similar yields of pairs were found for each species.

6.3.4 Discussion

The second objective of this analysis has been met by demonstrating the use of Λ , $\bar{\Lambda}$ and K_{Short}^0 particles as trigger and associated particles for correlations, providing a high purity source of baryons, anti-baryons, and mesons. The results, using the presently available datasets, are statistics limited and consequently no strong conclusions can be made.

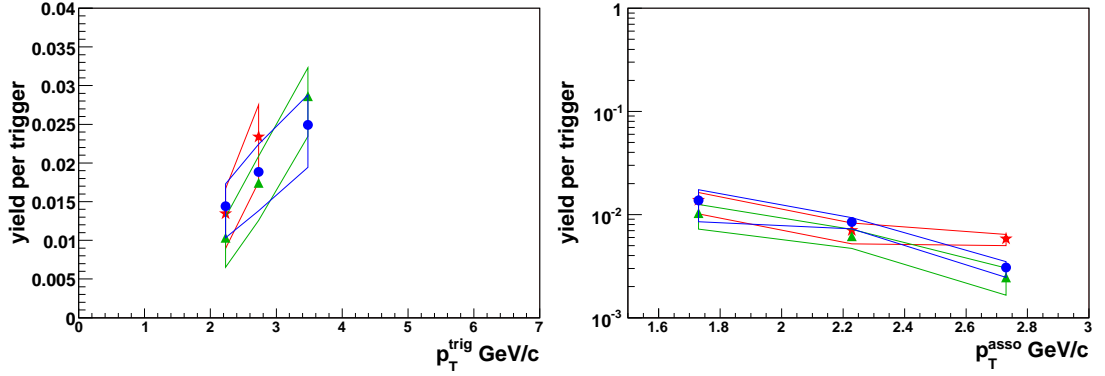


Figure 6.13: Total same side yields as a function of $p_T^{trig.}$ (left) and $p_T^{asso.}$ (right) of correlations with identified associated particles in 0 – 10% central $Au + Au$ collisions. Associated species are overlayed in each frame: red, green and blue markers represent yields from Λ , $\bar{\Lambda}$, and K_{Short}^0 associated correlations, respectively. For $p_T^{trig.}$ dependence, associated particles were selected with $1.5 \leq p_T^{asso.} \leq p_T^{trig.}$. For $p_T^{asso.}$ dependence, trigger particles were accepted with $3.0 \leq p_T^{trig.} \leq 6.0$ GeV/c. Error bars represent the fit error due to statistical uncertainties. Solid lines represent systematic uncertainties due to the evaluation of v_2 .

Although the per-trigger yield were similar between species, and the integrated number of trigger particles in the interval $2.0 \leq p_T^{trig.} \leq 6.0$ GeV/c were similar, correlations with K_{Short}^0 triggers were visibly better defined than correlations with Λ and $\bar{\Lambda}$ triggers. In order to understand this observation, it is necessary to consider the trigger particle distributions as a function of $p_T^{trig.}$, as shown in figure 3.13. Triggers were sourced from a p_T interval where the baryon-meson difference is found and parton coalescence is expected to dominate. This interpretation is therefore consistent with more K_{Short}^0 being related to jets. The lack of any strong species dependence observed in the jet yields of the same peak and components in $Au + Au$ collisions indicates that the level of any quark and gluon jet discrimination achieved by selecting trigger species for the p_T interval studied is smaller than the reported statistical uncertainties. If ridge yields do indeed exhibit a similar baryon-meson difference to the underlying event, then this would suggest that these particles originate from the underlying event, but have received a p_T boost due to interactions with a high- p_T particle. If jet and ridge components co-exist in the same events,

then fragmentation takes place, but is accompanied by additional interactions with the medium. If instead the two features are formed independently (as for the v_2 modulation of combinatorial background), then the ridge may at least in part be formed by jet quenching and shower-thermal recombination. See section 7.1.3.

Given the biases between quark and gluon jets, V0 triggers should offer a means of discrimination in future analyses. The datasets available to this project allowed a study of correlations with intermediate p_T triggers and associated tracks where few quark jets are expected. However, the technique can be directly applied to higher momentum triggers given sufficient statistics. Indeed such an analysis may be simpler due to reduced backgrounds and effects such as track merging.

Identified associated correlations are more demanding in terms of statistics, but can offer information regarding hadronisation mechanisms. A baryon-to-meson ratio of approximately unity was observed in the same side peak, in a kinematic range where the ridge dominates, indicating that the majority of the ridge yield may originate from the underlying event. Instead, had a ratio of one-half been observed, this would have suggested fragmentation was the dominant mechanism [40].

6.4 Summary of research findings

The principle achievements of the present analysis are as follows

- Two-particle correlations have been successfully extended to two dimensions by including pseudorapidity difference. To this end, new techniques were developed to correct for finite pair-wise acceptance and two-track resolution. The resulting $\Delta\eta - \Delta\phi$ correlations allowed a more complete description of the same side peak, which was characterised via the study of projections onto $\Delta\eta$ and $\Delta\phi$ axes.
- Studies of charged-track correlations have identified the enhancement in the same side yield observed in central $Au + Au$ collisions with the emergence of a $\Delta\eta$ ridge. This ridge increases monotonically with centrality, has a non-trivial $p_T^{trig.}$ dependence (and may be flat, neglecting the lowest $p_T^{trig.}$ bin), and dominates the same side peak for correlations of low- p_T tracks. Once the ridge has been accounted for, the same side yield is consistent in all systems. However, the width of the jet component in the $\Delta\eta$ projection does show a considerable degree of broadening in central $Au + Au$ compared to $d + Au$ collisions.
- Identified correlations have been successfully produced using Λ , $\bar{\Lambda}$, and K_{Short}^0 particles reconstructed from V0 tracks. The analysis of these correlations was statistics limited given the currently available datasets, and in general results were consistent with unidentified correlations. No strong species dependence was observed, although the ridge yield appeared larger for baryon than meson triggers. In future analyses of higher energy collisions, correlations using these identified trigger species should offer some discrimination between quark and gluon jets, due to the species bias outlined in section 2.1.2.

Chapter 7

INTERPRETATION AND OUTLOOK

7.1 Theoretical treatments of modifications to the same side peak

A variety of possible production mechanisms has been suggested to explain the modification of the same side peak in the $Au + Au$ system. All treatments to date are largely qualitative in their predictions, although the assumptions made in order to generate the desired features in each approach have lead to some intriguing possibilities for gaining new insights into the properties of the QGP at RHIC. Indeed some challenge key components to the current understanding of the medium.

7.1.1 Coupling to longitudinal flow

Armesto *et al.* proposed a coupling between collective flow and jets could generate the observed broadening of the same side peak [92]. This is illustrated schematically in figure 7.1. In addition to energy density, the degree of parton energy loss was demonstrated to depend upon the collective flow field. In their treatment, the

7.1. THEORETICAL TREATMENTS OF MODIFICATIONS TO THE SAME SIDE PEAK

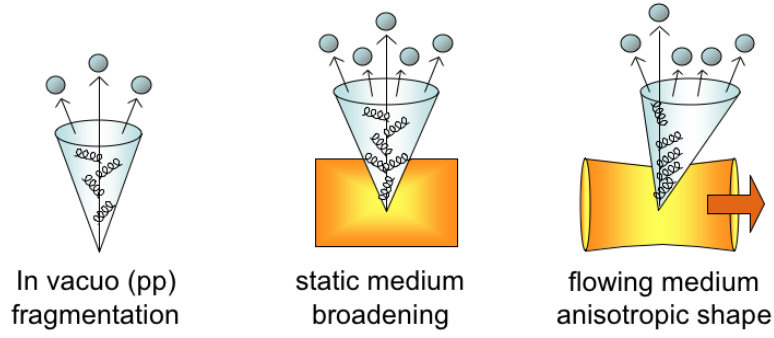


Figure 7.1: Schematic representation of longitudinal flow coupled to jet attenuation. The jet cone in the centre image is broader than the vacuum fragmentation (right) due to interactions with a static medium. Adding string longitudinal flow results in further elongation parallel to the flow.

medium was modelled as a collection of scattering centres with momenta reflecting the system expansion (flow). Although the direction of momentum transfer between a hard parton and a scattering centre was random, the final distribution of jet fragments after several interactions tends to be elongated in the direction of the flow. The magnitude of the effect increases with momentum difference between parton and medium. Since the longitudinal expansion increases with rapidity, so does the strength of the interaction. Two-particle correlations were predicted to show a small degree of broadening in the azimuthal direction and a much more substantial broadening in the pseudo-rapidity direction.

The paper predicts significant momentum transfer in the longitudinal direction due to flow, with little effect upon the transverse distribution. This is consistent with the observed modification to the jet component, which appears elongated in $\Delta\eta$ without any change to the yield for a given p_T selection. The ridge represents a significant increase in yield for a given p_T , and so is less easily explained by this mechanism. However, the paper neither considered the resulting distribution of radiated gluons coupled to longitudinal flow, nor the response of the medium to the jet. Were these to be remedied, the ridge may indeed emerge from this treatment.

7.1.2 Coupling to radial flow

A different treatment of jet coupling to collective flow was developed by Voloshin [93]. Instead of longitudinal expansion, this work concentrated upon the influence of radial flow, starting from the framework developed to study elliptic flow. The strong position-momentum correlations caused by the initial collision geometry result in a common transverse momentum boost to jet fragments and gluons radiated via interaction with the medium. This momentum correlation is localised in the azimuthal direction, and the longitudinal expansion of the system redistributes the correlated particles over a large rapidity range. Although the momentum transfer is transverse to the beam axis, the rescattering of jet fragments is also predicted to result in diffusion into the rapidity direction. These effects combined are expected to give rise to elongation of two-particle correlations in the $\Delta\eta$ direction. The model further predicts that the magnitude of the correlation should be sensitive to the thermalisation time of the system and the diffusion of particles in a thermalised medium.

This description offers a promising qualitative explanation for the ridge, and is bolstered by the success of this framework in describing elliptic flow. Transverse momentum transfer would result in an increased correlation yield for a given p_T interval, which could be accounted for by the presence of the ridge.

7.1.3 Parton recombination

This analysis has concerned trigger and associated tracks within p_T intervals where parton recombination is believed to dominate particle production. Consequently the modified jet and ridge features may also be explained by this mechanism. Chiu and Hwa considered the jet and ridge components separately in the context of a parton recombination model [94].

In considering the origin of the ridge, the experimentally determined background

7.1. THEORETICAL TREATMENTS OF MODIFICATIONS TO THE SAME SIDE PEAK

subtraction method was discussed. In terms of the recombination model, the background is populated by thermal recombination. Thus subtracting the background should remove these contributions, leaving hadrons that were at least partially formed from shower partons. However, this ignores the effect of medium heating due to interactions with jet (shower) partons. The heated region is localised in the azimuthal plane because the system expands radially, but can be extended in pseudorapidity due to the longitudinal expansion. Consequently by assuming the background level in correlations to be determined by the yield at $|\Delta\phi| = 1.0$ (see section 4.4.2), an enhanced thermal distribution at small angular separations can persist. These remaining hadrons that are thermally produced are identified with the ridge by the authors. Within this framework the magnitude of the ridge indicates the degree of medium heating by the jet.

The peak atop the ridge was described by the calculation in terms of shower-thermal and shower-shower contributions. The model successfully predicted the amplitude of this component, but the width in $\Delta\eta$ and $\Delta\phi$ were fit to data.

Parton recombination models make another prediction concerning multi-strange hadrons. Calculations suggest that these states should be predominantly produced by thermal recombination in heavy ion collisions [95]. This is a consequence of the relatively low contribution of shower s quarks within the framework. Therefore the amount of Ω baryons (sss) and ϕ mesons ($s\bar{s}$) that originate from fragmentation should be negligible. This outcome leads to the prediction that no correlation peak should be observed for correlations involving these particles. Studies of Ω -triggered azimuthal correlations at STAR do indeed show a same side peak, with comparable magnitude to other trigger species [96]. For this observation to be consistent with parton recombination models, the same side yield must be entirely composed of ridge. Moreover this could suggest that the ridge and jet features do not co-exist. Studies to verify the jet and ridge contributions of multi-strange triggered

correlations are ongoing.

7.1.4 Non-equilibrium QGP

Recent theoretical studies of plasma instabilities in non-equilibrium QGP have offered an alternative explanation for the longitudinal broadening of the same side peak. A QGP with an anisotropic position-momentum distribution has been shown to develop filamentation instabilities that result in a turbulent system [97]. This model offers a possible explanation for the short thermalisation times needed for hydrodynamical calculations. Majumder *et al.* considered the implications such a system would have for jet attenuation [98]. Instabilities were found to develop radially, which resulted in a tendency for soft gluons radiated from hard partons to be deflected in the longitudinal direction.

An important difference between this model and those introduced in the preceding discussions is in this calculation, partons were interacting with collective modes of the plasma as opposed to individual scattering centres.

7.2 Recent studies of away side peak

7.2.1 Re-emergence of di-jets at high- p_T

More recent studies benefiting from substantially larger datasets have demonstrated the re-emergence of the away side correlation peak at sufficiently high- p_T [99]. In figure 7.2 a comparison is drawn between correlations of unidentified charged tracks reconstructed from $d + Au$, 20–40% $Au + Au$ and 0–5% central $Au + Au$ collisions. The momentum interval of the trigger for all frames is $8.0 \leq p_T^{trig.} \leq 15$ GeV/c, and the p_T range of associated tracks is increased from top to bottom. For the highest range considered, negligible combinatorial background is observed in all three systems. An away side peak is clearly visible in the $Au + Au$ correlation,

albeit smaller than the $d + Au$ peak. For a given set of p_T intervals the correlation peaks have similar widths, suggesting fragmentation occurs outside any medium.

In selecting tracks with such high momenta, the accepted collection of di-jets is likely to be biased towards surface emission through the thinnest part of the medium. Even so, the remaining suppression of the away side peak in the $Au + Au$ correlation gives a compelling case for in-medium attenuation prior to fragmentation.

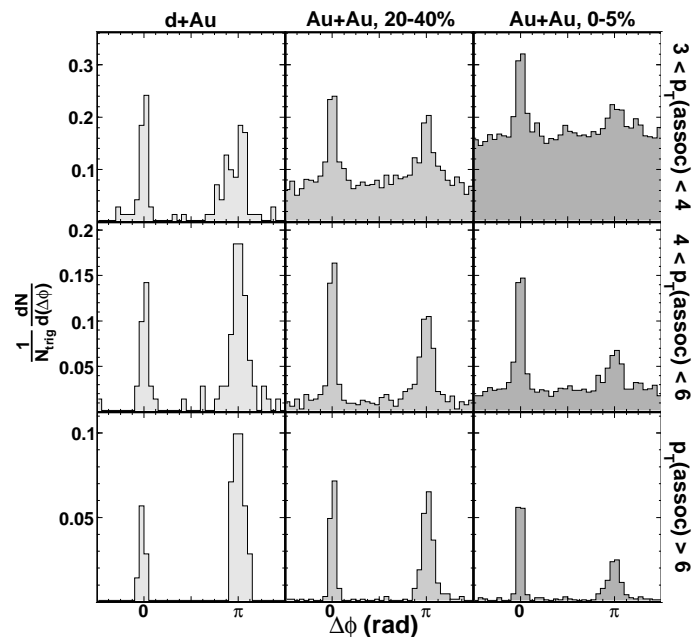


Figure 7.2: Raw azimuthal correlations of high p_T charged hadrons for $8 \leq p_T^{trig.} \leq 15$ GeV/c, for $d + Au$, 20 – 40% $Au + Au$ and 0 – 5% $Au + Au$ events. $p_T^{asso.}$ increases from top to bottom.

7.2.2 Medium response to jets at low- p_T

The momentum transferred through jet attenuation is expected to appear at momenta below that considered in the original correlation analysis at STAR. Recent studies at RHIC of correlations with charged tracks at lower p_T than the present analysis have revealed evidence of medium modification due to the presence of jets

in the away side peak. For pairs within the momentum interval $2.5 \leq p_T^{trig.} \leq 4.0$ GeV/c and $1.0 \leq p_T^{asso.} \leq 2.5$ GeV/c, the away side peak in central $Au+Au$ collisions is enhanced compared to $d + Au$ collisions. Furthermore, the enhanced peak shape comprises a double peak structure, symmetrical about $\Delta\phi = \pi$. Figure 7.3 displays a typical correlation of tracks in this low- p_T interval for $Au + Au$ correlations and $d + Au$ for comparison.

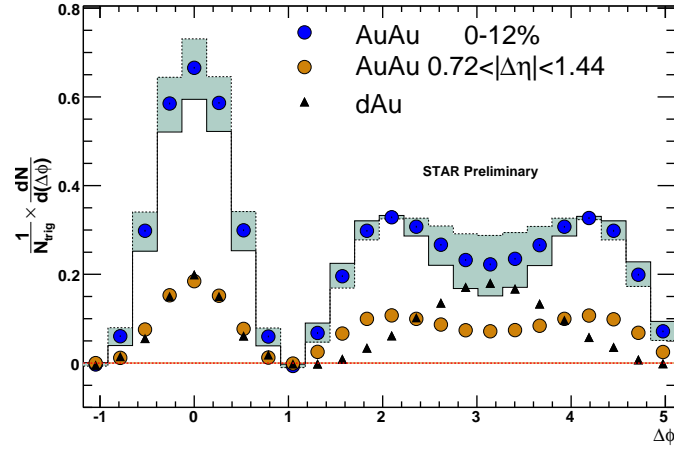


Figure 7.3: Low- p_T two-particle correlation involving unidentified charged tracks with $2.5 \leq p_T^{trig.} \leq 4.0$ GeV/c and $1.0 \leq p_T^{asso.} \leq 2.5$ GeV/c measured at STAR [100]. Triangle data points represent $d + Au$ collisions, circles show the correlation in 0 – 12% central $Au + Au$ collisions for pairs with different pseudorapidity separations. Unlike the simple dijet structure observed in $d + Au$, the $Au + Au$ results show double peak on the away side.

Several suggestions have been proposed to explain this structure. Two categories of theoretical approaches exist to date: conical emission, including Mach shocks [101] and Cerenkov radiation [102], and deflected jets [103]. The former set consider the two-peak structure to comprise the response of the medium to a hard parton. The second option suggests that the peaks are indeed jets, but they have incurred a (single) large radiative interaction with the medium.

In the case of conical emission, both peaks exist on an event-by-event basis, as the azimuthal correlation is essentially displaying the projection of a cone. However two peaks are observed only after summing over many events for the deflected jet

scenario. This distinction motivated three particle correlations, involving one trigger and two associated particles. In the left frame of figure 7.4, the expectations of three particle correlations as performed at STAR are illustrated. Each axis represents the azimuthal separation of one associated particle with the trigger. Projections onto either axis give the same two-particle distribution. The red region represents the same side correlation and the green peaks contain combinations where one associated particle was on the same side and the other on the away side. The blue and orange areas would be occupied by combinations where both associated particles are on the away side. Both associated particles have the same azimuthal position if located in the orange regions. Both theoretical approaches would predict peaks at these locations. The blue regions however, can only appear in the case of conical emission.

Three-particle correlations are shown for several systems to the right of figure 7.4. Although the uncertainties are large, the results support the hypothesis of conical emission [104]. Jet deflection could also be present as the two processes may coexist. Further insight into the nature of the away side in $Au + Au$ may be obtained via identified (associated) particle correlations as the meson-baryon difference within a jet cone should be similar to $p + p$, not the medium.

7.3 Prospects for correlation analyses

Two- and three-particle correlations will surely continue to play an integral role in future investigations of QGP formation in high energy nuclear collisions. The substantial modifications to both same side and away side peaks give some of the most compelling evidence of colour-deconfined matter through its interaction with hard partons that traverse it. Correlations appear to reveal both the jet response to the medium and the medium response to the jet. With the advance of theoretical treatments, the detailed study of correlation peaks as a function of system size, energy, pair kinematics and species can return quantitative properties of the medium,

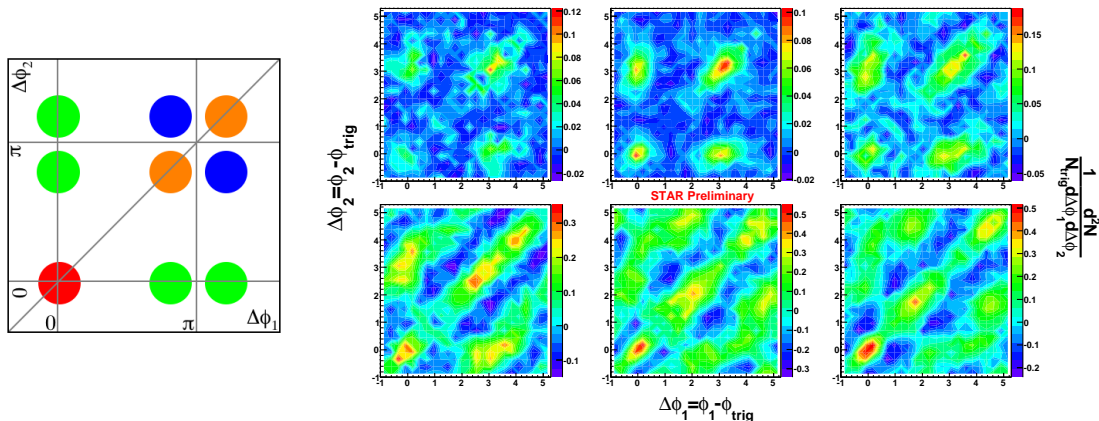


Figure 7.4: Intermediate- p_T three-particle correlations involving unidentified charged tracks measured at STAR [104]. Several collision systems are considered: $p + p$ (top-left), $d + Au$ (top middle), and 50 – 80% central $Au + Au$ (top right), 30 – 50% (bottom left), 10-30% (bottom middle), and 0 – 12% (bottom right). To the left of the results, a schematic of the expected $Au + Au$ result given different scenarios is shown. The red region represents the same side peak. Green peaks contain combinations where one associated particle was on the same side and the other on the away side. Blue and orange areas represent combinations where both associated particles are on the away side. If pairs are found in the blue region, the two peaks in the away side co-exist in the same event.

which ultimately can be used to test QCD.

7.3.1 Correlations with identified particles

The relationship between leading particle species and parent parton type can be exploited to discriminate between quark and gluon jets on a statistical basis, a method called jet tagging. Comparisons of correlations with different trigger species could offer an important test to parton attenuation models. A hard gluon traversing a QGP would suffer stronger attenuation by gluon radiation than a quark by a factor of ~ 2.25 because of the stronger QCD coupling [55].

Ascertaining whether the composition of the ridge is similar to the medium or the jet can give a strong indication of its origin. In particular the relative abundance of different species is useful as the ridge exists in the p_T region where the baryon

enhancement appears. If the particles forming the ridge originate from the jet, then baryons and mesons should be found according to $p + p$ spectra.

Correlations with identified associated particles can provide the relative abundance of baryons to mesons in both jet and ridge components. The present analysis has demonstrated comparable correlation shapes with associated $V0$ tracks to unidentified correlations, albeit at a greatly reduced yield per trigger. Preliminary results from parallel analyses at STAR indicate the ridge may exhibit a similar baryon-meson difference to spectra, and the jet component shows a greater similarity to $p + p$ spectra, but the measurement would benefit greatly from a larger dataset.

Such a dataset is being produced at the time of writing this thesis. Instead of minimum bias events, the majority of events in the new dataset are triggered on jet triggers using EMC detectors. A future analysis can take advantage of these data by forming correlations between EMC towers and associated $V0$ s (from TPC tracks). Using EMC towers as triggers also makes it possible to advance the analysis to a higher- p_T range where jets are more prominent.

A following analysis could attempt to isolate between photonic triggers. If possible, this would permit the analysis of photon-jets (where one of the jets is replaced by a photon). The great benefit of studying these phenomena is the knowledge of the complete jet energy provided by the photon.

7.3.2 Three particle analysis of the same side

Despite assertions from theory, there is currently no experimental evidence to suggest that the jet and ridge features coexist in the same events. Indeed they could relate to two mutually exclusive processes. For instance the jet component could be formed by surface emission, and the ridge could result from quenched jets (although this is unlikely if the ridge persists to much higher p_T^{trig}). If this could be proven, it would

have clear implications as to which theoretical treatments could apply.

A direct means to resolve this uncertainty is to perform three particle correlations of the same side peak. An identical arrangement could be used to the three particle correlations employed at STAR to study the away side peak: one trigger particle and two associations. Also similar to that study, the correlation between associated particles would reveal whether the ridge and jet are found together in the same event. For this analysis the pseudo-rapidity difference of associated particles would also be needed.

7.3.3 Momentum-weighted correlations

Particle identified correlations benefit from a high purity of a given particle species, but at the expense of statistics. If significantly larger datasets do not become available, it will be necessary to develop alternative measures to those presented in the current analysis. A particular disadvantage of the current studies of kinematics is the need to sub-divide correlations into p_T bins.

It may be possible to avoid this subdivision by producing p_T -weighted correlations. The principle is as follows: on a pair-wise basis correlations are filled weighted by the momentum of the associated particle. This results in correlation functions whose occupancies per angular bin are given by the product of the total number of pairs in that phasespace and the total momentum of the associated tracks in that bin. The mean momentum of associated particles (within the $p_T^{asso.}$ interval) as a function of the angular variable(s) can then be extracted by dividing the weighted correlation by an unweighted correlation. By this means the distribution of jet and ridge components can be compared. Note that no acceptance correction is required in this approach as detector acceptance is eliminated by taking the ratio of the two correlations.

7.3.4 Outlook

The results presented in this thesis form part of a larger effort to provide quantitative measurements of strong interaction dynamics in hot QCD matter. The earlier observations of strong elliptic flow and substantial effects of parton energy loss on high- p_T particle production have qualitatively shown that a strongly interacting QGP is formed in central heavy ion collisions at RHIC. The data analysed in this thesis are from the first large statistics heavy ion run at RHIC, which should provide a quantitative constraints for theoretical models and eventually allow the properties of hot QCD matter, such as the transport coefficient and viscosity to be determined.

It is an exciting time for experiment and theory alike, with a heavy ion programme at $\sqrt{s_{NN}} = 5500$ GeV at ALICE at the new Large Hadron Collider (LHC) at CERN to commence in the next few years. Higher energy collisions are likely to create longer lived QGP phases, and higher initial state parton densities. Complementary studies of sub-RHIC energy collisions are planned at RHIC and other facilities in order to search for the critical point of the QCD phase diagram.

Correlation techniques are likely to play an important role in these future endeavours, in particular at the LHC where the higher energy collisions should allow more quantitative comparisons of experiment to calculations, and where gamma jet, and tagged jet studies will become more viable. New challenges can be anticipated due to the increased di-jet cross-section (several hard parton scatters per collision are likely), and the reduced away side peak yield at mid rapidity due to the larger rapidity range. However, since correlation techniques have successfully extracted jet phenomena from the high background environments observed at RHIC, these methods represent a promising tool for future experiments to further characterise the QGP.

Appendices

Appendix A

COLLISION KINEMATICS

The following discussion is intended as an introduction to readers unfamiliar to the field of the basic formalism commonly applied to describe high energy particle collisions. Through the example of hard parton scatter in hadronic collisions, the variables used to characterise particles before and after the collision shall be reviewed, with the aim of demonstrating that these are the natural quantities to consider. This appendix was compiled largely from discussions given in [105] and [106].

The generalised hard scattering process is visualised in figure A.1, having been separated into parton distribution functions G , pQCD cross-section $d\sigma/dt$ (where t is momentum transfer, see below), and fragmentation functions D , as described in section 2.1. As is the convention, in the figure initial hadrons are labelled A and B , and the subsequent interaction involves constituent partons a and b . Partons c and d result from the interaction, and lead to the production of final state hadrons h_1 and h_2 respectively via fragmentation. The probability of finding a parton a in hadron A with momentum fraction $x_a < p_a/p_A < x_a + dx$ is given by the parton distribution function $G_{a/A}(x_a)$. Similarly, the probability for a hadron h_1 to fragment from parton c with momentum fraction $z_c < p_{h_1}/p_c < z_c + dz$ is given by the fragmentation function $D_{h_1/c}(z_c)$.

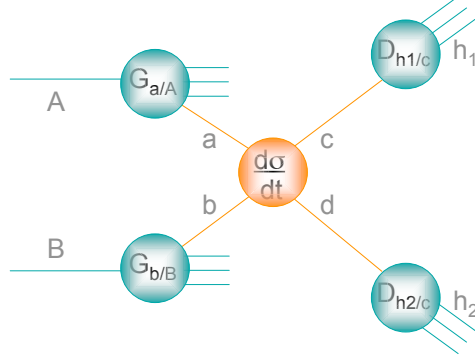


Figure A.1: Schematic representation of hard scatter between constituent partons a and b from hadrons A and B , resulting in partons c and d , and subsequently hadrons h_1 and h_2 . The process is factorised into non-perturbative (blue) and perturbative elements (orange): parton distribution functions G , pQCD cross-section $d\sigma/dt$ (where t is momentum transfer, see text), and fragmentation functions D .

In the interaction $A + B \rightarrow C + D$, the four momentum transfer can be described by the Mandelstam variables [107] s , t , and u , where s is the square of the centre-of-momentum energy, and t and u are the squares of the momentum transfer from each initial to final particle,

$$\begin{aligned} s &= (p_A + p_B)^2 = (p_C + p_D)^2, \\ u &= (p_A - p_C)^2 = (p_B - p_D)^2, \\ t &= (p_A - p_D)^2 = (p_B - p_C)^2, \end{aligned} \tag{A.1}$$

where $p_i = (E, p_x, p_y, p_z)$ is the four momentum of particle i . The sum of the Mandelstam variables provides the total mass of the particles, $s + t + u = \sum m$, which can be quickly verified by considering that the square of a particle's four-momentum is equal to its mass. In the hard scatter of massless constituent partons $a + b \rightarrow c + d$, this corresponding condition is $\hat{s} + \hat{t} + \hat{u} = 0$, where the *hat* symbols are used here and in subsequent formulas to denote quantities relating to partons.

Due to the typical arrangement of high energy particle collisions, transverse mo-

momentum, p_T , and longitudinal momentum, p_L , components relative to the incident trajectories are commonly used to characterise particle production. Parton a carries a fraction of its parent hadron's longitudinal momentum, $x_a = 2p_L/\sqrt{s}$. This scaled quantity is commonly referred to as the Bjorken x -parameter. For simplicity, intrinsic transverse momentum is ignored in this discussion, and thus the initial p_T of the partons are zero.

It is useful to describe particle spectra in terms of quantities that allow different experiments to be compared readily. Although p_T is invariant under any longitudinal boost, p_L is intimately linked to the collision arrangement. Consequently another measure called rapidity, y , is used in its place. Rapidity, which is defined

$$y = \frac{1}{2} \ln \left(\frac{E + p_L}{E - p_L} \right) \quad (\text{A.2})$$

is additive under a Lorentz transformation, $y' = y + \tanh^{-1} \beta$. Therefore the rapidity distributions of particles in collisions of different energies can be displayed upon the same axis. The only experimental disadvantage of rapidity is its mass dependence, which limits its use to identified particle analyses. For massless particles, the relation reduces to

$$y \xrightarrow{\lim m = 0} \eta = -\ln \tan \theta/2 \quad (\text{A.3})$$

where θ is the scattering angle in the c.m.s frame. This quantity, called pseudo-rapidity, is equivalent to rapidity in the relativistic limit, and is widely used in experimental studies of unidentified particles.

Using the notation introduced above, the initial and final (massless) parton four-momenta $p(E, p_T, p_L)$ are defined

$$\begin{aligned}
p_a &= \left(\frac{x_a \sqrt{s}}{2}, 0, \frac{x_a \sqrt{s}}{2} \right) \\
p_b &= \left(\frac{x_b \sqrt{s}}{2}, 0, -\frac{x_b \sqrt{s}}{2} \right) \\
p_c &= \left(p_T \cosh y_c, p_T, p_T \sinh y_c \right) \\
p_d &= \left(p_T \cosh y_d, p_T, p_T \sinh y_d \right)
\end{aligned} \tag{A.4}$$

where scattered partons c and d have been defined in terms of their (equal) p_T and y using the relations $E = p_T \cosh y$ and $p_L = p_T \sinh y$ derived from the definition of rapidity¹.

Given conservation of energy and momentum, the following relations apply

$$\frac{\sqrt{s}}{2}(x_a + x_b) = p_T \cosh y_c + p_T \cosh y_d \tag{A.5}$$

$$\frac{\sqrt{s}}{2}(x_a - x_b) = p_T \sinh y_c + p_T \sinh y_d \tag{A.6}$$

from which the initial Bjorken x of each parton can be expressed in terms of the final parton trajectories

$$\begin{aligned}
x_a &= \frac{1}{\sqrt{s}} \left(p_T e^{y_c} + p_T e^{-y_d} \right) \\
x_b &= \frac{1}{\sqrt{s}} \left(p_T e^{-y_c} + p_T e^{y_d} \right),
\end{aligned} \tag{A.7}$$

hence at mid rapidity, the relation is simplified to $x = 2p_T/\sqrt{s}$. Relations A.7 are useful to jet studies, since the total p_T and y of particles within a jet cone (i.e. the jet axis) are equal to the parton from which they fragmented. Thus the full reconstruction of both jets defines the initial parton momenta.

¹Note that for massive particles, p_T in these relations must be substituted for $m_T = \sqrt{p_T^2 + m_0^2}$.

Using equations A.4, the partonic Madelstam variables associated to parton c are found to be

$$\hat{s} = x_a x_b s, \quad \hat{t} = -x_a p_T \sqrt{s} e^{-y_c}, \quad \hat{u} = -x_b p_T \sqrt{s} e^{y_c}, \quad (\text{A.8})$$

with similar expressions for parton d .

Adopting the system of quantities introduced above, the dijet cross-section can be derived [106] by defining the global constraint $\delta(\hat{s} + \hat{t} + \hat{u})$ of the system in terms of the partonic variables over which the integrations must be made. The inclusive cross-section for the di-jet production $AB \rightarrow J_1 + J_2 + X$ depicted in figure A.1 can be written

$$\begin{aligned} \frac{d\sigma}{dy_c dy_d dp_T^2} (AB \rightarrow J_1 + J_2 + X) &= \sum_{ab} \int dx_a dx_b G_{a/A}(x_a) G_{b/B}(x_b) \\ &\times \frac{\hat{s}}{2} \frac{d\sigma}{d\hat{t}} (ab \rightarrow cd) \\ &\times \delta \left\{ \frac{\sqrt{s}}{2} (x_a + x_b) - p_T (\cosh y_c + \cosh y_d) \right\} \\ &\times \delta \left\{ \frac{\sqrt{s}}{2} (x_a - x_b) - p_T (\sinh y_c + \sinh y_d) \right\} \end{aligned} \quad (\text{A.9})$$

where the summation \sum_{ab} represents all possible initial state combinations of colour and spin. The pQCD cross-section is given by the summation of all parton $ab \rightarrow cd$ processes (matrix elements),

$$\frac{d\sigma}{d\hat{t}} (ab \rightarrow cd) = \frac{1}{16\pi \hat{s}^2} \sum |M(ab \rightarrow cd)|^2 \quad (\text{A.10})$$

The two δ functions introduce the conservation of energy and momentum constraints upon the system, and have been taken from equations A.5 and A.6 respectively. In this form the integration can be performed, giving

$$\frac{d\sigma}{dy_c dy_d dp_T^2} \left(AB \rightarrow J_1 + J_2 + X \right) = \sum_{ab} x_a G_{a/A}(x_a) x_b G_{b/B}(x_b) \frac{d\sigma}{d\hat{t}}(ab \rightarrow cd) \quad (\text{A.11})$$

To arrive at the cross-section for the production of hadrons h_1 and h_2 within the di-jet, the fragmentation functions D must also be included, and an integration over z be performed [105]. Finally, the invariant cross-section for the process $AB \rightarrow h_1 + h_2 + X$ is found to be

$$E \frac{d^3\sigma}{d^3p} \left(AB \rightarrow h_1 + h_2 + X \right) = \sum_{abcd} x_a G_{a/A}(x_a) x_b G_{b/B}(x_b) \frac{D_{h1/c}(z_c)}{\pi z_c} \frac{D_{h2/d}(z_d)}{\pi z_d} \frac{d\sigma}{d\hat{t}}(ab \rightarrow cd) \quad (\text{A.12})$$

where z is defined

$$z = \frac{p_T}{\sqrt{s}x_b} e^{-y} + \frac{p_T}{\sqrt{s}x_a} e^y \quad (\text{A.13})$$

Through this factorisation approach, pQCD can be used to calculate the interactions of partons in high energy collisions, with the aid of empirical measures of the non-perturbative initial and final states processes.

Appendix B

PHYSICAL INTERPRETATION OF CORRELATION PEAK WIDTHS

B.1 Same side width

A schematic of a same side pair is presented in figure B.1, together with quantities that shall be introduced in the following paragraphs. The peak width is related to the characteristics of the jet cone encompassing the jet fragments. The width of the cone depends upon the jet fragmentation process, and in particular the momentum distribution of fragments transverse to the jet axis. This is defined by the quantity j_T as shown in figure B.1, which can be calculated via the width of cone, and momenta of particles associated to the jet as illustrated from the geometrical relationship set out in figure B.1. The mean transverse momentum and cone width are inversely correlated, which reflects the independence of $\langle j_T \rangle$ upon the p_T of the jet fragments.

In triggered correlations, the quantity j_T relates to the momentum of associated

particles transverse to the trigger axis, $p_{out,S}$. Assuming Gaussian statistics, j_T can be deduced from the mean p_T of associated particles, $p_T^{asso.}$, and the same side correlation width, σ_{SS} ,

$$\langle j_T \rangle \approx \langle p_T^{asso} \rangle \sin \frac{\sigma_{SS}}{\sqrt{\pi}}. \quad (\text{B.1})$$

The angular deviation of the trigger away from the jet axis modifies the peak width and introduces an artificial dependence of the measured j_T on the transverse momentum of the trigger. Higher- p_T triggers tend to lie closer to the jet axis (carry a larger fraction of the total jet momentum), hence the width should narrow with increasing p_T^{trig} . Consequently in triggered correlations $\langle j_T \rangle$ increases with p_T^{trig} to a saturation level.

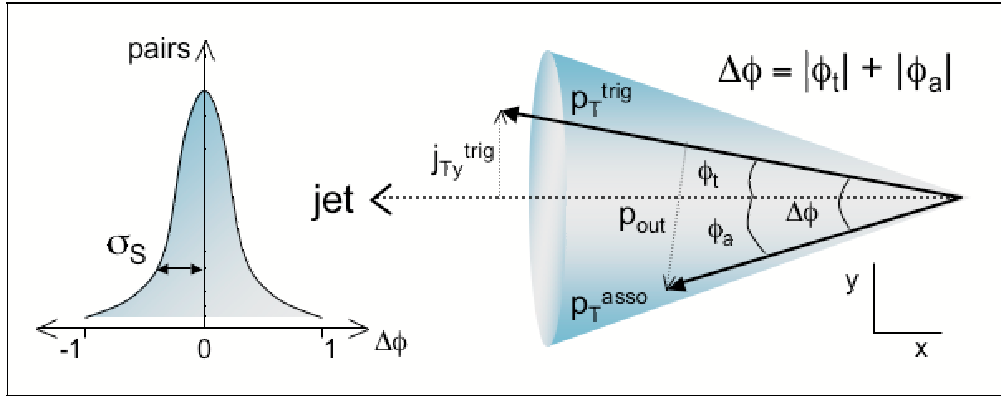


Figure B.1: Schematic representation of the same side peak in a two particle correlation.

B.2 Away side width

In triggered correlations, the away side peak width also depends upon $\langle j_T \rangle$, but is complicated by the acoplanarity of jet axes. This is illustrated in figure B.2. Ignoring experimental reconstruction efficiencies, di-jets are identically back-to-back if the total transverse momentum in the parton frame is zero. This is generally not

B.2. AWAY SIDE WIDTH

the case for hadron collisions, where the constituent partons possess intrinsic (fermi) momentum due to their confinement. This initial p_T is commonly referred to as k_T , and results in a broadening of the away side peak in correlations relative to the same side peak. Similarly to estimations of $\langle j_T \rangle$, $\langle k_T \rangle$ can be approximated from correlations via $p_T^{asso.}$ and peak widths by the relation

$$\langle k_T \rangle \approx \langle p_T^{asso} \rangle \sqrt{\sigma_{AS}^2 - \sigma_{SS}^2}. \quad (\text{B.2})$$

where σ_{AS}^2 and σ_{SS}^2 denote away side and near side widths respectively.

Two particle correlations of light nuclear systems have been characterised at RHIC via $\langle j_T \rangle$ and $\langle k_T \rangle$ estimates[108]. Alternative definitions to those given above can be derived from the pair geometry have also been applied to RHIC data. Regardless of the derivation, the interpretation of both $\langle j_T \rangle$ and $\langle k_T \rangle$ suffer from the bias introduced via the pair selection criteria, as shall be discussed in the following section. As for peak yields, direct comparisons of peak widths offer a more model independent means to compare different collision systems.

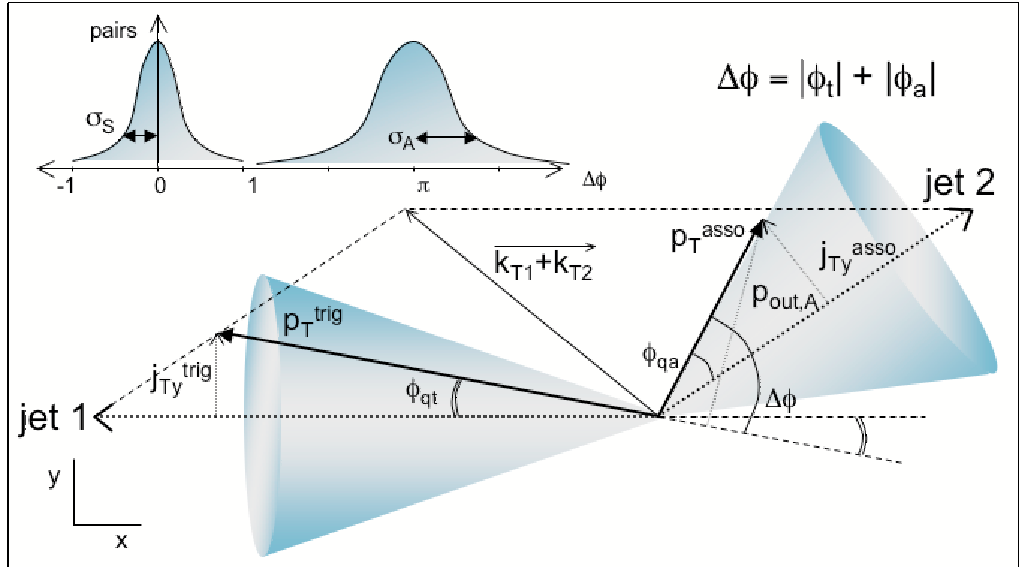


Figure B.2: Schematic representation of the away side peak in a two particle correlation.

Appendix C

NON-JET CONTRIBUTIONS IN TWO-PARTICLE CORRELATIONS

C.1 Uncorrelated background

Analytically, for two independent collections of particles, $f(p_1)$ and $f(p_2)$, the distribution of one relative to the other is given by a convolution. The proof of this statement is as follows. The density of pairs as a function of the difference variable, $\Delta p = p_1 + p_2$, is given by the product of singles,

$$f(\Delta p) = f(p_1) \cdot f(p_2) \cdot \delta(p_1 + p_2 - \Delta p) \quad (\text{C.1})$$

Integrating this expression with respect to one variable results in the distribution of the second as a function of the difference variable,

$$D(\Delta p) = \int dp_2 \cdot f(\Delta p - p_2) \cdot f(p_2) \quad (\text{C.2})$$

which is the standard relation for the convolution $f(p_1) \otimes f(p_2)$.

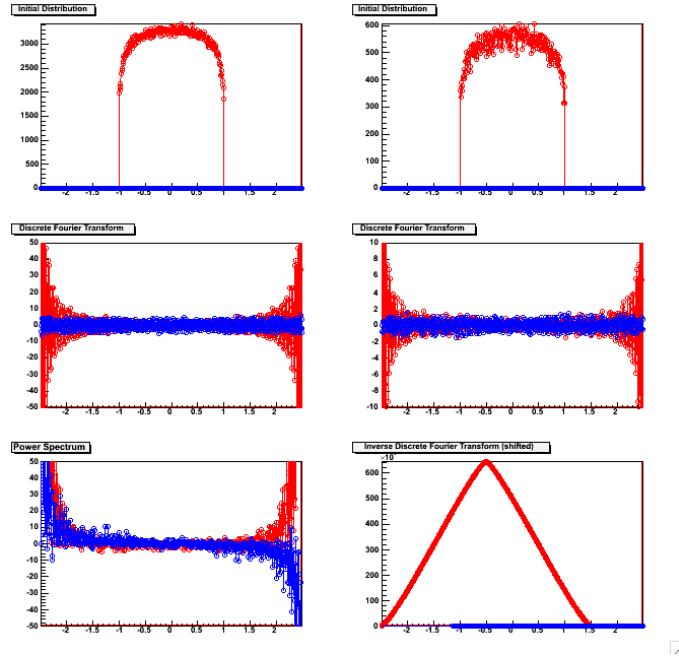


Figure C.1: Convolution of trigger and associated particle pseudorapidity distributions. In each panel the red markers display real coefficients and the blue imaginary.

To illustrate this, figures C.1 and C.2 show the discrete convolutions of the azimuthal and pseudorapidity distributions of real charged tracks in the STAR TPC. These convolutions were evaluated using a discrete Fast Fourier Transform algorithm, and implementing Parseval's Theorem¹. The convolution of a flat, finite distribution is triangular. This can be confirmed analytically, and is intuitively correct by way of considering the statistical weight of pairs across the difference co-ordinate range. The azimuthal distribution is periodic, which results in a flat convolution. The regular peaks in this distribution are caused by regions of poor acceptance between TPC sectors (see section 3.3). Therefore in correlations of TPC tracks, the background is expected to follow the shapes described by these convolutions.

¹inverse Fourier Transform of the product of the Fourier transforms of each collection. This is analogous to producing a power spectrum [109]

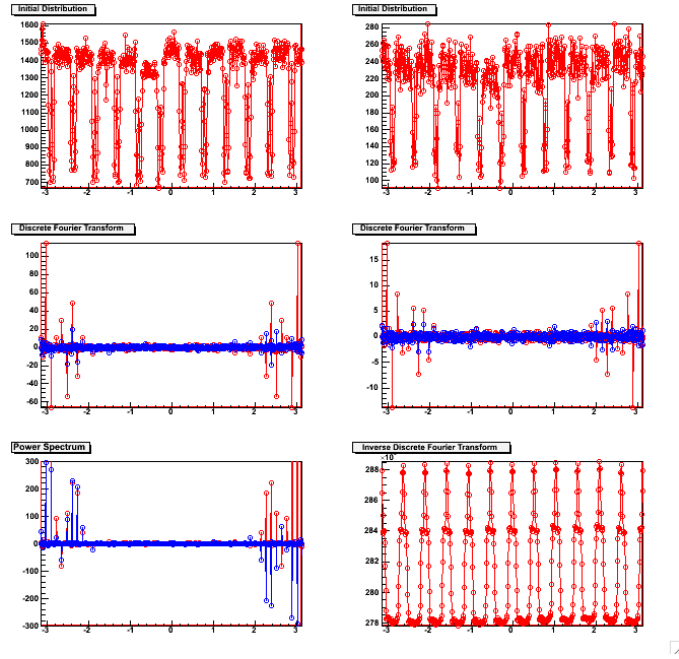


Figure C.2: Convolution of trigger and associated particle azimuthal distributions. In each panel the red markers display real coefficients and the blue imaginary.

C.2 Momentum conservation in two-particle correlations

The above description of combinatorial background assumed no correlation between the two distributions. Indeed the two distributions could have been taken from different collision events. For particles produced in the same event however, correlations can exist due to global constraints of the ensemble.

In particular, in the transverse plane momentum is well constrained, since the initial transverse momentum is small. The vector sum of the transverse momenta of final state particles is zero to good approximation. This conserved property alone introduces a back-to-back correlation between particles produced in the nuclear collision. The correlation is intuitive for low multiplicity events: in the extreme case of just two final state particles, these products will have equal and opposite momentum components in the transverse plane. This correlation clearly weakens

with higher multiplicities. The general form of the two-particle correlation due to global p_T conservation as a function of particle momenta \mathbf{p}_{T1} and \mathbf{p}_{T2} , and system multiplicity N can be written as

$$C(\mathbf{p}_1, \mathbf{p}_2) = -\frac{2\mathbf{p}_{T1} \cdot \mathbf{p}_{T2}}{N\langle p_T^2 \rangle} \quad (\text{C.3})$$

where represents the mean p_T of the ensemble. The cumulant is a scalar product of the two particle momenta. Thus in an azimuthal correlation one should expect a sinusoidal distribution of pairs, with period π and phase $-\pi$. Critically the magnitude of this effect depends upon the inverse of the system multiplicity. Therefore this contribution should be considerably more significant in $d + Au$ than central $Au + Au$ systems. The derivation of this cumulant is as follows, which has been adapted from [110].

Consider a system of N particles produced in a URHIC, with (normalised) p_T distribution $f(p)$ and globally satisfying $\mathbf{p}_{T1} + \dots + \mathbf{p}_{TN} = 0$. The two particle cumulant is obtained by the standard relation

$$C(\mathbf{p}_1, \mathbf{p}_2) = \frac{f_c(\mathbf{p}_1, \mathbf{p}_2)}{f_c(\mathbf{p}_1)f_c(\mathbf{p}_2)} - 1 \quad (\text{C.4})$$

where $f_c(\mathbf{p}_1)$ and $f_c(\mathbf{p}_1, \mathbf{p}_2)$ are the constrained single and two particle distributions of the system. Thus to find the cumulant due to global p_T conservation, it is necessary to find each of these given the constraint. The general form of the k -particle distribution (where $k < N$) is

$$f_c(\mathbf{p}_1, \dots, \mathbf{p}_k) \equiv \frac{\left(\prod_{i=1}^k f(\mathbf{p}_i) \right) \int \delta^2(\mathbf{p}_{T1} + \dots + \mathbf{p}_{TN}) \prod_{i=k+1}^N (f(\mathbf{p}_i) d^3\mathbf{p}_i)}{\int \delta^2(\mathbf{p}_{T1} + \dots + \mathbf{p}_{TN}) \prod_{i=1}^N (f(\mathbf{p}_i) d^3\mathbf{p}_i)} \quad (\text{C.5})$$

where the global constraint is introduced by the delta functions. According to the central limit theorem, for a large system of particles, the sum of momenta for M uncorrelated particles, given by $\mathbf{P}_T \equiv \sum_{i=1}^M \mathbf{p}_{T_i}$, should be described by Gaussian distribution. Using this assumption, the integrals of the numerator and denominator reduce to

$$\begin{aligned} F_M(\mathbf{P}_T) &\equiv \int \delta^2 \left(-\mathbf{P}_T + \sum_{i=1}^M \mathbf{p}_{T_i} \right) \prod_{i=1}^M (f(\mathbf{p}_i) d^3 \mathbf{p}_i) \\ &= \frac{1}{\pi \sigma^2} \exp \left(-\frac{\mathbf{P}_T^2}{\sigma^2} \right). \end{aligned} \quad (\text{C.6})$$

where the width is $\sigma^2 = \langle \mathbf{P}_T^2 \rangle = M \langle p_T^2 \rangle$. Equation C.5 therefore becomes

$$\begin{aligned} f_c(\mathbf{p}_1, \dots, \mathbf{p}_k) &= \left(\prod_{i=1}^k f(\mathbf{p}_i) \right) \frac{F_{N-k} \left(-\sum_{i=1}^k \mathbf{p}_{T_i} \right)}{F_N(0)} \\ &= \left(\prod_{i=1}^k f(\mathbf{p}_i) \right) \frac{N}{N-k} \exp \left(-\frac{\left(\sum_{i=1}^k \mathbf{p}_{T_i} \right)^2}{(N-k) \langle \mathbf{P}_T^2 \rangle} \right). \end{aligned} \quad (\text{C.7})$$

Expansion of the exponential with the aid of a Taylor series to leading order in N^{-1} gives the following approximations to the $k=1$ and $k=2$ distributions

$$\begin{aligned} f_c(\mathbf{p}) &= f(\mathbf{p}) \left(1 + \frac{1}{N} - \frac{\mathbf{p}_T^2}{N \langle p_T^2 \rangle} \right), \\ f_c(\mathbf{p}_1, \mathbf{p}_2) &= f(\mathbf{p}_1) f(\mathbf{p}_2) \left(1 + \frac{2}{N} - \frac{(\mathbf{p}_{T_1} + \mathbf{p}_{T_2})^2}{N \langle p_T^2 \rangle} \right) \end{aligned} \quad (\text{C.8})$$

which, when inserted into equation C.4 gives the following expression for the

correlation due to global p_T conservation

$$C(\mathbf{p}_1, \mathbf{p}_2) = -\frac{2\mathbf{p}_{T1} \cdot \mathbf{p}_{T2}}{N\langle p_T^2 \rangle} \quad (\text{C.9})$$

The final form of the cumulant is a scalar product of the two particle momenta. Thus in an azimuthal correlation one should expect a sinusoidal distribution of pairs, with period π and phase $-\pi$, and amplitude increasing with the magnitude of particle momenta and inversely proportional to the system multiplicity.

C.3 Elliptic flow in two-particle correlations

Although there may be no relationship between a jet axis and the reaction plane, elliptic flow enters correlations as a modulation of the combinatorial background: the distributions of background trigger and associated tracks are oriented to a common reaction plane, Ψ relative to the laboratory co-ordinate system. Therefore pairs will preferably be found with azimuthal separations of $\Delta\phi \sim 0$ and $\Delta\phi \sim \pi$.

Following on from the previous treatment of background as a convolution of single particle distributions, the relationship between the two particle modulation and the elliptic flow of trigger and associated particles can be determined by the considering the product of single particle distributions. Substituting equation 2.2 for $f(p_1)$ and $f(p_2)$, and denoting the trigger and associated particle azimuthal coordinates ϕ_t and ϕ_a respectively, the pair density as a function of $\Delta\phi = \phi_a - \phi_t$ is given by

$$\begin{aligned} f(\Delta\phi) &\propto \left[1 + 2v_2^t(p_T) \cos(2(\phi^t - \Psi))\right] \cdot \left[1 + 2v_2^a(p_T) \cos(2(\phi^a - \Psi))\right] \\ &\propto 1 + 2v_2^t(p_T) \cos(2(\phi^t - \Psi)) + 2v_2^a(p_T) \cos(2(\phi^a - \Psi)) \\ &\quad + 2v_2^t(p_T)v_2^a(p_T)(\cos(2(\phi^a + \phi^t)) + \cos(2(\phi^a - \phi^t))) \end{aligned} \quad (\text{C.10})$$

where the terms v_2^t and v_2^a represent the amplitude of the cosine function relative to the reaction plane, Ψ , for the trigger and associated particle distributions respectively. The product of cosine terms has been expanded using the standard two-angle identities. Using the relation $\Delta\phi = \phi^a - \phi^t$, the difference variable can be introduced into the expression, whilst eliminating the angular position of the associated particles, giving

$$\begin{aligned} f(\Delta\phi) \propto & 1 + 2v_2^t(p_T) \cos(2(\phi^t - \Psi)) + 2v_2^a(p_T) \cos(2(\phi^t - \Delta\phi - \Psi)) \\ & + 2v_2^t(p_T)v_2^a(p_T)(\cos(2(\phi^t - \Delta\phi)) + \cos(2(\Delta\phi))) \end{aligned} \quad (\text{C.11})$$

Integrating over ϕ^t , provides the distribution of the associated particles relative to the triggers. Three of the four terms containing v_2 depend upon ϕ^t and thus disappear through this operation. The surviving v_2 modulation in the two particle distribution has a frequency of $2\Delta\phi$ and amplitude given by the product of trigger and associated v_2

$$D(\Delta\phi) \propto 1 + 2v_2^t(p_T)v_2^a(p_T) \cos(2(\Delta\phi)) \quad (\text{C.12})$$

which enters the correlation function as shown in equation 4.3.

Appendix D

SOFTWARE AND INFRASTRUCTURE

The disk space required to retain ~ 50 million fully reconstructed events from heavy ion collisions with typical multiplicities of ~ 1000 particles, and the time required to analyse them, is necessarily large. Consequently an appropriate data handling pipeline must be employed in order to process events within practical time scales. In this analysis two computing facilities were used first to filter data and then to construct correlations. The former was performed at the RHIC Computing Facility (RCF), and the latter undertaken at a dedicated farm of twenty-four dual processor SUN units. The two systems both hosted Grid network interfaces to allow parallel processing of jobs, albeit at different levels of required user intervention.

D.1 Data Filtering

The first section of this analysis pipeline involved the reading and filtering of MuDST files at RCF, so that data could be transferred to a local facility for further analysis. These files had already themselves passed through several stages of reconstruction and compression, however only a portion of the information contained within these

data was required for the present analysis and thus a certain degree of filtering was possible. Root TTrees [111] with a simpler event-wise structure were used to hold the desired event, track and $V0$ information.

Events with exotic triggers were not of interest to this analysis; only events satisfying a minimum bias or a combined ZDC and CTB central trigger were accepted. A primary vertex range of $|z| < 30\text{cm}$ was imposed at this stage. Thresholds were introduced to limit the minimum p_T of tracks stored, and in addition only $V0$ s that passed the geometrical cuts described in section 3.7 (plus a loose hypothesised invariant mass criterion) were passed to the TTree. The resultant TTrees, for $Au + Au$ events with an approximate mix of 90% central, 10% minbias, occupied approximately 1.2 kB per event for a threshold of $p_T \geq 2.0 \text{ GeV}/c$ or 5.2 kB per event when all tracks with $p_T \geq 1.0 \text{ GeV}/c$ were recorded.

Job submission at RCF was handled using the SUMS scheduler [112]. Data were distributed amongst NFS disks, dedicated data nodes and HPSS (tape), and requests for data were managed via a file catalogue. Data would migrate across these resources according to demand, and this became an automated feature later on during the term of this research project. From a single catalogue query, SUMS would spawn several independent jobs, which would be monitored throughout the lifetime of the process and finally output would be copied from the temporary working directories to a large central scratch disk.

D.2 Correlation pipeline using a dedicated local farm

Filtered TTrees were transferred to a 1.5TB central disk at the Birmingham facility where they were first processed to produced files of similar size to ensure consistency for event mixing. Events were also sorted and grouped into files according to

primary vertex z-position and magnetic field orientation, again due to event mixing considerations.

The Sun Grid Engine (SGE) [113] was integrated with the computer farm at Birmingham in order to facilitate the submission and monitoring (via Ganglia [113]) of processes on data nodes from the server. The author developed tools to subdivide jobs into independent processes so that these could be submitted in parallel to several nodes. The method followed the SUMS approach, generating file lists for each process starting with the total list of files to be analysed. Unlike at RCF, the location of the data at Birmingham was static, so a catalogue-style query was unnecessary. However for each process, data files would be temporarily copied from the central data region to the local data disks of the node hosting that sub job. Indeed all files read and produced by each parallel process would be held in a single temporary directory that would exist only for the lifetime of the process. The only exception to this were the standard output and error streams that were handled by SGE and written directly to the home region. The advantage of exporting data to local disks and writing output to the same location was a considerable reduction in the amount of network traffic throughout most of the lifetime of a job submission.

Sibling correlations and mixed event correlations were stored in two separate files, and the correlation routine operated in such a way as to create one pair of files per input data file. Thus after their production, these output files would need to be gathered together to form a single pair of sibling and mixed event files. This merging process was performed in two stages to optimise processing time. First for each parallel process sibling and mixed event files would be merged together to form a single pair. The pair resulting from each process (a maximum of 48) would then be transferred to the central data disk for a second phase of merging. Thus the final product of the correlation routine submitted at the Birmingham farm, for specific selection of events, corrections, trigger and associated particle criteria, was

a pair of sibling and mixed event correlation files. Analysis of these was performed interactively with the aid of Root macros.

References

- [1] E. D. Bloom *et al.*, Phys. Rev. Lett. **23** (1969) 930
- [2] J. D. Bjorken and E. A. Paschos, Phys. Rev. **185** (1969) 1975
- [3] M. Gell-Mann, Phys. Lett. **8:3** (1964) 214
- [4] N. Kaiser, S. Fritsch, W. Weise, Nucl. Phys. A **697** (2002) 255
- [5] N. Werner (for H1 and Zeus Collaborations), *hepl-ex/0305109*
- [6] D. H. Perkins, *Introduction To High Energy Physics*, 4th Ed.,
- [7] G. S. Bali, K. Schilling, and A. Wachter, Phys. Rev. D **56**, 2566 (1997)
- [8] M. Acciarri *et al.*, L3 Collaboration, Phys. Lett B **411** (1997) 339
- [9] N. K. Nielsen, Am. J. Phys. **49** (1981) 1171
- [10] N. F. Mott, Rev. Mod. Phys. **40** (1968) 677
- [11] F. Karsch, *et al.*, Nucl. Phys. A **698** (2002) 199
- [12] E. Laermann and O. Philipsen, *hep-ph/0303042*
- [13] D. H. Rischke, Prog. Part. Nucl. Phys. **52** (2004) 197 *nucl-th/0305030*
- [14] J. Schaffner-Bielich, Phys. Rev. Lett. **84**, 3261 (2000).
- [15] S. A. Bass, *et al.* (UrQMD Collaboration), “Microscopic Models for Ultra-relativistic Heavy Ion Collisions”, Prog. Part. Nucl. Phys. **41** (1998) 225
- [16] I. G. Bearden *et al.* (BRAHMS collaboration), Phys. Rev. Lett. **93** (2004) 102301 *nucl-ex/0312023*
- [17] J. Adams *et al.* (STAR Collaboration), Phys. Re. Lett. **92** (2004) 112301 *nucl-ex/0310004*

- [18] J. D. Bjorken, Phys. Rev. D **27** (1983) 140
- [19] S. S. Adler *et al.*, (PHENIX collaboration), *nucl-ex/0409015*
- [20] H. Caines, “What’s Interesting About Strangeness Production? - An Overview of Recent Results”, J. Phys. G**31** (2005) S101-S118 *nucl-ex/0412016*
- [21] I. Arsene *et al.* (BRAHMS collaboration), “Quarkgluon plasma and color glass condensate at RHIC? The perspective from the BRAHMS experiment”, Nucl. Phys. A **757**, (2005) 1-27
- [22] B. B. Back *et al.* (PHOBOS collaboration), “The PHOBOS perspective on discoveries at RHIC” Nucl. Phys. A **757**, (2005) 28-101
- [23] J. Adams *et al.* (STAR collaboration), “Experimental and theoretical challenges in the search for the quarkgluon plasma: The STAR Collaboration’s critical assessment of the evidence from RHIC collisions”, Nucl. Phys. A **757**, (2005) 102-183
- [24] K. Adcox *et al.* (PHENIX collaboration), “Formation of dense partonic matter in relativistic nucleusnucleus collisions at RHIC: Experimental evaluation by the PHENIX Collaboration”, Nucl. Phys. A **757**, (2005) 184-283
- [25] J. Rafelski and B. Muller, Phys. Rev. Lett. **48** (1982) 1066
- [26] Matsui and Satz, Phys. Lett. B **178** (1986) 416
- [27] J. Adams *et al.* (STAR Collaboration), “Multi-strange baryon production in $Au + Au$ collisions at $\sqrt{s_{NN}} = 130$ GeV”, Phys. Rev. Lett. **92**, 182301 (2004) *nucl-ex/0307024*
- [28] B. I. Abelev *et al.* (STAR Collaboration), “Enhanced strange baryon production in $Au + Au$ collisions compared to $p + p$ at $\sqrt{s} = 200$ GeV”, *nucl-ex0705.2511*
- [29] E. Anderson *et al.*, (WA97 experiment), Phys. Lett. B **449** (1999) 401
- [30] U. Heinz, M. Jacob, “Evidence for a new state of matter: an assessment of the results from the CERN lead beam programme.” (2000) *nucl-th/0002042*

- [31] J.-Y. Ollitrault, “Anisotropy as a signature of transverse collective flow”, Phys. Rev. D **46** (1992) 229.
- [32] J. Adams *et al.* (STAR collaboration), *nucl-ex/0409033*
- [33] R. Baier, Y. L. Dokshitzer, A. H. Mueller, S. Peigné, and D. Schiff, “Radiative energy loss of high energy quarks and gluons in a finite volume quark-gluon plasma”, Nucl. Phys. B **483** 291 (1997) *hep-ph/9607355*
- [34] M. Gyulassy and M. Plumer, Phys. Lett. B **243**, 432 (1990).
- [35] C. Adler *et al.* (STAR collaboration), Phys. Rev. Lett. **89** (2002) 202301
- [36] D. Karzeev, E. Levin, L. McLerran, Phys. Lett. B **561** (2003) 93
- [37] L. McLerran, *hep-ph/0311028*
- [38] J. Adams *et al.* (STAR collaboration), Phys. Rev. Lett. **91** (2003) 072304
- [39] D. Antreasyan, J. W. Cronin, *et al.*, Phys. Rev. D **19** (1979) 764
- [40] M. A. C. Lamont (for the STAR collaboration), J. Phys. G. **30** (2004) S963
- [41] R. J. Fries *et al.*, Phys. Rev. C. **68** (2003) 044902
- [42] C. Adler *et al.* (STAR collaboration), Phys. Rev. Lett. **90** (2003) 082302
- [43] D. Hardtke, T.J. Humanic, *nucl-th/0405064*
- [44] Y. Guo, PhD Thesis, Wayne State University (2005)
- [45] D. de Florian, W. Vogelsang, “Resummed cross section for jet production at hadron colliders”, (2007) *hep-ph/0704.1677*
- [46] S. Kretzer, “Fragmentation functions from flavor-inclusive and flavor-tagged e^+e^- annihilations”, Phys. Rev. D **62** (2000) 054001
- [47] B. A. Kniehl, G. Kramer and B. Potter, Nucl. Phys. B **597** (2001) 337
- [48] M. Jacob, P. V. Landshoff, “Large Transverse Momentum and Jet Studies”, Phys. Rep. C **48** 286 (1978)
- [49] G. Boca *et al.*, “Average fraction of jet momentum carried by high P_T leading hadrons”, Z. Phys. C. **49** 543-554 (1991)
- [50] K. Ackerstaff *et al.* [OPAL Collaboration], “Multiplicity distributions of gluon

- and quark jets and tests of QCD analytic predictions”, Eur. Phys. J. C **1** (1998) 479 *hep-ex/9708029*
- [51] K. Ackerstaff *et al.* [OPAL Collaboration], “Production of K_{Short}^0 and Λ in quark and gluon jets from Z^0 decay”, Eur. Phys. J. C **8** (1999) 241 *hep-ex/9805025*
- [52] X.-N. Wang, Phys. Lett. B **579** (2004) 299
- [53] M. H. Thoma and M. Gyulassy, “QUARK DAMPING AND ENERGY LOSS IN THE HIGH TEMPERATURE QCD,” Nucl. Phys. B **351** (1991) 491.
- [54] L. D. Landau and I. Ya. Pomeranchuk, Dokl. Akad. Nauk. SSSR, **92** (1953) 535, A. B. Migdal, Phys. Rev. **103** (1956) 1811
- [55] A. Dainese, C. Loizides, G. Paic, *hep-ph/0406201* (2004)
- [56] K.J. Eskola, H. Honkanen, C.A. Salgado and U.A Wiedemann, Nucl.Phys. **A747** (2005) 511 *hep-ph/0406319*
- [57] M. Gyulassy, P. Levai, I. Vitev, Nucl. Phys. A **661** (1999) 637
- [58] B. G. Zakharov, “Radiative energy loss of high energy quarks in finite-size nuclear matter and quark-gluon plasma”, JETP Lett. **65** 615 (1997) *hep-ph/9704255*
- [59] E. Wang and X.-N. Wang, “Parton energy loss with detailed balance”, Phys. Rev. Lett. **87** 14 (2001)
- [60] K. Gallmeister and W. Cassing, Nucl.Phys. **A748** (2005) 241 *hep-ph/0408223*
- [61] X.-N. Wang, *nucl-th/0305010*
- [62] S. Adler *et al.* (PHENIX Collaboration), Phys. Rev. Lett. **96** (2006) 202301
- [63] M. A. C. Lamont, *for the STAR Collaboration*, “Investigation of the High- p_T Strange Baryon Anomalies at RHIC”, Eur. Phys. J. C **49** (2007) 35
- [64] V. Greco, C.M. Ko, P. L vai, Phys. Rev. C **68**, 034904 (2003), Phys. Rev. Lett. **90**, 202302 (2003)
- [65] R.C. Hwa and C.B. Yang, Phys. Rev. C **67**, 034902 (2003)

- [66] I. Vitev and M. Gyulassy, Phys. Rev. C **65**, 041902(R) (2002)
- [67] L.D. Landau, “On the multiparticle production in high energy collisions”, Izv. Akad. Nauk Ser. Fiz. 17 (1953) 51
- [68] R. V. Gavai, S. Gupta, and S. Mukherjee, “Speed of sound and specific heat in the QCD plasma: hydrodynamics, fluctuations, and conformal symmetry”, Phys. Rev. D **71** (2005) 074013
- [69] E. Schnedermann and U. Heinz, “A hydrodynamical assessment of 200 AGeV collisions”, Phys. Rev. C 50 (1994) 1675.
- [70] K. M. O’Hara, S.L. Hemmer, M.E. Gehm, S.R. Granade, J.E. Thomas, “Observation of a Strongly Interacting Degenerate Fermi Gas of Atoms”, Science **298** (2002) 2179
- [71] P.F. Kolb and U. Heinz, “Emission angle dependent HBT at RHIC and beyond”, Nucl. Phys. A 715 (2003) 653c. *nucl-th/0208047*
- [72] S.A. Voloshin and Y. Zhang, “Flow study in relativistic nuclear collisions by Fourier expansion of Azimuthal particle distributions”, Z. Phys. C 70 (1996) 665 *hep-ph/9407282*
- [73] P. Huovinen, P.F. Kolb, U. Heinz, P.V. Ruuskanen, and S.A. Voloshin, “Radial and elliptic flow at RHIC: further predictions”, Phys. Lett. B **503** (2001) 58.
- [74] H. Hahn *et al.*, Nucl. Instrum. Methods A **499**, (2003) 245-263
- [75] J. W. Harris and B. Muller, Annu. Rev. Nucl. Part. Sci. **46** (1996) 71
- [76] M. Adamczyk *et al.*, Nucl. Instrum. Methods A **499**, (2003) 437-468
- [77] B. B. Back *et al.*, Nucl. Instrum. Methods A **499**, (2003) 603-623
- [78] K. Adcox *et al.*, Nucl. Instrum. Methods A **499**, (2003) 469-479
- [79] K. H. Ackermann *et al.*, Nucl. Instrum. Methods A **499**, (2003) 624-632
- [80] F. S. Bieser *et al.*, Nucl. Instrum. Methods A **499**, (2003) 766-777
- [81] T. Alber *et al.* (NA49 collaboration), Eur. Phys. J. A **2** (1998) 383
- [82] M. A. C. Lamont, PhD Thesis, The University of Birmingham (2002)

- [83] C. Adler *et al.* (STAR Collaboration), Phys. Rev. Lett. **89** (2002) 202301
- [84] B. B. Back *et al.* (PHOBOS collaboration), Phys. Rev. C **65** (2002) 031901
- [85] W.-M. Yao *et al.*, J. Phys. G **33** (2006) 1
- [86] H. Bichsel, “Comparison of Bethe-Bloch and Bichsel functions”, (2002) STAR Note SN0439
- [87] K. H. Ackermann *et al.*, Nucl. Inst. Meth. A **499**, (2003) 659
- [88] M. J. Horner, PhD Thesis, The University of Cape Town, (2007)
- [89] C. Adler *et al.*, (STAR collaboration), *nucl-ex/0206001*
- [90] N. N. Ajitanand *et al.*, Phys. Rev. C **72**, (2005) 011902
- [91] J. Adams *et al.*, (STAR Collaboration), “Pion interferometry in $Au + Au$ collisions at $\sqrt{s_{NN}} = 200$ GeV”, Phys. Rev. C **71** (2005) 044906
- [92] N. Armesto, C. A. Salgado and U. A. Wiedemann, “Measuring the collective flow with jets” Phys. Rev. Lett. **93**, 242301 (2004) *hep-ph/0405301*
- [93] S. A. Voloshin, “Two particle rapidity, transverse momentum, and azimuthal correlations in relativistic nuclear collisions and transverse radial expansion”, Nucl. Phys. A **749** 287 (2005) *nucl-th/0312065*
- [94] C. B. Chiu and R. C. Hwa, “Pedestal and peak structure in jet correlation”, Phys. Rev. C **72**, 034903 (2005) *nucl-th/0505014*
- [95] R. C. Hwa and C. B. Yang, “Production of strange particles at intermediate pT at RHIC”, (2006) *nucl-th/0602024*
- [96] B. I. Abelev, “Multi-strange baryon correlations at RHIC”, (2007) *nucl-ex/0705.3371*
- [97] P. Romatschke and M. Strickland, “Collective modes of an anisotropic quark gluon plasma,” Phys. Rev. D **68**, 036004 (2003) *hep-ph/0304092*
- [98] A. Majumder, B. Müller, and S. A. Bass, “Longitudinal broadening of quenched jets in turbulent color fields”, (2007) *hep-ph/0611135*
- [99] J. Adams, *et al.*, (STAR Collaboration) Phys. Rev. Lett. **97** (2006) 162301

REFERENCES

- nucl-ex/0604018*
- [100] M.J.N. Horner, *for the STAR Collaboration*, *nucl-ex/0701069*
 - [101] H. Stoecker, Nucl. Phys. **A750**, 121 (2005); J. Casalderrey-Solana, E. Shuryak and D. Teaney, J. Phys. Conf. Ser. **27**, 23 (2005).
 - [102] V. Koch, A. Majumder and X.-N. Wang, Phys. Rev. Lett. **96**, 172302 (2006).
 - [103] I. Vitev, Phys. Lett. B **630**, 78 (2005).
 - [104] J. G. Ulery, *for the STAR Collaboration*, *nucl-ex/0609047*
 - [105] G. Sterman *et al.*, “Handbook of perturbative QCD”, Rev. Mod. Phys. **67** 157 (1995)
 - [106] J. F. Owens, “Large-momentum-transfer production of direct photons, jets, and particles”, Rev. Mod. Phys. **59** 465 (1987)
 - [107] S. Mandelstam, “Determination of the Pion-Nucleon Scattering Amplitude from Dispersion Relations and Unitarity”, Phys. Rev. **112** 1344 (1958)
 - [108] J. Jia, “Probing jet properties via two-particle correlation method”, J. Phys. G. Nucl. Part. Phys. **31** S521 (2005)
 - [109] M. L. Boas “Mathematical methods in the physical sciences”, 2nd Ed., (Wiley 1983)
 - [110] N. Borghini, P. M. Dinh, J-Y. Ollitrault *nucl-th/0004026*
 - [111] R. Brun and F. Rademakers, “ROOT - An Object Oriented Data Analysis Framework”, Nucl. Inst. & Meth. in Phys. Res. A **389** (1997) 81-86. *See also* <http://root.cern.ch/>
 - [112] for STAR computing resources, see <http://www.star.bnl.gov/STAR/comp>
 - [113] Sun Grid Engine, see <http://gridengine.sunsource.net>

Appendix E

PUBLISHED PROCEEDINGS TO THE CONFERENCE: HOT QUARKS 2006